

University of Wollongong - Research Online

Thesis Collection

Title: Nanostructured materials for electrodes in lithium-ion batteries

Author: See How Ng

Year: 2007

Repository DOI:

Copyright Warning

You may print or download ONE copy of this document for the purpose of your own research or study. The University does not authorise you to copy, communicate or otherwise make available electronically to any other person any copyright material contained on this site.

You are reminded of the following: This work is copyright. Apart from any use permitted under the Copyright Act 1968, no part of this work may be reproduced by any process, nor may any other exclusive right be exercised, without the permission of the author. Copyright owners are entitled to take legal action against persons who infringe their copyright. A reproduction of material that is protected by copyright may be a copyright infringement. A court may impose penalties and award damages in relation to offences and infringements relating to copyright material.

Higher penalties may apply, and higher damages may be awarded, for offences and infringements involving the conversion of material into digital or electronic form.

Unless otherwise indicated, the views expressed in this thesis are those of the author and do not necessarily represent the views of the University of Wollongong.

Research Online is the open access repository for the University of Wollongong. For further information contact the UOW Library: research-pubs@uow.edu.au

University of Wollongong Thesis Collections

University of Wollongong Thesis Collection

University of Wollongong

Year 2007

Nanostructured materials for electrodes in lithium-ion batteries

See How Ng
University of Wollongong

Ng, See H, Nanostructured materials for electrodes in lithium-ion batteries, PhD thesis, Institute for Superconducting and Electronic Materials, University of Wollongong, 2007.
<http://ro.uow.edu.au/theses/764>

This paper is posted at Research Online.
<http://ro.uow.edu.au/theses/764>

NOTE

This online version of the thesis may have different page formatting and pagination from the paper copy held in the University of Wollongong Library.

UNIVERSITY OF WOLLONGONG

COPYRIGHT WARNING

You may print or download ONE copy of this document for the purpose of your own research or study. The University does not authorise you to copy, communicate or otherwise make available electronically to any other person any copyright material contained on this site. You are reminded of the following:

Copyright owners are entitled to take legal action against persons who infringe their copyright. A reproduction of material that is protected by copyright may be a copyright infringement. A court may impose penalties and award damages in relation to offences and infringements relating to copyright material. Higher penalties may apply, and higher damages may be awarded, for offences and infringements involving the conversion of material into digital or electronic form.

**NANOSTRUCTURED MATERIALS FOR
ELECTRODES IN LITHIUM-ION BATTERIES**

A thesis submitted in fulfillment of the
requirements for the award of the degree

DOCTOR OF PHILOSOPHY

from

UNIVERSITY OF WOLLONGONG

by

SEE HOW NG, B. ENG. (HONS.), M. ENG.

**INSTITUTE FOR SUPERCONDUCTING
& ELECTRONIC MATERIALS,
FACULTY OF ENGINEERING**

2007

CERTIFICATION

I, See How Ng, declare that this thesis, submitted in fulfillment of the requirements for the award of Doctor of Philosophy, in the Institute for Superconducting & Electronic Materials, Faculty of Engineering, University of Wollongong, is wholly my own work unless otherwise referenced or acknowledged. The document has not been submitted for qualifications at any other academic institution.

A handwritten signature in black ink, appearing to read 'See How Ng', with a horizontal line drawn through the middle of the signature.

See How Ng

25 September 2007

*For my parents, siblings, and Sau Yen
who wonder what I do all day*

ACKNOWLEDGEMENTS

It is my pleasure to acknowledge the considerable assistances that I have received from the people of the University of Wollongong (UoW), Australia and also from the Paul Scherrer Institute (PSI), Switzerland, during the course of my doctoral studies. I wish to express my utmost gratitude to my thesis supervisor, *Professor Hua Kun Liu*, and co-supervisor, *Dr. Jiazhao Wang*, for their invaluable advice, encouragement, understanding and trust during my stay at UoW. Many thanks also for their careful review of the manuscripts. Any remaining errors are my responsibility.

I would like to express my deepest appreciation to *Prof. Shi Xue Dou*, Director of the Institute for Superconducting & Electronic Materials (ISEM), and *Prof. Gordon Wallace*, Director of the ARC Center of Excellence for Electromaterials Science (ACES), for providing me with the appropriate facilities and expertise during the course of my studies. I would like to thank ISEM, ACES, and the University of Wollongong, for providing me with the financial support during my doctoral studies, by means of a Tuition Fee Waiver Scholarship and also a matching PhD Scholarship.

I would like to thank *P.D. Dr. Petr Novák*, Head of Batteries Group, *P.D. Dr. Thomas Lippert*, Head of Materials Group, and *Prof. Alexander Wokaun*, Head of the General Energy Department, all from the Paul Scherrer Institute, Switzerland, for their scientific assistance and support, during my appointment as a Visiting Scientist in PSI, from October 2006 till April 2007. I would also like to thank *Prof. Dr. Sotiris E. Pratsinis*,

Director of the Particle Technology Laboratory (PTL), Swiss Federal Institute of Technology Zurich, Switzerland, for providing me with the facilities for the production of nanoparticles via the flame spray pyrolysis process.

I wish to thank *Mrs. Franziska Simmen*, PhD student from PSI, for her assistance in preparing and analyzing the PLD-made LiMn_2O_4 thin films for my thesis work. Many thanks also go to *Mr. Timothy Patey* (PhD student, PSI) and *Mr. Robert Büchel* (PhD student, PTL) for their assistance in the synthesis of vanadium-based oxides nanoparticles via the flame spray pyrolysis process, for use as cathode materials in my research work. During my Visiting Scientist appointment at the Paul Scherrer Institute, Switzerland, I had the pleasure working with a number of scientists and postgraduate students such as *Dr. Matthias Hahn*, *Dr. Nicolas Tran*, *Dr. Maire Pascal*, *Dr. Joachim Ufheil*, *Mr. Werner Scheifele*, *Mr. Hermann Kaiser*, *Mr. Patrick Ruch*, *Mr. Fabio La Mantia*, and *Mr. Fabio Roschiano*. Their help and discussion are greatly appreciated. Also the administrative help from *Ms. Isabella Kalt* is greatly acknowledged.

Technical assistance from the people of the University of Wollongong such as *Dr. David Wexler* (TEM), *Dr. Jun Chen* (FT-IR, Raman, and TGA), *Dr. Konstantin Konstantinov* (spray pyrolysis, BET, TGA/DTA, and SEM/EDX), *Dr. Zaiping Guo* (EIS), and *Assoc. Prof. Chee Too* (bucky paper) are gratefully acknowledged. It is also my pleasure to work with a number of overseas collaborators such as *Prof. Dayse dos Santos* (UNESP, Brazil), *Prof. Chuanqi Feng* (Wuhan University, China), *Mr. Yann Tournayre* (France), *Ms. Dong Yun Zhang* (Shanghai Jiao Tong University, China), and *Mr. Roshan Shanmukaraj* (India) during my studies in ISEM.

I also wish to thank *Mr. Kieran de Silva, Dr. Wai Kong Yeoh, Dr. Jung Ho Kim, Dr. Steve Bewlay, Dr. Scott Needham, Mr. Bernie Huang, Mr. Min-Sik Park, Mr. Jin-Soo Park, Mr. Joe Xu, Mr. Dapeng Chen, Ms. Olga Scherbakova, Mr. Andrey Scherbakov, Dr. Germanas Peleckis, Dr. Marie Roussel, Dr. Ling Yuan, Ms. Jane Yao, Mr. Brad Winton, Mr. Georgin Lao, and Mr. Jerry Zhao*, for all their friendly support and helpful discussions during my doctoral studies in ISEM. I wish to thank *Dr. Tania Silver* for the critical reading of all my publications, improving the standard of my written English, and also proofreading of my thesis. My heartfelt thanks also go to *Mr. Ron Kinnell*, for all the technical assistance with the maintenance of equipment and scientific facilities.

I would like to thank my mum, dad, and sisters, for their continue support and love, which translates into the strength and guidance path for me during my PhD studies. Finally, my greatest debt, however, is to my wife, *Ms. Sau Yen (Sophie) Chew*, who endured my long days in my study with particular grace and understanding. She has been, simply, indispensable.

TABLE OF CONTENTS

CERTIFICATION	i
DEDICATION	ii
ACKNOWLEDGEMENTS	iii
TABLE OF CONTENTS	vi
ABSTRACT	xiii
NOMENCLATURE	xv
LIST OF FIGURES	xx
LIST OF TABLES	xxx
CHAPTER 1	
INTRODUCTION	1
1.1 General Background	1
1.2 Statement of Problem	3
1.3 Importance of Study	5
1.4 Objectives and Scopes of Research	6

CHAPTER 2	LITERATURE REVIEW	8
2.1	Lithium-ion Rechargeable Batteries	8
2.1.1	Basic Concepts and Principles of Operation	10
2.1.2	Components	17
2.1.3	Advantages	19
2.1.4	Commercial Applications	22
2.1.5	On-going Scientific Challenges	26
2.2	Negative Electrode Materials For Lithium- ion Batteries	27
2.2.1	Carbonaceous Materials	28
2.2.2	Lithium-Metal Alloys	31
2.2.3	Transition Metal Oxides	36
2.2.4	Titanium Compounds	38
2.3	Positive Electrode Materials For Lithium-ion Batteries	39
2.3.1	Layered Oxides	41
2.3.2	Spinel Oxides	43
2.3.3	Olivines	46
2.3.4	Vanadates	49
2.4	Nanotechnology – The Great Leap Forward	53
2.4.1	Definition and Terminology	55
2.4.2	Nanostructures vs. Microstructures	56
2.4.3	Advantages and Disadvantages	58
2.4.4	On-going Challenges	60

CHAPTER 3	EXPERIMENTAL DETAILS	62
	3.1 Materials	62
	3.2 Experimental Procedures	64
	3.3 Preparation of Nanostructured Materials	65
	3.3.1 Filtration Technique (Positive Pressure)	65
	3.3.2 Spray Pyrolysis	66
	3.3.3 Co-precipitation Method	67
	3.3.4 Flame Spray Pyrolysis (FSP)	68
	3.3.5 Pulsed Laser Deposition (PLD)	70
	3.4 Physical and Structural Characterization of Nanostructured Materials	71
	3.4.1 X-Ray Diffraction (XRD)	72
	3.4.2 Thermogravimetric Analysis (TGA)	74
	3.4.3 Scanning Electron Microscopy (SEM)	74
	3.4.4 Transmission Electron Microscopy (TEM)	75
	3.4.5 Brunauer Emmett Teller (BET) Specific Surface Area Measurement	76
	3.4.6 Raman Spectroscopy	76
	3.4.7 Four-Point Probe Conductivity Measurement	77
	3.4.8 Atomic Force Microscopy (AFM)	78

3.4.9	Rutherford Backscattering Spectrometry (RBS)	80
3.4.10	Elastic Recoil Detection Analysis (ERDA)	82
3.4.11	Surface Profilometry	83
3.5	Electrode Preparation and Test Cell Assembly	84
3.5.1	Electrode Preparation	84
3.5.2	Test Cell Assembly	85
3.6	Electrochemical Characterization	86
3.6.1	Cyclic Voltammetry (CV)	87
3.6.2	Galvanostatic Measurements	88
3.6.3	Electrochemical Impedance Spectroscopy (EIS)	89
CHAPTER 4	SINGLE-WALLED CARBON NANOTUBE PAPER AS FREE-STANDING ANODE FOR LI-ION BATTERIES	90
4.1	Introduction	90
4.2	Synthesis Method	92
4.3	Physical and Structural Characterizations	94
4.4	Electrochemical Performance	100
4.5	Conclusions	110

CHAPTER 5	SPRAY-PYROLYZED LEAD OXIDE AND LEAD OXIDE-CARBON NANOCOMPOSITES AS ANODES FOR LI-ION BATTERIES	111
	5.1 Introduction	111
	5.2 Synthesis Method	113
	5.3 Physical and Structural Characterizations	115
	5.4 Electrochemical Performance	128
	5.5 Conclusions	139
 CHAPTER 6	 CARBON-COATED SILICON NANOCOMPOSITES AS HIGH-CAPACITY LI-ION BATTERY ANODES	 140
	6.1 Introduction	140
	6.2 Effect of Spray Pyrolysis Processing Temperature	143
	6.2.1 Synthesis Method	143
	6.2.2 Physical and Structural Characterizations	144
	6.2.3 Electrochemical Performance	150
	6.3 Effect of Precursor Solution (Nano-Si/Citric Acid/Ethanol) Concentration	161
	6.3.1 Synthesis Method	161
	6.3.2 Physical and Structural Characterizations	161
	6.3.3 Electrochemical Performance	164
	6.4 Conclusions	165

CHAPTER 7	VANADIUM PENTOXIDE NANOSTRUCTURES FOR LITHIUM-ION BATTERY CATHODES	167
7.1	Introduction	167
7.2	V₂O₅ Nanostructures Prepared via a Precipitation Process	170
7.2.1	Synthesis Method	170
7.2.2	Physical and Structural Characterizations	170
7.2.3	Electrochemical Performance	173
7.3	V₂O₅ Nanoparticles Prepared via a Flame Spray Pyrolysis Process	176
7.3.1	Synthesis Method	176
7.3.2	Physical and Structural Characterizations	177
7.3.3	Electrochemical Performance	181
7.4	Conclusions	186
CHAPTER 8	LITHIUM TRIVANADATE NANOPARTICLES SYNTHESIZED BY FLAME SPRAY PYROLYSIS AS CATHODE MATERIAL FOR LITHIUM-ION BATTERIES	187
8.1	Introduction	187
8.2	Synthesis Method	189
8.3	Physical and Structural Characterizations	189
8.4	Electrochemical Performance	193
8.5	Conclusions	199

CHAPTER 9	LITHIUM MANGANESE OXIDE THIN FILM SYNTHESIZED BY PULSED LASER DEPOSITION AS MODEL CATHODE FOR LITHIUM-ION BATTERIES	200
	9.1 Introduction	200
	9.2 Synthesis Method	203
	9.3 LiMn₂O₄ Thin Films Deposited on Silicon Substrate	205
	9.3.1 Physical and Structural Characterizations	206
	9.3.2 Electrochemical Performance	207
	9.4 LiMn₂O₄ Thin Films Deposited on Stainless Steel Substrate	208
	9.4.1 Physical and Structural Characterizations	209
	9.4.2 Electrochemical Performance	214
	9.5 Conclusions	220
CHAPTER 10	GENERAL CONCLUSIONS AND OUTLOOK	221
	10.1 General Conclusions	221
	10.1.1 Nanostructured Anode Materials for Li- ion Storage	221
	10.1.2 Nanostructured Cathode Materials as Li- ion Providers	224
	10.2 Outlook	227
REFERENCES		230
APPENDICES		252
APPENDIX A	LIST OF PUBLICATIONS	252

ABSTRACT

The commercially available lithium-ion cells, which are the most advanced among the rechargeable battery systems available so far, employ polycrystalline micro-sized powder as the electrode materials, which function as the Li-ion insertion hosts. With the advancement of nanotechnology, there is an interest in the replacement of conventional materials by nanostructured materials. The use of nanoparticles in composite electrodes for Li-ion batteries may have considerable kinetic advantages due to the reduction of the diffusion length for lithium-ion insertion into the active mass, and also because of the reduction of the overall charge transfer resistance of the electrodes. In this doctoral work, several nanostructured materials were examined and characterized for possible application as electrode materials in Li-ion rechargeable batteries. Among the anode candidates studied were free-standing single-walled carbon nanotube (SWCNT) paper, lead oxide (PbO) and lead oxide-carbon (PbO-C) nanocomposite, and carbon-coated silicon (Si-C) nanocomposite materials. Meanwhile, several cathode candidates were also studied: nanostructured vanadium oxide (V_2O_5), lithium trivanadate (LiV_3O_8) nanoparticles, and lithium manganese oxide ($LiMn_2O_4$) thin film electrode.

Free-standing SWCNT paper electrodes have been synthesized by a simple filtration method via positive pressure. The free-standing electrode was produced without any binder or metal substrate, which reduced the weight significantly. The free-standing SWCNT paper electrodes were also flexible and had good electrical conductivity. With the addition of both carbon black and nanosized Si particles, the electrical conductivity and specific capacity of the free-standing SWCNT paper electrode were greatly enhanced, so that they retained a capacity of 400 mAh g⁻¹ beyond 100 cycles. A new approach has been used to prepare nanostructured PbO and PbO-C composites via the spray pyrolysis technique. The prepared powders consist of fine nanocrystalline PbO homogeneously distributed within an amorphous carbon matrix with highly developed surface area. The combination of spray technology and carbon addition increased the specific surface area (above 6 m² g⁻¹) and the conductivity of PbO, and also improved

the specific capacity, with a reversible capacity above 100 mAh g⁻¹ retained beyond 50 cycles. An effective, inexpensive, and industrially oriented approach was applied to produce carbon-coated Si nanocomposites. Carbon-coated Si nanocomposites spray-pyrolyzed in air at 400 °C showed the best cycling performance, retaining a specific capacity of 1120 mAh g⁻¹ beyond 100 cycles, with a capacity fading of less than 0.4 % per cycle. The beneficial effect of the carbon-coating in enhancing the dimensional stability of the Si nanoparticles appears to be the main reason for this markedly improved electrochemical performance.

One-dimensional (1D) nanostructures of V₂O₅ have been successfully synthesized via a precipitation process followed by heating in vacuum at 300 °C. The increase in crystallinity and higher yield of one-dimensional nanostructured oxides contributed significantly to the improved capacity and enhanced cycle life. V₂O₅ nanoparticles were also synthesized via the flame spray pyrolysis (FSP) process in air. They showed an improved cycle life when the cut-off potential for discharging was increased from 1.5 V to 2.5 V. The significant capacity loss when discharging to 1.5 V is possibly related to the dissolution of vanadium active mass and the structural changes upon cycling in the larger potential span. The flame spray pyrolyzed V₂O₅ nanoparticles show excellent cyclability when cycled between 2.5 V and 4.0 V vs. Li/Li⁺, retaining a discharge capacity of 120 mAh g⁻¹ beyond 100 cycles at a cycling rate of 100 mA g⁻¹. LiV₃O₈ nanoparticles (~24 nm in size) have been synthesized by FSP for the first time. The as-synthesized LiV₃O₈ nanoparticles proved to be a promising cathode material for lithium rechargeable batteries, retaining a specific discharge capacity of 180 mAh g⁻¹ beyond 50 cycles. A series of LiMn₂O₄ thin films on either Si (100) or stainless steel substrate were successfully prepared via pulsed laser deposition (PLD). The as-deposited LiMn₂O₄ thin films on stainless steel substrate are highly lithium- and oxygen-deficient, as confirmed by ERDA/RBS and Raman analysis. Lithium and oxygen content increased when the pulse rate was increased, leading to thicker films. However, the LiMn₂O₄ thin film with the lowest deposition pulse rate (or thinnest film) exhibited the best electrochemical performance, retaining a charge capacity of 48 μAh cm⁻² μm⁻¹ beyond 100 cycles.

NOMENCLATURE

• List of Symbols

Symbol	Name	Unit
a_i	Activity of species i	mol dm^{-3}
C	Concentration	M
$C\text{-rate}$	Rate of charge or current density	mA g^{-1} or $\mu\text{A cm}^{-2}$
C_C	Charge capacity	Ah kg^{-1} or mAh g^{-1}
C_D	Discharge capacity	Ah kg^{-1} or mAh g^{-1}
C_{dl}	Double-layer capacitance	F m^{-2}
D_P	Average crystal size	nm
d	Distance between atomic layers in a crystal	\AA or nm
d_t	Tube diameter	nm
d_{t-s}	Target-substrate distance	cm
E	Potential of half-reactions	V or mV
E_{dc}	DC potential	V or mV
E_f	Final potential	V or mV
E_i	Initial potential	V or mV
E_s	Switching potential	V or mV
E^0	Standard electrode potential	V or mV
$E^{0,(-)}$	Negative electrode potential	V or mV
$E^{0,(+)}$	Positive electrode potential	V or mV
$\Delta E^0, U^0$	Cell potential	V or mV
f	Frequency	Hz
ΔG^0	Standard Gibbs free energy	J mol^{-1}
I	Current	A or mA
K	Shape factor of the average crystallite	(dimensionless)

• List of Symbols (con't)

Symbol	Name	Unit
L	Crystal size	nm
M_p	Mass of the target atom	kg or g
M_r	Mass of the incident ion	kg or g
m, m_i	Mass of species i	kg or g
N^0	Number of pulses	(dimensionless)
n	Number of electrons exchanged or integer	(dimensionless)
P_d	Downstream pressure	bar
P_{O_2}	Oxygen background pressure	mbar
P_u	Upstream pressure	bar
P_v	Power density	W dm ⁻³
p	Specific power	W kg ⁻¹
Q	Solution flow rate	mL min ⁻¹
Q	Capacity	Ah or mAh
Q_{irrev}	Irreversible capacity loss	%
q_{th}	Theoretical specific charge capacity	Ah kg ⁻¹ or mAh g ⁻¹
R_n	Reversible capacity at cycle n	Ah kg ⁻¹ or mAh g ⁻¹
R_{ct}	Charge-transfer resistance	Ω
Q	Capacity	Ah or mAh
Q_{irrev}	Irreversible capacity loss	%
q_{th}	Theoretical specific charge capacity	Ah kg ⁻¹ or mAh g ⁻¹
R_n	Reversible capacity at cycle n	Ah kg ⁻¹ or mAh g ⁻¹
R_{ct}	Charge-transfer resistance	Ω
S_{BET}	Specific surface area	m ² g ⁻¹
T	Temperature	K or °C
T_s	Substrate temperature	K or °C
t	Time	h
v	Scan rate	mV s ⁻¹
v_i	Stoichiometric coefficients of species i	(dimensionless)
$W_{V.th}$	Theoretical energy density	Wh dm ⁻³
w_{th}	Theoretical specific energy	Wh kg ⁻¹
Δx	Amount of guest species	mol

- List of Symbols (con't)

Symbol	Name	Unit
β	Full width at half maximum in radians	radians
ω_{RBM}	RBM frequency	cm^{-1}
λ	Wavelength of the incident X-ray beam	nm
φ	Laser fluence	J cm^{-2}
θ	Angle of incidence	° or degrees
σ	Electrical conductivity	S cm^{-1}
τ	Pulse width	ns

- List of Fundamental Constants

Quantity	Symbol	Value	Power of Ten	Unit
Avogadro constant	N_A	6.022	10^{23}	mol^{-1}
Boltzmann constant	k	1.381	10^{-23}	J K^{-1}
Elementary charge	e	1.602	10^{-19}	C
Faraday constant	$F = N_A \times e$	9.6487	10^4	C mol^{-1}
Gas constant	$R = N_A \times k$	8.319	10^0	$\text{J K}^{-1} \text{mol}^{-1}$

- List of Conversion Factors

Value	Equivalence
1 eV	$1.602 \times 10^{-19} \text{ J}$
	86.5 kJ mol^{-1}
	8066 cm^{-1}
1 cm^{-1}	$1.986 \times 10^{-23} \text{ J}$
$1 \text{ }\mu\text{m}$	10^{-6} m
1 nm	10^{-9} m
$1 \text{ }\text{\AA}$	10^{-10} m

• **List of Abbreviations**

Abbreviation	Meaning
AFM	Atomic force microscopy
a.u.	Arbitrary unit
BET	Brunauer Emmett Teller
CB	Carbon black
CCCC	Computer controlled cell capture
CNT	Carbon nanotube
CV	Cyclic voltammetry
CVD	Chemical vapor deposition
DC	Disordered carbon
dc	Dynamic current
DEG	Diethylene glycol
DMC	Dimethyl carbonate
DWCNT	Double-walled carbon nanotube
EC	Ethylene carbonate
EDS	Energy dispersive spectroscopy
EIS	Electrochemical impedance spectroscopy
ERDA	Elastic recoil detection analysis
ETH	Swiss Federal Institute of Technology
EV	Electric vehicle
FE-SEM	Field-emission scanning electron microscopy
FSP	Flame spray pyrolysis
FWHM	Full width at half maximum
hcp	Hexagonal-close-packed
HEV	Hybrid electric vehicle
HR-TEM	High-resolution transmission electron microscopy
IPRI	Intelligent Polymer Research Institute
ISEM	Institute for Superconducting and Electronic Materials
JCPDS	Joint committee on powder diffraction standards
LTB	Lithium tert-butoxide
MWCNT	Multi-walled carbon nanotube
Ni-Cd	Nickel-cadmium

• **List of Abbreviations (con't)**

Abbreviation	Meaning
Ni-MH	Nickel-metal hydride
NMP	1-methyl-2-pyrrolidinone
NMR	Nuclear magnetic resonance
NNI	National nanotechnology initiative
NRA	Nuclear reaction analysis
OCP	Open circuit potential
OEM	Original equipment manufacturer
PC	Propylene carbonate
PLD	Pulsed laser deposition
PSI	Paul Scherrer Institute
PSPD	Position sensitive photo-detector
PVDF	Polyvinylidene fluoride
PZT	Piezo-electric
RBM	Radial breathing mode
RBS	Rutherford backscattering spectrometry
R & D	Research and development
rms	Root mean square
SAEDP	Selected area electron diffraction pattern
SEI	Solid-electrolyte interphase
SEM	Scanning electron microscopy
SEM	Scanning electron microscopy
SHE	Standard hydrogen electrode
SS	Stainless steel
SWCNT	Single-walled carbon nanotube
TEM	Transmission electron microscopy
TGA	Thermogravimetric analysis
THF	Tetrahydrofuran
TMO	Transition metal oxide
UV	Ultra-violet
XRD	X-ray diffraction

LIST OF FIGURES

Figure 2.1	Overview of the different reaction potentials of electrode materials for the lithium-ion battery. White rectangles represent the positive electrode materials, and shaded rectangles the negative electrode material. On the left y-axis the materials are plotted against potential vs. Li/Li^+ , and on the right y-axis against potential vs. the standard hydrogen electrode (SHE) [Tarascon and Armand, 2001; Whittingham, 2004].	9
Figure 2.2	Some standard potentials of battery electrodes [Novak, 2007].	13
Figure 2.3	Principles of Li-ion battery operation [courtesy of Paul Scherrer Institute, Switzerland].	17
Figure 2.4	Schematic drawing showing the shape and components of various Li-ion battery configurations: (a) cylindrical, (b) coin, (c) prismatic, and (d) thin and flat [Tarascon and Armand, 2001].	19
Figure 2.5	Comparison of the specific energy and energy density of rechargeable lithium batteries with those of other systems [Manthiram and Kim, 1998].	20
Figure 2.6	Discharge behaviors of batteries [Piotto, 2004].	20
Figure 2.7	Ragone plot of numerous battery systems and supercapacitors [Broussely, 2005].	22
Figure 2.8	Uses for each type of rechargeable battery [Source: Institute of Information Technology Ltd., Japan, 2002].	23
Figure 2.9	Li-ion battery market share for 2002 [Source: Institute of Information Technology Ltd., Japan, 2002].	24
Figure 2.10	(a) Structure of layered lithium cobalt oxide (LiCoO_2), and (b) schematic diagram of the layered LiCoO_2 structure showing the ABCABC stacking of the O-Li-O-Co-O-Li-O layers, adapted from [Reimers and Dahn, 1992; Winter et al., 1998].	41

Figure 2.11	(a) The three-dimensional structure of LiMn_2O_4 spinel and (b) the crystal structure of a typical AB_2O_4 spinel structure. Hatched, solid, and open circles refer to Li^+ , $\text{Mn}^{3+/4+}$, and O^{2-} ions, respectively, for LiMn_2O_4 . The numbers refer to various crystallographic positions in the spinel structure. Adapted from [Pervov et al., 1997; Winter et al., 1998].	44
Figure 2.12	The crystal structure of olivine LiFePO_4 in projection along [001]. On the left, expanded view of the framework built on FeO_6 octahedra and PO_4 tetrahedra, with Li-ions in red. The FeO_6 octahedra are linked together through corner sharing in the (b, c) plane. On the right, restricted view of Li, Fe and P distribution between two distorted, hexagonal close packed (hcp) oxygen-dense layers ($\text{P}_{\text{Td}}[\text{LiFe}]_{\text{oct}}\text{O}_4$). LiO_6 octahedra share edges and Li-ions may diffuse along [010] and [001]. Image taken from Tarascon and Armand [2001].	47
Figure 2.13	Structures of layered LiVO_2 , LiV_2O_5 , double sheet $\text{LiV}_4\text{O}_{10}$, V_6O_{13} , and LiV_3O_8 . VO_5 square pyramids are pink, VO_6 octahedra are blue, and lithium atoms are green [Adapted from Whittingham et al., 2005].	49
Figure 2.14	Electrochemical behaviour of bulk and nanostructured $\alpha\text{-Fe}_2\text{O}_3$ as shown by voltage-composition curves. The capacity retention and scanning electron micrographs of both samples are shown in the insets [Adapted from Aricò et al., 2005].	57
Figure 2.15	Voltage profile of a 6 nm anatase (TiO_2) electrode cycled at 0.1 A g^{-1} , 1 A g^{-1} , and 10 A g^{-1} . Inset shows the cycle performance at 10 A g^{-1} [Adapted from Jiang et al., 2006].	59
Figure 2.16	The supply value chain for commercializing nanotechnology, starting with nanomaterials and technology and ending with commercial applications. The factors that impede commercialization are shown in the inner circle and NNI initiatives to overcome these challenges are shown in the outer circle [Helmus, 2006].	61
Figure 3.1	The overall framework of my experimental studies.	64
Figure 3.2	Schematic diagram of the filtration cell used for the fabrication of composite bucky papers.	66
Figure 3.3	Schematic diagram of the spray pyrolysis process, with inset illustrating oxides-carbon nanocomposites formation, redrawn with modifications from Needham [2007].	67
Figure 3.4	Experimental set-up of the FSP process [Mädler et al., 2002].	69

Figure 3.5	Schematic diagram of the experimental set-up for the PLD process at the Paul Scherrer Institute, Switzerland [courtesy of Mrs. Franziska Simmen]: (1) cylindrical target rod, (2) plasma plume generated by the laser beam, (3) heated and rotating substrate, (4) focusing lens, (5) laser beam, (6) vacuum pump, and (7) inlet for oxygen.	71
Figure 3.6	Reflection of X-rays from lattice planes according to Bragg's law [Giacovazzo, 2002].	73
Figure 3.7	Experimental set-up for resistivity measurement via the four-point probe technique (Jandel multi-height four-point probe and resistivity test unit, model RM2).	77
Figure 3.8	Schematic diagram of a contact mode AFM [Campana, 2005].	78
Figure 3.9	Sketch of the inter-atomic forces variation vs. distance between the AFM tip and sample [Campana, 2005].	80
Figure 3.10	Principle of Rutherford Backscattering Spectrometry [Dumont et al., 2006]. E is the ion energy, M_r is the mass of the incident ion, M_p is the mass of the target atom, and θ is the scattering angle.	81
Figure 3.11	Principle of Elastic Recoil Detection Analysis [Dumont et al., 2006]. E is the ion energy, M_r is the mass of the incident ion, M_p is the mass of the target atom, and θ is the scattering angle.	82
Figure 3.12	Profilometer (Dektak 8000) for measurements of film thickness and surface roughness [courtesy of Paul Scherrer Institute, Switzerland].	83
Figure 3.13	Cross-sectional schematic diagram of the coin-type cell, CR2032, used in ISEM (Chew, 2006).	85
Figure 3.14	Schematic diagram of the homemade electrochemical cell used in PSI (Coluccia, 2000).	86
Figure 3.15	A common impedance spectrum and the corresponding equivalent circuit for such spectra [Lindsay, 2004].	89
Figure 4.1	Photograph of a typical 4-cm diameter SWCNT-derived bucky paper.	93
Figure 4.2	TEM images of SWCNT precursor powder: (a) low resolution image shows inter-mingled bundles of nanotubes, and (b) high resolution image revealing the outer diameter of the SWCNT as approximately 2.7 nm.	95

Figure 4.3	(a) XRD pattern of SWCNT precursor powder. (b) Raman spectrum of the SWCNT precursor powder, using a 532 nm laser line. The inset shows the RBM region of the SWCNTs, with the numbers indicating the diameters of the SWCNTs.	95
Figure 4.4	Field emission scanning electron microscopy (FE-SEM) images of SWCNT-derived bucky paper: (a) low resolution cross-sectional image of SWCNT paper, exhibiting densely packed layers of nanotubes; (b) corresponding high resolution image of (a), clearly showing highly entangled SWCNTs between the layers; (c) low resolution image of SWCNT composite paper with carbon black, where the wide distribution of tiny white spots indicates carbon black nanoparticles; and (d) the corresponding high resolution image of (c), where the carbon black agglomerates are highlighted as white circles.	97
Figure 4.5	Raman spectra for the SWCNT electrodes with 532 nm laser line: (a) carbon black powder, (b) SWCNT powder, (c) SWCNT paper, and (d) SWCNT composite paper with carbon black.	98
Figure 4.6	Electrical conductivity as a function of thickness for SWCNT papers.	100
Figure 4.7	Impedance plots for the SWCNT electrodes: (a) bucky paper and bucky paper with 10 wt.% carbon black, and (b) bucky paper with different thicknesses.	101
Figure 4.8	Nyquist plots for SWCNT electrodes: (a) SWCNT powder on Ni foam, (b) thin SWCNT paper, (c) thick SWCNT paper, and (d) SWCNT paper with 10 wt.% carbon black.	103
Figure 4.9	Charge-discharge profiles of SWCNT electrodes: (a) conventional slurry-coated electrode, and (b) “free-standing” bucky paper electrode.	105
Figure 4.10	Discharge capacities vs. cycle number. Current density was 0.08 mA cm ⁻² .	106
Figure 4.11	Cyclic voltammograms of the SWCNT composite paper electrodes: (a) SWCNT paper with 10 wt.% carbon black, and (b) SWCNT paper with 10 wt.% carbon black and 10 wt.% nanosized Si particles addition. The scan rate applied is 0.5 mV s ⁻¹ and the numbers indicate the cycle number.	107
Figure 4.12	(a) Cycle life of the composite bucky paper electrodes. The current density was 0.08 mA cm ⁻² . (b) Discharge capacities of the composite bucky paper electrodes at different cycling rates. The electrodes were cycled between 0.02 and 1.20 V vs. Li/Li ⁺ .	108

Figure 4.13	SEM images of “free-standing” SWCNT paper electrodes: (a) before cycling, and (b) after 100 cycles.	109
Figure 5.1	Typical XRD patterns of α -PbO powders sprayed at different temperatures. The solution concentration was 0.5 M, and the flow rate was 3.14 mL min ⁻¹ . The traces of β -PbO are marked by *.	115
Figure 5.2	TEM dark-field images obtained from samples sprayed at (a) 600 °C and (b) 800 °C. Individual crystallites are marked as C.	117
Figure 5.3	Typical SEM images of powders sprayed at (a) 600 °C, (b) 700 °C, and (c) 800 °C. The solution concentration was 0.5 M, and the flow rate was 3.14 mL min ⁻¹ .	119
Figure 5.4	TGA curves of PbO-C nanocomposites with different PbO/C ratios.	121
Figure 5.5	XRD patterns of PbO-C nanocomposites from (a) pure PbO; (b) 97PbO/3C; (c) 91PbO/9C; and (d) 90PbO/10C.	123
Figure 5.6	SEM images of PbO and PbO-C nanocomposites from (a) pure PbO; (b) 97PbO/3C; (c) 91PbO/9C; and (d) 90PbO/10C.	124
Figure 5.7	TEM images of nanocrystalline PbO and PbO-C nanocomposites: (a) centered dark-field image of pure PbO, where individual crystallites are marked as C; (b) bright-field image of 97PbO/3C, with large PbO particles marked as P; (c) and (d) bright field images and selected area electron diffraction patterns (inset) of 90PbO/10C at different magnifications. The lead oxide particles in the carbon rich cluster in (c) are significantly smaller than those in (b). Some carbon rich clusters, such as that shown in (d), contained no lead oxide particles, as indicated by the diffuse contrast in the associated SAED pattern.	126
Figure 5.8	Raman spectra of PbO-C nanocomposites from (a) 97PbO/3C, (b) 91PbO/9C, and (c) 90PbO/10C; and (d) pure disordered carbon produced from sugar.	128
Figure 5.9	EDX mapping of PbO-C nanocomposites made from 90PbO/10C (left) and 97PbO/3C (right).	129
Figure 5.10	CVs of (a) pure nanocrystalline PbO and (b) 90PbO/10C nanocomposite. The scan rate was 0.1 mV s ⁻¹ .	131
Figure 5.11	The 1 st , 2 nd , 5 th and 10 th charge/discharge profiles of (a) pure nanocrystalline PbO and (b) 90PbO/10C nanocomposite. The current density was 0.1 mA cm ⁻² .	133

Figure 5.12	Discharge capacity dependencies of PbO materials sprayed at (a) different temperatures at 0.5 M and 3.14 mL min ⁻¹ , and at (b) different solution concentrations at 700 °C and 1.57 mL min ⁻¹ . The current density applied was 0.1 mA cm ⁻² .	135
Figure 5.13	Cycle life of PbO-C nanocomposites. The current density was 0.1 mA cm ⁻² . The inset figure presents the specific capacity vs. cycle number data for the bare carbon powder, and the current density applied was also 0.1 mA cm ⁻² .	136
Figure 5.14	Impedance plots for (a) pure PbO and (b) 90PbO/10C electrodes in the de-lithiated state.	138
Figure 6.1	Thermogravimetric analysis (TGA) curves of nanocrystalline Si precursor powder; carbon-coated Si nanocomposites spray-pyrolyzed in air at 500 °C, 400 °C, and 300 °C; and amorphous carbon spray-pyrolyzed from citric acid at 400 °C in air. The ratio Si/DC refers to the ratio of the amount of silicon by weight to the amount of disordered carbon in the spray-pyrolyzed nanocomposites, as estimated from the TGA curves.	144
Figure 6.2	X-ray diffraction patterns of (a) nanocrystalline Si precursor powder; carbon-coated Si nanocomposites spray-pyrolyzed in air at (b) 500 °C; (c) 400 °C; and (d) 300 °C; and (e) amorphous carbon spray-pyrolyzed from citric acid at 400 °C in air.	147
Figure 6.3	SEM images of carbon-coated Si nanocomposites spray-pyrolyzed in air at (a) 400 °C (low-magnification image); (b) 500 °C; (c) 400 °C; and (d) 300 °C.	148
Figure 6.4	TEM images of nanocrystalline Si and carbon-coated Si nanocomposites: (a) low-magnification image of nanocrystalline Si, with the indexed selected area diffraction pattern (inset) confirming the presence of Si particles; and (b) carbon-coated Si nanocomposite spray-pyrolyzed at 400 °C. (c), (d), and (e) are TEM images of carbon-coated Si nanocomposites spray-pyrolyzed at 300 °C, 400 °C, and 500 °C, respectively, revealing the thickness of the carbon-coating layer for each nanocomposite. (f) High-resolution image of carbon-coated Si spray-pyrolyzed at 400 °C, clearly showing the presence of an interface between the nanocrystalline Si particle and the amorphous carbon layer.	149
Figure 6.5	The first discharge/charge plots of nanocrystalline Si and carbon-coated Si nanocomposite electrodes. Cycling took place between 0.02 V and 1.20 V versus Li/Li ⁺ at a cycling rate of 100 mA g ⁻¹ .	152

Figure 6.6	(a) First cycle differential capacity plots of nanocrystalline Si and carbon-coated Si nanocomposite electrodes (inset: enlarged plot of (a)). (b), (c), and (d) are differential capacity plots for carbon-coated Si nanocomposites spray-pyrolyzed at 500 °C, 400 °C, and 300 °C, respectively, with the numbers indicating the cycle number. Cycling took place between 0.02 V and 1.20 V versus Li/Li ⁺ at a cycling rate of 100 mA g ⁻¹ .	153
Figure 6.7	(a) Cycle life of nanocrystalline Si and carbon-coated Si nanocomposite electrodes cycled between 0.02 V and 1.20 V versus Li/Li ⁺ at a cycling rate of 100 mA g ⁻¹ . (b) The corresponding capacity retained with respect to the first discharge capacity in (a).	155
Figure 6.8	Cycling behaviour for electrodes of (a) carbon-coated Si nanocomposite spray-pyrolyzed at 400 °C, with 44 wt.% Si content; and (b) amorphous carbon spray-pyrolyzed at 400 °C. Cycling took place between 0.02 V and 1.20 V versus Li/Li ⁺ at a cycling rate of 100 mA g ⁻¹ .	157
Figure 6.9	Impedance plots for electrodes of (a) nanocrystalline Si; and (b) carbon-coated Si nanocomposite spray-pyrolyzed at 400 °C. All measurements were conducted in the de-lithiated state.	159
Figure 6.10	Thermogravimetric analysis (TGA) curves of nanocrystalline Si precursor powder; carbon-coated Si nanocomposites spray-pyrolyzed in air at 400 °C with different initial precursor solution concentrations; and amorphous carbon spray-pyrolyzed from citric acid at 400 °C in air, with an initial precursor solution weight ratio (nano-Si/citric acid) of 1/10.	162
Figure 6.11	X-ray diffraction patterns of (a) nanocrystalline Si precursor powder, (b) 83Si/17DC, (c) 68Si/32DC, (d) 51Si/49DC, (e) 44Si/56DC, and (f) amorphous carbon spray-pyrolyzed from citric acid at 400 °C in air.	163
Figure 6.12	(a) Cycling behaviour of the nanocrystalline Si and Si/DC nanocomposite electrodes cycled between 0.02 V and 1.20 V vs. Li/Li ⁺ at a cycling rate of 100 mA g ⁻¹ . (b) The corresponding discharge capacity retained, compared to the first discharge capacity in (a).	164
Figure 7.1	XRD patterns for (a) commercial V ₂ O ₅ , (b) V ₂ O ₅ annealed for 45 mins at 300 °C (sample A), and (c) V ₂ O ₅ annealed for 1 hr at 300 °C (sample B).	171
Figure 7.2	SEM images of nanostructured V ₂ O ₅ electrodes: (a) and (b) are for V ₂ O ₅ annealed for 45 mins at 300 °C (sample A), while (c) and (d) are for V ₂ O ₅ annealed for 1 hr at 300 °C (sample B).	172

Figure 7.3	Cyclic voltammograms of nanostructured V_2O_5 electrodes. The applied scan rate was 0.5 mV s^{-1} .	173
Figure 7.4	The 1 st , 10 th , and 20 th charge-discharge profiles of nanostructured V_2O_5 electrodes: (a) V_2O_5 annealed for 45 mins at 300°C (sample A), and (b) V_2O_5 annealed for 1 hr at 300°C (sample B). (c) Charge capacity vs. cycle number for nanostructured V_2O_5 electrodes cycled between 1.5 V and 4.0 V at a cycling rate of 50 mA g^{-1} .	175
Figure 7.5	Cycling behaviour for sample B V_2O_5 electrode at different cut-off voltages: (a) 1.5 V, (b) 2.0 V, and (c) 2.5 V. The current density applied was 50 mA g^{-1} .	176
Figure 7.6	XRD patterns for (a) commercial V_2O_5 (micron-sized), and (b) V_2O_5 (nano-sized) produced by a one-step flame spray pyrolysis process.	178
Figure 7.7	SEM images of V_2O_5 nanoparticles synthesized via FSP: (a) low magnification image, revealing the homogeneity of the spherical-shaped particles, and (b) high-magnification, field emission SEM images, confirming the nanosized nature of the particles, with sizes ranging from 20-40 nm.	179
Figure 7.8	TEM images of V_2O_5 nanoparticles synthesized via FSP: (a) and (b) are low resolution images, showing that the nanoparticles are not exactly spherical in shape; (c) is a high-resolution TEM image, with the (200) crystalline lattice parameter highlighted; and (d) is the corresponding selected area electron diffraction (SAED) pattern for the V_2O_5 nanoparticles in image (c).	180
Figure 7.9	Cyclic voltammograms (CVs) of the FSP-made nanostructured V_2O_5 electrodes for the first 20 cycles at different cut-off voltages: (a) 1.5 V, (b) 2.0 V, and (c) 2.5 V. The applied scan rate was 0.1 mV s^{-1} . (d) Plot of discharge capacity vs. cycle number for the corresponding CVs in plots (a), (b), and (c).	182
Figure 7.10	Prolonged cycling behaviour for the FSP-made nanostructured V_2O_5 electrodes at different discharge cut-off voltages: 1.5 V, 2.0 V, and 2.5 V. The current density applied was 100 mA g^{-1} .	183
Figure 7.11	(a) Electrochemical performance for the FSP-made nanostructured V_2O_5 electrode, cycled between 2.5 V and 4.0 V versus Li/Li^+ at a cycling rate of 100 mAh g^{-1} . (b) Cycling behaviour for the FSP-made nanostructured V_2O_5 electrode at different current densities, when cycled between 2.5 V and 4.0 V versus Li/Li^+ .	185
Figure 8.1	XRD pattern of the LiV_3O_8 nanoparticles synthesized by FSP.	190

Figure 8.2	SEM image of the LiV_3O_8 nanoparticles synthesized by FSP.	191
Figure 8.3	TEM images of LiV_3O_8 nanoparticles synthesized via FSP: (a) low resolution image, showing the nanosized nature of the particles; and (b) high-resolution image, with the (100) crystalline lattice parameter highlighted (inset: the corresponding selected area electron diffraction (SAED) pattern for the LiV_3O_8 nanoparticles).	192
Figure 8.4	Cyclic voltammograms (CVs) of flame spray pyrolyzed LiV_3O_8 nanoparticles, recorded at 0.1 mV s^{-1} from 1.5 to 4.0 V for the first 20 cycles.	194
Figure 8.5	Cycle life behaviour for a compound electrode with the FSP-made LiV_3O_8 nanoparticles as the active electromaterial. The current density applied was 100 mA g^{-1} , with cut-off potentials of 2 and 4 V.	196
Figure 8.6	The 2 nd , 10 th , and 50 th cycle discharge/charge plots of LiV_3O_8 electrode, with the numbers indicating the cycle number. Cycling took place between 2 V and 4 V versus Li/Li^+ at a cycling rate of 100 mA g^{-1} .	197
Figure 8.7	Cycling behaviour for the FSP-made nanostructured LiV_3O_8 electrode at different current densities, when cycled between 2 V and 4 V versus Li/Li^+ . The 1C rate is assumed to be equivalent to 150 mA g^{-1} in this case.	198
Figure 9.1	(a) Schematic diagram of the experimental set-up for the pulsed laser deposition (PLD) of LiMn_2O_4 thin films: (1) cylindrical target rod, (2) plasma plume generated by the laser beam, (3) heated and rotating substrate, (4) focusing lens, (5) laser beam, (6) vacuum pump, and (7) inlet for oxygen; (b) a photograph depicting a real PLD chamber used in this research work at the Materials Group, Paul Scherrer Institute, Switzerland; and (c) a photograph showing a PLD experiment in action, where a plasma plume (purple cloud) that was generated from the laser beam heating the target is deposited onto the heated substrate [image obtained from Mrs. Franziska Simmen].	204
Figure 9.2	X-ray diffraction (XRD) pattern of LiMn_2O_4 thin film on Si (100) substrate [analyzed by Mrs. Franziska Simmen]. Numbers on peaks denote the hkl index (JCPDS 35-0782).	206
Figure 9.3	XRD patterns of LiMn_2O_4 thin films deposited on stainless steel (SS) substrate: (a) 8400 pulses, and (b) 27000 pulses [analyzed by Mrs. Franziska Simmen].	211

Figure 9.4	Film thickness vs. number of pulses used in the deposition conditions when LiMn_2O_4 thin films were deposited onto stainless steel substrate heated to $500\text{ }^\circ\text{C}$ and then cooled in an oxygen atmosphere [analyzed by Mrs. Franziska Simmen].	212
Figure 9.5	Surface topography (flat images) as measured by atomic force microscopy (AFM) of the as-deposited LiMn_2O_4 thin films grown on stainless steel substrate at different numbers of pulses: (a) 8400 pulses, (b) 13200 pulses, (c) 18000 pulses, and (d) 27000 pulses. The films were cooled in air without post-deposition annealing.	213
Figure 9.6	Cyclic voltammograms (CVs) of different types of LiMn_2O_4 electrode recorded at 0.1 mV s^{-1} from 3.5 to 4.4 V for the first 20 cycles: (a) classical method, where a (70 wt.% LiMn_2O_4 + 20 wt.% CB + 10 wt.% PVDF) slurry mixture was coated onto aluminium foil, and (b) as-deposited LiMn_2O_4 thin film grown on stainless steel substrate via PLD [analyzed by Mrs. Franziska Simmen]. The LiMn_2O_4 thin film was deposited at $N^0 = 27000$ pulses, $T_s = 500\text{ }^\circ\text{C}$, $d_{t-s} = 4\text{ cm}$, $\phi = 4.3\text{ J cm}^{-2}$, and cooled in air with no post-deposition annealing.	215
Figure 9.7	(a) Cycle life of the as-deposited LiMn_2O_4 thin film electrodes on stainless steel substrate cycled between 3.5 V and 4.4 V versus Li/Li^+ at a cycling rate of $50\text{ }\mu\text{A cm}^{-2}$. (b) The corresponding capacity retained compared to the first discharge capacity in (a) [analyzed by Mrs. Franziska Simmen].	217
Figure 9.8	Cycle life behaviour of the as-deposited LiMn_2O_4 thin film electrode on stainless steel substrate cycled between 3.5 V and 4.4 V versus Li/Li^+ at a cycling rate of $50\text{ }\mu\text{A cm}^{-2}$. The LiMn_2O_4 thin film was deposited at $N^0 = 8400$ pulses, $T_s = 500\text{ }^\circ\text{C}$, $d_{t-s} = 4\text{ cm}$, $\phi = 4.3\text{ J cm}^{-2}$, and cooled in air with no post-deposition annealing [analyzed by Mrs. Franziska Simmen].	218
Figure 9.9	Cycle life behaviour of the as-deposited LiMn_2O_4 thin film electrode on stainless steel substrate cycled between 3.5 V and 4.4 V versus Li/Li^+ at different cycling rates. The LiMn_2O_4 thin film was deposited at $N^0 = 13200$ pulses, $T_s = 500\text{ }^\circ\text{C}$, $d_{t-s} = 4\text{ cm}$, $\phi = 4.3\text{ J cm}^{-2}$, and cooled in air with no post-deposition annealing [analyzed by Mrs. Franziska Simmen]. The 1C rate is assumed to be equivalent to $5\text{ }\mu\text{A cm}^{-2}$ in this case.	218
Figure 9.10	SEM images of the as-deposited LiMn_2O_4 thin film electrode on stainless steel substrate: (a) before cycling, and (b) after 100 charge-discharge cycles. Cycling took place between 3.5 V and 4.4 V versus Li/Li^+ at a cycling rate of $50\text{ }\mu\text{A cm}^{-2}$. The LiMn_2O_4 thin film was deposited at $N^0 = 18000$ pulses, $T_s = 500\text{ }^\circ\text{C}$, $d_{t-s} = 4\text{ cm}$, $\phi = 4.3\text{ J cm}^{-2}$, and cooled in air with no post-deposition annealing [measured by Dr. Anja Weber].	219

CHAPTER 1

INTRODUCTION

1.1 General Background

Electrochemical energy conversion and storage devices undoubtedly have a major role to play in the new clean energy economy. There are several driving influences that are working to promote change in our current fossil fuel dominated energy economy. Firstly, we are rapidly approaching the position where cheap oil and gas are no longer readily available. It is predicted that by 2015 our cheap crude oil supply will cease to exist, as demand will outstrip the supply [IEA, 1998]. Secondly, there is the issue of security of energy supply. This is partly a consequence of the demise of certain fossil fuel resources, but to a greater extent due to the perceived political problems, with many of the developed nations keen on ensuring a secure energy supply by implementing major changes in the energy economy. Thirdly, and also most importantly, concerns regarding green-house gas emissions, especially from carbon dioxide (CO₂), strongly advocate against utilization of fossil fuel sources, unless there are significant improvements in conversion efficiency.

There are probably two dominant types of energy storage systems required for the new energy economy, one related to static load leveling of renewables and the other related

to transport. For both, cost and reliability are extremely important; energy and power density are also important, although to differing degrees. For energy storage related to transport, high-power batteries are being developed for hybrid electric vehicles. Amongst the available energy storage systems, the lithium-based rechargeable battery system is of particular interest for hybrid electric vehicle applications. Of all the rechargeable battery systems, the lithium-ion (Li-ion) battery possesses the greatest energy density and has a power density close to that of the nickel-cadmium (Ni-Cd) battery [Tarascon and Armand, 2001]. In less than 5 years after its inception in the portable power sources market in the early 1990s, the Li-ion battery system has taken the largest market share of small portable power sources, to the detriment of traditional Ni-Cd, or even the newly developed nickel-metal hydride (Ni-MH) battery, which represents an evolutionary development in alkaline aqueous batteries [Broussely and Archdale, 2004].

Although the Li-ion battery concept appeared rather suddenly, one must consider that this is in fact the result of many years of research activity, from the early beginning of “lithium battery history”, which started about 40 years ago [Scrosati, 1995]. The concept of the “rocking chair battery”, which is applied in this doctoral work, was proposed a long time ago [Tarascon and Guyomard, 1993] to circumvent the poor reversibility of lithium metal. Graphite, which is the current negative electrode in commercial lithium-ion batteries, was also investigated very early [Armand, 1978]. Unfortunately, graphite was not seriously considered at that time, probably for two main reasons. Firstly, solvent co-insertion with lithium induced graphite exfoliation and subsequent material destruction. Secondly, when comparing the specific capacity of Li metal (3860 Ah kg^{-1}) and lithiated carbon (372 Ah kg^{-1}), it was not very attractive. After

years of intensive but rather unsuccessful research activity on the reversibility of lithium plating, a major avenue was opened with the discovery of the insertion of Li-ions into the amorphous carbon structure, without exfoliation. From a combination with LiCoO_2 , an already well known positive material that had been studied with lithium metal, the battery system was born [Yoshino, 1985], which was practically developed and named “Li-ion” a few years later [Nagaura and Tozawa, 1990]. In spite of the lower specific capacity of the amorphous carbon compared to Li metal, reasonable energy density was obtained with the first prototypes, in comparison with rechargeable lithium, in which lithium metal was introduced in very large excess as a trade-off for the poor reversibility.

This short history is recounted to point to the possible evolution from now on. The chances of finding a practical new battery system with a significantly higher energy density in the next 10 years are extremely small [Broussely and Archdale, 2004]. Li-ion has, however, been in constant evolution since its inception and will continue to evolve. The purpose of this doctoral work is to discuss possible ways of improvement via nanotechnology and extrapolate to the possible opportunities for future research directions.

1.2 Statement of Problem

Today lithium-ion batteries are the power sources of choice for popular portable electronics, such as cellular phones and notebooks [Scrosati, 1995]. However, despite their outstanding commercial success, these batteries are still open to improvements. Active research is continuing on all aspects of Li-ion batteries, i.e., anodes, cathodes,

electrolytes, and cell construction. The major factors limiting wider application of lithium-ion batteries remain cost and safety. New developments are taking place to address these limitations.

Graphite is the most common anode material used in commercially established lithium batteries. Graphite has a good cycling stability, but a relatively low specific capacity, not exceeding 372 mAh g^{-1} . Thus, if an improvement in energy content is desired, new, high-capacity alternative electrode materials have to be developed. In this respect, lithium storage metals appear to be very appealing candidates. A number of metals, e.g. Al, Si, Sn, and Sb, are capable of reacting with lithium to reversibly form intermetallic lithium alloy compounds. These alloys are in principle almost ideal anodes for lithium batteries: they can store and release a large amount of lithium-ions, assure high voltages when combined with lithium metal oxide cathodes, and provide specific capacities exceeding that of graphite by an order of magnitude [Huggins, 1989].

Unfortunately, the accommodation of the large amount of lithium is accompanied by severe volume changes in the host metal. These in turn induce mechanical strains, which lead the electrode to crack and eventually disintegrate, resulting in failure after a few cycles [Winter, 1998]. An effective way to improve the cycling stability of the metal alloy electrodes is modifying their morphology by reducing their particle size to a few nanometers or by designing special nanostructures [Patrissi and Martin, 2001].

Improvements on the cathode side are also critical for the progress of lithium batteries. Indeed, considerable efforts are presently being directed towards the replacement of the high cost, partially toxic LiCoO_2 with more affordable and sustainable materials.

Promising candidates are iron phosphates, such as the phospho-olivine, LiFePO_4 , which in a lithium cell may be reversibly delithiated to FePO_4 [Padhi, 1997]. This material is an appealing cathode material for lithium batteries: it is cheap, environmentally benign, and it has a reasonably high capacity (170 mAh g^{-1}), i.e., approaching that of LiCoO_2 . Meanwhile, LiV_3O_8 as a cathode material also has the advantages of higher capacity, lower cost, and better safety features [Kannan and Manthiram, 2006].

1.3 Importance of Study

Nanotechnology is the best tool for achieving breakthroughs in lithium-ion battery electrode materials. In this doctoral work, investigations were carried out with the aim of developing advanced lithium-ion batteries based on nanostructured materials. Indeed, this strategy is expected to have a two-fold effect on the performance of the electrodes: (i) improvement in cycling stability, since small particles will more easily accommodate the mechanical strains (since the absolute volume changes are smaller than for larger particles, although the relative changes are the same), and (ii) enhancement of power due to the reduction of the lithium-ion diffusion length.

Nanostructures are also highly beneficial for other classes of alternative electrode materials, e.g. for metal oxide electrodes [Li et al., 2000]. It is believed that the nanosized powders act as nucleation sites for the growth of the metal oxide particles, as well as forming conducting bridges between them, resulting in an improvement of the intra- and inter-conductivity of the nanoparticles.

It is necessary to understand how nanostructured materials influence the electrochemical performance of lithium-ion batteries when applied as electrodes and also to investigate the mechanism involved during electrochemical cycling when nanostructured materials are used instead of microstructured materials, which form the basis of current electrode materials. Therefore, it is of the utmost importance to carry out these investigations, as shown in this doctoral work, for the realization of nanotechnology in lithium-ion battery applications, especially for use in hybrid electric vehicle.

1.4 Objectives and Scopes of Research

The driving question behind the work of this doctoral thesis is how the lithium-ion battery performance is affected when nanostructured materials are used as electrode materials instead of the conventional micro-sized counterparts. Once the nanostructured materials are identified as potential candidates for use as electrode materials for both anode and cathode, the next question would be on how to further improve the rate capabilities and specific capacities of these nanostructured materials, by means of electrode engineering or even in-situ analysis for kinetics and thermodynamics studies.

Thus, the overall objective of this doctoral work is to synthesize nanostructured materials and apply them as electrode materials for use in lithium-ion batteries, with the emphasis on understanding the structural, morphological, physical, and also most importantly, electrochemical changes that occur when nanomaterials are used to replace conventional micro-sized materials as electrode materials in the lithium-ion battery system.

Meanwhile, some of the scope of the research that was carried out in this doctoral work is briefly outlined as follows:

- (a) A thorough literature review of current state-of-the-art lithium-ion battery technologies, especially on the role of nanotechnology and possible techniques for the synthesis of such nanomaterials (Chapter 2).
- (b) Carrying out the synthesis of nanostructured materials via different techniques, with an emphasis on the scalability of these processes, which include filtration (Chapter 4), spray pyrolysis (Chapter 5 and Chapter 6), co-precipitation (Chapter 7), and also flame spray pyrolysis (Chapter 7 and Chapter 8) methods.
- (c) Combining pulsed laser deposition (PLD) of thin layer oxides with the electrochemical characterization of the created interfaces, in order to gain better understanding and control of the solid-electrolyte interphase (Chapter 9).
- (d) Investigation of the structural and physical properties of the as-synthesized nanostructured materials by means of X-ray diffraction (XRD), thermogravimetric analysis (TGA), scanning electron microscopy (SEM), transmission electron microscopy (TEM), Brunauer-Emmett-Teller (BET) specific surface area measurements, Raman spectroscopy, four-point probe conductivity measurements, atomic force microscopy (AFM), Rutherford backscattering spectrometry (RBS), elastic recoil detection analysis (ERDA), and surface profilometry measurements.
- (e) Application and characterization of these electrochemically active nanostructured materials as electrodes for use in lithium-ion rechargeable batteries, via cyclic voltammetry (CV), galvanostatic charge-discharge cycling, and also the electrochemical impedance spectroscopy (EIS) technique.
- (f) Finally, summarizing the overall doctoral work and providing some suggestions for further research work related to these nanostructured materials (Chapter 10).

CHAPTER 2

LITERATURE REVIEW

2.1 Lithium-ion Rechargeable Batteries

Over the past few years, the battery industry has seen a major shift in the technology for portable power applications. Li-ion batteries, which did not come into existence until the early 1990s [Dresselhaus and Thomas, 2001], have become a standard for high-energy rechargeable battery technology and have captured the bulk of the portable device market. They have four times the energy and twice the power capacity of nickel cadmium (Ni-Cd) batteries, do not experience a memory effect (where partial discharge before recharge reduces the length of the next cycle), and have a 50 percent longer life cycle. Compared with nickel-metal hydride (Ni-MH) batteries, they have twice the energy, and they can be produced at a much lower cost. They are environmentally friendly, and their high average voltage of 3.6V make them ideal for powering a new generation of low-power 3-G electronics. These factors all have contributed to this relatively new battery technology's complete domination of the notebook computer and cellular telephone markets. An outline of the different reaction potentials of common electrode materials for the lithium-ion battery is illustrated in Figure 2.1.



See print copy for figure 2.1

Fig. 2.1. Overview of the different reaction potentials of electrode materials for the lithium-ion battery. White rectangles represent the positive electrode materials, and shaded rectangles the negative electrode material. On the left y-axis the materials are plotted against potential vs. Li/Li^+ , and on the right y-axis against potential vs. the standard hydrogen electrode (SHE) [Tarascon and Armand, 2001; Whittingham, 2004].

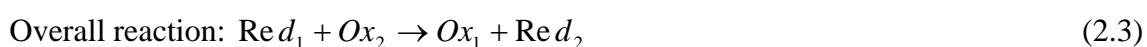
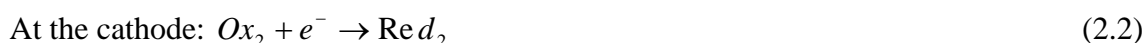
Demand and competition is driving the quest for higher storage capacity, longer operating times, faster recharging times, and other optimization of performance. Steady progress has been made by using improved materials for the anode, cathode and electrolyte, and the interfaces between them. Tarascon and Armand [2001] present an optimistic review of the technology, covering its historical background, its present status, and the challenges and opportunities now on the horizon. Three areas of opportunity, also common to most of the other alternative energy technologies are: advances in nanostructured materials provide a chance to improve both anode and cathode performance; new *in-situ* characterization techniques are helping to identify

materials problems in a format that permits rapid assessment of possible solutions; and advanced computer simulation modeling promises rapid progress in surveying new combinations of materials and geometries.

2.1.1 Basic Concepts and Principles of Operation

Electrochemistry covers all reactions in which a chemical change is the result of electric forces and in the reverse case, where an electric force is generated by a chemical process [Linden and Reddy, 2002].

A galvanic cell is an electrochemical cell that generates electricity as result of the spontaneous reaction occurring inside it. The cell consists of two dissimilar electrodes (the anode and the cathode) immersed in an electrolyte solution. The electrodes are electronic conductors and the electrolyte solution is an ionic conductor. At the interface between electronic and ionic conductors the passage of electrical charge is coupled with a chemical reaction. This type of reaction is known as a redox reaction, where there is a transfer of electrons from one species to another. These are two half reactions and involve at the anode the *oxidation* (*Ox*) of one species (the removal of electrons) and at the cathode the *reduction* (*Red*) of another (the addition of electrons).



Each of these reactions is related to a *standard electrode potential*, E^0 , which can be calculated from the thermodynamic data of the reaction. Under equilibrium conditions:

$$E^0 = \frac{-\Delta G^0}{nF} \quad (2.4)$$

where, $-\Delta G^0$ = standard Gibbs free energy

n = number of electrons

F = Faraday constant (96487 C)

As it is impossible to measure individual electrode potentials in an absolute sense, so they are each measured with reference to another electrode, which is used as standard electrode. The electrode normally used for this purpose is the *standard hydrogen electrode* (SHE), where the temperature is equal to 25 °C, the pressure is equal to 1 bar, and all species are at unity activity. For non-standard conditions, the *Nernst equation* can be used to calculate the potential of the half-reactions (E) at equilibrium:

$$E = E^0 - \frac{RT}{nF} \sum \ln a_i^{v_i} \quad (2.5)$$

where, a_i = activity of relevant species

v_i = stoichiometric coefficients of relevant species

R = gas constant

T = absolute temperature

The cell voltage of an electrochemical cell is calculated from the electrode potentials (reduction potentials) of the half-reactions. The overall *theoretical cell voltage*, ΔE^0 or U^0 , is obtained by subtracting the negative electrode potential, $E^{0,(-)}$, from the positive electrode potential, $E^{0,(+)}$:

$$U^0 = \Delta E^0 = E^{0,(+)} - E^{0,(-)} \quad (2.6)$$

Batteries, which are made up of two or more cells connected either in parallel or in series, can be separated into two classes: primary and secondary. Primary batteries are non-rechargeable, because the electrochemical reactions are irreversible under practical conditions (alkaline-manganese dioxide, zinc-air), and therefore are single use. In secondary batteries, the electrochemical reactions are reversible; therefore, these types of batteries are reusable (lead-acid, lithium-ion). In this type of battery during discharge, the chemical energy is transformed into electrical energy. The battery can be reused again once electrical energy has been converted into chemical energy during the charging process.

The terms *cathode* and *anode* cannot be properly defined in a rechargeable cell since the anode is identified as the electrode, which gives electrons to the external circuit, and the cathode is the electrode that receives electrons from the external circuit. Therefore depending on whether the cell is being charged or discharged the two terms are mixed. To avoid confusion, the electrodes can be simply categorized as either *positive* or *negative* because the term refers to their respective electrode potentials. Values of potentials for various half-cell reactions have been tabulated [Brett and Brett, 1993], and these enable theoretical cell voltages to be calculated if the two half-cell reactions are

known. Some important standard potential values in the battery technology are shown in Figure 2.2. A high cell voltage is obtained by combining two electrode systems with potentials far from each other.



See print copy for figure 2.2

For several of the performance criteria of electrochemical power sources, a distinction must be made between the theoretical values and the practical values. Theoretical values are calculated from the thermodynamics of the electrochemical cell reaction. Practical values are related to the total mass of the complete battery, including the mass of the electrolyte, the separators, the current collectors, the terminals, and the cell housing [Linden and Reddy, 2002]. In this work, the specific capacity always refers to the weight of the active component only.

The maximum accessible energy is simply the free energy of reaction, ΔG . Consequently, high energy results from the choice of electrode materials. This can be achieved by the selection of electrodes with the greatest difference of electrochemical potential, μ [Pletcher, 1991]. The cell voltage can be derived from the standard Gibbs free energy of the equivalent chemical reaction:

$$U^0 = \Delta E^0 = \frac{-\Delta G^0}{nF} \quad (2.7)$$

To evaluate the properties of electrodes in a secondary cell some general concepts are introduced, such as the follows:

- *Charge capacity*

The charge capacity, Q (Ah), is the total amount of charge obtainable from a cell and can be derived from Faraday's equation:

$$Q = \int_{t_1}^{t_2} I(t) dt = mnF \quad (2.8)$$

- *Theoretical specific charge capacity*

The theoretical specific charge capacity, q_{th} (Ah kg⁻¹), is the amount of charge per kg of reactants, m_i , and it can be calculated from the stoichiometry of the overall cell reaction:

$$q_{th} = \frac{nF}{\sum_i m_i} \quad (2.9)$$

It is usually desirable that the amount of energy stored in a given mass or volume is as high as possible. To compare the energy content or energy density content of cells, the terms *specific energy* (Wh kg⁻¹) or *energy density* (Wh dm⁻³) are employed, whereas the rate capability is expressed either as *specific power* (W kg⁻¹) or *power density* (W dm⁻³):

- *Theoretical specific energy*

The theoretical specific energy, w_{th} (Wh kg⁻¹), is the amount of electrical energy per unit of mass that a battery is able to deliver, and is a function of the cell potential (V) and charge capacity (Ah kg⁻¹):

$$w_{th} = \frac{nF\Delta E^0}{\sum_i m_i} \quad (2.10)$$

- *Theoretical energy density*

The theoretical energy density, $W_{V.th}$ (Wh dm⁻³) is the amount of electrical energy per unit of volume:

$$W_{V.th} = \frac{nF\Delta E^0}{\sum_i V_i} \quad (2.11)$$

- *Specific power*

The specific power, p (W kg⁻¹), is the ability of the cell to deliver power per unit mass:

$$p = \frac{I\Delta E^0}{\sum_i m_i} \quad (2.12)$$

- *Power density*

The power density, P_v (W dm^{-3}), is the power divided by the volume of the cell:

$$P_v = \frac{I\Delta E^0}{\sum_i V_i} \quad (2.13)$$

- *The charge/discharge rate*

When electrochemically cycling a cell, the term charge/discharge rate or C-rate ($C/\Delta t$) is often employed to describe the time frame for either one full charge or discharge. C denotes either the theoretical charge capacity of a cell or battery (Ah) or the nominal capacity of a cell or battery, as indicated by the manufacturer. For example C/37, therefore means a current theoretically allowing a full discharge in 37 hours.

- *Irreversible capacity loss*

It is also important to define how much capacity is lost after each cycle. Irreversible capacity loss is therefore explained by the following equation:

$$\text{Irreversible Capacity Loss} = (n_{th} \text{ Charge} - n_{th} \text{ Discharge})/n_{th} \text{ Charge} \times 100 \% \quad (2.14)$$

The main feature of Li-ion cells is that current is carried by lithium ions from the positive electrode (cathode) to the negative electrode (anode) during charging, and from negative to positive during discharging, as shown in Figure 2.3. No lithium metal is present in the cell, thereby alleviating some serious safety concerns. The ions are small and reside within the crystal structure of the electrode materials. The overall cell

chemical reactions (Eq. 2.15) for cell charging and discharging are shown below for a typical LiCoO_2 cathode and graphite anode:



The charge reaction proceeds to the right and the discharge to the left [Winter and Brodd, 2004]. As the cell is charged, lithium ions move to the carbon ($x = 1$) from the cobalt ($x = 0$). In actual practice, not all ions are transported back and forth, i.e. $0 < x < 1$.

See print copy for figure 2.3

2.1.2 Components

A battery consists of one or more electrochemical cells, connected in series or parallel, or both, depending on the desired output voltage and capacity. The electrochemical cell generally consists of only a few major components, as shown in Figure 2.4:

1. The anode, or negative electrode, or the reducing electrode, which gives up electrons to the external circuit and is oxidized during the electrochemical reaction.
2. The cathode, or positive electrode, or the oxidizing electrode, which accepts electrons from the external circuit and is reduced during electrochemical reaction.
3. The electrolyte or the ionic conductor, which provides the medium for transfer of electrons, as ions, inside the cell between the anode and cathode. The electrolyte is typically a liquid (an organic solvent, such as EC-DMC), with dissolved salts (such as LiPF_6) to impart ionic conductivity. Some batteries use solid electrolytes, which are ionic conductors at the operating temperature of the cell.
4. The separators, which serve two functions. Not only do they keep the positive and negative electrodes apart, but they serve as a safety device as well. In the event that a cell becomes too hot, the low-melting polymers melt, closing off the pores through which the ions travel and thereby shutting off the cell current. It is expected that control circuits will shut the cell down before this happens, since the cell cannot be reused once the shutdown separator melts.

The basic cell chemistry and design are the same for all types of Li-ion cells. Numerous types of cell configurations for Li-ion batteries, with details showing the shapes and components of these cells, are shown in Figure 2.4 [Tarascon and Armand, 2001]. For example, in Figure 2.4(a), thin layers of cathode, separator, and anode are rolled up on a central mandrel and inserted into a cylindrical can. The gaps are filled with liquid electrolyte. The basic design remains unchanged on substitution of one electrode material for another, although the layer thickness might change. This is the same design used for most small commercial cells, such as the 18650, which used in such devices as camcorders.

See print copy for figure 2.4

2.1.3 Advantages

Considering the use of conventional batteries as power sources for consumer electronics or electric vehicles, the principal problem is their low specific energy compared with other batteries. This low specific energy is mainly due to their low voltage. This relationship is demonstrated in Figure 2.5. The most important property a battery should have is a high energy density, and this parameter is much more important than voltage or specific charge alone. The second important property to consider is how this energy is supplied: the potentials should be as constant as possible. In operative terms, it is better not having any flex in the curve “*Potential vs. Capacity*” (Fig. 2.6). The presence of flexes indicates that the energy is furnished at different potentials. Of course, this potential can be stabilized easily by an appropriate electronic component, but with additional costs. That is why it is preferable to have a no-flexes discharge shape.

See print copy for figures 2.5 and 2.6

From the user's point of view, Li-ion batteries have the following advantages [Scrosati, 1995; Owen, 1997; Winter et al., 1998; Tarascon and Armand, 2001]:

- High energy density: approximately double that of Ni-Cd batteries.
- High output voltage: 3 time greater output power than Ni-Cd batteries.
- Low self-discharge rate: around 2 % per month at 20 °C.
- Long life cycle: 500 recharging cycles with consistent performance.
- Cost saving: money is saved on disposal of waste batteries.
- Environmentally friendly: Li-ion batteries do not contain cadmium, mercury, or other toxic heavy metals.
- Wide operating temperature range due to non-aqueous electrolytes.
- Lithium has a very negative redox potential, -3.04 V vs. SHE, and also a low weight of approximately 7 g mol⁻¹.

For large batteries, for example in electric vehicles, this higher voltage is an additional advantage, because it reduces the number of cells required to achieve the necessary voltage. This makes the battery management system less complex [Scrosati, 1995]. The present specific power and energy density for commercial lithium-ion batteries at the cell level stands at approximately 100 W kg⁻¹ and 160 Wh kg⁻¹, respectively. High power lithium-ion cells can reach power densities of 3000 W kg⁻¹, but there is a trade-off with a lower energy density of 80 Wh kg⁻¹ [Whittingham, 2004]. A Ragone plot (Fig. 2.7) furthermore shows the superior performance of the lithium ion battery compared to alternative battery systems, such as lead acid and nickel-metal hydride, where the maximum respective energy densities are only 30 and 70 Wh kg⁻¹, respectively.

See print copy for figure 2.7

2.1.4 Commercial Applications

Lithium-ion (Li-ion) batteries are currently in large-scale commercial production for use in such consumer electronic products as laptop computers and portable telephones. Figure 2.8 shows the distribution of the rechargeable battery market for different applications. Among the major producers are Sony, Sanyo, Varta, and SAFT. Most Li-ion production is in Japan, but Polystor is now producing small cells in California [Ritchie, 2004]. In the case of small batteries for consumer electronics, Japanese market dominance is already established. The experience, infrastructure, and established supply lines would provide a definite advantage for Japanese producers; however, large volume production of batteries for electric and hybrid batteries has not yet been established.

See print copy for figure 2.8

Sony, Matsushita, and Sanyo all have had significant R&D programs in this area, and each invested about \$150 million in production facilities in quick succession. Starting in 1991, they invested heavily in production capability; this investment continued throughout the decade and, in some cases, amounted to as much as \$1 to \$2 billion or more. Motorola had a significant R&D effort to develop its own Li-ion polymer technology. After completing the development, rather than pilot and produce the cells themselves, Motorola decided to license the technology, as did Telcordia (now SAIC).

Today the principal manufacturers of Li-ion batteries are, with the exception of BYD in China, large, vertically integrated Japanese and Korean producers of consumer electronics. These accounts for all of the Li-ion batteries produced in Japan, where about 80 percent of the world's production of Li-ion batteries is located (the rest is in China, Taiwan, and South Korea). Japanese Li-ion battery production goes first to captive in-house uses for a company's own portable electronic devices. The remaining production (a sizable percentage of the total production) is sold to other original equipment manufacturers (OEMs) of portable devices. These manufacturers have established very high standards for quality, performance, and safety for their products. Device designers will share future product development and designs within their own company, but are reluctant to share the same data with outside suppliers. Figure 2.9 summarizes current market shares for Li-ion batteries, as assessed by the Institute of Information Technology, Ltd. Its data show that volume exceeded 800 million cells by 2002, when the value reached nearly \$3 billion.

See print copy for figure 2.9

In 2003, BYD of China became a significant supplier, as did South Korean companies Samsung and LG Chemical. The manufacture of Li-ion batteries has begun to shift from Japan to China as some major producers take advantage of the Chinese government's willingness to provide low-cost loans and production facilities or support for companies that bring strategic new technologies to China. South Korea also provides government incentives and has essentially the same cost structure as China. In the past three years, Samsung and LG Chemicals entered the market. Samsung penetrated the market and captured the fifth spot in production capability, with LG not far behind.

Major Japanese and Korean manufacturers of portable electronic devices have their own integrated Li-ion battery production facilities. They have pursued aggressive research and development efforts, leading the way in making engineering improvements as well as developing new materials to enhance Li-ion performance. The governments of South Korea and China have made Li-ion systems a strategic technology. Both governments have encouraged investment in the development of new technology, and support new production facilities with loans or grants.

In preparation for the 2008 Olympics, the Chinese government has designated both Li-ion and fuel cell systems as strategic technologies. This has attracted new production from Japan to China, given the potential size of Chinese markets for portable electronics devices. New production facilities are being constructed in China, some as joint ventures between Chinese companies and major Japanese companies. As a complimentary partnership, Chinese participants get government funding to assist in building facilities, and the Japanese partner supplies the technology.

2.1.5 On-going Scientific Challenges

The technology used to produce small consumer cells is essentially transferable to production of the larger cell sizes that would be put together into battery packs for electric vehicles (EVs) and hybrid electric vehicles (HEVs). However, the cost of the small cells is far too high for such batteries to be used economically in mass-market vehicles. Therefore, to improve their competitive position and also with a view to potential long-term development of the vehicle market, considerable research and development (R&D) work has been devoted to lowering the costs of Li-ion batteries. Much of the effort has focused on reducing the extremely high cathode costs. However, as cathode costs are brought down, efforts to reduce other cost components are also appropriate. These price reductions will be achieved by substitution of less expensive materials, as well as by utilization of improved production processes and more efficient production in larger plants. If electric vehicles were ever to be produced for the U.S. mass market, production or imports of several materials would need to be stepped up considerably, with the impact on price depending on the material. For some, such as cobalt, supplies could eventually be constrained, driving up the price. Material supply constraints would be a factor for pure electric vehicles (EVs) long before they would affect the hybrids, simply because of the larger quantities of materials required per vehicle. Similarly, hybrids would be less adversely affected in the event that battery costs remain above the goals set by the US government, because batteries represent a much smaller percentage of the total cost of hybrid vehicles. Therefore, the research on material cost reduction is more crucial for EV development than for HEV development. This can be seen from the several hybrid models expected to be introduced into the automobile market in 2-3 years time.

2.2 Negative Electrode Materials For Lithium-ion Batteries

Graphitic carbons are at currently the most often employed material for the negative electrode due to their low cost, excellent cyclability and reliability, and non-toxicity [Owen, 1997; Winter et al., 1998; Tarascon and Armand, 2001;]. Table 2.1 lists possible alternative materials for the negative electrode in Li-ion batteries. The compounds for negative electrodes are generally divided into two major categories: the *carbonaceous* and *non-carbonaceous* based materials. Most of the present research is moving towards replacing carbonaceous anode with non-carbonaceous anode, as with metal-alloys, transition metal oxides, and also most recently, hybrid compounds. The driving force behind this current research trend is to obtain a new generation of anode materials with higher specific capacities ($> 372 \text{ mAh g}^{-1}$), while retaining the good properties of carbonaceous materials such as cyclability, cost, and safety features.

See print copy for table 2.1

2.2.1 Carbonaceous Materials

Carbonaceous-based materials are the most attractive and widely investigated materials for use as anode in Li-ion batteries [Winter et al., 1998; Tarascon and Armand, 2001]. This has been mainly due to the following reasons:

- low cost,
- high safety for people and the environment,
- low Li-ion insertion potential (~ 0.1 V vs. Li/Li^+), which is very close to that for metallic lithium,
- good cycling stability due to the high mechanical integrity (compared to metal alloys) of the electrode even after 500 charge-discharge cycles, and
- higher specific charge compared to transition metal oxides or transition metal sulphides (see Table 2.1).

The insertion of lithium into carbon is referred to as *intercalation*, with intercalation being formally described as the insertion of a guest species into a layered host structure, without any major resulting structural changes [Winter et al., 1998]. In half-cell reactions against metallic lithium, lithium-ion intercalation into carbon is referred to as the discharge step, while the de-intercalation process is the charge step.



At ambient temperature, graphitic carbon intercalates one lithium atom per six carbon atoms to form the compound, LiC_6 [Winter et al., 1998]. The maximum attainable specific charge capacity of the LiC_6 electrode is 372 Ah kg^{-1} (based on the carbon

weight only). Particularly during the first charge step of graphite electrodes, some amount of charge is consumed in an irreversible way. This is typical for all types of carbon electrodes. It is caused by side reactions involving the decomposition of the electrolyte, which induces the formation of a *solid-electrolyte interphase* (SEI) on the electrode surface [Peled, 1979]. The SEI prevents further electrolyte decomposition and allows the transfer of ions from the electrolyte into the electrode [Besenhard et al., 1995; Aurbach et al., 1999; Xu, 2004].

The type of electrolyte used strongly affects the formation of the SEI film. A common electrolyte solvent, propylene carbonate (PC), undergoes reduction at around 0.8 V vs. Li/Li⁺ [Buqa et al., 2005; Spahr et al., 2006]. At a slightly more positive potential, the intercalation of PC solvated lithium ions into graphite takes place. This leads to an expansion of the graphene layers. Therefore, exfoliation of the graphite will take place before a stable SEI film can be formed. On the other hand, ethylene carbonate (EC) is reduced much faster than PC. Thus, the SEI is formed rapidly and prevents further solvated intercalation of lithium [Fong et al., 1990].

Amongst the non-graphitic carbons, there are hard carbons. Here, the lithium can be inserted not only between the graphene layers but also into the voids of this material and onto the sides of isolated graphene layers. Such carbons show specific charge capacities of around 400 to 2000 Ah kg⁻¹, and are mainly obtained by pyrolysis of sugars or polymers [Larcher et al., 1999]. The main problem associated with these hard carbons is the high irreversibility, leading to poor cycling stability. This suggests that lithium becomes trapped in the carbon matrix and indicates the possible formation of stable LiC_x compounds [Winter et al., 1998].

Recently, with the discovery of new crystalline forms of carbon, i.e. the single-walled carbon nanotubes (SWCNTs) and multi-walled carbon nanotubes (MWCNTs), with dimensions of less than 100 nm in tube diameter, it appears that there may be a new paradigm in carbonaceous-based battery electrode materials [Baughman et al., 2002]. These one-dimensional carbon materials have attracted considerable attention, because they exhibit an increased capacity as an active material and induce highly improved cyclic characteristics as additive to the anode material [Che et al., 1998; Gao et al., 1999; Leroux et al., 1999; Claye et al., 2000; Endo et al., 2000; Lu and Chung, 2001; Frackowiak and Béguin, 2002; Shimoda et al., 2002; Wu et al., 2003a; Yoon et al., 2003; Ng et al., 2005].

Nanotubes confer a high mobility to ion exchange processes, a fundamental for the dynamic response of batteries based on lithium intercalation. For instance, recent experimental results have shown that it is possible to charge SWCNTs up to one lithium for every three carbon atoms and higher [Meunier et al., 2002]. Lithium capacities of crude material have been determined experimentally to exceed 600 mAh g^{-1} [Frackowiak and Béguin, 2002; Yang et al., 2002]. The maximum reported reversible capacity is 1000 mAh g^{-1} for SWCNTs that are mechanically milled in order to enable filling of the nanotube cores [Gao et al., 1999], as compared to 372 mAh g^{-1} for graphite and 708 mAh g^{-1} for ball-milled graphite [Disma et al., 1997]. However, the large irreversible component of the capacity (coexisting with the large reversible storage capacity), the absence of a voltage plateau during discharge, and the large hysteresis in voltage between charge and discharge [Gao et al., 1999; Frackowiak and Béguin, 2002] currently limit energy storage density and energy efficiency, as compared with those of other competing carbonaceous materials.

2.2.2 Lithium-Metal Alloys

Due to their much higher theoretical specific charge capacities compared to graphite, binary or ternary lithium-metal alloys with metals such as tin [Winter and Besenhard, 1999; Tirado, 2003], aluminium [Lindsay et al., 2003], lead [Martos et al., 2001 and 2003], antimony [Tirado, 2003], silicon [Wilson and Dahn, 1995], and copper-tin [Kepler et al., 1999] are among the most well investigated classes of materials. However the main problem encountered with these alloys is due to the huge volume changes when lithium is either incorporated or removed [Besenhard et al., 1997]. As a result, mechanical stress and cracks occur during cycling, which leads to electrochemically inactive particles and thus quite poor cycle stabilities. In this doctoral work, only lead (Pb) and silicon (Si)-based compounds are reviewed in detail, as only these materials are investigated in this dissertation.

Today, the use of lithium alloys as anodic materials in Li-ion batteries is an interesting field of research on account of the promising results provided by tin-based compounds. Martos et al. focused on the ability of lead to form lithium alloys [2001 and 2003]. They have reported on the potential of lead oxide as an anodic material. The toxic effects of this element can be avoided by strictly adhering to lead-acid battery collection and recycling regulations currently in force in most countries. This system was selected for two reasons [Martos et al., 2001], namely: (i) the low cost of lead; and (ii) the commercial significance of the lead-acid battery. A lead-based material usable in both lead-acid and Li-ion batteries would be attractive for manufacturers wishing to complement or replace the role of lead-acid batteries in its traditional market (the automotive industry).

Martos et al. [2003] also examined the electrochemical performance of various lead-based systems as anodic materials for Li-ion cells. Three different procedures were used to obtain three different samples the main components of which were PbO_2 , PbO , and Pb , respectively. The first sample consisted of micron-sized particles and the other two of sub-micron particles. The most interesting electrochemical reaction indicated their usefulness as anodic materials in the formation of reversible Li_xPb alloys, together with the irreversible formation of Li_2O in the reduction of lead oxides during the first discharge. The presence of this species enhances the cycling properties of the electrode by acting as a dispersion agent, preventing the formation of large Pb aggregates and increasing the reversibility of alloying/de-alloying processes.

Thus, the best electrochemical response was that of samples composed of lead oxides; by contrast, the cell made from the sample with a high lead content delivered a lower capacity. However, the specific capacity of these lead-based compounds fades on cycling. This shortcoming was circumvented by depositing the active material on lead sheets. The efficient adherence of particles to the substrate, via a mechanism that resembles curing of the positive plate of the lead-acid battery, may account for the good capacity retention observed.

Since it has the highest known theoretical capacity (4200 mAh g^{-1}), silicon would seem to be a superior anode material for high energy-density Li-ion batteries [Tarascon and Armand, 2001]. However, severe capacity fade during initial cycling has been found to be a limiting issue for Si anodes. During the last decade, intensive research has been conducted to understand the reasons for this poor capacity retention, and several methodologies have been proposed to overcome the problem.

In powder-based Si anodes, the decrease in capacity during cycling results from the increasingly large volume changes in Si as Li insertion proceeds. Since Si undergoes 400 % volume expansion at maximum Li insertion, it may not be possible to achieve a reversible volume change. Because of this expansion, stresses created in the anode may exceed the breaking stress of Si, resulting in particle cracking and the unavailability of progressive amounts of Si for further Li insertion and extraction due to loss of inter-particle electronic contact. In addition, when Si is charged to potentials less than 0.03 V versus Li/Li^+ , formation of a two-phase system occurs, leading to higher internal stresses in the anode material [Winter et al., 1998].

Several methods have been examined to attempt to improve the capacity retention of Si anodes. Among these, reduction of the silicon particle size to nanometers has been somewhat helpful, but it has failed to completely prevent capacity fade [Li et al., 1999a; Guo et al., 2005a]. Since the stresses are very high, it may not be possible to accommodate them by dispersing Si in a brittle matrix, which usually has a very low plastic deformation region. When such brittle matrices are used, stress relief takes place via the new surfaces arising from particle cracking. However, this is not a desirable process, since it results in capacity fade. To prevent this and obtain improved cycle life, it is essential to disperse Si in a highly ductile matrix with a large plastic deformation region and a large fracture stress value. The matrix should also have high electronic conductivity for effective charge transfer reactions to take place.

Dispersed Si in an inactive host matrix results in lower reversible capacity. Among the various materials tested, a Ni-Si alloy dispersed in a carbon matrix [Park et al., 2005] showed higher capacity retention. During the initial cycle, a Ni-Si/graphite anode showed a reversible capacity of 830 mAh g^{-1} , which decreased to 730 mAh g^{-1} after 40 cycles. The improved capacity retention of this anode compared with that of pure Si was due to better accommodation of volume change by the NiSi and NiSi₂ phases and the disordered graphite matrix.

When Si is dispersed in an active metal matrix such as Mg [Kim et al., 1999; Moriga et al., 2000; Roberts et al., 2002], Ag [Hwang et al., 2001; Wu et al., 2003b], Sn [Beaulieu et al., 2003], or other metals [Kasamatsu et al., 2003; Asao et al., 2004], a further decrease in capacity retention is observed. This is due to increased pulverization of the anode, which results from Li insertion into the active metal matrix.

When the inactive metal matrix is replaced by soft carbon, a significant improvement in capacity retention has been observed. This is due to the compliant nature of carbon, which maintains contact during the volume changes, at least to a certain extent. Carbon permits formation of a conductive network inside the anode, which results in improved electronic connection between the anode active particles [Winter et al., 1998]. Among the Si/C composite anodes prepared by different methods, one prepared by Si deposition on graphite [Holzapfel et al., 2005a] was found to have a reversible capacity of 900 mAh g^{-1} after 100 cycles. However, the thermal vapor deposition process makes anode fabrication expensive, making it unsuitable for practical Li-ion cells.

A nano-Si cluster/SiO_x-C composite anode prepared by milling, polymerization, and heat treatment showed a reversible capacity of 620 mAh g⁻¹ after 200 cycles [Morita and Takami, 2006]. Although the reported cycle life was the highest of all the powder-based Si anodes, its larger irreversible capacity observed during initial cycling is disadvantageous. A Si/C composite anode prepared from dispersion of Si in a carbon aerogel [Wang et al., 2004] showed a stable reversible capacity of 1450 mAh g⁻¹ for 50 cycles. Its reported cycle life was still insufficient to meet commercial requirements.

Among the various powder based Si anodes reported in the published US patent application literature, systems prepared from Si dispersed in a matrix containing multiple metallic species or intermetallic compounds gave high reversible capacity and excellent cycling stability. One such anode was fusion fabricated Si-Mg-graphite [Kasamatsu et al., 2003], which retained over 80 % of its initial capacity after 300 cycles because of its excellent electronic conductivity. Several other similar Si alloy anodes prepared by a melting process have shown high capacity retention.

The recently commercialized Sony Nexelion cell uses a tin-based amorphous alloy anode [Miyaki, 2005]. Although tin experiences a large volume change on Li insertion, the tin-based amorphous alloy prepared by Sony was shown to exhibit 92 % capacity retention after 100 cycles. This was attributed to the inclusion of multiple metallic elements into the anode, which minimized dimensional change. These results appear to indicate that alloy-based Si anodes may show potential for commercial Li-ion secondary cells. Future work might focus on identifying alloys, which might suppress the large volume change on Li insertion in Si.

2.2.3 Transition Metal Oxides

One of the main challenges in the design of Li-ion batteries is to ensure that the electrodes maintain their integrity over many discharge-charge cycles. Although promising electrode systems have been proposed [Shodai et al., 1996; Idota et al., 1997; Kepler et al., 1999], their lifespans are limited by Li-alloying agglomeration [Courtney, 1999] or the growth of passivation layers [Denis, 1997], which prevent the fully reversible insertion of Li-ions into the negative electrodes.

Transition metal oxides with a layered structure favorably permit lithium intercalation or de-intercalation. Nevertheless the potentials at which this process takes place often occurs in a region far above the Li/Li^+ couple and much lower than the 4 V positive electrode material. Therefore a greatly reduced voltage is obtained when these materials are combined in the cell, resulting in low energy and power densities for these systems [Winter et al., 1998].

Poizot et al. [2000] were the first to report that electrodes made of nanoparticles of transition-metal oxides (MO, where M is Co, Ni, Cu or Fe) demonstrate electrochemical capacities of 700 mAh g^{-1} , with 100 % capacity retention for up to 100 cycles and high charging rates. The mechanism of Li reactivity differs from the classical Li insertion/de-insertion or Li-alloying processes and involves the formation and decomposition of Li_2O , which accompany the reduction and oxidation of metal nanoparticles (in the range from 1-5 nm), respectively. They also expect that the use of transition-metal nanoparticles to enhance surface electrochemical reactivity will lead to further improvements in the performance of lithium-ion batteries.

Co_3O_4 nanotubes were reported as anode materials by Li et al. [2005]. The results show that the Co_3O_4 nanotubes prepared by a porous alumina template method display high discharge capacity and superior cycling reversibility. The nanosized Co_3O_4 synthesized through pyrolysis of the oxalate precursor also exhibited large lithium storage capacities and reversible capacities greater than 900 mAh g^{-1} [Yuan et al., 2003]. To improve the initial coulombic efficiency of Co_3O_4 , Ni was added by a ball-milling method. The irreversible capacity was decreased from 30 to 20 % [Kang et al., 2003].

The electrochemical reactions with lithium are complex and involve the initial formation of an insertion product, $\text{Li}_x\text{Co}_3\text{O}_4$. When nanosized Co_3O_4 was used as a starting material, the first plateau was described as due to the formation of CoO . Subsequently, reversible formation of Li_2O occurred on cycling, in which oxygen recombination takes place in a poorly crystalline state. The ultra-fine cobalt spinel oxide was obtained by two different routes: the reaction of octacarbonyl cobalt with oxygen [Wang et al., 2002] and the reaction with Co (II) alkoxide propanediol [Larcher et al., 2002].

Good electrochemical performance was also found with NiO and FeO , in which reversible capacities close to 700 mAh g^{-1} were reported with high cycling efficiency, and later in Cu_2O prepared by the polyol process, with a capacity of approximately 400 mAh g^{-1} [Grugeron et al., 2001]. Although the potential applicability of these materials has been the subject of some debate, the important role of nanomaterials has been clearly demonstrated [Wilkinson et al., 2000].

2.2.4 Titanium Compounds

Titanium containing compounds such as the anatase form of titanium dioxide (TiO_2) [Sudant et al., 2005] and titanium spinel ($\text{Li}_4\text{Ti}_5\text{O}_{12}$) insert lithium at potentials around 1.78 and 1.56 V vs. Li/Li^+ respectively [Strobel et al, 1996]. This potential would lead to a low overall cell voltage and poor energy densities. Nevertheless these materials are of interest because of their rapid discharge and charge properties, due to a high diffusion rate of lithium within these materials. $\text{Li}_4\text{Ti}_5\text{O}_{12}$ is under serious consideration as the negative electrode in high-power cells since a lithium insertion potential of 1.56 V avoids the danger of lithium metal deposition at high charge rates, which may occur if graphitic carbon is used [Whittingham, 2004].

Further interest in anatase was developed in the study of lithium diffusion properties inside nanocrystalline samples. Chemical diffusion coefficients of approximately $1 \times 10^{-17} \text{ cm}^2 \text{ s}^{-1}$ during lithium insertion and approximately $4 \times 10^{-17} \text{ cm}^2 \text{ s}^{-1}$ during extraction have been reported [Lindstrom et al., 1997]. Recently, Wagemaker et al. [2002] reported the direct observation by solid state NMR of continuous lithium-ion exchange between the intermixed crystallographic lithium-rich and lithium-deficient phases, with a continuous flux of lithium-ions across the phase boundaries of $1.2 \times 10^{20} \text{ s}^{-1} \text{ m}^{-2}$.

Concerning the spinel $\text{Li}_4\text{Ti}_5\text{O}_{12}$ with a $(\text{Li})_{8a}(\text{Li}_{1/3}\text{Ti}_{5/3})_{16d}\text{O}_4$ cation distribution in the $Fd3m$ space group, Ohzuku et al. [1995] reported its possible use as a lithium insertion material. After lithium insertion up to one lithium per formula, they proposed that the cations are redistributed using the $16c$ sites, which are empty in the normal spinel,

leading to $(\text{Li}_2)_{16c}(\text{Li}_{1/3}\text{Ti}_{5/3})_{16d}\text{O}_4$. This process was found to induce little change in the unit cell parameters. Such a zero-strain property allowed enhanced stability and little damage to the electrode on cycling. The electrochemical curves showed a plateau at approximately 1.56 V and capacity values close to 150 mAh g^{-1} beyond 100 cycles.

2.3 Positive Electrode Materials For Lithium-ion Batteries

There is a wide range of materials that can be used as positive electrodes for Li-ion batteries. The best ones are those with no or little structural modification during cycling. Typical insertion or intercalation compounds are therefore preferred candidates. In these materials, removal and subsequent insertion of lithium-ions in the host lattice precedes *topotactically* (without change in the structure). The reaction at the positive electrode can be described as follows:



where (HOST) is an insertion cathode material.

Several key requirements that must be considered carefully when choosing a cathodic compound [Whittingham, 2004]:

- high free energy of reaction with lithium,
- wide range of x (amount of Li-ion insertion),
- a reasonably low mass and volume per Faraday charge stored,
- small structural changes on reactions,
- good reversibility of reaction,

- rapid diffusion of lithium within the host lattice,
- good electronic conductivity,
- non-solubility in electrolyte, and
- ease and low cost of synthesis.

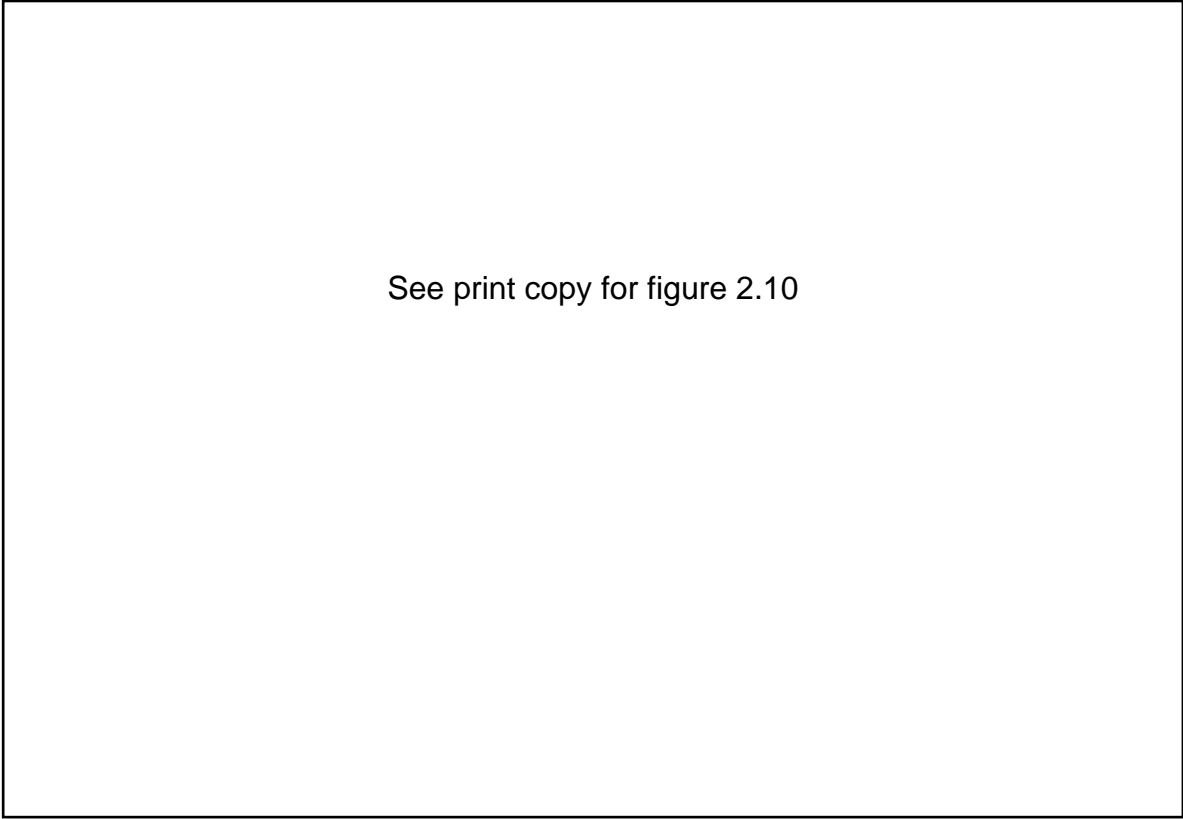
Table 2.2 displays the possible alternative cathode materials and their corresponding characteristics. The compounds for positive electrodes are generally divided into four major categories: the *layered transition metal oxides*, the *spinel oxides*, the *olivines*, and non-lithiated compounds such as the *vanadates*.

See print copy for table 2.2

2.3.1 Layered Oxides

The good cyclability and stability of lithium cobalt oxide (LiCoO_2) has allowed it to become the most widely used positive electrode material in commercial lithium-ion batteries [Winter et al., 1998; Tarascon and Armand, 2001; Linden and Reddy, 2002; Whittingham, 2004]. Alternatives to the use of LiCoO_2 are being investigated due to its high toxicity and low natural abundance.

The $\alpha\text{-NaFeO}_2$ structure of LiCoO_2 is built up from a cubic close-packed oxygen array [Mizushima et al., 1980; Reimers and Dahn, 1992; Ohzuku and Ueda, 1994; Winter et al., 1998]. The lithium and transition metal atoms are distributed in the octahedral interstitial sites in such a way that CoO_2 layers are formed, consisting of edge sharing (CoO_6) octahedra. Between these layers lithium resides in octahedral holes, which give LiO_6 coordination (Fig. 2.10) [Johnston et al., 1958].



See print copy for figure 2.10

Although the theoretical capacity of LiCoO_2 is 248 mAh g^{-1} , the material delivers only around 137 mAh g^{-1} due to structural restrictions. LiCoO_2 crystallizes in the space group $R\bar{3}m$. The lithium-ion reversibly intercalates into or out of the van der Waals gap between the CoO_2 layers. In general, the a -axis changes little, but the c -axis changes from 14.1 to 14.6 Å with lithium de-intercalation [Hoshino et al., 1994]. Since a new phase appears near $x = 0.5$ in Li_xCoO_2 , cycling is usually performed for x -values, $0 < x < 0.5$.

Many synthesis routes have been used to prepare electrochemically active LiCoO_2 compounds, including the conventional sintering of carbonate mixtures [Ohzuku et al., 1990; Fey et al., 1993], nitrate mixtures [Antaya et al., 1993], and LiOH and either a carbonate [Antaya et al., 1993], an oxide [Lecerf et al., 1989; Broussely et al., 1993], or a nitrate of cobalt [Yoshio et al., 1992]. The general trend suggests that the high temperature routes have little or no influence on the electrochemical properties of the LiCoO_2 materials. However, most reports on materials prepared by a low-temperature method [Gummow et al., 1993; Garcia et al., 1995; Yazami et al., 1995] show a high initial capacity, which unfortunately fades very quickly with cycling. Recently, Kawamura et al. [2005] reported that the rate capability of Li cells was very much improved by using cathodes made of nanosized LiCoO_2 ($\sim 5 \text{ nm}$), compared with that of cathodes made with the usual $5 \text{ }\mu\text{m}$ LiCoO_2 . Although the energy density of LiCoO_2 containing commercial cells has doubled since their introduction to 400 Wh dm^{-3} , the high price of this material limits its use to the small cells found in mobile phones and laptops. LiNiO_2 is isostructural with LiCoO_2 , but its use as a viable electrode material is limited due to safety issues arising from its instability at low lithium content [Reimers et al., 1993; Rougier et al., 1996].

2.3.2 Spinel Oxides

Although the reversible specific capacities for manganese oxides are lower than those of cobalt and nickel based LiMO_2 compounds, they potentially represent the least expensive options available as cathode materials. Much of the earlier work has been concentrated on the spinel phase of lithium manganese oxide (LiMn_2O_4) [Thackeray et al., 1997].

Spinel LiMn_2O_4 has the following four advantages over Co- or Ni- containing systems:

- lower cost with the substitution of Mn for Co or Ni,
- larger thermal stability domain, especially during overcharge,
- higher discharge voltage, which is useful for telecommunication appliances, and
- more environmentally friendly.

However, LiMn_2O_4 suffers from some major difficulties, such as the following:

- low specific capacity, with a theoretical capacity of only 148 mAh g^{-1} ,
- potentially lower power density compared to layered materials (LiCoO_2 and LiNiO_2), and
- high capacity fading with cycling, especially at elevated temperature.

Lithium manganese oxide (LiMn_2O_4) has a cubic spinel structure (Fig. 2.11). The structure can be expressed as a cubic close-packed oxygen array with the oxygen anions on the crystallographic $32e$ sites of the $Fd3m$ space group. The manganese cations reside in half of the octahedral interstitial sites, $16d$, and the lithium cations in one eighth of the tetrahedral sites, $8a$. The interstitial space in the Mn_2O_4 framework

corresponds to a diamond-type network of tetrahedral $8a$ and surrounding octahedral $16c$ sites. These vacant tetrahedral and octahedral sites are interconnected with one another by common faces and edges to form 3D diffusion pathways for the lithium ions [Ohzuku et al., 1990; Mukerjee et al., 1998; Winter et al., 1998; Whittingham, 2004]. The anionic lattice of LiMn_2O_4 is closely related to the $\alpha\text{-NaFeO}_2$ layered structure, differing only in the distribution of the cations amongst the available tetrahedral and octahedral holes.



See print copy for figure 2.11

The $\text{Li}_x\text{Mn}_2\text{O}_4$ electrode can be cycled between 4.5 and 3.0 V vs. Li/Li^+ . Lithium-ions can be further inserted into the LiMn_2O_4 to form $\text{Li}_{1+x}\text{Mn}_2\text{O}_4$ at 3 V against lithium. This reaction is accompanied by a phase transition from cubic spinel to an ordered, tetragonal, NaCl-type structure [Ohzuku et al., 1990]. Therefore, there are two phases

co-existing in the LiMn_2O_4 electrode, a cubic phase and a tetragonal phase. In the voltage domain between 3.0 and 4.5 V, the discharge curve corresponds to the lithium occupation of tetrahedral sites. Good cycling performance cannot be obtained in the 3 V region ($1 < x < 2$), because a volume expansion of about 6.4 % is associated with the phase transition. The reason for the phase transition is an increase in the concentration of Mn^{3+} ($3d^4$) ions that form during intercalation of lithium [Tarascon and Guyomard, 1991], causing a Jahn-Teller distortion.

LiMn_2O_4 compound is traditionally made by sintering the corresponding carbonates in the approximate temperature range between 700 and 900 °C, although in general, it can be prepared by heating lithium carbonate, or lithium nitride, or lithium hydroxide with manganese carbonate or manganese oxide. Synthesis of LiMn_2O_4 by the conventional solid-state method has several disadvantages, such as the following:

- difficulty in controlling particle sizes, due to high temperatures,
- high operating cost, due to long and repeated heat treatments followed by grinding,
- inhomogeneous product with irregular morphology, and
- poor control of stoichiometry.

A solution-based method has been recently proposed for the preparation of high performance LiMn_2O_4 materials. The sol-gel method has also been used in preparing nanoparticles of LiMn_2O_4 spinel, using lithium acetate, manganese acetate, and citric acid as the chelating agent [Bach et al., 1990; Tsumura et al., 1993; Pereira-Ramos, 1995]. The obtained LiMn_2O_4 powder has good cycling performance and rate capability.

Nanoparticles of LiMn_2O_4 synthesized by a one-step intermediate-temperature solid-state reaction [Guo et al., 2004] demonstrated much higher initial capacity (130 mAh g^{-1}) than that of the commercial material (110 mAh g^{-1}) produced by the conventional solid-state reaction. Nanostructured LiMn_2O_4 electrodes consisting of LiMn_2O_4 nanotubules that protrude from the current collector surface like the bristles of a brush were prepared using the template method [Li et al., 2000b]. This material is of particular interest as the positive electrode of a high-power lithium-ion battery for hybrid electric vehicles, even though at high charge rates this material only has a specific charge capacity of 80 Ah kg^{-1} .

2.3.3 Olivines

One promising cathode material which has attracted a considerable amount of interest recently is lithium iron phosphate (LiFePO_4). Though pure LiFePO_4 has a very low conductivity ($10^{-9} \text{ S cm}^{-1}$), it can be used at 90 % of its theoretical charge capacity (165 Ah kg^{-1}) at a steady voltage of around 3.4 V [Goodenough et al., 1997], by reducing the particle size ($< 1 \text{ }\mu\text{m}$) and ensuring that electrodes possess a well dispersed conductive carbon matrix. The main advantage of this olivine compound is that it does not use expensive and toxic metals (such as Ni or Co), but instead uses a cheap, abundant, and non-toxic metal, iron (Fe) [Ritchie, 2004].

LiFePO_4 has the olivine structure, which consists of corner sharing FeO_6 octahedral and PO_4^{3-} tetrahedral anions (see Fig. 2.12), with lithium occupying the octahedral holes. LiFePO_4 , which has the same generalized AB_2O_4 formula as the spinel structure, has a hexagonal-close-packed (hcp) oxygen array, in which the octahedra share both edges

and faces. The cation arrangement in LiFePO_4 differs significantly from that in the layered (e.g. LiCoO_2) and spinel (e.g. LiMn_2O_4) structures. There is no continuous network of FeO_6 edge-sharing octahedra that might contribute to electronic conductivity; instead, the divalent Fe^{2+} ions occupy corner-sharing octahedra. The phosphorus ions are located in tetrahedral sites, and the lithium-ions reside in chains of edge-sharing octahedra [Chung et al., 2002].

See print copy for figure 2.12

Results on undoped and doped $\text{Li}_{1-x}\text{M}_x\text{FePO}_4$ ($\text{M} = \text{Mg, Al, Ti, Nb, or W}$) synthesized by solid-state reaction demonstrated that controlled cation stoichiometry combined with solid solution doping by metals increases the electronic conductivity of LiFePO_4 by a factor of approximately 10^8 [Chung et al., 2002]. Nanosized LiFePO_4 powder synthesized by heating amorphous LiFePO_4 achieved nearly the full theoretical capacity (170 mAh g^{-1}) at the C/10 rate [Prosini et al., 2002]. Carbon-coated LiFePO_4 cathode prepared by a carbon aerogel synthesis [Wang et al., 2005] or by a spray solution [Bewlay et al., 2004; Konstantinov et al., 2004a] technique, where LiFePO_4 particles are embedded in an amorphous carbon matrix, demonstrated a high capacity and stable cyclability. The carbon-coating significantly enhanced the electronic conductivity of the LiFePO_4 particles.

A nanocomposite consisting of monodispersed nanofibers of LiFePO_4 electrode material mixed with an electronically conductive carbon matrix delivered almost 100 % of its theoretical discharge capacity at the high 3C discharge rate, and 36 % of its theoretical discharge capacity at the enormous discharge rate of 65C [Sides et al., 2005]. This new nanocomposite electrode shows such excellent rate capabilities due to the nanofiber morphology, which mitigates the problem of slow Li-ion transport in the solid state, while the conductive carbon matrix overcomes the inherently poor electronic conductivity of LiFePO_4 . Thus the performance of nanocrystalline LiFePO_4 makes it feasible as a cathode active material for high-energy-density, and high-power lithium-ion batteries, suitable for use in EVs, HEVs, and stationary storage batteries [Prosini et al., 2002].

2.3.4 Vanadates

Vanadium oxides have been considered for use as the cathode in lithium batteries for 30 years. Initially vanadium pentoxide, V_2O_5 , was the subject of much investigation and was shown to react by an intercalation mechanism [Walk and Gore, 1975; Whittingham, 1976]. The structure of this compound is shown in Figure 2.13.

See print copy for figure 2.13

V_2O_5 is comprised of VO_5 square pyramids, which share the corners of their bases to form a sheet, which, in the absence of any vacancies, has the composition V_2O_4 , whose structure is also shown in Figure 2.13. When V_2O_4 is formed in the presence of lithium-ions by a hydrothermal mechanism, water molecules are found between the layers, and on dehydration the compound $Li_xV_{2-\delta}O_{4-\delta}$ is formed. Some of the lithium-ions reside on the vanadium sites. Oxidation of this VO_2 to V_2O_5 occurs by the formation of ordered vacancies, giving rows of square pyramids with their apices ordered as follows: up-down-down-vacant row-etc. Another way of organizing these square pyramids is in double sheets, V_4O_{10} , with all the apices up in one sheet, down in the other, and joined back-to-back, so that all the vanadium atoms have the octahedral coordination, but still with one shorter $V=O$ bond, and opposing it, a longer bond to the opposite oxygen $V\cdots O-V$, but shorter than in V_2O_5 itself. This is known as the *delta-structure* [Whittingham et al., 2005].

V_6O_{13} , V_2O_5 , and LiV_3O_8 have been the most studied, with some emphasis on xerogel type vanadium oxides. V_2O_5 itself has a tendency on over-discharge to forming the disordered rock-salt compound $Li_3V_2O_5$. Both V_6O_{13} and the xerogel have a vanadium oxide double sheet as an element of their structure. Zhang et al. [1997 and 2000] have investigated the δ -structure class of vanadium oxide materials. The compound $[(CH_3)_4N]_yMn_zV_4O_{10}$ had a reversible capacity exceeding 220 Ah kg^{-1} ; the organic ions do not impede reaction as in the single sheet V_2O_5 materials, such as $N(CH_3)_4V_3O_7$. If the large tetramethyl-ammonium ion could be replaced by a smaller ion such as ammonium, then the lattice size should be reduced, thereby increasing the volumetric energy density. Their results show that this compound has an initial capacity close to 300 Ah kg^{-1} . However, the median discharge voltage is about 2.6 V, significantly lower

than the manganese oxides discussed above and the lithium iron phosphate discussed earlier. These high capacity compounds are most likely to find application where the electrolyte has low stability, such as has been found for several polymers, or where capacity is critically important in a 2.5 V application.

V_6O_{13} was first reported as a positive electrode material by Murphy et al. [1979 and 1981]. Up to eight Li^+ ions per formula unit can be chemically inserted into stoichiometric V_6O_{13} using butyl lithium, and even more can be inserted into non-stoichiometric V_6O_{13+z} [West et al., 1983]. However, only up to six Li^+ ions can be reversibly inserted into V_6O_{13} electrochemically [Abraham et al., 1981]. *In-situ* X-ray diffraction during electrochemical Li^+ insertion revealed four phases, identified as $Li_{0.5}V_6O_{13}$, $Li_{1.5}V_6O_{13}$, $Li_3V_6O_{13}$, and $Li_6V_6O_{13}$, which were also observed during chemical insertion studies [Lampe-Önnerud et al., 1995]. The lithium diffusion coefficient ranges from 3×10^{-13} to $8 \times 10^{-14} \text{ m}^2 \text{ s}^{-1}$ [West et al., 1983 and 1985].

Practical problems with the rechargeable V_6O_{13} electrode are capacity loss during cycling, the high electronic resistivity of lithiated V_6O_{13} [West et al., 1983; Chaklanabish and Maiti, 1986], and a relatively high lattice expansion of ~15 %, which is observed when x tends to six in $Li_xV_6O_{13}$ [Hopper and North, 1983; Steele et al., 1983; West et al., 1983 and 1987; Chaklanabish and Maiti, 1986; Macklin et al., 1992; Wang et al., 1992]. Possible solutions to these problems that lead to fairly promising results are the use of: i) thin film electrodes [West et al., 1983 and 1987; Lampe-Önnerud et al., 1995], and ii) a suitable electronically conductive matrix in which the V_6O_{13} particles are embedded [Uchiyama et al., 1987].

The vanadates, $\text{Li}_{1+x}\text{V}_3\text{O}_8$ [Nassau and Murphy, 1981; Panero et al., 1983; Pistoia et al., 1984, 1985a, 1985b, 1986, 1987, 1990, 1995; Pasquali et al., 1986; Bonino et al., 1987 and 1988; Hammou and Hammouche, 1988; Scrosati et al., 1988; Pasquali and Pistoia, 1991; Maingot et al., 1993; Manev et al., 1995] are examples of insertion compounds in which the alkaline metal atoms function as pillars between the vanadium oxide units. They stabilize the oxide structure during the insertion/de-insertion process and optimize the space between the vanadium oxide units. This enhances not only the amount of insertable guest species but also the lithium diffusion rate, both leading to a superior electrode performance. The monoclinic structure of $\text{Li}_{1+x}\text{V}_3\text{O}_8$, illustrated in Figure 2.13, shows distorted $[\text{VO}_6]$ octahedra that are connected via shared edges and vertices to form $[\text{V}_3\text{O}_8]^-$ units. These units are stacked one on top of the other to form quasi-layers. The alkali metal ions are situated between these layers, electrostatically holding the $[\text{V}_3\text{O}_8]^-$ units together [Wadsley, 1957]. The spacing between the strands is sufficiently flexible to accommodate other guest species on octahedral and tetrahedral interstitial sites [Pistoia et al., 1984].

X-ray diffraction showed only a slight lattice expansion upon lithiation and no major structural changes even on long-term cycling for $\text{Li}_{1+x}\text{V}_3\text{O}_8$ [Pistoia et al., 1984, 1985a, and 1987; West et al., 1987], thus providing evidence of the strongly topotactic nature of the insertion process. A specific capacity for lithium insertion of more than 300 Ah kg^{-1} has been reported for these compounds [Pistoia et al., 1984]. The lithium diffusion coefficient ranges from 10^{-12} to 10^{-14} $\text{m}^2 \text{s}^{-1}$ [Pistoia et al., 1984, 1985a, and 1987; Hammou and Hammouche, 1988]. Chemical lithiation leading to the composition $\text{Li}_{3.8}\text{V}_3\text{O}_8$ [Pistoia et al., 1984 and 1985b] allows the use of these positive electrode materials as the lithium source in cells containing a carbon negative electrode.

2.4 Nanotechnology – The Great Leap Forward

Nanotechnology is a word mentioned in the press virtually every day. With nanotechnology it is possible to create materials from building blocks the size of atom clusters, which exhibit enhanced electronic, magnetic, optical, and chemical properties. The enhanced properties extend far beyond and offer far greater potential than just the inherent ‘economy of geometry’ of miniaturization. Nanomaterials are powders and materials optimized at the nanoscale (1-100 nm). On the nanoscale the theories of classical and quantum mechanics overlap, and a rich variety of unexpected properties is possible.

New applications for materials can be created with novel or significantly enhanced properties. Such properties include transparency, hydrophobicity, photoluminescence, toughness and hardness, chemical sensing, and bioavailability. Products produced from these materials exhibit unique properties and have a wide range of high value commercial applications in rapidly expanding markets. The key characteristics demanded of nanoparticles to capture high value markets include: small particle size, narrow size distribution, low levels of agglomeration, and high dispersibility.

The strong interest in nanotechnology stems from the concept that structures may be designed and built that exhibit superior electrical, mechanical, chemical, or optical properties compared to the materials we know today. Traditionally, products are constructed by etching away materials to make them smaller, while nanotechnology takes something at the molecular scale and builds by adding one atom or molecule at a time. Nanoparticles are produced in two main ways. The traditional way of producing

tiny particles has been “top-down” referring to reduction through attrition and various methods of comminution in the traditional sense. During the past few years and increasingly, methods of production using “bottom-up” techniques [Zhang, 2003] are being increasingly utilized. Research into self-assembling, smart materials with many and varied applications are producing potential performance greater than we have seen previously.

The unique properties of nanomaterials and structures on the nanometer scale have sparked the attention of materials developers. Incremental shifts in product performance using these materials, for example, as fillers in plastics, as coatings on surfaces, and as UV-protectants in cosmetics, are already occurring. Nanotechnology is entering many industry sectors, including medicine, plastics, energy, electronics, and aerospace. Carbon nanotubes have been demonstrated to be 100 times stronger than steel, yet have only one-sixth the weight [Baughman et al., 1999]. They can be made in structures that are as electrically conductive as copper or in structures that act as semiconductors.

The array of nanomaterials is very wide, so a selection follows, but is by no means exhaustive. New applications for nanomaterials are being worked on in hundreds of laboratories around the globe. Some will find useful applications that will revolutionize much of how we will live in the years ahead. In this doctoral work, the role and importance of nanostructured materials have been investigated thoroughly with a view towards their use as electrode in Li-ion batteries, with the results presented in the subsequent chapters.

2.4.1 Definition and Terminology

The term “nanotechnology” was first introduced by a Japanese engineer, Norio Taniguchi. The term originally implied [Taniguchi, 1974] a new technology that went beyond controlling materials and engineering on the micrometer scale, which had dominated the twentieth century. However, today’s meaning of the word relates more closely to the visionary formulation of Eric Drexler [1986] and corresponds to the atom-by-atom manipulative, “hard tech” processing methodology. Nanoscience is here defined as the study of phenomena and the manipulation of physical systems that produce significant information on a spatial scale known as “nano” (10^{-9} m = 1 nm), with critical boundaries that do not exceed 100 nm in length, at least in one direction [Drexler, 1986]. Therefore, nanotechnologies focus on the design, characterization, production, and application of nanoscale systems and components.

According to Wikipedia, nanotechnology is a field of applied science and technology covering a broad range of topics. The main unifying theme is the control of matter on a scale smaller than 1 micrometre, normally between 1-100 nanometers, as well as the fabrication of devices on this same length scale. It is a highly multidisciplinary field, drawing from fields such as colloidal science, device physics, and supramolecular chemistry. Despite the apparent simplicity of this definition, nanotechnology actually encompasses diverse lines of inquiry. Nanotechnology cuts across many disciplines, including colloidal science, chemistry, applied physics, materials science, and even mechanical and electrical engineering. It could variously be seen as an extension of existing sciences into the nanoscale, or as a recasting of existing sciences using a newer, more modern term.

2.4.2 Nanostructures vs. Microstructures

The boundaries between the physical regions of the macroscopic, the microscopic, and the nanoscopic are not sharp, and they depend on the effects being considered [Wautelet, 2001]. However, reducing the grain size of a material below certain limits results in the appearance of either new or changed properties of the material due to:

- inherent crystalline grains approaching the size of the characteristic physical lengths of the relevant properties,
- an increase in the proportion of interface defects and their impact on dependent properties, and
- the appearance of new structural properties that characterize the grain boundaries of the material [Andrievski and Glezer, 2001].

For example, a material comprised of spherical crystalline grains 3 nm in diameter might find approximately half of its atoms positioned at grain surfaces, which implies more pronounced reactivity of the system. However, a decrease in grain size, equivalent to an increase in the specific surface area of the system, indicates not only increased reactivity but also that those physical properties are no longer dominated by the physics of the bulk matter. Since specific disciplines within materials science are normally divided, based on the properties of bulk materials, an understanding of the transition from the macro to the nano scale offers the opportunity to bridge imposed gaps and creates a new multi-disciplinary field of nanoscience [Wautelet, 2001; Komiyama et al., 2004].

Aricò et al. [2005] reported that working at the nanoscale may radically change chemical-electrochemical reaction paths of inorganic materials from recent studies carried out on the reactivity of macroscopic versus nanoscale haematite ($\alpha\text{-Fe}_2\text{O}_3$) particles with Li. With nanometer-scale haematite particles (20 nm), reversible insertion of 0.6 Li per Fe_2O_3 is possible through a single-phase process, whereas large haematite particles (1 to 2 μm) undergo an irreversible phase transformation as soon as ~ 0.05 Li per Fe_2O_3 are reacted (see Fig. 2.14). In this respect, many active electromaterials, previously rejected because they did not fulfill the criteria as classical intercalation hosts for lithium, are now worth reconsideration.

See print copy for figure 2.14

Physical properties such as electrical conductivity, micro-hardness, coercivity, and permittivity decrease in proportion to the average particle size of a material. Mechanical failure of a material frequently takes place through crack migration processes along grain interfaces, so the fact that materials with nanosized grains (down to ~ 10 nm) are stronger compared with their bulk counterparts implies significant modifications of strength and toughness mechanisms as a result of the transition from bulk to the nanoscale [Edelstein et al., 1997]. Metals that become malleable when microstructurally arranged may prove to have unacceptable levels of creep when their grains are reduced to the nanolevel. In contrast, the formability of ceramics is known to improve with the reduction of grain size towards the nanoscale. As a result, simple linear extrapolations down to the nanolevel, using rules that are valid within micro domains, do not work well in all circumstances.

2.4.3 Advantages and Disadvantages

Generally, the potential advantages of nanostructured electrode materials can be summarized as follows [Aricò et al., 2005; Jiang et al., 2006; Liu et al., 2006]:

- new useful reactions that are not possible with bulk materials, leading to higher specific capacities (see Fig. 2.14),
- a larger electrode-electrolyte contact area, leading to higher charge-discharge rates (see Fig. 2.15),
- short path lengths for both electronic and Li ion transport (permitting operation even with low electronic or low Li ion conductivity, or at higher power), and
- stable cycling performance with nanostructured electrodes.

See print copy for figure 2.15

Meanwhile, some of the potential disadvantages of nanostructured electrode materials can be summarized as follows [Aricò et al., 2005; Jiang et al., 2006; Liu et al., 2006]:

- complicated synthesis process for the nanostructured materials, leading to increase of operational cost,
- difficult in handling the nanosized powder for logistic purposes,
- potential unknown health and safety hazards from contact with the nanostructured materials,
- unsuitability for existing electrode making processes, such as the classical casting method, due to an inhomogeneous slurry and problems with attachments to the current collector, and
- low production rate with almost all existing technologies, especially for the production of one-dimensional nanostructures (i.e. nanowires or nanotubes).

2.4.4 On-going Challenges

The difficulty of communication between macroscopic and nanoscopic entities is the central issue in the development of nanotechnologies. Increased sensitivity to environmental effects, as dimensions are diminished towards the nanoscale, represents a major challenge. For instance, gaseous particles that are constantly being adsorbed and desorbed from a device's surface create weight fluctuations that might prove to be a significant constraint in the development of everyday nano-appliances [Roukes, 2001]. According to the laws of quantum mechanics, every form of measurement and communication necessarily perturbs the measured and communicated system. Therefore, designing and performing feedback permeated macro-to-nano communications with quantum effects that become significant in the nano-domain present additional challenges.

Another key challenge is the commercialization of nanotechnology. The ability to commercialize nano-enabled products will depend on governments and companies meeting regulatory requirements and satisfying societal needs and concerns. The inherent value of nanotechnology will need to be protected by proper intellectual property laws, as well as having the requisite 'freedom of operation'. Ownership of patents alone does not necessarily allow the commercialization of a product, because if one company has a patent that dominates a technology, it can prevent other companies from developing new products. Successful commercialization will require scaling up to commercial quantities, along with evidence that employee and environmental safety is maintained during manufacture. It goes without saying that maintaining the safety of the consumer and the environment during use and disposal must be inherent to the product.

Commercialization will require new infrastructure for manufacturing with a significant capital investment, and government support for this will be required in the near term. It is therefore encouraging that the National Nanotechnology Initiative (NNI) in the US is addressing the commercialization of nano-enabled products in all its complexity. In Figure 2.16, the supply value chain for commercializing nanotechnology is represented by the colored boxes: the factors that impede commercialization are shown in the inner circle and the NNI initiatives are highlighted in the outer circle.



See print copy for figure 2.16

CHAPTER 3

EXPERIMENTAL DETAILS

3.1 Materials

The list of materials and chemicals used during my PhD studies for the synthesis, characterization, and electrochemical testing is summarized in Table 3.1. The details of the suppliers are also provided for better reference.

Table 3.1: Description of materials and chemicals used during my PhD studies.

Materials/Chemicals	Formula	Purity (%)	Name of Supplier
Single-walled carbon nanotubes powder	C	95 (5 % Fe)	Carbon Nanotechnologies Incorporated (CNI), USA
Triton X-100	$(\text{C}_2\text{H}_4\text{O})_n \cdot \text{C}_{14}\text{H}_{22}\text{O}$	100	Sigma Aldrich, Australia
Milli-Q Water	H_2O	5 ppb (TOC)	Millipore, USA
Polyvinylidene fluoride (PVDF) membrane	$(\text{CH}_2\text{CF}_2)_n$	0.22 μm thick	Millipore, USA
Ethanol	$\text{C}_2\text{H}_5\text{OH}$	Reagent	Sigma Aldrich, Australia
Methanol	CH_3OH	Reagent	Sigma Aldrich, Australia
Carbon black	C	Super P Ensaco 350	Timcal, Belgium
Polyvinylidene fluoride (PVDF) powder	$(\text{CH}_2\text{CF}_2)_n$	N/A	Sigma Aldrich, Australia
1-methyl-2-pyrrolidinone (NMP)	$\text{C}_5\text{H}_9\text{NO}$	99.5	Sigma Aldrich, Australia

Table 3.1 (cont.): Description of materials and chemicals used during my PhD studies.

Materials/Chemicals	Formula	Purity (%)	Name of Supplier
LP30 electrolyte	LiPF ₆ in EC/DMC (1/1 by weight)	N/A	Merck KgaA, Germany
Copper foil	Cu	N/A	China
Aluminium foil	Al	N/A	China
Nickel mesh/foam	Ni	N/A	China
Lead nitrate	Pb(NO ₃) ₂	99	Sigma Aldrich, Australia
Sucrose	C ₁₂ H ₂₂ O ₁₁	99	Sigma Aldrich, Australia
Silicon powder	Si	325 mesh 40 nm, and 100 nm	Sigma Aldrich, Australia Nanostructured and Amorphous Materials Inc., USA
Citric acid anhydrous	C ₆ H ₈ O ₇	100	Sigma Aldrich, Australia
Polypropylene separator	(C ₃ H ₆) _n	Celgard 2500	Hoechst Celanese Corporation, USA
CR2032 coin-type cells	N/A	N/A	Hohsen, Japan
Ammonium hydroxide	NH ₄ OH	98	Sigma Aldrich, Australia
Vanadium oxytrichloride	VOCl ₃	99	Sigma Aldrich, Australia
Vanadium (V) oxytripropoxide	OV(OC ₃ H ₇) ₃	98	Aldrich, Switzerland
Diethylene glycol (DEG)	(HOCH ₂ CH ₂) ₂ O	99	Fluka, Switzerland
Toluene	C ₇ H ₈	99.9	Riedel-de Haën, Switzerland
Whatman glass fiber filter	N/A	257 mm (diameter)	Aldrich, Switzerland
Glass fiber separator	N/A	N/A	Paul Scherrer Institute (PSI), Switzerland
Lithium tert-butoxide in tetrahydrofuran	(CH ₃) ₃ COLi	1.0 M	Aldrich, Switzerland
Lithium metal	Li	99.9	Aldrich, Switzerland
Lithium manganese oxide powder	LiMn ₂ O ₄	N/A	Honeywell, USA
Silicon wafer	Si	N/A	Paul Scherrer Institute (PSI), Switzerland
Stainless steel substrate	N/A	N/A	Paul Scherrer Institute (PSI), Switzerland
Magnesium oxide substrate	MgO	N/A	Paul Scherrer Institute (PSI), Switzerland

3.2 Experimental Procedures

This research work consists of two main parts: the first part covers the fabrication and characterization of the electrochemically active nanostructured materials; while the second part involves the application of these electrochemically active nanostructured materials as electrodes for use in lithium-ion rechargeable batteries. Figure 3.1 illustrates the overall framework of my experimental studies.

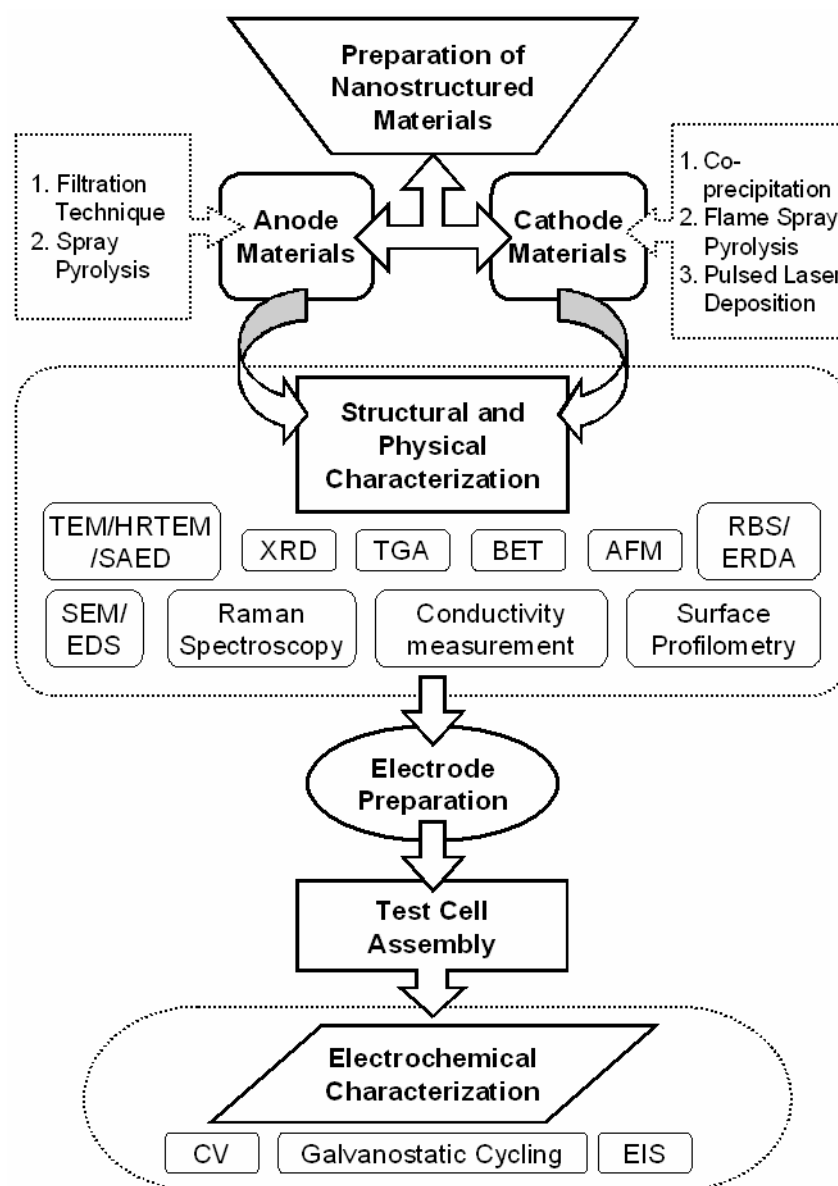


Fig. 3.1. The overall framework of my experimental studies.

3.3 Preparation of Nanostructured Materials

The electrochemically active nanostructured materials used in this study were prepared via either physical or chemical methods. In this section, these methods and the procedures used in preparing the electrochemically active nanostructured materials are elaborated in detail.

3.3.1 Filtration Technique (Positive Pressure)

Firstly, a dispersion of single-walled carbon nanotubes (SWCNTs)/Triton X-100 in Milli-Q water is prepared. In this case, Triton X-100 acts as a surfactant for preventing the SWCNTs from agglomerating in the Milli-Q water. Moreover, the usage of a high purity solvent such as Milli-Q water will prevent contamination of the final product. The mixture is then ultrasonicated for 2 hours. Subsequently, a polyvinylidene fluoride (PVDF) membrane with a pore size of 0.22 μm is cut into a 4-cm disk to fit the filtration cell (see Fig. 3.2). The membrane acts as a filter paper and is wetted in 50:50 v/v Milli-Q water to ethanol solution for 30 minutes.

Passing the prepared SWCNT suspension through the wetted PVDF filter in the filtration cell under a positive nitrogen gas pressure of 400 kPa produces a “free-standing” mat of entangled SWCNT ropes, which is known as “bucky paper”. Subsequently, the resultant SWCNT mat is washed with 200 mL of Milli-Q water followed by 100 mL of methanol, with the methanol used to remove any residual surfactant. Finally, the SWCNTs mat is peeled off from the PVDF filter after letting it dry overnight in a vacuum oven.

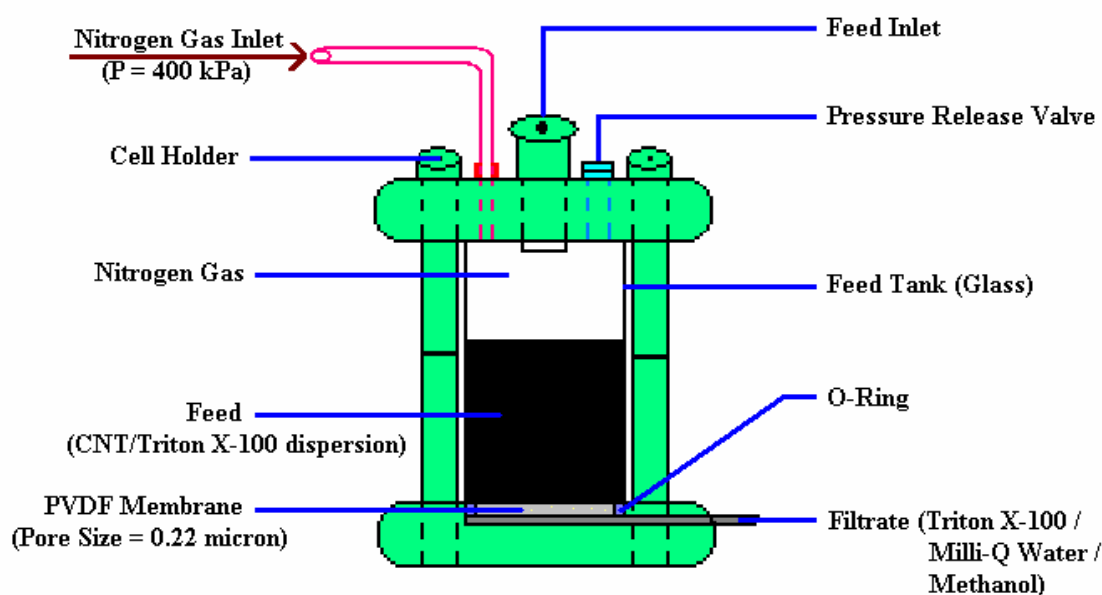


Fig. 3.2. Schematic diagram of the filtration cell used for the fabrication of composite bucky papers.

3.3.2 Spray Pyrolysis

The spray pyrolysis experimental set-up is depicted in Figure 3.3. The set-up is composed of a peristaltic pump that feeds the liquid at the desired flow rate, an atomizing nozzle in combination with compressed air, a tubular furnace, and an extractor pump. The liquid is sprayed with the aid of an air compressor into the quartz tube, which has an inner diameter of 20 cm and a length of 2 m. The furnace consists of 3 heating zones, which can be controlled accurately for a wide temperature range (150 – 1400 °C). The precursor solution is first prepared in an aqueous solution. The solution is then atomized into small droplets in the pyrolysis chamber in order to produce a fine powder, which is subsequently sucked into the particle collector via the extractor pump. At the end of the spray process, the power of the extractor pump is slowly reduced, and the fine powder is carefully collected while using safety gloves and a respiratory mask.

See print copy for figure 3.3

3.3.3 Co-precipitation Method

Co-precipitation reactions involve the simultaneous occurrence of nucleation, growth, coarsening, and/or agglomeration processes. Due to the difficulties in isolating each process for independent study, the fundamental mechanisms of co-precipitation are still not thoroughly understood. The advantage of this method is its simplicity for the synthesis of several crystalline and amorphous oxides [Cushing et al., 2004]. The process consists of the solubilization of metal salts in an aqueous or nonaqueous solvent followed by their hydrolysis in a strong hydrolyzing agent such as NH_4OH . The precipitated hydroxides are then filtered, washed, and heat-treated to yield the oxides. In

some cases, the precipitation allows us to obtain materials with high surface area, since it is relatively easy to make porous materials with this method. However the powder may often be shapeless or aggregated, resulting in pieces of oxide, and therefore the particle size distribution will not be homogeneous. In cases where calcination or annealing of the samples is necessary, some agglomeration will be unavoidable. Nanoparticles can nonetheless be so obtained, but there is little chance of the particles being monodispersed.

3.3.4 Flame Spray Pyrolysis (FSP)

Flame spray pyrolysis (FSP) is a heterogeneous process, where the liquid precursor droplets are sprayed and combusted in the flame [Stark and Pratsinis, 2002]. FSP is capable of producing mixed metal oxide powders with particle sizes ranging from 1 to 200 nm, using low-cost precursors and production rates up to 250 g h⁻¹ [Mädler et al., 2002]. The advantages of FSP include the ability to dissolve the precursor directly into the fuel, the simplicity of introduction of the precursor into the hot reaction zone (or the flame), and the flexibility of using the high-velocity spray jet for rapid quenching during the aerosol formation. All the FSP experiments in this study were conducted in the laboratory of Prof. Pratsinis, also known as the Particle Technology Laboratory, Institute of Process Engineering, Swiss Federal Institute of Technology (ETH), Zurich, Switzerland. The flame spray pyrolysis set-up used in this study is shown in Figure 3.4.

The spray apparatus consists of an external-mixing gas-assisted nozzle that is made from a capillary tube with an outer diameter of 0.91 mm (inner diameter 0.6 mm) that lies in an opening 1.2 mm in diameter, creating an annular gap with a maximum area of

0.48 mm². Precursor and fuel flow through the capillary tube, while the dispersion gas passes through the annular gap. The capillary ends 0.5 mm above the opening to give a constant spray angle at all liquid flow rates.



See print copy for figure 3.4

Furthermore, good atomization can be achieved even at very low liquid flow rates, and the penetration of liquid into the gas line can be prevented, as well as plugging of the nozzle. The apparatus is designed in such a way that external adjustment of the dispersion gas nozzle provides continuous variation of the gas exit gap area from zero to the maximum of 0.48 mm². The mass flow rate is determined by the gap, according to the applied atomization pressure, which is the difference between the nozzle upstream pressure (P_u) and the downstream pressure (P_d) (~ 1 bar).

3.3.5 Pulsed Laser Deposition (PLD)

Pulsed laser deposition (PLD) is one of the few techniques applied for the deposition of thin films. Other popular methods include electron beam evaporation [Shokoohi et al., 1992], chemical vapor deposition (CVD) [Liu et al., 1999b], and also sputtering methods [Hwang et al., 1994]. In the 1990s, the development of new laser technology, such as lasers with high repetition rates and short pulse durations, has made PLD a very competitive tool for the growth of thin and well-defined films with complex stoichiometry [Willmott, 2004].

The principle of PLD is very complicated, including the ablation of the target material by the laser irradiation, the development of a plasma plume with highly energetic ions, electrons, and also neutrons, and finally, the crystalline growth of the film itself on the heated substrate. The process of PLD can generally be divided into four stages [Dumont et al., 2006]:

1. Laser ablation of the target material and creation of a plasma,
2. Dynamics of the plasma,
3. Deposition of the ablation material on the substrate, and
4. Nucleation and growth of the film on the heated substrate surface.

Figure 3.5 shows a schematic diagram of the experimental set-up for the PLD process. Prof. Dr. Thomas Lippert (Materials Group Head, General Energy Department, Paul Scherrer Institute, Switzerland) provided this set-up for the thin film work during my PhD studies, and the thin films were prepared by Mrs. Franziska Simmen (PhD student,

Materials Group, Battery Group, Paul Scherrer Institute, Switzerland) for application in the lithium-ion battery system.

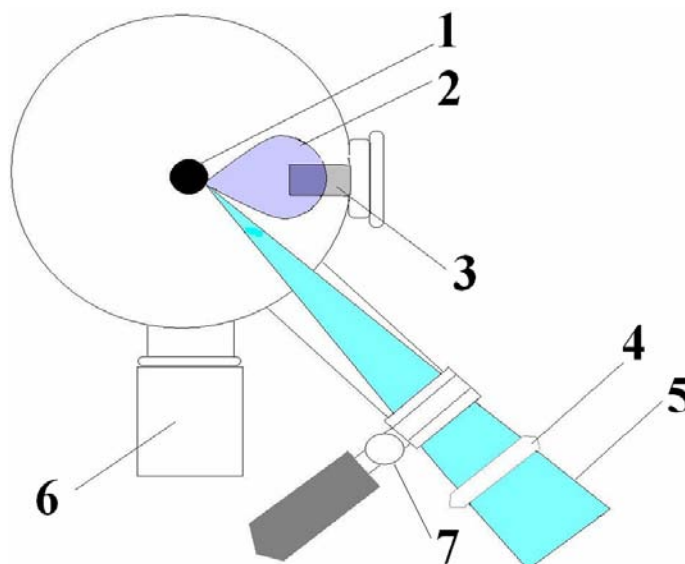


Fig. 3.5. Schematic diagram of the experimental set-up for the PLD process at the Paul Scherrer Institute, Switzerland [courtesy of Mrs. Franziska Simmen]: (1) cylindrical target rod, (2) plasma plume generated by the laser beam, (3) heated and rotating substrate, (4) focusing lens, (5) laser beam, (6) vacuum pump, and (7) inlet for oxygen.

3.4 Physical and Structural Characterization of Nanostructured Materials

Physical and structural characterizations of the as-synthesized nanostructured materials were based on techniques described in detail in the following section. Most of the equipment for these characterization techniques was available in our Institute, with the exception of a few used at the Paul Scherrer Institute (PSI), Switzerland.

3.4.1 X-Ray Diffraction (XRD)

X-ray diffraction (XRD) is generally used to study bulk structures of materials. XRD is a non-destructive technique, which can be used to identify crystalline phases. The X-rays are scattered by each set of lattice planes at a characteristic angle, and the scattered intensity is a function of the arrangement of atoms in the crystal. The scattering from all the different sets of planes results in a pattern, which is unique to the crystal structure of a given compound. X-rays are formed in X-ray tubes when the anode material (usually copper) is irradiated with a beam of high-energy electrons. When the electrons collide with the anode, a continuous spectrum of X-rays is emitted. In addition, photons with energies characteristic of the target material are emitted. A monochromator is used that preferentially suppresses photons with other energies than the desired characteristic one. The X-rays produced are directed to the sample being studied, and X-rays with a wavelength on the order of the lattice spacing are elastically diffracted from the atomic planes in a crystalline material. Re-emitted X-rays interfere, giving constructive or destructive interferences. Bragg's law (Eq. 3.1) describes the diffraction condition from planes with spacing, d :

$$n\lambda = 2d \sin \theta \quad (3.1)$$

The variable d is the distance between atomic layers in a crystal; the variable λ is the wavelength of the incident X-ray beam; n is an integer; and θ is the angle of incidence experienced by the X-ray beam reflection from the faces of the crystal [Bragg and Bragg, 1913]. Figure 3.6 illustrates the interference between waves scattered from two adjacent planes of atoms in a crystal.

See print copy for figure 3.6

In addition to identifying crystalline phases, X-ray diffraction can also be used to determine the crystal size. This can be obtained from the broadening of the peaks according to the Scherrer formulae (Eq. 3.2):

$$L = \frac{K\lambda}{\beta \cos \theta} \quad (3.2)$$

where L is the crystal size, λ is the X-ray wavelength used, K is the shape factor of the average crystallite (with a typical shape factor in the neighborhood of 0.9), β is the full width at half maximum (FWHM) in radians, and θ is the peak position. XRD patterns were collected in a 2θ configuration using a Philips PW 1730 diffractometer (Cu K_α radiation, $\lambda = 1.5418 \text{ \AA}$).

3.4.2 Thermogravimetric Analysis (TGA)

Precise disordered carbon contents in the spray-pyrolyzed nanocomposites were determined by thermogravimetric analysis (TGA) via Setaram 92 (France) equipment in ISEM. Micro-sized alumina crucibles (9.7 mm high x 4.87 mm outer diameter) were loaded with powdered nanostructured material for determination of the composition. The sample could be heated up to 1000 °C in air, high purity nitrogen, or high purity argon. The Setaram's microbalance kept track of the sample weight moment-by-moment, and digital data files were available at the end of each heating measurement. Normally, a sample mass of approximately 10-20 mg is required, depending on the sample density.

3.4.3 Scanning Electron Microscopy (SEM)

Scanning electron microscopy (SEM) is used primarily to observe the electrode's surface topography or the morphology of powder samples. During the SEM measurements, the sample is bombarded with a scanning beam of electrons. The slow moving electrons that are generated by the specimen are collected. These are then amplified and displayed on a cathode ray tube. The electron beam and the cathode ray tube scan synchronously so that an image of the surface of the specimen is formed. Electrodes obtained after electrochemical cycling that were analyzed by SEM study were first washed with a solvent (DMC) to remove the electrolyte and subsequently dried in an argon atmosphere.

Powder morphologies were investigated using a JEOL JSM 6460A scanning electron microscope (SEM) in ISEM. Some of the higher resolution SEM images in this research work were obtained by using a field emission scanning electron microscope (FE-SEM), model Supra 55VP (Carl Zeiss), functioning at an accelerating voltage of 4 kV and using an in-lens detector to obtain the secondary electron images. All FE-SEM measurements were carried out with the kind collaboration of Mr. Patrick Ruch, a PhD student from the Paul Scherrer Institute (PSI), Switzerland.

3.4.4 Transmission Electron Microscopy (TEM)

In Transmission Electron Microscopy (TEM), the sample is again bombarded with a beam of electrons, and the intensity of diffraction of these electrons depends on the orientation of the planes of atoms in the crystal relative to the electron beam. At certain angles the electron beam is diffracted strongly, sending electrons away from the axis of the incoming beam, while at other angles the beam is largely transmitted. The sample can be tilted with respect to the electron beam in order to obtain specific diffraction conditions. A high contrast image can be created by blocking electrons deflected away from the optical axis of the microscope by placing the aperture so as to allow only non-scattered electrons through. This allows a resolution on the order of Angstroms, which allows the imaging of individual atoms in a crystal.

TEM investigations were performed using a JEOL 2011 200 keV analytical electron microscope (Faculty of Engineering) and also a Zeiss microscope, a 912 Omega with ProScan, and a slow scan charge-coupled device camera at 100 keV (ETH Zurich). TEM samples were prepared by deposition of ground particles onto lacey carbon

support films. Most of the TEM measurements in this research work were performed with the kind collaboration of Dr. David Wexler from the Faculty of Engineering, University of Wollongong. In addition, part of the TEM measurements for powder samples made in the Paul Scherrer Institute, Switzerland were performed with the kind collaboration of Dr. Frank Krumeich from the Laboratory of Inorganic Chemistry, Swiss Federal Institute of Technology (ETH), Zurich, Switzerland.

3.4.5 Brunauer Emmett Teller (BET) Specific Surface Area Measurement

Specific surface areas of the nanostructured particles were measured with a Quantachrome Nova 1000 nitrogen gas analyzer using the Brunauer-Emmett-Teller (BET) method. The BET specific surface area was determined through a 15-points nitrogen adsorption isotherm at 77 K after degassing the powder samples with nitrogen at 150 °C. Typically, a sample mass of approximately 200-500 mg is required, depending on the sample density.

3.4.6 Raman Spectroscopy

Laser Raman spectroscopy gives information about the vibration of atoms in crystals and molecules and can be used as a complementary tool to XRD. Raman spectroscopy was used in this study to monitor the variations in the disordered carbon content using a JOBIN YVON HR800 Confocal Raman system with 632.8 nm diode laser excitation on a 300 lines/mm grating at room temperature. This Raman system was provided by the Intelligent Polymer Research Institute (IPRI), and spectroscopy was performed with the kind collaboration of Dr. Jun Chen from IPRI.

3.4.7 Four-Point Probe Conductivity Measurement

Resistivity measurements of the composite bucky papers were performed on strips (0.3 cm x 2.5 cm) via Jandel multi-height four-point probes, connected to a Jandel resistivity test unit, model RM2 (see Fig. 3.7), provided by IPRI. A constant current of 1 mA was passed through the outer two electrodes and the voltage difference between the two inner electrodes was measured after 10 s. This measurement was repeated 4 times for each sample. The electrical conductivity of the bucky paper was calculated based on Equation 3.3 as follows:

$$\text{Conductivity, } \sigma = 10000 / [(\text{Voltage/Current}) \times 4.532 \times \text{Thickness}] \quad (3.3)$$

where σ is the bucky paper's electrical conductivity in S cm^{-1} , the voltage is measured in mV, the applied current is in mA, the film thickness is measured by a digital micrometer in μm , and finally, 4.532 is the correction factor recommended by Jandel for film measurements.

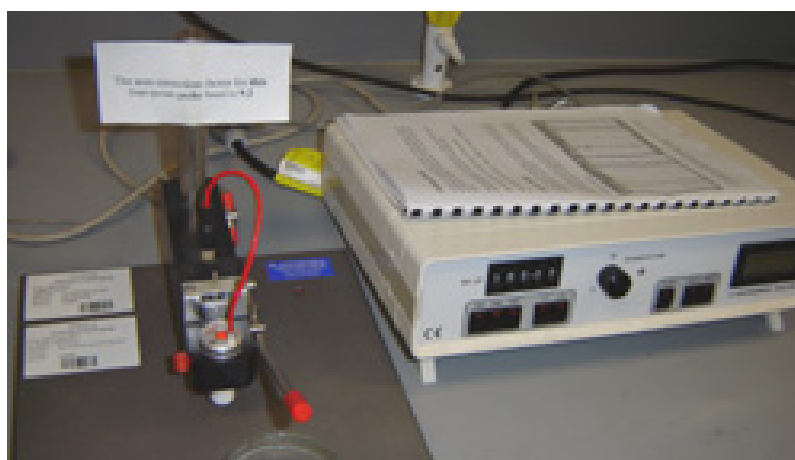
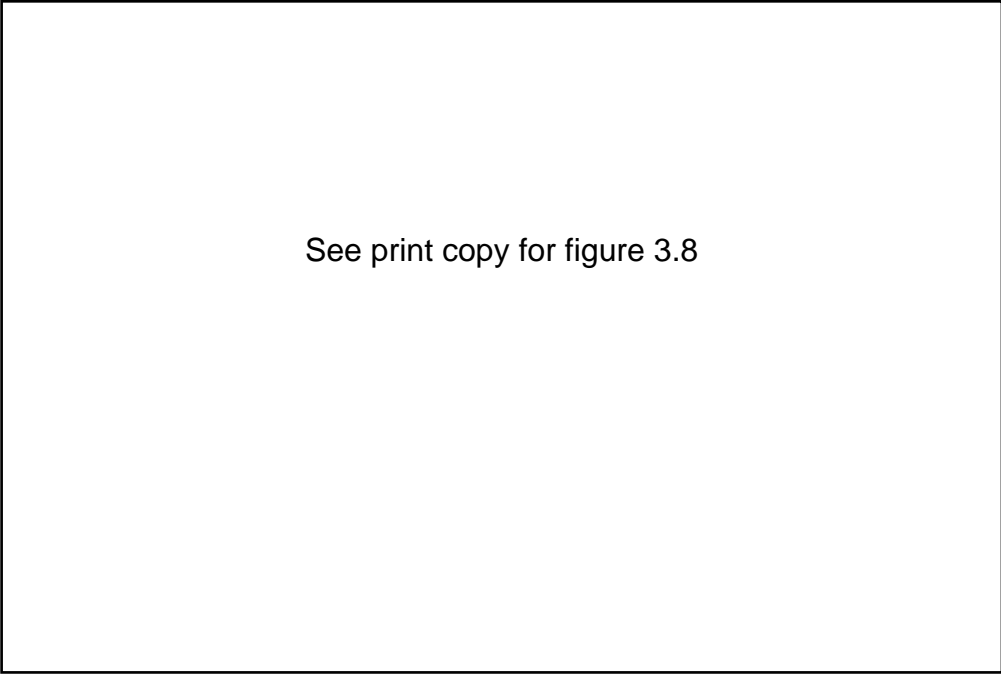


Fig. 3.7. Experimental set-up for resistivity measurement via the four-point probe technique (Jandel multi-height four-point probe and resistivity test unit, model RM2).

3.4.8 Atomic Force Microscopy (AFM)

The atomic force microscopy (AFM) technique has turned out to be a useful tool for direct measurements of intermolecular forces with atomic resolution. AFM provides additional information compared to traditional microscope techniques (e.g. SEM and TEM) in the study of surfaces and microstructures. A conventional AFM system works in the following manner (see Fig. 3.8).



See print copy for figure 3.8

A micro-machined cantilever attached on a silicon chip, with an integrated sharp tip, is mounted on a piezo-electric (PZT) actuator. A laser diode beam is focused on the reflective end of the cantilever, and the reflected laser beam hits a position sensitive photo-detector (PSPD) with two to four detector units. After the laser alignment procedure, the tip is brought into contact until the required cantilever deflection is attained. A PZT positioning element is used to position the tip and apply the required force on the sample. Now, the tip is scanned laterally over the sample and the cantilever

deflection is recorded by the PSPD system. While the tip scans the surface topography, the laser beam deflection from the cantilever provides measurements of the difference in light intensity between the upper and lower PSPD detectors. The adjusted force acting between the tip and the sample is kept constant by a feedback loop. The PZT transducer monitors real-time height deviation by measurement in the constant force mode. The measured value of deflection is compared to a set value in a DC feedback amplifier. The resulting error signal from the amplifier is used to actuate the PZT positioning element by applying the required voltage. This, in turn, raises or lowers the cantilever, to restore the desired deflection and thus maintains a constant force between the tip and sample. The voltage applied by the feedback amplifier to the PZT element is a measure of the surface topography. This voltage is expressed as a function of the lateral position of the sample, resulting in a relief of the surface topography of the sample.

In contact mode AFM, also known as repulsive mode AFM, the tip is in close contact with the sample, while scanning the surface. In this case, the interaction forces between the tip and the sample are repulsive. An examination of the force curve plotted vs. the inter-atomic distance (see Fig. 3.9) reveals that the slope of the curve in the contact region is very steep. The reason for this behavior is electrostatic repulsion between the electron clouds in the atoms of the tip and the sample. The main drawback of the contact mode is that the shear forces resulting from the lateral movement of the tip tend to damage soft samples. Therefore, this mode is not suited for examining soft biological and polymer surfaces, as it may cause a distorted AFM image and may also irreversibly affect the sample surface. However, in our case, the thin film samples prepared by pulsed laser deposition (PLD) were rather hard materials. Therefore, contact mode AFM was still suitable to be used.

See print copy for figure 3.9

AFM measurements carried out for the thin films in this study were collected in the contact mode with an Atomic Force Microscope (AFM) from Park Scientific Instruments, which was made available by the Paul Scherrer Institute, Switzerland.

3.4.9 Rutherford Backscattering Spectrometry (RBS)

Rutherford Backscattering Spectrometry (RBS) is a method for composition analysis of thin films down to a sampling depth of 1-2 μm . RBS can also be utilized as a technique for elemental analysis of thin films. It can determine the concentration of atomic species, as well as the film depth at which these atoms are located. The technique is based on the loss of energy that results from the collision of an energetic ion directed on the sample with an atom from the target, i.e. the sample. The incident ion can lose kinetic energy in two ways:

1. By colliding with an atom of the target. The difference in energy is a function of the mass of the target atom. This allows us to determine the molecular mass of the target atom and finally to identify it.
2. By passing through the sample film. The further the incident atom penetrates through the film, the more energy is lost because of interactions with the neighboring atoms.

As a consequence, the loss of kinetic energy by collision of the incident ion with the same atomic species at the surface of the sample or below the surface is different. This allows distinguishing between atomic species at the surface and the ones further below. This information yields the film thickness. The principle is illustrated in Figure 3.9. In more detail, the atomic mass and elemental concentrations as well as the depth profile of concentrations can be determined by measuring the number and energy of the ions, e.g., He ions, in the beam, which has been backscattered by the atoms of the sample.

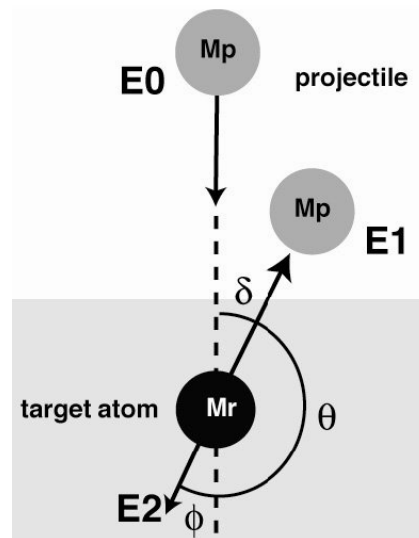


Fig. 3.10. Principle of Rutherford Backscattering Spectrometry [Dumont et al., 2006]. E is the ion energy, M_r is the mass of the incident ion, M_p is the mass of the target atom, and θ is the scattering angle.

The thin film stoichiometry (O/Mn ratio) was determined by Rutherford Backscattering Spectrometry (RBS) measurements using a 2 MeV ^4He beam and a surface barrier silicon detector. The collected data were analyzed using the standard RUMP program. Dr. Max Döbeli from the Institute of Particle Physics at the Swiss Federal Institute of Technology (ETH), Zurich, Switzerland kindly performed these measurements.

3.4.10 Elastic Recoil Detection Analysis (ERDA)

Elastic Recoil Detection Analysis (ERDA) was used to quantify the amount of lithium (Li/Mn ratio) in the thin film because lithium is too light for analysis by RBS. The principle of ERDA is illustrated in Figure 3.11.

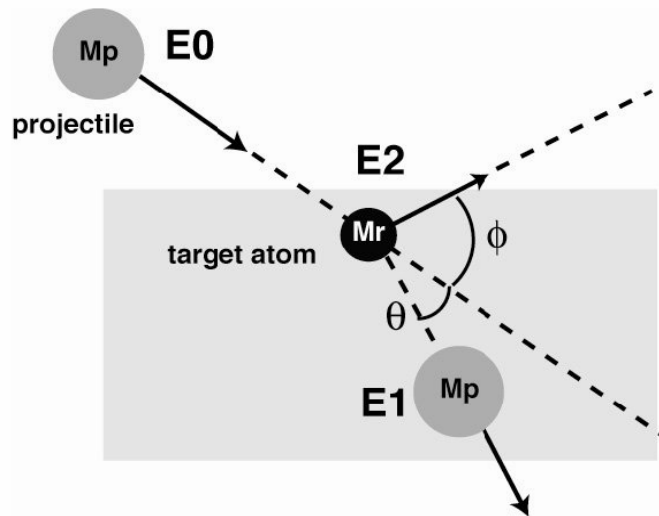


Fig. 3.11. Principle of Elastic Recoil Detection Analysis [Dumont et al., 2006]. E is the ion energy, M_r is the mass of the incident ion, M_p is the mass of the target atom, and θ is the scattering angle.

The sample is bombarded with highly energetic heavy ions, such as Xe. The energy and the number of the backscattered atoms, i.e., recoils, are measured at a fixed angle

relative to the beam. The precision of the result is much improved if one utilizes a standard such as LiF in the ERDA measurements. The obtained data are fitted with a program to determine the exact amount of the atoms. Possible deviations of the data from the fitting can be caused by impurities in the sample. The concentration of lithium was calculated by comparing the Mn/O ratio obtained by RBS with the Li/O ratio obtained by ERDA. Both methods have a relative error no greater than 5 %. Dr. Max Döbeli, from the Institute of Particle Physics at the Swiss Federal Institute of Technology (ETH), Zurich, Switzerland, also conducted ERDA measurements.

3.4.11 Surface Profilometry

The thin film thickness (in nm) and surface roughness (rms, in nm) were determined with a Dektak 8000 profilometer (see Fig. 3.12). The Paul Scherrer Institute (PSI), Switzerland, provided this set-up, and Mrs. Franziska Simmen (PhD student, Materials Group, Battery Group, PSI, Switzerland) performed the measurements.

See print copy for figure 3.12

3.5 Electrode Preparation and Test Cell Assembly

3.5.1 Electrode Preparation

The working electrodes were prepared by mixing nanostructured electrochemically active materials with 10-20 wt.% carbon black, which acts as the electrical conductor, and 10 wt.% polyvinylidene fluoride (PVDF), which acts as the binder, in N-methyl-2-pyrrolidinone (NMP), which act as the solvent, to form a homogeneous slurry. The slurry was then spread onto a copper (anode)/aluminium (cathode) foil, which serves as the current collector, by means of pasting (in ISEM) or doctor-blading (in PSI).

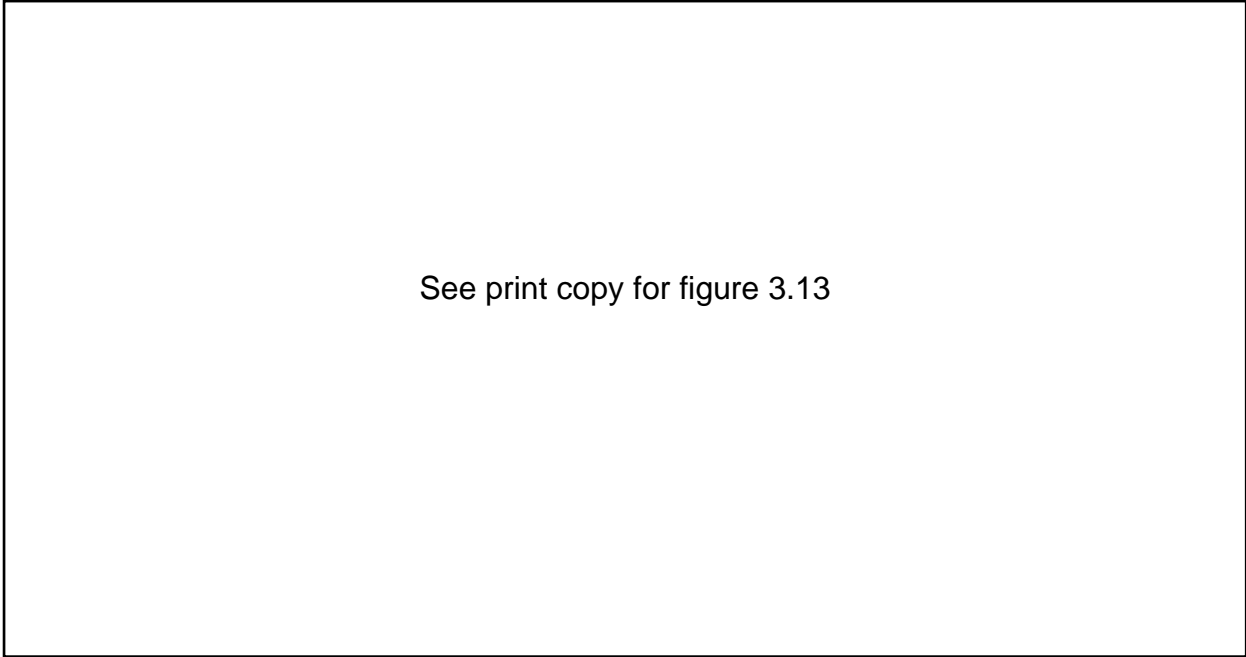
The typical active mass loading of the electrodes was $2\text{-}5\text{ mg cm}^{-2}$, depending on the density of the electrochemically active samples. Subsequently, the coated electrodes (average thickness of $\sim 50\text{ }\mu\text{m}$) were dried in a vacuum oven at $110\text{ }^{\circ}\text{C}$ for 24 hrs and then pressed to enhance the contact between the nanostructured electrochemically active materials and the conductive carbon black.

If not otherwise specified, all measurements were performed using metallic lithium as the counter electrode. Because the potential of metallic lithium is nearly constant at moderate or low current densities, the counter electrode also acts as the reference electrode. These working electrodes were used for electrochemical cell assemblies for further electrochemical testing.

3.5.2 Test Cell Assembly

In order to perform electrochemical measurements and investigations, electrochemical cells had to be assembled. The electrochemical cells were assembled in an argon-filled (O_2 and H_2O levels less than 1 ppm) glove box (Mbraun, Unilab, Germany) by stacking a porous separator containing liquid electrolyte between the working electrode and a lithium metal counter electrode. The electrolyte used was 1 M $LiPF_6$ in a 50:50 (w/w) mixture of ethylene carbonate (EC) and dimethyl carbonate (DMC), provided by MERCK KgaA, Germany. During my PhD studies, two types of electrochemical cells were used. The one used in ISEM was the coin-type cell (CR2032), while the other used in PSI was a homemade titanium-based electrochemical cell.

A schematic diagram of the coin-type cell is shown in Figure 3.13. The separator used in the coin-type cell is made of porous polypropylene membrane (Celgard 2500) with a lower thickness (25 μm) compared to the glass fiber separator used in the homemade cell.



See print copy for figure 3.13

During my visiting fellowship appointment at the PSI, a homemade cell was used (Fig. 3.14). This homemade cell was mainly made of titanium. The counter electrode was placed on a titanium cylinder (8) and pressed with a spring (5) against the working electrode, which formed a coating on a copper (anode)/aluminium (cathode) current collector (10). A glass fiber separator soaked with the electrolyte was put between the two electrodes.

See print copy for figure 3.14

3.6 Electrochemical Characterization

If an electrochemical system is subjected to the passage of current between the two electrodes, it is out of equilibrium. Usually we are interested in investigating the electrode process of one electrode, which is the *working electrode*. The other electrode, the *counter electrode*, is used to complete the external circuit. Occasionally a third electrode is employed, the *reference electrode*. When this is the case, the electrode potential is monitored with respect to the reference electrode.

3.6.1 Cyclic Voltammetry (CV)

Cyclic voltammetry is a widely used method for studying electrode processes, especially for the determination of the thermodynamics and kinetics of electron transfer at the electrode-electrolyte interface. It is often employed as the first method to characterize new systems. The cell is cycled in a potential window, where the potential applied on the working electrode is continuously changed at a constant rate. Essentially, the potential is swept through the potential range where an electrode reaction occurs before the direction of scan is reversed, in order to define whether (a) the product of electron transfer is stable or (b) reaction intermediates or the final products are electroactive. The change of potential as a function of time is called the *scan rate*. The potential sweep can be described by its initial (E_i), switching (E_s), and final (E_f) potentials, and also by the scan rate, ν . The potential as a function of time (t) is:

$$E = E_i + \nu t \text{ (forward sweep)} \quad (3.4)$$

$$E = E_s - \nu t \text{ (reverse sweep)} \quad (3.5)$$

with the scan rate (in mV s^{-1}) defined as:

$$\nu = \frac{\Delta E}{\Delta t} \quad (3.6)$$

Other important parameters are the maximum and minimum potential ranges, which define the potential window. The choice of this potential window must take into account the stability range of the chosen electrolyte, to therefore avoid its decomposition. A positive sweep rate causes the oxidation of the working electrode, and the resulting current has a positive sign. With a negative sweep rate, the reduction of the working electrode causes a negative current.

Cyclic voltammetry (CV) measurements were conducted via a Computer Controlled Cell Capture device (CCCC, Astrol Electronics AG, Oberrohrdorf, Switzerland) in PSI or via a CHI 660 electrochemical workstation (CH Instrument, Cordova, TN) in ISEM.

3.6.2 Galvanostatic Measurements

In a galvanostatic measurement a constant current is applied between the working and counter electrodes. The current is applied until the set upper or lower potential limits are reached. For the working electrode a negative current would cause reduction and a positive current oxidation. The examination of the variation of potential with time is also called chronopotentiometry. This method has an important advantage over cyclic voltammetry, because the current or current density is kept constant, so the electrode process is investigated under real battery working conditions.

For an insertion/de-insertion process into a compound M :



The amount of the guest species (Δx) can be calculated as follows:

$$\Delta x = \frac{I \Delta t M_r}{n F m} \quad (3.8)$$

where, I is the applied current in A, Δt is the time interval in s, M_r is the molecular mass of the compound in g mol^{-1} , m is the active mass loading in g, F is the Faraday constant ($9.649 \times 10^4 \text{ C mol}^{-1}$), and n is the number of electrons exchanged.

The cells were galvanostatically discharged and charged at constant current density via a Neware battery tester (China) in ISEM or a Computer Controlled Cell Capture device (CCCC, Astrol Electronics AG, Oberrohrdorf, Switzerland) in PSI.

3.6.3 Electrochemical Impedance Spectroscopy (EIS)

The ac impedance spectroscopy technique involves the application of a small potential perturbation (E) at various frequencies (f) at a given dc potential (E_{dc}). The current response is monitored and as a result, the variation of resistance with frequency for the material can be examined. A common impedance spectrum consists of a low-frequency semi-circle and a high-frequency tail. The semi-circle is the result of the kinetic processes involved in the interaction between the resistor (R_{ct}) and the capacitor (C_{dl}) elements. The tail, on the other hand, results from diffusion processes and is represented in the model by a *Warburg* element.

See print copy for figure 3.15

The ac impedance spectroscopy measurements were carried out using a CHI 660A electrochemical workstation system (CH Instrument, Cordova, TN) by applying a sine wave of 5 mV amplitude over a frequency range of 100.00 kHz to 0.01 Hz. All impedance measurements were carried out in the de-lithiated state (state of charge).

CHAPTER 4

SINGLE-WALLED CARBON NANOTUBE PAPER AS FREE-STANDING ANODE FOR LI-ION BATTERIES

4.1 Introduction

Nanotechnology is the creation of functional materials, devices, and systems through control of matter on the nanometer scale and the exploitation of novel phenomena and properties of matter (physical, chemical, biological, electrical, etc.) at that length scale [Kroto et al., 1985]. Carbon nanotubes (CNTs) are supposed to be a key component of nanotechnology. Almost every week, a new potential application of CNTs is identified, stimulating scientists to peep into this tiny tube with ever increasing curiosity. CNTs, born in the Ando lab [Iijima, 1991; Ando and Iijima, 1993] and introduced to the world by Iijima, are now 16 years old, and much has been said, written, and discussed about this fascinating subject. But will they give rise to commercially viable applications? CNTs are rolled up sheets of sp^2 -bonded graphite with no surface broken bonds. Their possible applications arise from the remarkable properties of single-walled carbon nanotubes (SWCNTs), such as the highest Young's modulus, highest thermal conductivity, ballistic electron transport, and high aspect ratio structure [Baughman et al., 2002; de Heer, 2004].

Recent developments in the field of portable equipment have been the main driving force behind the search for batteries with high energy density and form flexibility [Hikmet, 2001; Morris et al., 2004]. It is well known that lithium batteries have the highest energy density of all the commercialized rechargeable batteries [Scrosati, 1995; Ceder et al., 1998; Morris et al., 2004]. They typically consist of a positive electrode and a negative electrode spaced by a separator, an electrolyte, a case, and feed-through pins respectively connected to the electrodes and extending externally from the case. Each electrode is formed from a metal substrate that is coated with a mixture of an active material, an electrical conductor, a binder, and a solvent. The negative electrode is formed from a copper substrate with graphite as the active material. The positive electrode is typically formed from an aluminium substrate with lithium cobalt dioxide as the active material.

Porous mats of carbon nanotubes, also referred to as bucky paper, fabricated by a filtering procedure from highly stable suspensions of single-walled carbon nanotubes (SWCNTs), have exhibited possible uses as hydrogen storage material [Liu et al., 1999], anode materials in lithium ion batteries [Claye et al., 2000a], actuators [Baughman et al., 1999] or artificial muscles [Vohrer et al., 2004], and sensors [Sumanasekera et al., 2000]. This is due to an intrinsic highly accessible surface area (derived from their nanosized diameter), and high manipulability. However, limited research work [Morris et al., 2004] has been done on the fabrication and evaluation of a “free-standing” carbon nanotube paper electrode without any electrode substrate that is produced with a simple filtration method via positive pressure.

Note that the manufacturing process for the “free-standing” electrode is considerably simplified compared with that of the conventional electrode, in which a metal substrate is coated with a mixture of an active material, an electrical conductor, a binder, and a solvent. Moreover, in order for this free-standing electrode to be viable for commercialization, or even practical usage, there is a need to increase its specific capacity by replacing a small portion of the SWCNTs with elements (e.g. Si, Sn, Sb or Ge) that could alloy with lithium and have much larger specific capacities than carbonaceous materials (Si: 4200 mAh g⁻¹ [Boukamp et al., 1981], Sn: 990 mAh g⁻¹ [Lee et al., 2003], SnO₂: 780 mAh g⁻¹ [Idota et al., 1997], Sb: 660 mAh g⁻¹ [Li et al., 2001], and Ge: 1600 mAh g⁻¹ [Pereira et al., 2003]).

In this work, we aim to develop a unique and simple electrode-making technique with a view to improving specific energy density, simplifying the manufacturing procedures for lithium-ion batteries, and consequently reducing the manufacturing cost. We will also report on the effects of carbon black (CB) powders and/or nanosized Si particle addition into the composite SWCNT bucky papers on their electrochemical performances as “free-standing” anode in lithium-ion rechargeable batteries.

4.2 Preparation of Single-Walled Carbon Nanotube Paper

A standard single-walled carbon nanotube (SWCNT)/Triton X-100 dispersion was prepared via addition of 50 mg of high purity (95 %, with remainder, ionic Iron (Fe) impurities from catalyst source) SWCNTs (Lot No. PO257) and 0.5 g of a surfactant,

Triton X-100, into 50 mL of Milli-Q water, followed by ultrasonication for 2 hours. A polyvinylidene fluoride (PVDF) membrane with pore size of 0.22 μm was cut into a 4-cm disk to fit the filtration cell (see Fig. 3.2 in Section 3.3.1).

The membrane is intended to act as a filter paper and was wetted in 50:50 v/v Milli-Q water to ethanol solution for 30 minutes. Passing the prepared SWCNT suspension through the wetted PVDF filter in a filtration cell under a positive nitrogen gas pressure of 400 kPa produced a “free-standing” mat of entangled SWCNT ropes, which is known as “bucky paper”. Subsequently, the resultant SWCNT mat was washed with 200 mL of Milli-Q water followed by 100 mL of methanol, where methanol was used to remove any residual surfactant. Finally, the SWCNT mat was peeled off from the PVDF filter after letting it dry overnight in a vacuum oven. Figure 4.1 shows a typical 4-cm SWCNT-derived bucky paper, ready for further measurements.

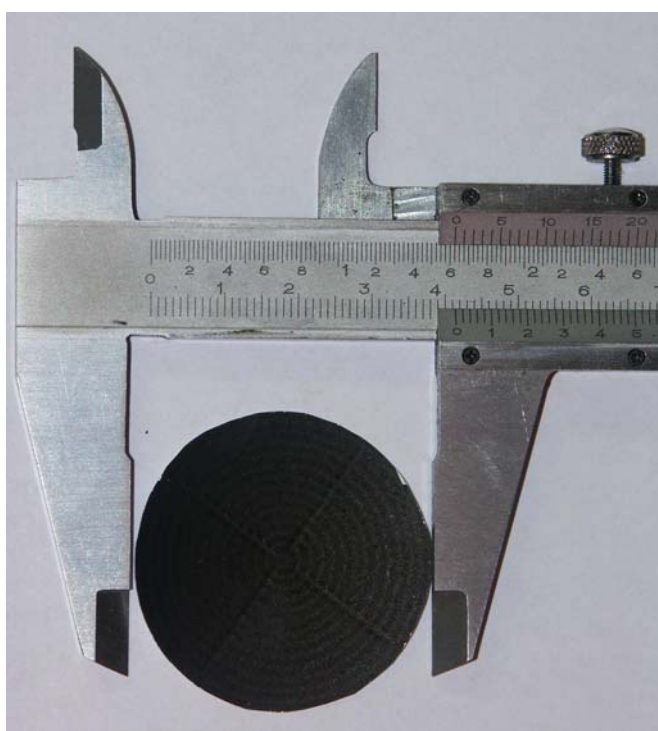


Fig. 4.1. Photograph of a typical 4-cm diameter SWCNT-derived bucky paper.

Meanwhile, for the SWCNT paper containing carbon black and/or nanosized Si particles, the dispersion was prepared by substituting 10-20 wt.% of the SWCNTs with carbon black or nanosized Si particles (< 100 nm). Then, the same procedures as were applied in the fabrication of SWCNT paper were repeated to produce a composite paper of SWCNTs with carbon black and/or nanosized Si particles. The thickness of the SWCNT-derived composite paper was controlled by the concentration of the SWCNT suspension.

4.3 Physical and Structural Characterizations

Figure 4.2 shows the transmission electron microscopy (TEM) images of the SWCNT precursor powder. We could observe a highly entangled web of hollow tube bundles, with diameters in the range of 10 to 30 nm (Fig. 4.2(a)). Meanwhile, the high-resolution transmission electron microscopy (HRTEM) image in Figure 4.2(b) clearly shows that our SWCNT is approximately 2.7 nm in outer diameter. Moreover, the X-ray diffraction (XRD) pattern of the SWCNT precursor powder, shown in Figure 4.3(a), reveals a broad (002) diffraction peak, indicating the amorphous structure of the SWCNTs. Based on the Bragg equation (see Eq. 3.1 in Section 3.4.1), as calculated from the (002) diffraction peak, the average SWCNT diameter is approximately 0.38 nm. In addition, Figure 4.3(b) shows the Raman spectrum of the SWCNT precursor powder, which presents a typical example of the SWCNT Raman spectrum with four peaks in the radial breathing mode (RBM) region and two sharp peaks corresponding to the tangential modes (G band) [Rao et al., 1997; Kataura et al., 1999; Strano et al., 2004].

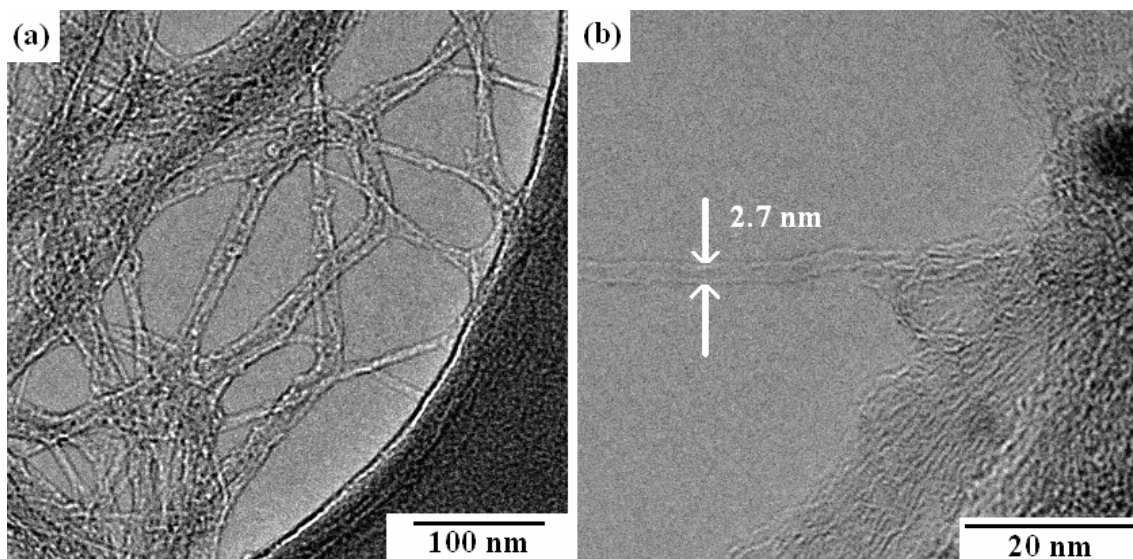


Fig. 4.2. TEM images of SWCNT precursor powder: (a) low resolution image shows inter-mingled bundles of nanotubes, and (b) high resolution image revealing the outer diameter of the SWCNT as approximately 2.7 nm.

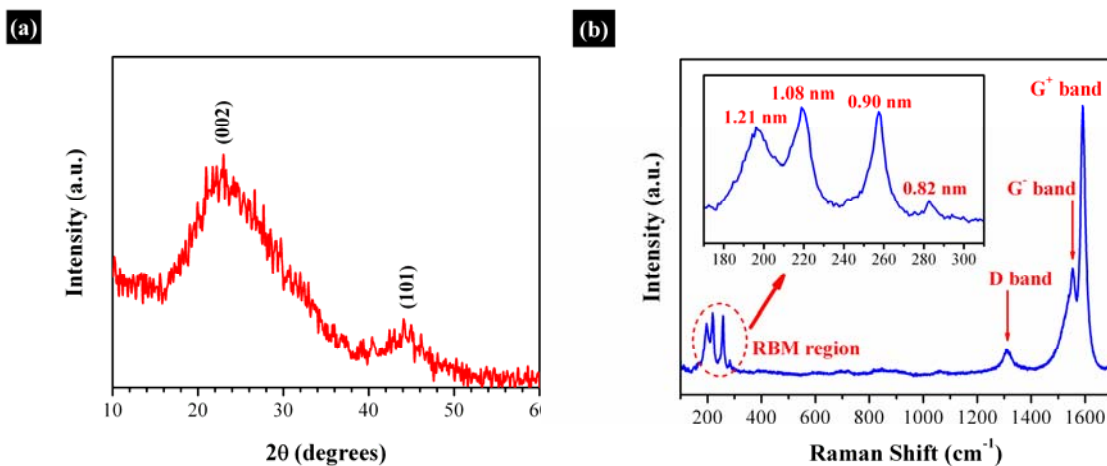


Fig. 4.3. (a) XRD pattern of SWCNT precursor powder. (b) Raman spectrum of the SWCNT precursor powder, using a 532 nm laser line. The inset shows the RBM region of the SWCNTs, with the numbers indicating the diameters of the SWCNTs.

The peak position at 1591.3 cm^{-1} is referred to as the G^+ band, with a triplet of A_{1g} , E_{1g} , and E_{2g} modes [Jorio et al., 2003]. In this SWCNT precursor powder, the G^+ band has a narrow and strong spectrum peak, indicating a good arrangement of the hexagonal lattice of graphite, whereas, the other peak at 1553.4 cm^{-1} , also known as the G^- band, is considered to be characteristic of the Raman spectrum for SWCNTs [Ha et al., 2006]. The weak D band at the peak of 1306.8 cm^{-1} in the spectrum reveals the high purity of the SWCNT precursor powder. The diameter of an individual SWCNT can be determined by the radial breathing mode (RBM) from 100 to 300 cm^{-1} . It is well known that the RBM frequency is inversely related to the tube diameter [Alvarez et al., 2000; Jorio et al., 2003]. The values in Figure 4.3(b) indicate the calculated diameters of the SWCNTs using the following correlation [Jorio et al., 2003]:

$$\omega_{RBM} = 218.3/d_t + 15.9 \quad (4.1)$$

where d_t is the tube diameter (nm) and ω_{RBM} is the RBM frequency (cm^{-1}). Therefore, the RBM spectral peaks at 196.2, 218.9, 257.5, and 282.8 cm^{-1} correspond to the SWCNTs with diameters of 1.21, 1.08, 0.90, and 0.82 nm, respectively. From the Raman analysis, the average diameter of a SWCNT is approximately 1.1 nm, and this result is in fairly good agreement with the HRTEM observation (see Fig. 4.2(b)).

It is well known that nanosized CNTs have a high tendency toward self-aggregation due to strong Van der Waals forces [Thess et al., 1996]. By utilizing this intrinsic nature of CNTs, we are able to fabricate bucky paper from CNTs dispersed in solution via a filtration process. As expected, bucky paper results from physical entanglement of SWCNT bundles (Fig. 4.4). From the cross-sectional field emission scanning electron

microscopy (FE-SEM) image of the SWCNT-derived bucky paper (Fig. 4.4(a) and (b)), we could observed the densely packed and highly entangled nature of the nanotubes in the bucky paper. Meanwhile, the SWCNT composite paper with carbon black nanoparticles, which is shown in Figure 4.4(c) and (d), revealed homogeneously distributed carbon black nanoparticles in the form of nano-agglomerates (100-150 nm) all over the SWCNT bundles.

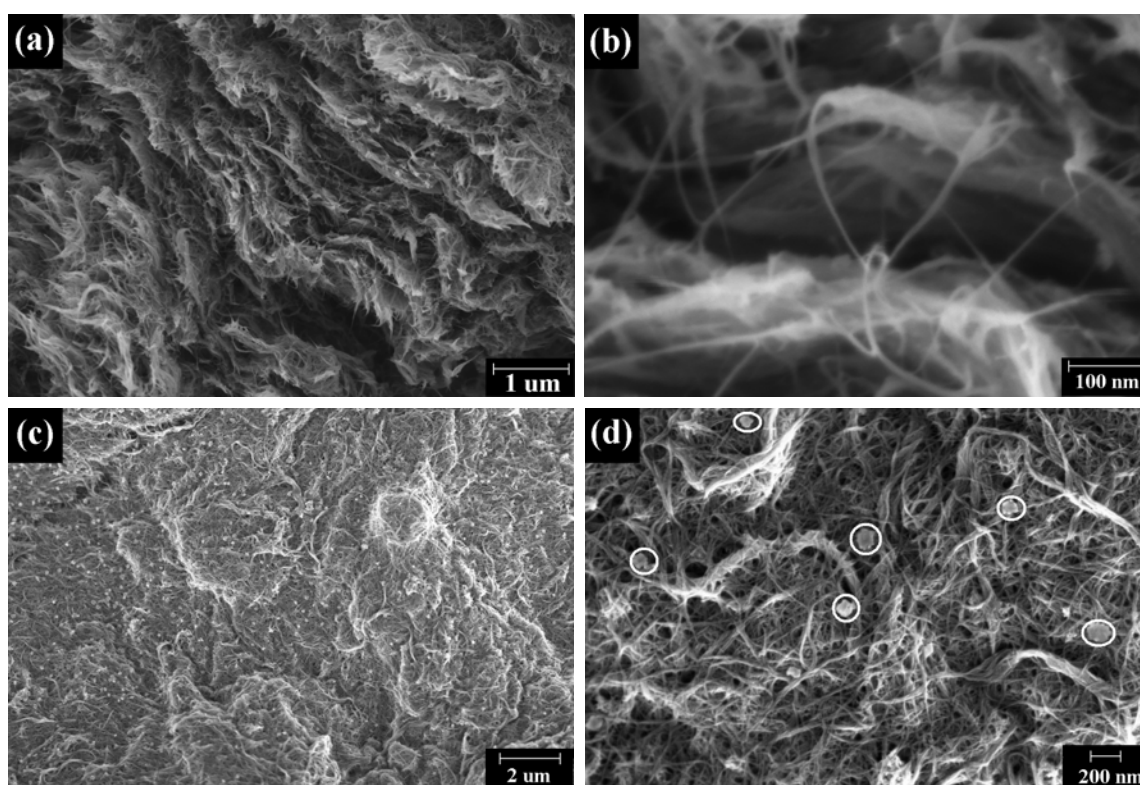


Fig. 4.4. Field emission scanning electron microscopy (FE-SEM) images of SWCNT-derived bucky paper: (a) low resolution cross-sectional image of SWCNT paper, exhibiting densely packed layers of nanotubes; (b) corresponding high resolution image of (a), clearly showing highly entangled SWCNTs between the layers; (c) low resolution image of SWCNT composite paper with carbon black, where the wide distribution of tiny white spots indicates carbon black nanoparticles; and (d) the corresponding high resolution image of (c), where the carbon black agglomerates are highlighted as white circles.

In Figure 4.5, we present the Raman spectra of carbon black powder, SWCNT powder, SWCNT paper and composite paper of SWCNTs with carbon black. It displays the great differences between carbon black powder and SWCNT powder, which shows four peaks in the radial breathing mode (RBM) region and two sharp peaks corresponding to the tangential modes (G-band). Note that no peak shifts were observed between the SWCNT powder and the SWCNT paper.

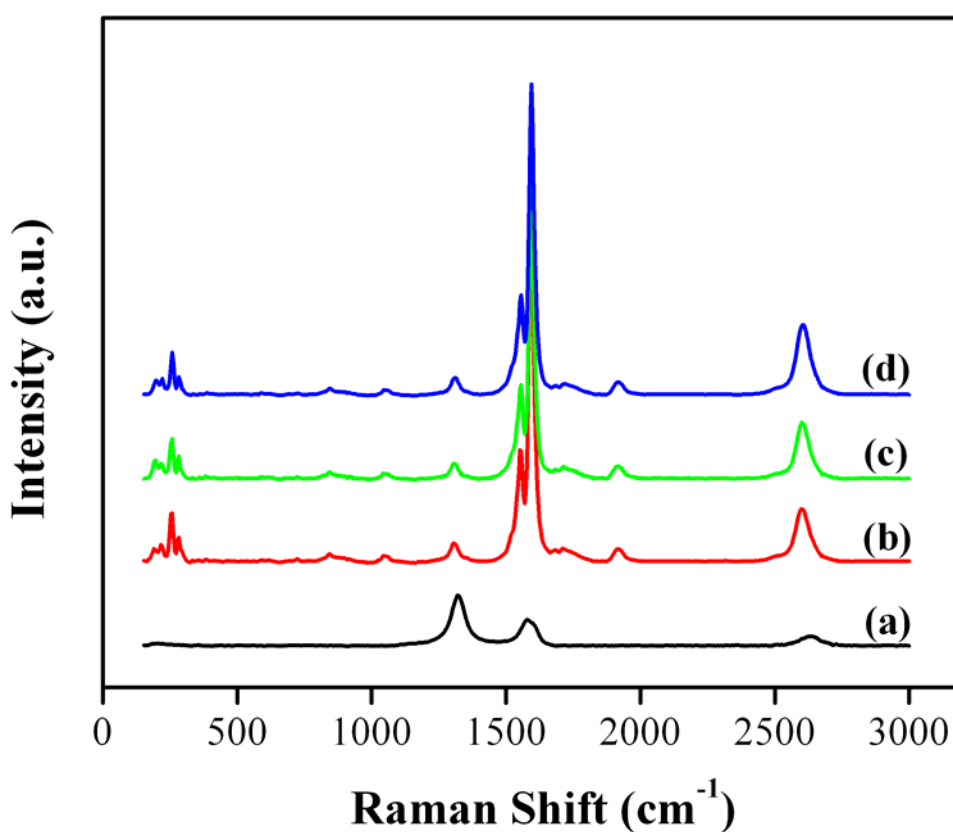


Fig. 4.5. Raman spectra for the SWCNT electrodes with 532 nm laser line: (a) carbon black powder, (b) SWCNT powder, (c) SWCNT paper, and (d) SWCNT composite paper with carbon black.

In a conventional cell, each electrode consists of a metal substrate that is coated with a mixture of an active material, a binder, and a solvent. The purpose of the electrode substrate in the battery is to hold the active material in a mechanically robust form and conduct electricity between the active material and the cell terminals [Torralba, 1976/1977; Prengaman, 1997]. Since a major function of the substrate is to be a collector for current during charge and discharge reactions in the battery, the conductivity of the substrate is one of the most important parameters in selecting electrode substrates.

In this work, the electrodes were prepared without using any metal substrate. These electrodes are self-supported “free-standing” electrodes. The conductivity of the “free-standing” electrodes is shown in Figure 4.6. It can be seen that the conductivity was improved when 10 wt.% carbon black was added as an electrode conductor (Fig. 4.6). The conductivity decreased as the thickness of the bucky paper increased for samples both with and without carbon black (Fig. 4.6). The conductivity of the SWCNT paper electrode is lower than that of the conventional electrode using metal as the substrate, but the conductivity could be potentially improved by adding a different type and different amount of carbon black powder as an electrical conductor during the fabrication of the electrode.

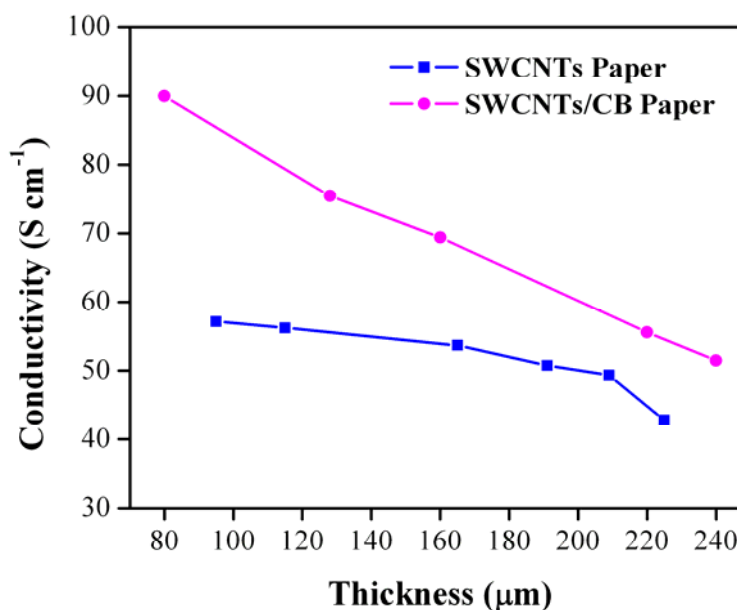


Fig. 4.6. Electrical conductivity as a function of thickness for SWCNT papers.

4.4 Electrochemical Performance

Electrochemical impedance spectroscopy (EIS) was performed on SWCNT paper electrodes of different thickness and with or without carbon black as an additive. Figure 4.7(a) shows the impedance results obtained for the cells using SWCNT paper and composite paper with 10 wt.% carbon black. The results indicate that the electrical impedance of the cell using SWCNT paper with carbon black as electrode is lower than that of the SWCNT paper without carbon black. It is obvious that the cell conductivity was improved by carbon black addition. The impedance of the cells increased as the thickness of the SWCNT papers increased (Fig. 4.7(b)). This is probably due to the lacked of compactness between the layers of SWCNT as the thickness of the bucky paper increases, which will then results in the presence of dead volume in the SWCNT paper.

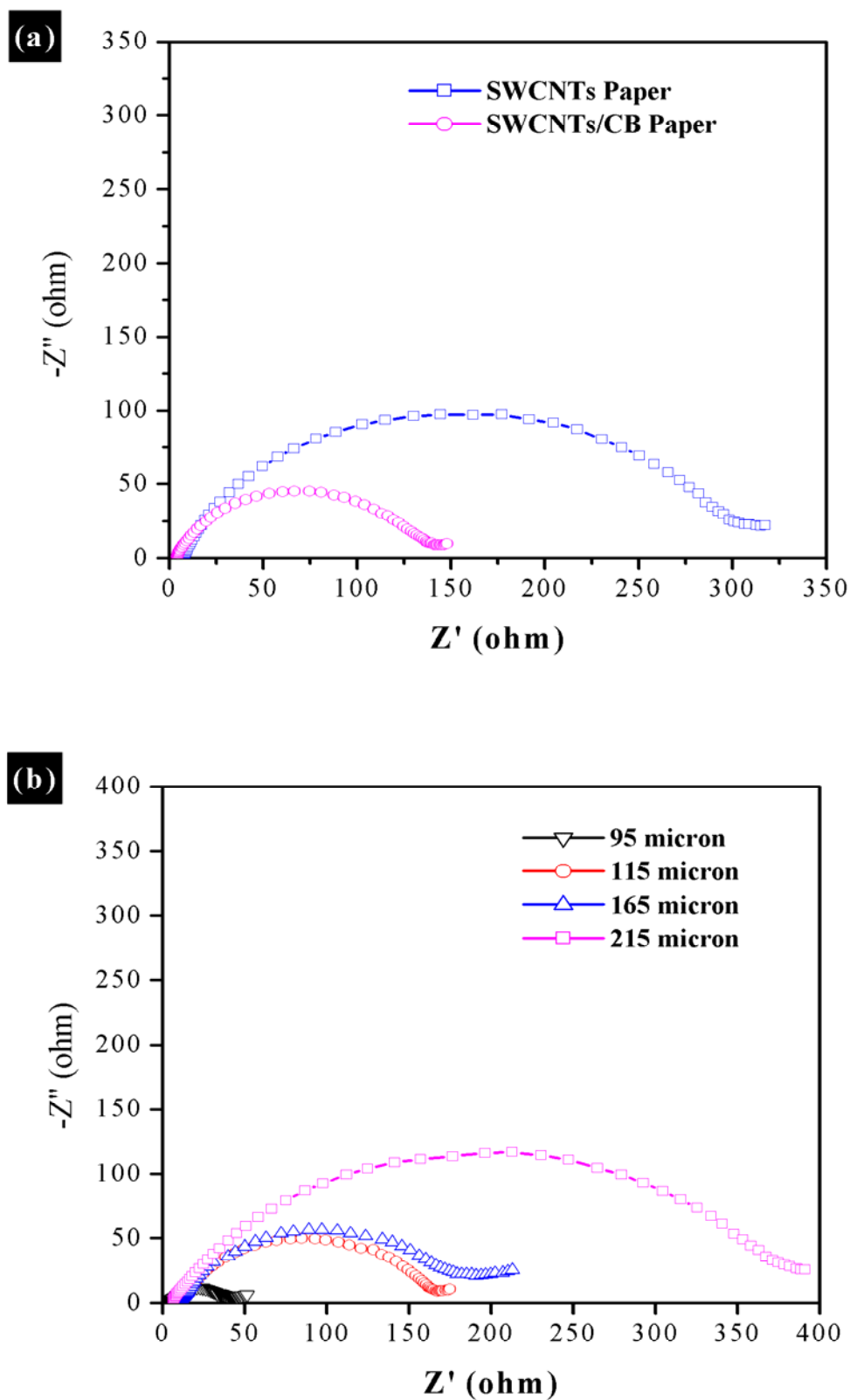


Fig. 4.7. Impedance plots for the SWCNT electrodes: (a) bucky paper and bucky paper with 10 wt.% carbon black, and (b) bucky paper with different thicknesses.

In order to determine the evolution of the kinetic parameters, especially the transport of lithium ions within the SWCNT paper electrodes, ac impedance measurements were performed on the fresh SWCNT paper electrodes in different equilibrium states. The impedance of the conventional slurry coated SWCNT electrode using Ni foam as the substrate was also measured to compare with the SWCNT paper electrodes. The cell was potentiostatically conditioned to a certain potential (2.5 V, 1.5 V, 0.8 V, 0.5 V, 0.3 V, 0.1 V, and 0.05 V, respectively) and equilibrated for 2 hrs. After that, the ac impedance spectroscopy was conducted by applying a sine wave of 5 mV amplitude over a frequency range of 100.00 kHz to 0.01Hz.

EIS graphs of all the electrodes presented in Figure 4.8 show only one depressed semicircle instead of two semicircles in the high and intermediate frequency region, which generally correspond to migration within the surface layer and the charge transfer process, respectively. The reason for this phenomenon is that the electrodes under measurement were fresh electrodes, so that the resistance of the solid-electrolyte interphase (SEI) passivation layer was very small. The two semicircles in the high and intermediate frequency regions overlap and appear to be one. The 45° line in the low-frequency region shows the typical characteristics of the Warburg impedance, which generally reflects the diffusion process of lithium within the bulk electrode. A comparison of the EIS Nyquist complex plots shows that the size of the semicircle drastically decreases with decreasing voltage for the thin SWCNT paper and SWCNT electrodes that were fabricated by coating SWCNT powder on Ni foam.

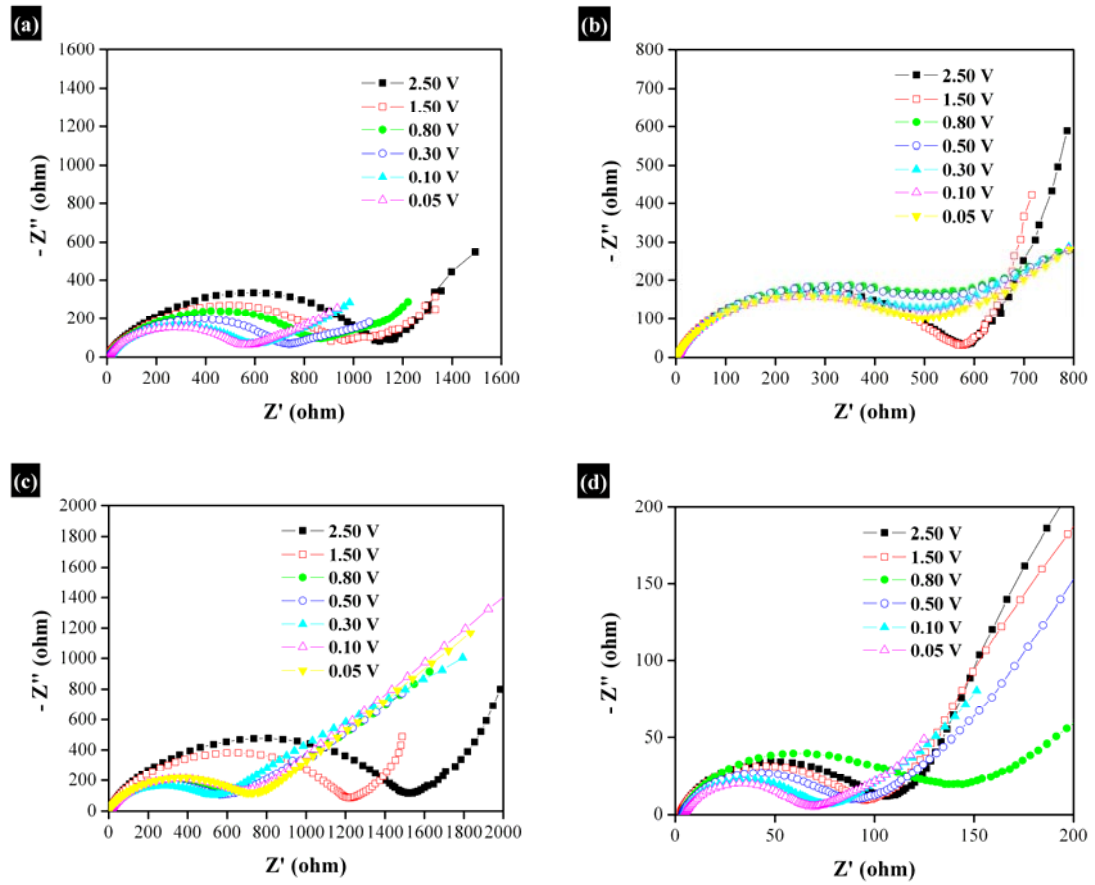


Fig. 4.8. Nyquist plots for SWCNT electrodes: (a) SWCNT powder on Ni foam, (b) thin SWCNT paper, (c) thick SWCNT paper, and (d) SWCNT paper with 10 wt.% carbon black.

For the thick SWCNT paper and the SWCNT paper with carbon black, the impedance does not monotonically decrease with decreasing voltage. Instead, the impedance decreases in the high voltage regime (above 0.5 V) and then increases afterwards. This phenomenon might be related to the build up and dissolution of the solid-electrolyte interphase (SEI) on the thick SWCNT paper and the SWCNT paper electrode with carbon black. The low frequency portion of the EIS spectra can be further divided into two regimes: the 45° line and an almost vertical line.

Claye et al. [2000b] also observed such a phenomenon during EIS measurement of SWCNTs, and they assigned the 45° line in the low frequency region to diffusion through the pores of the bucky paper and the near-vertical line to diffusion inside the bundles of SWCNTs. By comparing the EIS spectra in Figure 4.8, it can be concluded that the rate-determining step for SWCNT paper electrode in a high electrode potential state should be different from that in a low potential state. Since the Li^+ concentration increases with decreasing electrode potential, therefore, Li^+ mainly diffuses inside the bundles of SWCNTs at low Li^+ concentration, while Li^+ diffuses through the pores of SWCNT bucky paper at high Li^+ concentration.

Figure 4.9 shows the galvanostatic charge and discharge curves for the conventional SWCNT electrode and a “free-standing” bucky paper electrode. The first cycle of both electrodes exhibits enormous irreversible capacity, which could be attributed to various causes such as the reduction of dioxygen molecules or oxygenated functional groups on the surface of the SWCNT paper electrodes [Frackowiak et al., 1999] and the formation of the SEI passivation layer on the surface of the electrodes. The irreversible capacity of the “free-standing” SWCNT electrode was slightly larger than that of the conventional slurry-coated electrode. The galvanostatic charge-discharge curves of both electrodes show that the curves are quite typical for all this family of materials, including SWCNTs and multi-walled carbon nanotubes (MWCNTs) [Frackowiak and Béguin, 2002].

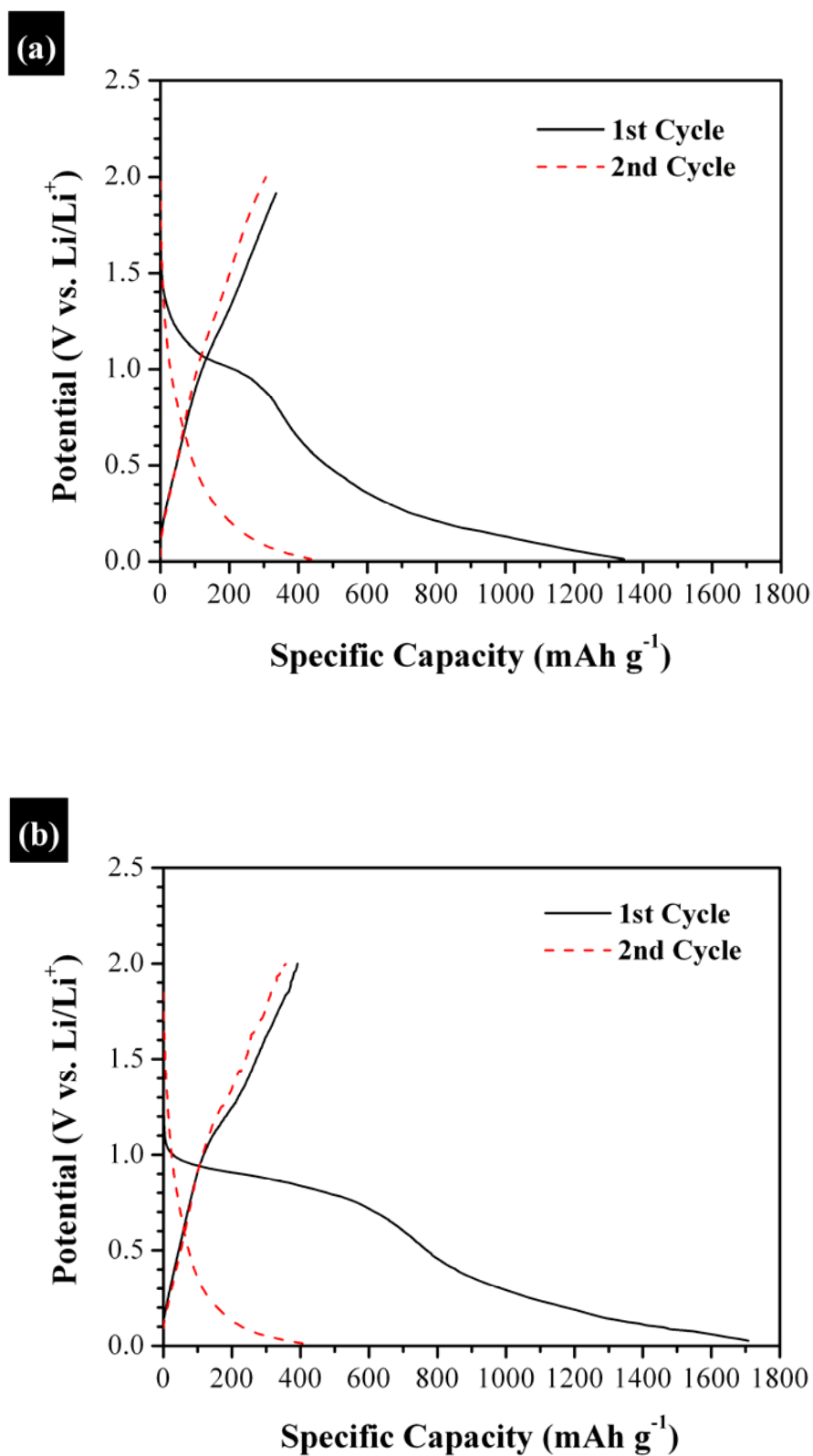


Fig. 4.9. Charge-discharge profiles of SWCNT electrodes: (a) conventional slurry-coated electrode, and (b) “free-standing” bucky paper electrode.

Figure 4.10 shows the discharge capacity versus the cycle number for cells made from the conventional electrode, “free-standing” SWCNT paper electrode, and SWCNT composite bucky paper with carbon black. The thickness of both SWCNT papers was about 80 μm . It can be seen that the capacity was improved by using carbon black as an additive for the “free-standing” SWCNT paper electrode, due to the fact that the electrode conductivity was improved (See Fig. 4.5). Although the capacity of “free-standing” SWCNT paper electrodes was slightly lower than that of conventional electrode, based on the active materials calculation, the “free-standing” electrodes have the potential to have considerably higher specific energy than those conventional electrodes currently in use, due to the fact that the electrode does not require any substrate or binder to provide mechanical integrity. On the other hand, the fabrication procedures for the electrode were greatly simplified, so the manufacturing cost will be reduced significantly.

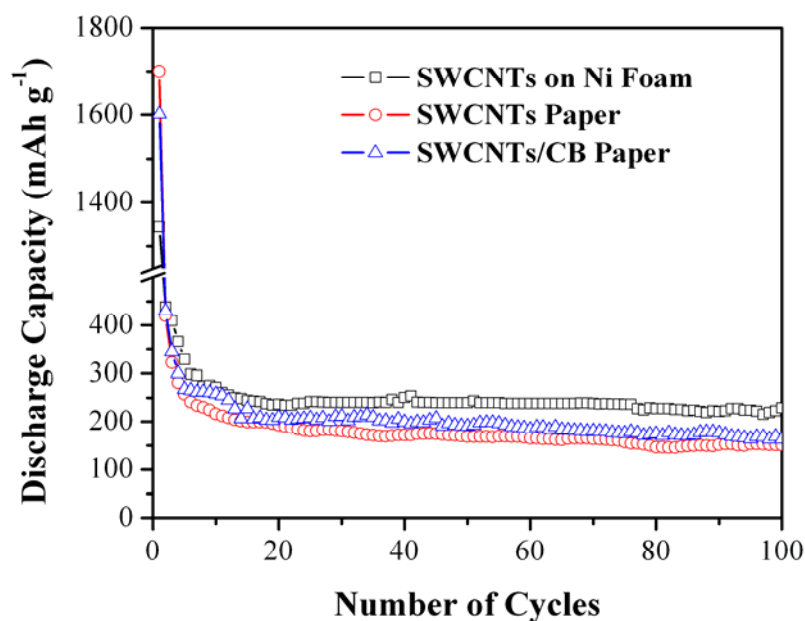


Fig. 4.10. Discharge capacities vs. cycle number. Current density was 0.08 mA cm⁻².

In order to improve the specific capacity of the SWCNT paper, nanosized silicon (Si) particles were added into the SWCNT/CB composite paper by substituting 10 wt.% of the SWCNTs with the Si nanoparticles. This concept proved to be in the right direction, as the kinetics and the reversibility of the bucky paper were greatly enhanced by the presence of the Si nanoparticles, as shown in the cyclic voltammograms in Figure 4.11. An additional pair of reduction (0.2 V)/oxidation (0.5 V) reactions was observed in the Si-based bucky paper, indicating the alloying reaction of Si with lithium metal [Ng et al., 2006b]. Meanwhile, as the cycle number increased, the Li^+ insertion (discharge) kinetics decreased for both SWCNT composite bucky papers, suggesting the possibility of Li^+ entrapment in the SWCNTs matrix, which lead to the irreversible capacity.

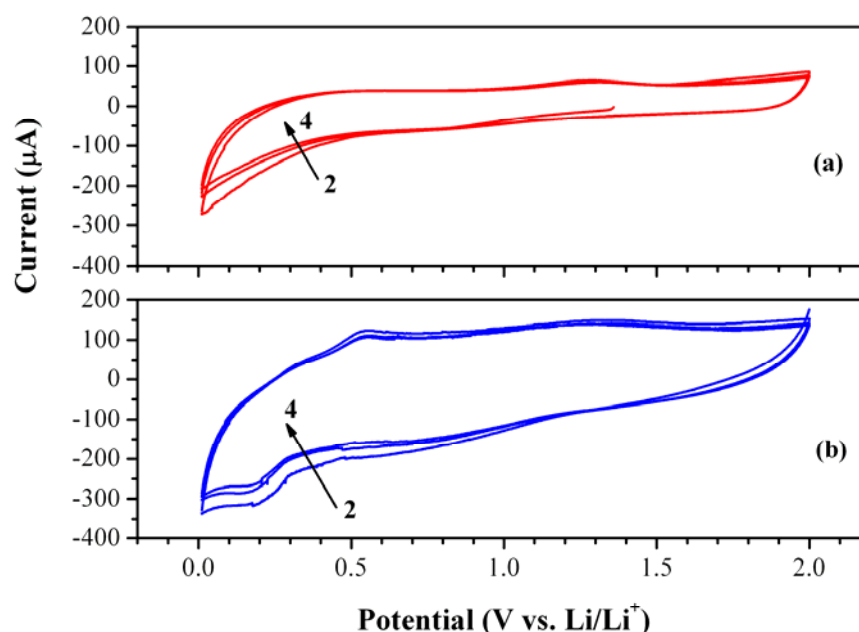


Fig. 4.11. Cyclic voltammograms of the SWCNT composite paper electrodes: (a) SWCNT paper with 10 wt.% carbon black, and (b) SWCNT paper with 10 wt.% carbon black and 10 wt.% nanosized Si particles addition. The scan rate applied is 0.5 mV s^{-1} and the numbers indicate the cycle number.

Figure 4.12 shows the electrochemical cycling behaviour of the SWCNT composite bucky paper. The addition of nanosized Si particles greatly enhanced the discharge capacity of the bucky paper electrodes, so that they retained a capacity of 400 mAh g^{-1} beyond 100 cycles (Fig. 4.12(a)). Meanwhile, at high current density, all the SWCNT composite bucky paper electrodes show high capacity fading behaviour, which might hamper its usage in high-power density applications.

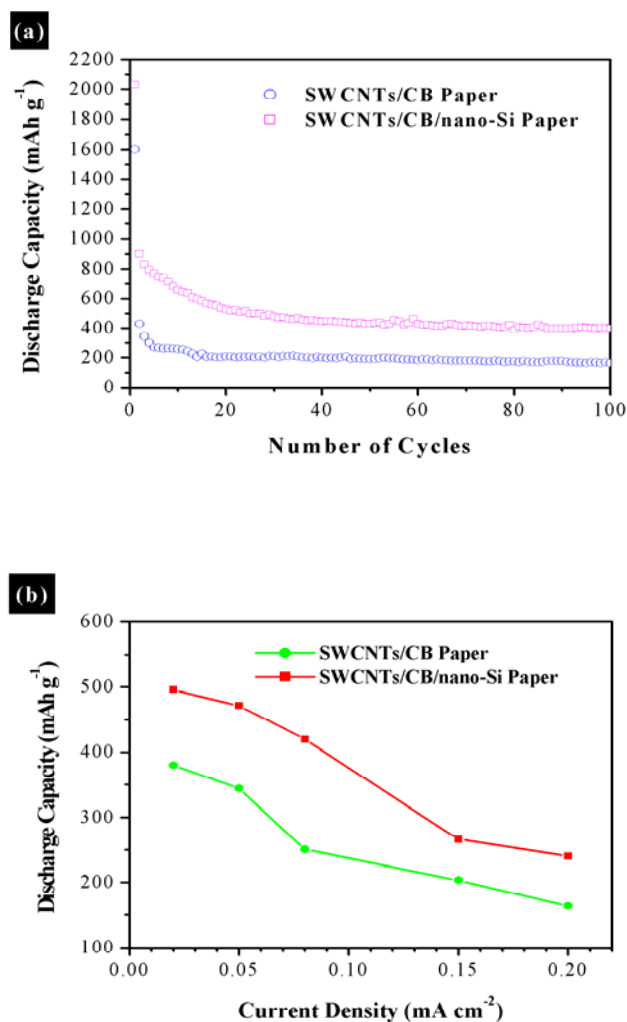


Fig. 4.12. (a) Cycle life of the composite bucky paper electrodes. The current density was 0.08 mA cm^{-2} . (b) Discharge capacities of the composite bucky paper electrodes at different cycling rates. The electrodes were cycled between 0.02 and 1.20 V vs. Li/Li^+ .

SEM images of “free-standing” SWCNT paper electrodes before and after cycling are shown in Figure 4.13. After 100 cycles, only some very tiny cracks were observed on the bucky paper electrodes.

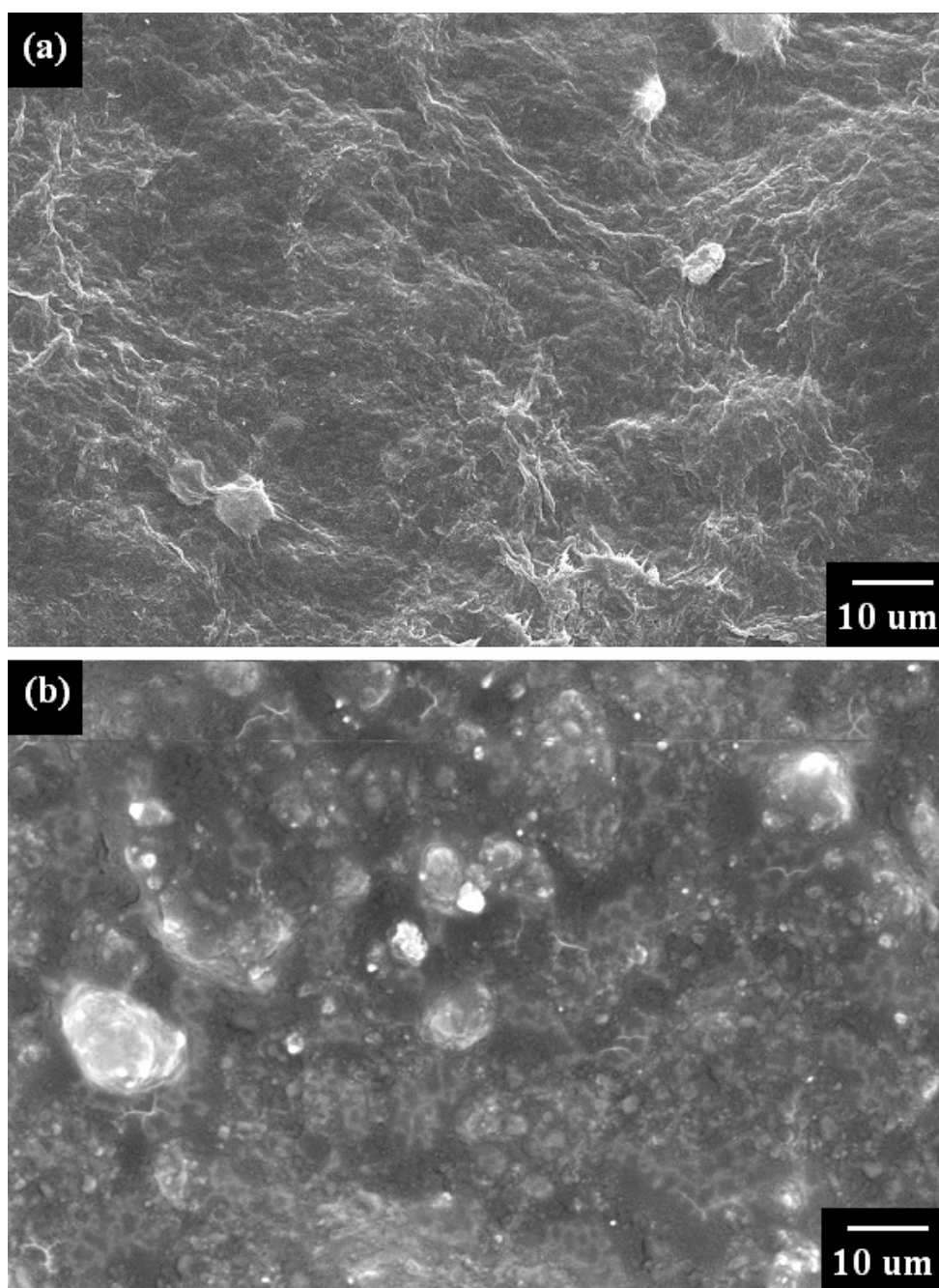


Fig. 4.13. SEM images of “free-standing” SWCNT paper electrodes: (a) before cycling, and (b) after 100 cycles.

4.5 Conclusions

“Free-standing” SWCNT paper electrodes are lightweight, flexible, have good conductivity, and can be fabricated easily without using any metal substrate or binder. The weight of the electrode was reduced significantly compared with a conventional electrode that was made by pasting a mixture containing an active material on the metal substrate. The results show that the capacity of the “free-standing” electrode was improved by using 10 wt.% carbon black as an additive. Moreover, the addition of nanosized silicon particles greatly enhanced the specific capacity of the SWCNT composite paper, so that it retained a capacity of 400 mAh g⁻¹ beyond 100 cycles. The use of the new design electrode will provide lightweight, low cost lithium-ion batteries.

CHAPTER 5

SPRAY-PYROLYZED LEAD OXIDE AND LEAD OXIDE- CARBON NANOCOMPOSITES AS ANODES FOR LI-ION BATTERIES

5.1 Introduction

A new generation of lithium-ion rechargeable batteries was developed in the early 1990s with the introduction of Stalion[®] lithium-ion cells by Fuji Photo Film Celltec [Idota et al., 1994; Idota and Mishima, 1995], whose anodes consisted of amorphous tin-based oxides instead of carbonaceous-based materials. It was reported that these electrodes have twice the theoretical gravimetric capacity and four times more theoretical volumetric capacity than carbon. This marvelous discovery has sparked off an intensive research on new materials that are capable of alloying with lithium, such as Al, Sn, Pb, In, Bi, Cd, Ag, Mg, Zn, Si, and Sb [Wang et al., 1986; Huggins, 1989 and 1998; Li et al., 1999a], which have all been investigated in the past decade. These materials show satisfactory Li-ion transport properties as well as a good lithium packing density and electrochemical potential. However, a substantial change in specific volume of the electrode upon continuous charging/discharging leads to loss of electrical contact,

and thus capacity loss, as well as macroscopic dimensional problems within the cell structure. Several methods have been proposed to solve this volume expansion problem, mainly by reducing the metal particle size [Yang et al., 1996; Poizot et al., 2000], limitation of cycling depth with a very thin reaction layer [Martos et al., 2001; Cruz et al., 2002], or by construction of bonded electrodes using Li^+ -conducting intermetallic phases [Besenhard et al., 1990; Huggins, 1999] as binder materials for small particle size active Li-alloys.

Despite the various methods available for the production of the ultra-fine nanoparticles used in Li-ion batteries, it is highly desirable to apply simple and highly productive techniques to produce both the anode and cathode materials. Moreover, if possible, we should fabricate them in-situ to avoid the complicated and expensive technological procedures that might be featured in some methods [Konstantinov et al., 2003]. The spray pyrolysis method fully satisfies these requirements, because it is versatile, inexpensive, industrially-oriented, and can be operated over a large temperature range ($100\text{ }^{\circ}\text{C} - 1000\text{ }^{\circ}\text{C}$) [Martos et al., 2001 and 2003; Cruz et al., 2002; Konstantinov et al., 2003; Yuan et al., 2005].

Studies by Martos et al. [2003] using sprayed lead oxide powders as anode material in Li-ion batteries show that the specific capacity fades on cycling when bulk powders are used. Therefore, we suggest the addition of a carbon source (sucrose solution) to enhance the electric conductivity of PbO and also increase its specific capacity and cycle life. This concept has proven to be successful in other studies [Yoshio et al., 2002; Bewlay et al., 2004; Yuan et al., 2005].

Although there have been reports on the usage of sprayed PbO [Martos et al., 2001 and 2003] as an anode material in Li-ion batteries, there have been scarcely any studies reported on PbO-carbon anodes in Li-ion batteries. In this chapter, I report the synthesis of both nanostructured PbO and nanocomposite PbO-carbon using an in-situ spray pyrolysis approach and investigate their electrochemical performance as anode materials for Li-ion batteries. A systematic investigation of the effect of temperature, solution concentration, and solution flow rate on the morphological, physical, and electrochemical characteristics of in-situ prepared PbO nanostructured materials will also be presented here in detail.

5.2 Synthesis Method

All powders were obtained in-situ by spraying various concentrations of Pb(NO₃)₂ aqueous solutions under different conditions, which are summarized in Table 5.1. The composite materials were prepared by mixing the initial solutions with aqueous sucrose (C₁₂H₂₂O₁₁) solutions in weight ratios (Pb(NO₃)₂ : sugar) of 100 : 0, 70 : 30, 40 : 60, 15 : 85, and 0 : 100, respectively (see Table 5.2). A vertical-type spray pyrolysis reactor was used for the experiments. The reactions are as follows:

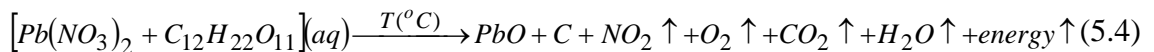
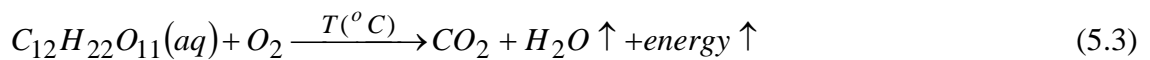
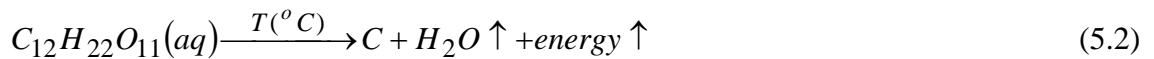
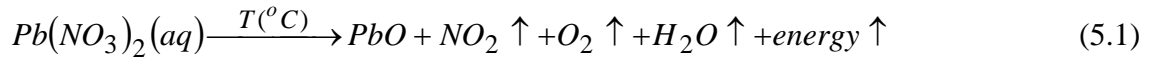


Table 5.1: Summary of experimental conditions and some physical characteristics of the sprayed PbO nanoparticles.

Sample No.	1	2	3	4	5	6	7
Furnace Temperature, T (°C)	600	700	800	700	700	700	700
Solution Concentration, C (M)	0.50	0.50	0.50	0.15	0.30	0.50	0.50
Solution Flow Rate, Q (mL min ⁻¹)	3.14	3.14	3.14	1.57	1.57	1.57	4.71
Average Crystal Size, D _P (nm)	31	53	102	127	75	25	62
Specific Surface Area, S _{BET} (m ² g ⁻¹)	4.5	2.4	2.2	6.6	2.6	1.8	2.0

Table 5.2: Summary of experimental conditions and some physical characteristics of the sprayed PbO-C nanocomposites.

Sample No.	3	8	9	10	PbO (Sigma-Aldrich)
Furnace Temperature, T (°C)	800	800	800	800	
Solution Concentration, C (M)	0.50	0.50	0.50	0.50	Not Applicable
Solution Flow Rate, Q (mL min ⁻¹)	3.14	3.14	3.14	3.14	
Pb(NO ₃) ₂ / C ₁₂ H ₂₂ O ₁₁ (wt.%/wt.%)	100/0	70/30	40/60	15/85	
Average Crystal Size, D _P (nm)	102	74	53	26	> 500
Specific Surface Area, S _{BET} (m ² g ⁻¹)	2.2	2.5	4.4	6.5	0.4

5.3 Physical and Structural Characterizations

The XRD analysis shows that all powders exhibit either single tetragonal α -PbO phase with the lattice parameters: $a = 0.3973$ nm and $c = 0.5022$ nm (JCPDS Card No. 05-0561) or α -PbO phase together with additional traces of orthorhombic β -PbO phase with the lattice parameters: $a = 0.5489$ nm, $b = 0.4755$ nm, and $c = 0.5891$ nm (JCPDS Card No. 05-0570), when the furnace temperature is increased from 600 to 800 °C. There were no traces of Pb_3O_4 in any of the materials. Some typical X-ray patterns are shown in Figure 5.1. The well-known Debye-Scherrer formula was used to calculate the average crystal size using crystalline silicon as the reference material.

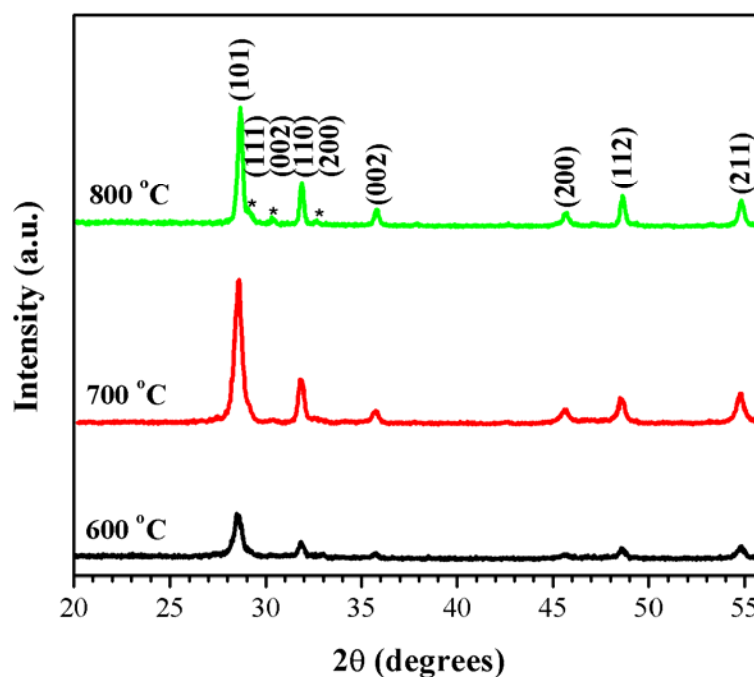


Fig. 5.1. Typical XRD patterns of α -PbO powders sprayed at different temperatures. The solution concentration was 0.5 M, and the flow rate was 3.14 mL min^{-1} . The traces of β -PbO are marked by *.

Additional confirmation of crystallite size was obtained by TEM centered dark-field imaging (Fig. 5.2), where individual lead oxide crystallite sizes were obtained by imaging particle clusters using lead oxide diffraction spots. Figure 5.2 shows dark-field images of crushed particles and the approximate lead oxide crystallite sizes in samples sprayed at 600 °C (Fig. 5.2(a)) and at 800 °C (Fig. 5.2(b)).

First of all, the effect of furnace temperature on the average crystal size was evaluated (Table 5.1). As seen from Table 5.1, a temperature increase from 600 to 800 °C leads logically to a crystal size increase from 31 to 102 nm (samples 1, 2, and 3). To determine the temperature effect, both the concentration and flow rate were kept constant (0.5 M and 3.14 mL min⁻¹).

In contrast to the temperature effect, an increase in the solution concentration has a pronounced negative effect on the crystal growth (samples 4, 5, and 6). The average crystal size decreases almost linearly from 127 to 25 nm when the concentration increases from 0.15 to 0.5 M. All materials were sprayed at 700 °C using a flow rate of 1.57 mL min⁻¹. This result can be explained by the increased number of crystallization centers in solutions with higher Pb concentration and the consequent blocking effect on crystal growth due to the simultaneous crystallization of more crystallites within the particles. Finally, I studied the effect of the flow rate on the crystallization process and average crystal size. The result for samples 2, 5, and 7 show that there is no clear dependence between these parameters. These materials were sprayed at 700 °C using 0.5 M solutions.

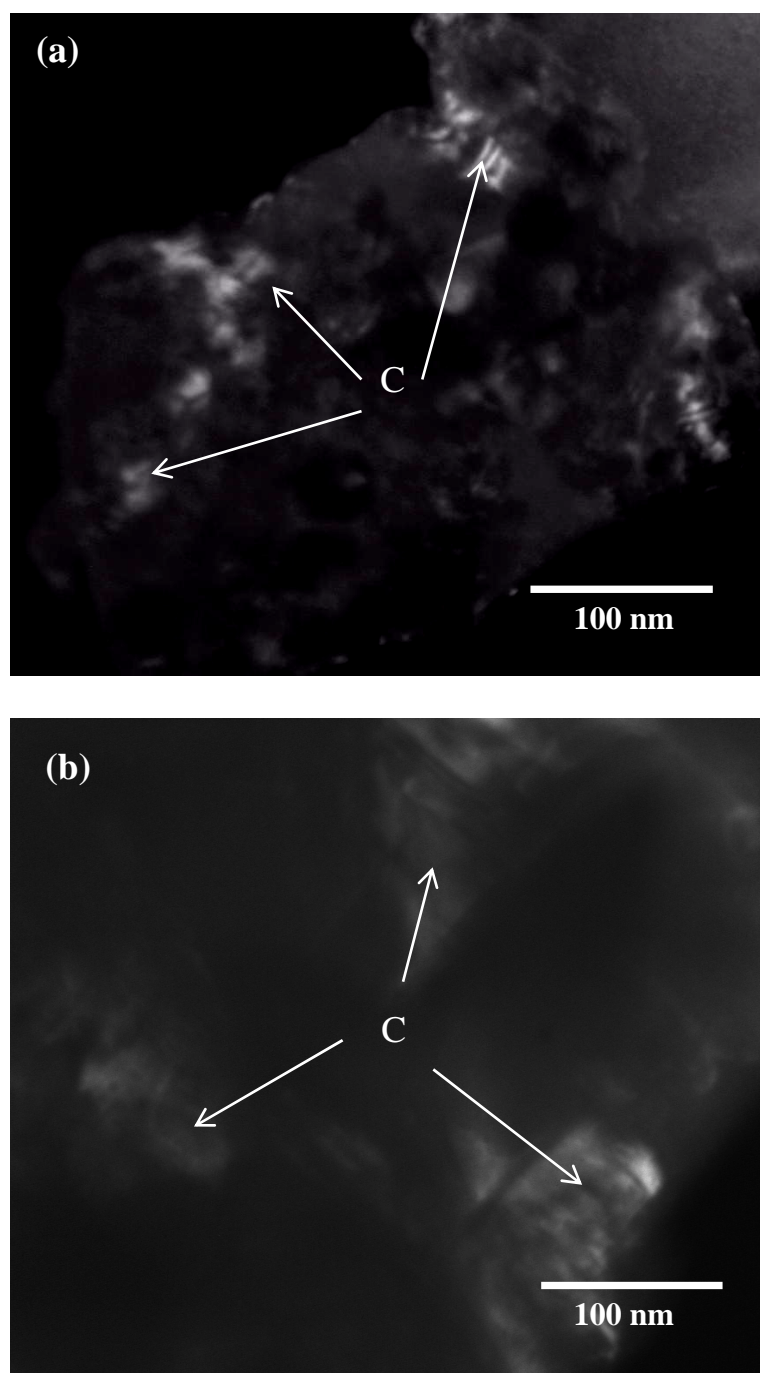


Fig. 5.2. TEM dark-field images obtained from samples sprayed at (a) 600 °C and (b) 800 °C. Individual crystallites are marked as C.

It was expected that variation of the flow rate could affect the particle size of the in-situ PbO powders. However, SEM results did not confirm this assumption either. Agglomerates with spherical shape, which is typical for the spray process, are in the range of 0.5-5 microns for all powders, and the size is not dependent on the flow rate. The temperature has a small effect for this temperature range (Fig. 5.3), and the materials obtained at 800 °C reveal more crystalline and inter-grown particles, while powders obtained at 600 °C have particles with fine nano-porous structure. The particle size appears to increase at higher temperature due to the intergrowth process. This would be expected to result in a lower specific surface area of the materials (S_{BET}).

The BET results clearly confirm the SEM observations. An increase in the temperature causes a pronounced decrease of the S_{BET} (see the results for samples 1, 2, and 3 in Table 5.1). The powders obtained at 600 °C exhibit a remarkably high S_{BET} value of 4.5 $\text{m}^2 \text{g}^{-1}$ (for comparison, the conventional Sigma-Aldrich PbO has only 0.4 $\text{m}^2 \text{g}^{-1}$). The materials obtained at 800 °C have only 2.2 $\text{m}^2 \text{g}^{-1}$. Note that all other factors were kept constant: solution concentration 0.5 M and flow rate 3.14 mL min^{-1} .

The effect of solution concentration on S_{BET} was found to be similar (Table 5.1, samples 4, 5, and 6). A higher concentration promotes a lower specific surface area. Increasing the concentration from 0.15 to 0.5 M causes a decrease of S_{BET} from 6.6 to 1.8 $\text{m}^2 \text{g}^{-1}$. These results were obtained for 700 °C and a flow rate of 3.14 mL min^{-1} .

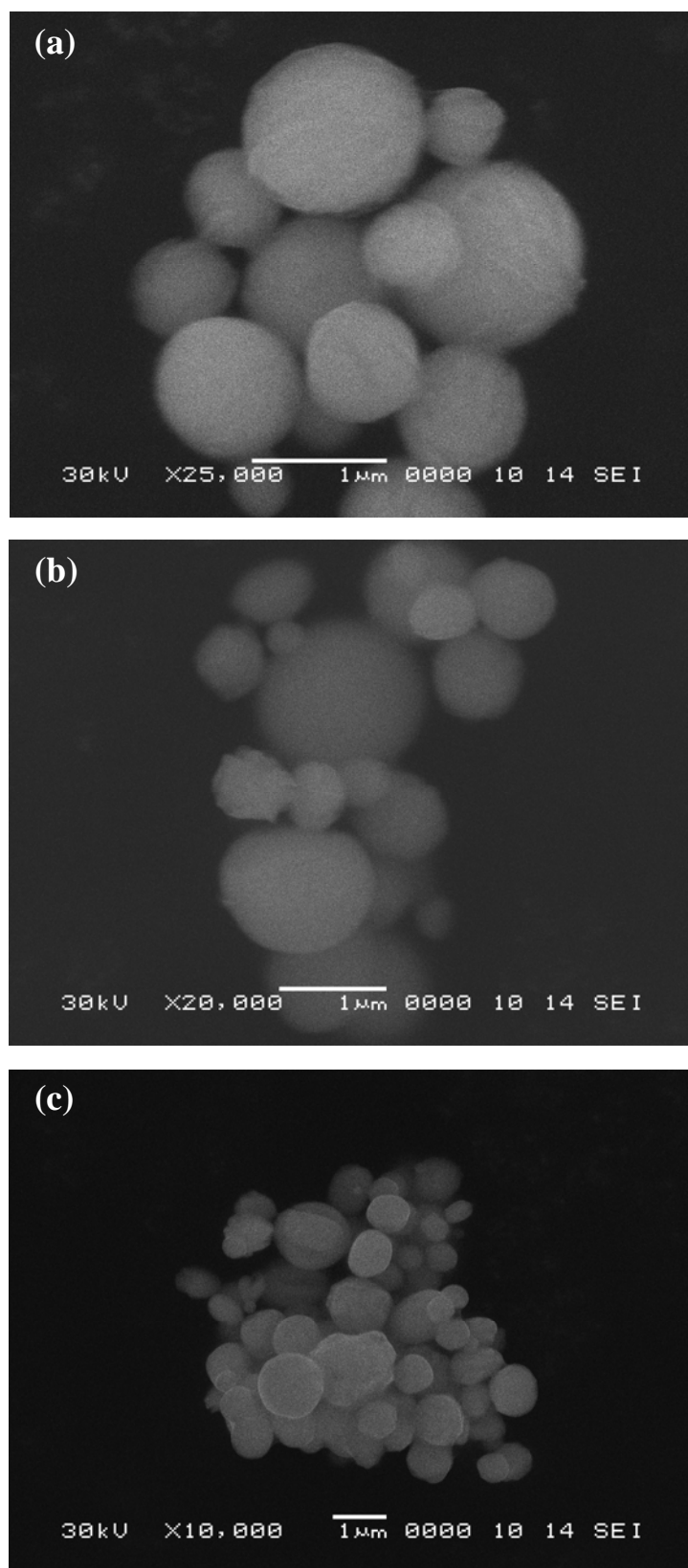


Fig. 5.3. Typical SEM images of powders sprayed at (a) 600 °C, (b) 700 °C, and (c) 800 °C. The solution concentration was 0.5 M, and the flow rate was 3.14 mL min⁻¹.

The results regarding the S_{BET} are very important because they demonstrate that large specific surface area should not be always associated with small crystal size. Our group has previously reported [Konstantinov et al., 2004] similar results for nano-structured oxides, e.g. Co_3O_4 , CoO , NiO , and SnO_2 obtained in-situ by spray technology. Quite often the very small nano-crystallites stack together due to their high surface energy and create very dense packing, which reduces the specific surface area. The strong agglomeration effect observed for nano-structured oxides is an important problem that should be taken into account for practical utilization of such materials in energy saving applications where a large specific surface area is an important factor.

For quantifying the amount of carbon in the PbO-C composite materials, thermogravimetric analysis (TGA) was carried out in air. The samples were heated from $60\text{ }^\circ\text{C}$ to $600\text{ }^\circ\text{C}$ at a rate of $5\text{ }^\circ\text{C min}^{-1}$. Figure 5.4 shows the TGA analysis of the PbO-C composite samples along with those of bare PbO and carbon powders. As can be seen from Figure 5.4, bare carbon powder burns off at $460\text{ }^\circ\text{C}$, while the bare PbO powder remains stable in the temperature range used for this experiment. It can also be seen that the composites show weight loss at a temperature of $460\text{ }^\circ\text{C}$, which corresponds to the oxidation of carbon. There is no further weight change in the composites after the initial oxidation of carbon. Therefore, the change in weight before and after the oxidation of carbon directly translates into the amount of carbon in the PbO-C composites. Using this method, it was found that the amounts of carbon in the composites were 3.3 wt.%, 8.7 wt.%, and 9.5 wt.% for the precursor solutions with weight ratios $(\text{Pb}(\text{NO}_3)_2/\text{sugar})$ of 70/30, 40/60, and 15/85, respectively.

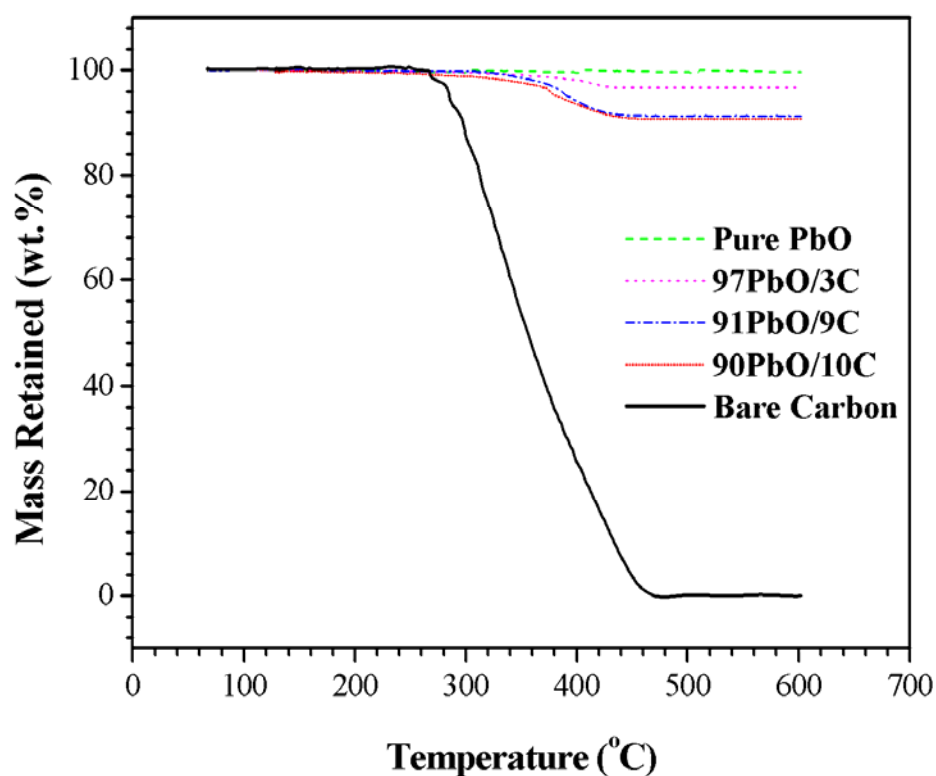


Fig. 5.4. TGA curves of PbO-C nanocomposites with different PbO/C ratios.

Table 5.3 summarizes the actual carbon content in the spray pyrolyzed PbO-C nanocomposites. The carbon concentrations obtained after spray pyrolysis were significantly below the targeted levels. All samples undergo more than 80 wt.% carbon losses during the spray process. This can be explained by the reactions during the spray pyrolysis process mentioned earlier in Section 5.2.

There are mainly 3 reactions during the spray pyrolysis process: (Eq.5.1) oxidation of lead nitrate to produce lead oxide and release gases such as nitrogen dioxide and oxygen; (Eq. 5.2) decomposition of sugar to carbon and water vapour (in the absence of oxygen/air); and (Eq. 5.3) combustion of sugar in air to produce gases such as carbon

dioxide and water vapour. All the reactions are exothermic and thus release excess energy produced during the reactions. As the spray pyrolysis process was carried out in air, reaction (5.3) is more favourable compared to reaction (5.2). Therefore, most of the sugar will be burnt out during the spray pyrolysis process, which accounts for the high percentage of carbon mass loss (> 80 wt.%). However, due to the instantaneous nature of the spray pyrolysis process, decomposition of sugar will still occur [Bewlay et al., 2004; Yuan et al., 2005]. Equation 5.4 summarizes the whole reaction during the spray pyrolysis process.

Table 5.3: Theoretical and actual carbon content in PbO-C nanocomposites sprayed from starting solutions with different concentrations of Pb(NO₃)₂/sugar*.

Starting Solution wt.% Pb(NO ₃) ₂ /wt.% sugar*	Theoretical weight % of carbon	Actual weight % of carbon (via TGA)	Mass loss % of carbon during spray pyrolysis
70/30	21.12	3.27	84.52
40/60	48.38	8.73	81.96
15/85	77.98	9.53	87.78

* C₁₂H₂₂O₁₁

X-ray diffraction investigations (Fig. 5.5) revealed products comprising nanocrystalline PbO (Fig. 5.5(a)) and PbO-carbon nanocomposites (Fig. 5.5(b-d)) with confirmation of both the α -PbO phase (JCPDS Card No. 05-0561) and the β -PbO (JCPDS Card No. 05-0570) phase. Figure 5.5 also reveals that as the carbon content increases (from Fig. 5.5(a) to (d)), the intensity of the orthorhombic β -PbO phase increases significantly,

while the intensity of the tetragonal α -PbO phase is reduced. The well-known Debye-Scherrer formula was used to estimate the approximate average crystal size using crystalline silicon as the reference material. The estimated average crystal size was reduced from 102 nm to 26 nm when the carbon content was increased. The reduction of the average crystal size led to an increase in specific surface area (S_{BET}) from $2.2 \text{ m}^2 \text{ g}^{-1}$ to $6.5 \text{ m}^2 \text{ g}^{-1}$. For comparison, the commercial Sigma-Aldrich PbO powders have a specific surface area of only $0.4 \text{ m}^2 \text{ g}^{-1}$.

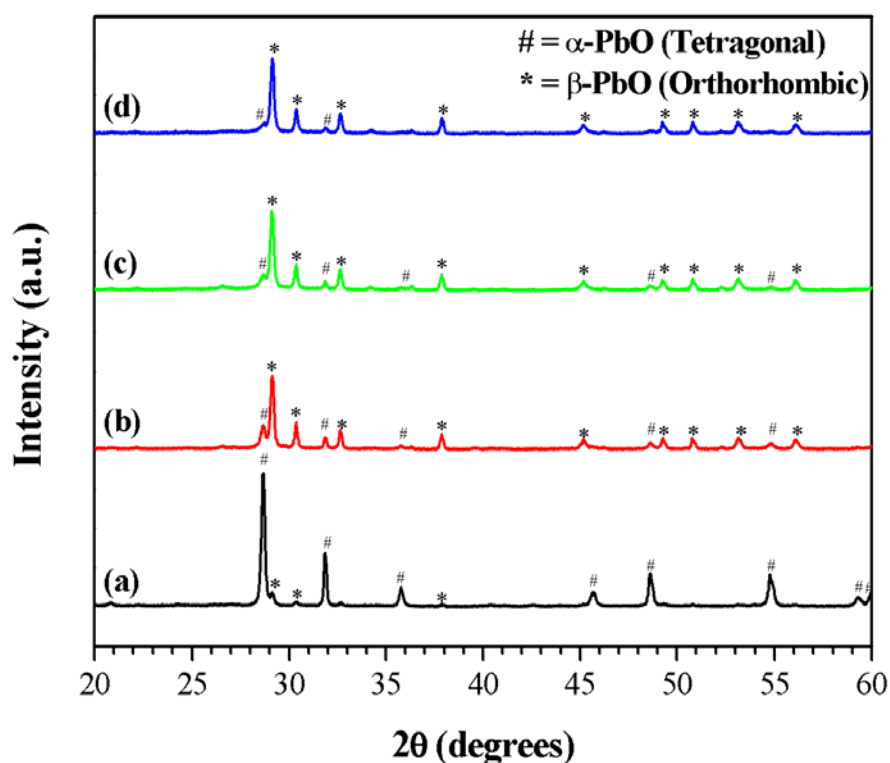


Fig. 5.5. XRD patterns of PbO-C nanocomposites from (a) pure PbO; (b) 97PbO/3C; (c) 91PbO/9C; and (d) 90PbO/10C.

From SEM observations (Fig. 5.6), it was revealed that the particles are mainly spherical agglomerates, which is typical for the spray process, with sizes in the range of 0.2-2 microns for all powders. All the samples sprayed with sugar addition were morphologically alike, presenting a structure resembling broken hollow spheres with porosity on both the inside and the outside particle surfaces (Fig. 5.6(b-d)). This may be due to the decomposition of sugar, resulting in the release of gases such as carbon dioxide and water vapour, leaving holes in the hollow spherical structure [Yuan et al., 2005].

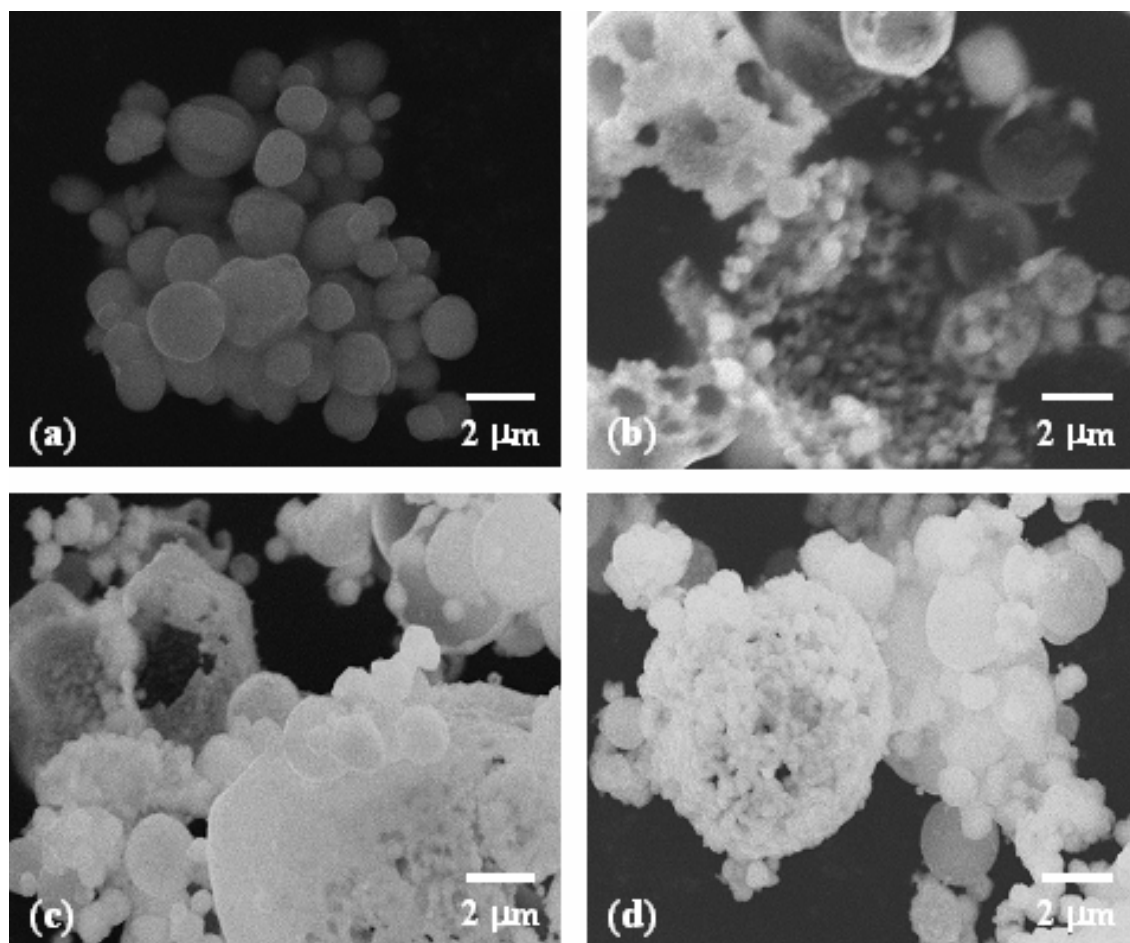


Fig. 5.6. SEM images of PbO and PbO-C nanocomposites from (a) pure PbO; (b) 97PbO/3C; (c) 91PbO/9C; and (d) 90PbO/10C.

Transmission electron microscopy (Fig. 5.7) confirmed the trend in average crystallite sizes as a function of carbon content, giving additional information about lead oxide morphology. The morphology of individual lead oxide crystallites in samples containing no carbon is shown in the TEM centered dark-field image (Fig. 5.7(a)), obtained using lead oxide diffraction spots. In the PbO-carbon samples, TEM combined with selected area electron diffraction (SAED) confirmed that the particle sizes ranged from 50-100 nm for the sample with 3 wt.% carbon (Fig. 5.7(b)), and approximately 5-50 nm for the sample with 10 wt.% carbon (Fig. 5.7(c)). Particles, such as those marked P in Figure 5.7(b), were found to be spheroidal or disk-like in shape, while others were found to be slightly more faceted. Low magnification bright-field imaging combined with SAED also confirmed that carbon rich clusters formed during atomization, at least for the sample with 10 wt.% carbon, and that these contained varying amounts of PbO. Some were solidified droplets containing no PbO nanoparticles at all (Fig. 5.7(d)), while many contained a uniform dense distribution of PbO such as that observed in Figure 5.7(c).

As a general trend, the increase in process temperature from the excess energy generated by the exothermic reactions in Section 5.2 should have led to an increase in average crystal size due to the higher kinetics and intergrowth process. However, the results in Table 5.2 show otherwise. This can be explained by the phase transformation of α -PbO phase to β -PbO phase as the temperature increases. The excess energy generated by the spray pyrolysis process was used for the phase transformation process instead of crystal growth as the carbon content in the starting solution increased. This led to the reduction of crystal size and subsequently resulted in a higher specific surface area of the PbO-carbon nanocomposites.

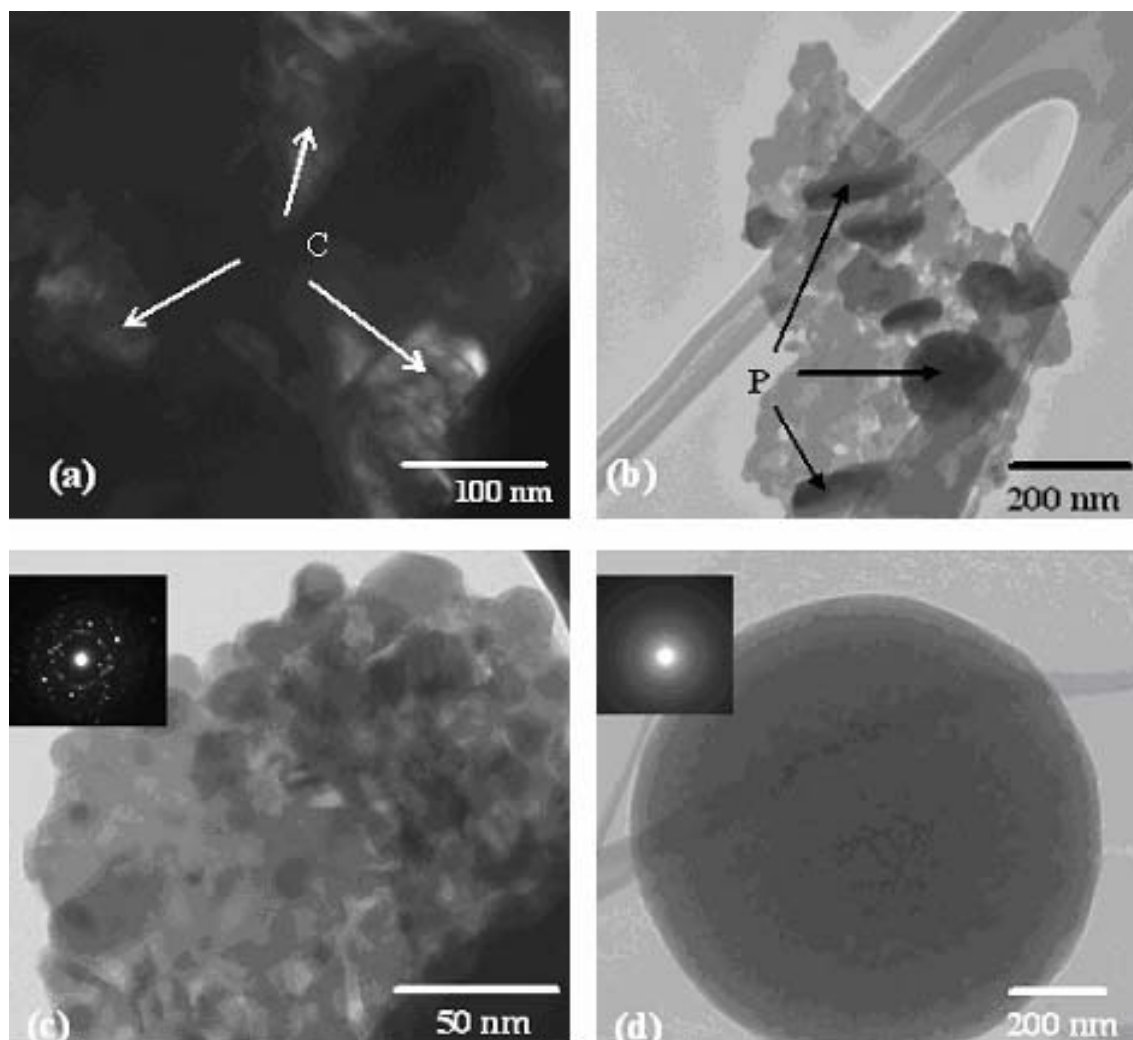


Fig. 5.7. TEM images of nanocrystalline PbO and PbO-C nanocomposites: (a) centered dark-field image of pure PbO, where individual crystallites are marked as C; (b) bright-field image of 97PbO/3C, with large PbO particles marked as P; (c) and (d) bright field images and selected area electron diffraction patterns (inset) of 90PbO/10C at different magnifications. The lead oxide particles in the carbon rich cluster in (c) are significantly smaller than those in (b). Some carbon rich clusters, such as that shown in (d), contained no lead oxide particles, as indicated by the diffuse contrast in the associated SAED pattern.

Laser Raman Spectroscopy gives information about the vibration of atoms in crystals and molecules and can be used as a complementary tool to XRD. Figure 5.8 presents Raman spectra of PbO-carbon nanocomposites obtained with 632.8 nm diode laser excitation on a 300 lines/mm grating at room temperature. The Raman spectrum of 97PbO/3C nanocomposite (Fig. 5.8(a)) displays two main peaks over 1000 cm^{-1} at around 1355 cm^{-1} and 1597 cm^{-1} , which are designated as the D band and the G band [Yoshikawa et al., 1988] of disordered carbon, and another three peaks under 500 cm^{-1} which are due to α/β -PbO (143 cm^{-1}) and β -PbO (285 cm^{-1} and 387 cm^{-1}) [Wiechert et al., 2005]. This confirms that this kind of nanocomposite contains both PbO and disordered carbon (produced from spray pyrolysis of sugar). It also shows that the Raman intensity of disordered carbon increased with an increased percentage of sugar in the $\text{Pb}(\text{NO}_3)_2/\text{sugar}$ raw material (see Raman spectra of PbO-C nanocomposites from (a) 97PbO/3C; (b) 91PbO/9C; and (c) 90PbO/10C; as well as (d) disordered carbon produced from sugar, respectively, in Fig. 5.8). This indicates the increase of disordered carbon in the PbO-C nanocomposites. This result is in good agreement with results obtained by both the XRD and TGA methods. Energy Dispersive X-ray (EDX) mapping of different elements (C and Pb) was conducted to investigate the distribution of the species within the agglomerated particles (Fig. 5.9). The bright spots correspond to the presence of each element. Based on the EDX elemental maps of PbO-C nanocomposites from 90PbO/10C (left) and 97PbO/3C (right), respectively, in Figure 5.9, distribution of carbon in the PbO-carbon nanocomposites is, within the limits of SEM-EDS resolution, apparently homogeneous, regardless of the carbon content in the samples. This indicates that a uniform distribution of carbon on all PbO particles can be achieved by spray pyrolyzing a sugar solution.

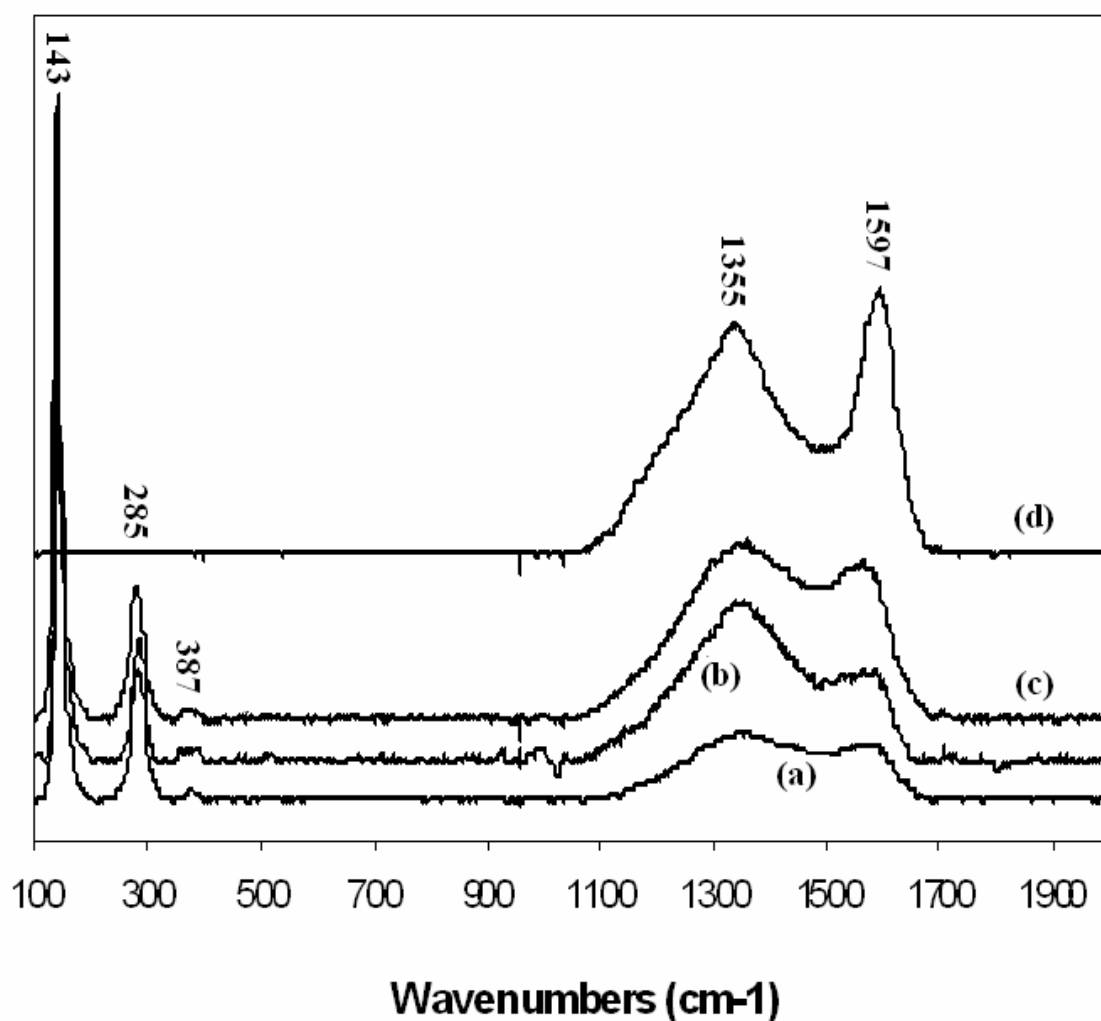


Fig. 5.8. Raman spectra of PbO-C nanocomposites from (a) 97PbO/3C, (b) 91PbO/9C, and (c) 90PbO/10C; and (d) pure disordered carbon produced from sugar.

5.4 Electrochemical Performance

The anode was prepared by mixing PbO, PbO-carbon composites or spray pyrolyzed carbon as active materials with 10 wt.% carbon black and 10 wt.% polyvinylidene fluoride (PVDF) binder.

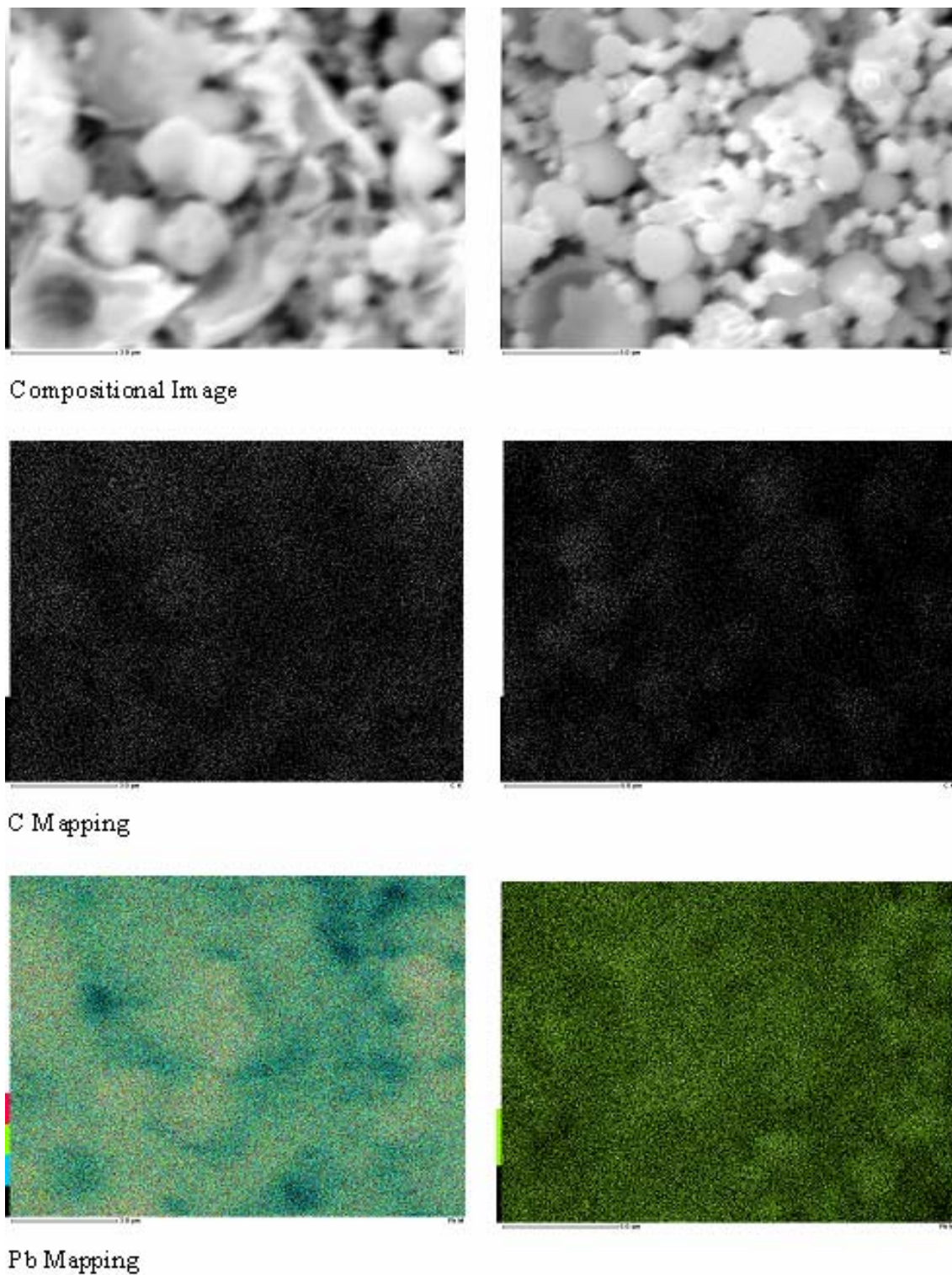


Fig. 5.9. EDX mapping of PbO-C nanocomposites made from 90PbO/10C (left) and 97PbO/3C (right).

Cyclic voltammograms (CVs) of nanocrystalline PbO (Fig. 5.10(a)) and 90PbO/10C (Fig. 5.10(b)) nanocomposite electrodes in lithium-ion coin cells, in which a lithium foil was used as the counter electrode and reference electrode, are shown in Figure 5.10. The coin cells were cycled at a scan rate of 0.1 mV s^{-1} . The CV curves for both the nanocrystalline PbO and for the electrodes with 10 wt.% carbon clearly indicate the irreversible reactions during the first discharge with two reduction peaks; one between 1.45 V and 0.9 V, and another at 0.7 V. The peak between 1.45 V and 0.9 V can be assigned to the replacement reaction converting PbO to Pb with the formation of Li_2O .

According to Martos et al. [2001 and 2003], this transformation of $\text{Pb (II)} \rightarrow \text{Pb (0)}$ takes place through some intermediates, i.e. Pb (I) . Meanwhile, the reduction peak at 0.7 V can be ascribed to the formation of the solid electrolyte interface (SEI) layers, which only happens in the first discharge cycle [Pan et al., 2002; Wang et al., 2003; Naoi et al., 2005]. The low potential region ($< 0.7 \text{ V}$) exhibits several peaks corresponding to the formation of Li_xPb alloys. Huggins [1989 and 1998] identified four potential plateaus at 0.601, 0.449, 0.374, and 0.292 V over the composition range $0 < x < 4.5$ (i.e. LiPb , $\text{Li}_{3.0}\text{Pb}$, $\text{Li}_{3.2}\text{Pb}$, and $\text{Li}_{4.5}\text{Pb}$). In the first discharge for both the nanocrystalline PbO and 90PbO/10C nanocomposite electrodes, three cathodic peaks were found at 0.50, 0.38 (weak), and 0.28 V, which are slightly different from the values reported by Huggins [1989 and 1998]. Subsequent charging and discharging of both the nanocrystalline PbO and 90PbO/10C nanocomposite electrodes show that the potential peaks of the anodic and cathodic waves correspond better to the lithium-lead alloys formed according to Huggins [1989 and 1998].

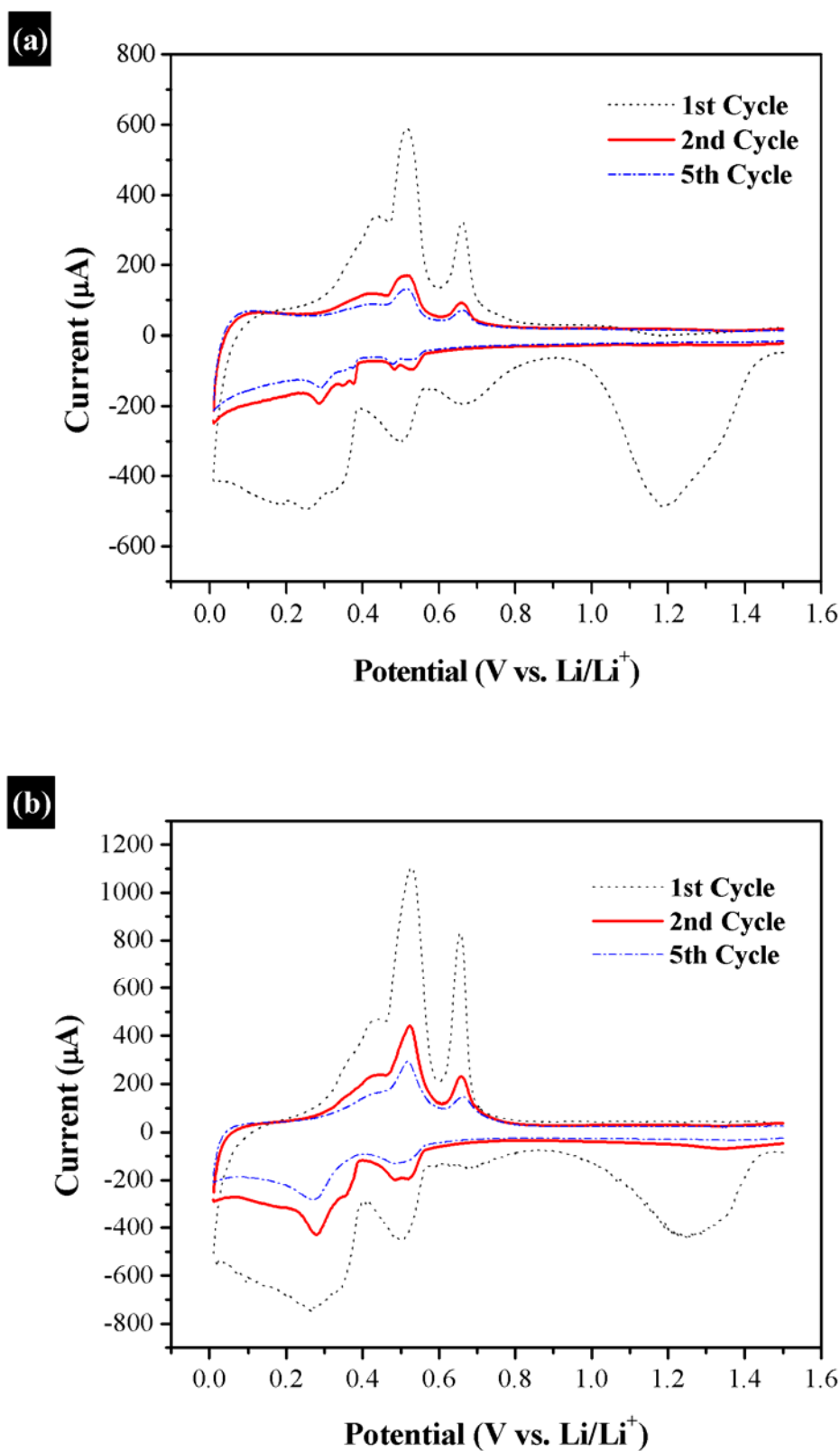


Fig. 5.10. CVs of (a) pure nanocrystalline PbO and (b) 90PbO/10C nanocomposite. The scan rate was 0.1 mV s^{-1} .

A large volume change occurs in the Pb region during lithium insertion and extraction reactions. Consequently, the mechanical stress and aggregation of particles leads to the cracking and crumbling of the electrodes. As a result, electrical contacts between particles are lost, which causes a sharp decrease in the specific capacity and cycle life of the electrodes. The specific capacity and cycling stability of the nanocrystalline PbO and PbO-carbon nanocomposite electrodes were measured by constant current charging/discharging at 0.1 mA cm^{-2} between 0.01 V and 1.50 V.

Figure 5.11 shows the 1st, 2nd, 5th, and 10th charge/discharge curves of the nanocrystalline PbO (Fig. 5.11(a)) and 90PbO/10C (Fig. 5.11(b)) nanocomposite electrodes. The discharge curves of nanocrystalline PbO and 90PbO/10C nanocomposite are fairly similar in appearance. In addition, irreversible capacity losses during the first cycle were 611 and 405 mAh g⁻¹ for pure PbO and 90PbO/10C nanocomposite, respectively. The irreversible capacity loss decreased with increased carbon content, due to the presence of the carbon matrix, which is a good electronic conductor and provides an effective cushion for volume expansion [Yoshio et al., 2002; Bewlay et al., 2004; Yuan et al., 2005]. Furthermore, the reversibility of the 90PbO/10C nanocomposite electrodes was better than that of the nanocrystalline PbO electrodes, as indicated by the retention of the potential plateaus after 10 cycles.

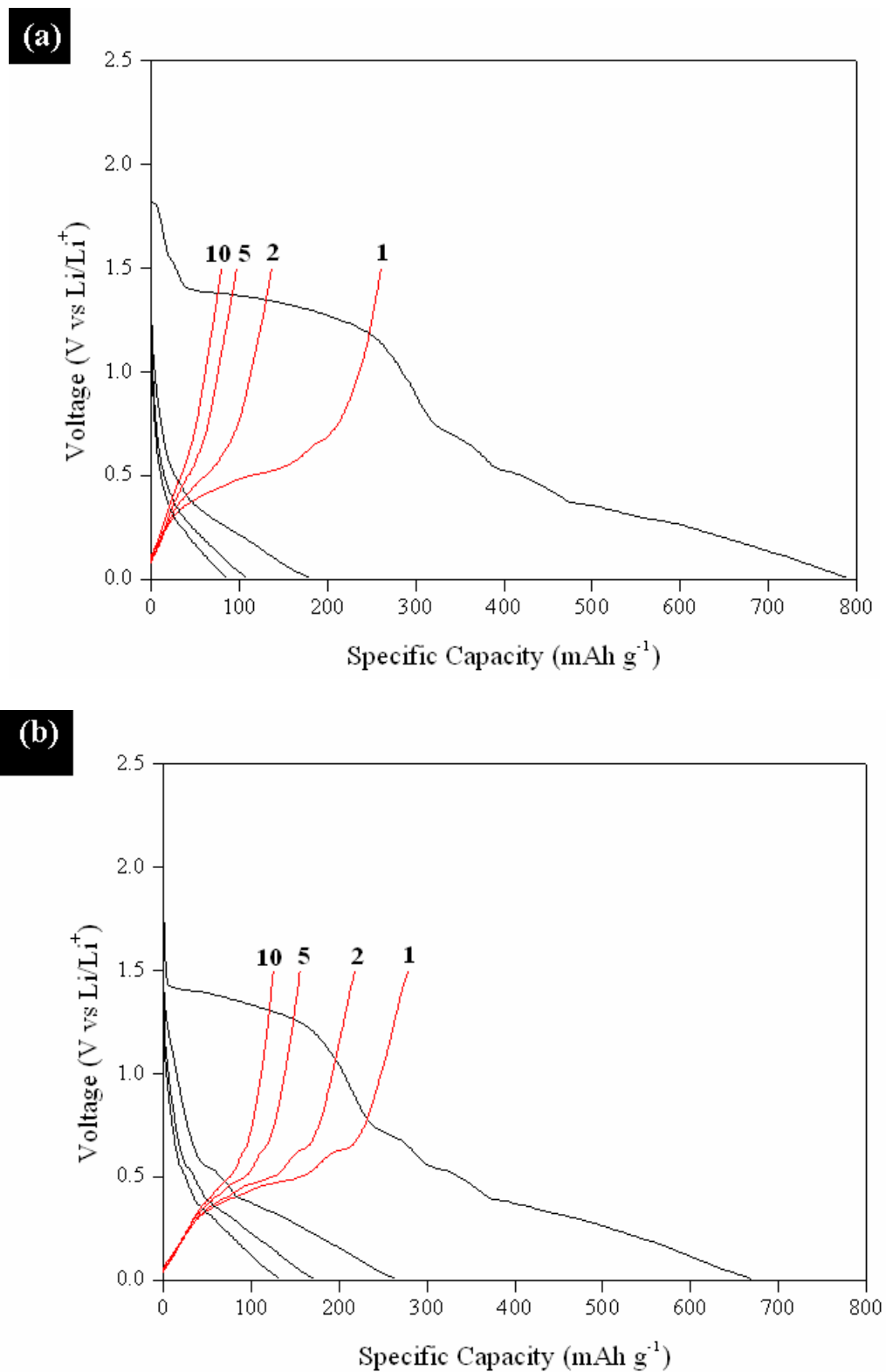


Fig. 5.11. The 1st, 2nd, 5th and 10th charge/discharge profiles of (a) pure nanocrystalline PbO and (b) 90PbO/10C nanocomposite. The current density was 0.1 mA cm⁻².

In Figure 5.12, some typical discharge capacity dependencies for materials obtained under different conditions are given. We could not find a simple dependence between the irreversible capacity or cycle life and the specific surface area or average crystal size. As a general trend, materials with crystal sizes around 100-120 nm exhibit better cycle life, when compared to the powders with small crystal size. However, it is worth remembering that the cycle life and capacity depend on many other factors, including preparation conditions, and complementary detailed experiments are needed before making any definitive conclusions regarding the role and dependency of all these parameters. The best performing powder was the PbO sprayed at 800 °C from a 0.5 M solution at a flow rate of 3.14 mL min⁻¹. It had a discharge capacity of 61 mAh g⁻¹ after 50 cycles. This result is much better than those produced by Martos et al. [2001], where the PbO powders gave a discharge capacity of less than 20 mAh g⁻¹ beyond 30 cycles.

The reversible capacities as a function of cycle number for the PbO-carbon nanocomposites are compared in Figure 5.13. Initial reversible capacity is as high as 265 mAh g⁻¹ for the 90PbO/10C nanocomposite electrodes. Subsequently, the reversible capacity was maintained above 100 mAh g⁻¹ beyond 50 cycles for the 90PbO/10C nanocomposite electrodes, which is higher than the values reported by Martos et al. [2001] for lead oxide powder anodes in lithium-ion rechargeable batteries. This shows that PbO-carbon nanocomposites are promising as anode materials for Li-ion batteries. Meanwhile, the spray pyrolyzed carbon powder (from sucrose solution) was found to have a capacity of 170 mAh g⁻¹ after 50 cycles, as shown in the inset of Figure 5.13.

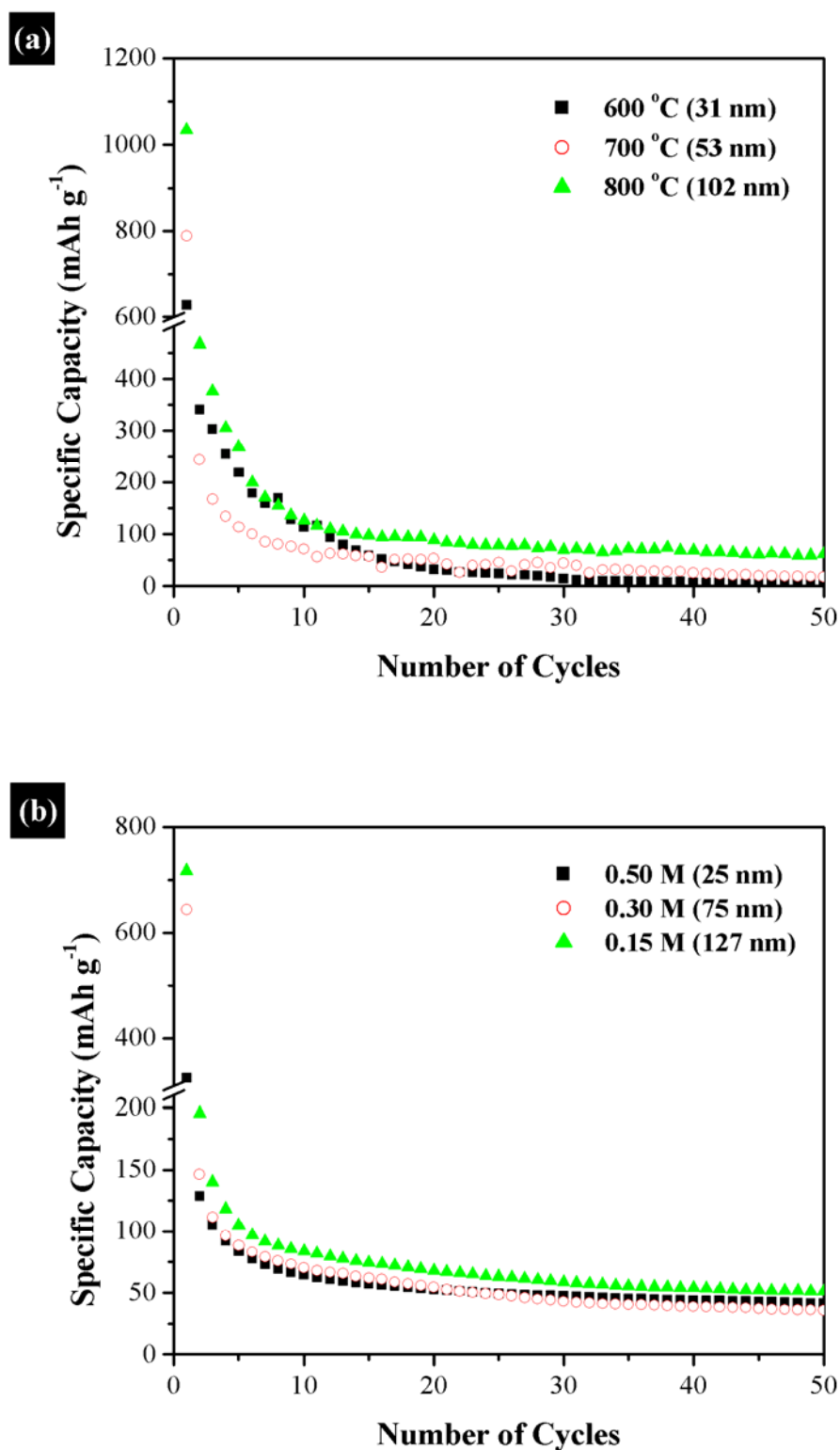


Fig. 5.12. Discharge capacity dependencies of PbO materials sprayed at (a) different temperatures at 0.5 M and 3.14 mL min^{-1} , and at (b) different solution concentrations at 700°C and 1.57 mL min^{-1} . The current density applied was 0.1 mA cm^{-2} .

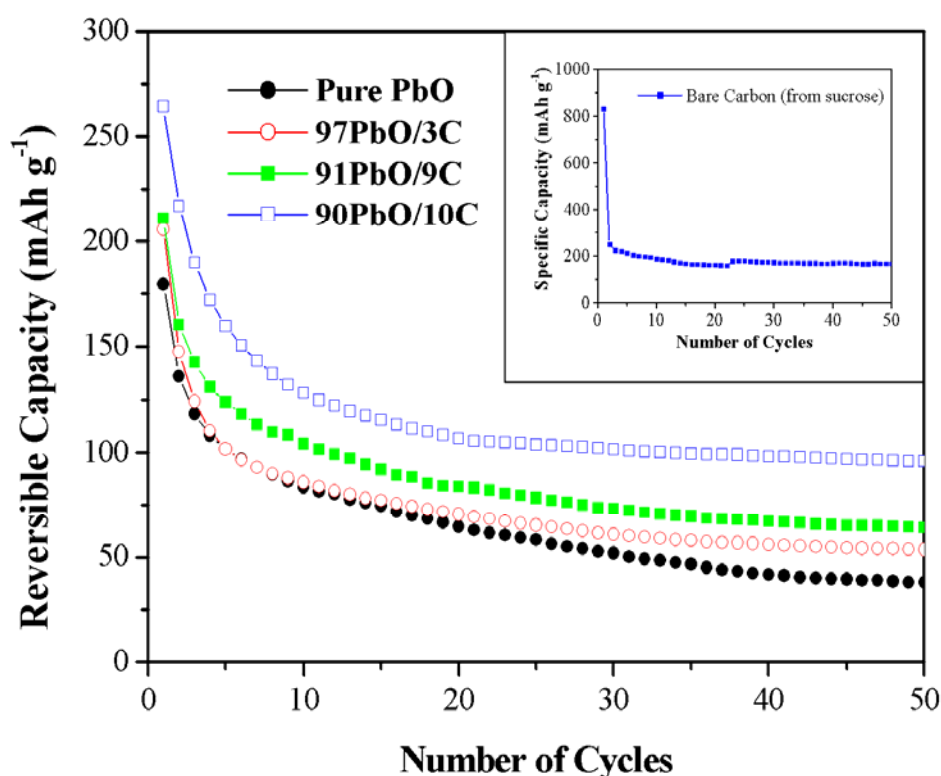


Fig. 5.13. Cycle life of PbO-C nanocomposites. The current density was 0.1 mA cm^{-2} . The inset figure presents the specific capacity vs. cycle number data for the bare carbon powder, and the current density applied was also 0.1 mA cm^{-2} .

This means that the spray-pyrolyzed carbon in the composite materials, which is considered as an active material in this study, contributed only 17 mAh g^{-1} for the 90PbO/10C nanocomposite, accounting for 17 % of its total reversible capacity (100 mAh g^{-1}). In addition, we also found that the cycle life increased with increasing carbon content in the nanocomposites. For example, the reversible capacity efficiency ($R_{\text{cycle number}}/R_{\text{1st cycle}}$) for 90PbO/10C nanocomposite electrodes after 50 cycles is 36.3 % compared to 21.1 % for nanocrystalline PbO electrodes.

We believe that the nanostructure of the spray pyrolyzed powder, and the conductivity and ductility of the carbon matrix are responsible for the good cyclability of the PbO-carbon nanocomposites. To verify the effect of carbon content on the electronic conductivity of the nanocomposites, ac impedance measurements were conducted. The Nyquist plots obtained for the nanocrystalline PbO (Fig. 5.14(a)) and 90PbO/10C (Fig. 5.14(b)) nanocomposite electrodes after 1 and 101 cycles are compared in Figure 5.14. The thickness of the electrodes was controlled at 50 μm , and the coated area of the electrodes at 1 cm^2 . To maintain uniformity, electrochemical impedance spectroscopy (EIS) experiments were performed on working electrodes in the fully charged state.

In general, one semicircle in the high frequency range was observed for all samples. The diameter of the semicircle represents the inter-particle contact resistance [Fan and Fedkiw, 1998]. Meanwhile, in the low frequency region, an angled straight line was obtained, which represents a diffusion-controlled process in the solid electrolyte interface [Li et al., 1999b]. In addition, we also found that the diameters of the semicircles were enlarged after 101 cycles for all the samples. However, when Figure 5.14(a) is compared to Figure 5.14(b), considerable differences are observed. The diameter of the semicircle after 101 cycles increased by more than 40000 ohms cm^{-1} in the case of nanocrystalline PbO electrodes, compared to 6000 ohms cm^{-1} for 90PbO/10C nanocomposite electrodes. Therefore, it can be assumed that the inter-particle resistance was suppressed with the addition of carbon, resulting in better cycling of the cells during the charge/discharge process [Fan and Fedkiw, 1998].

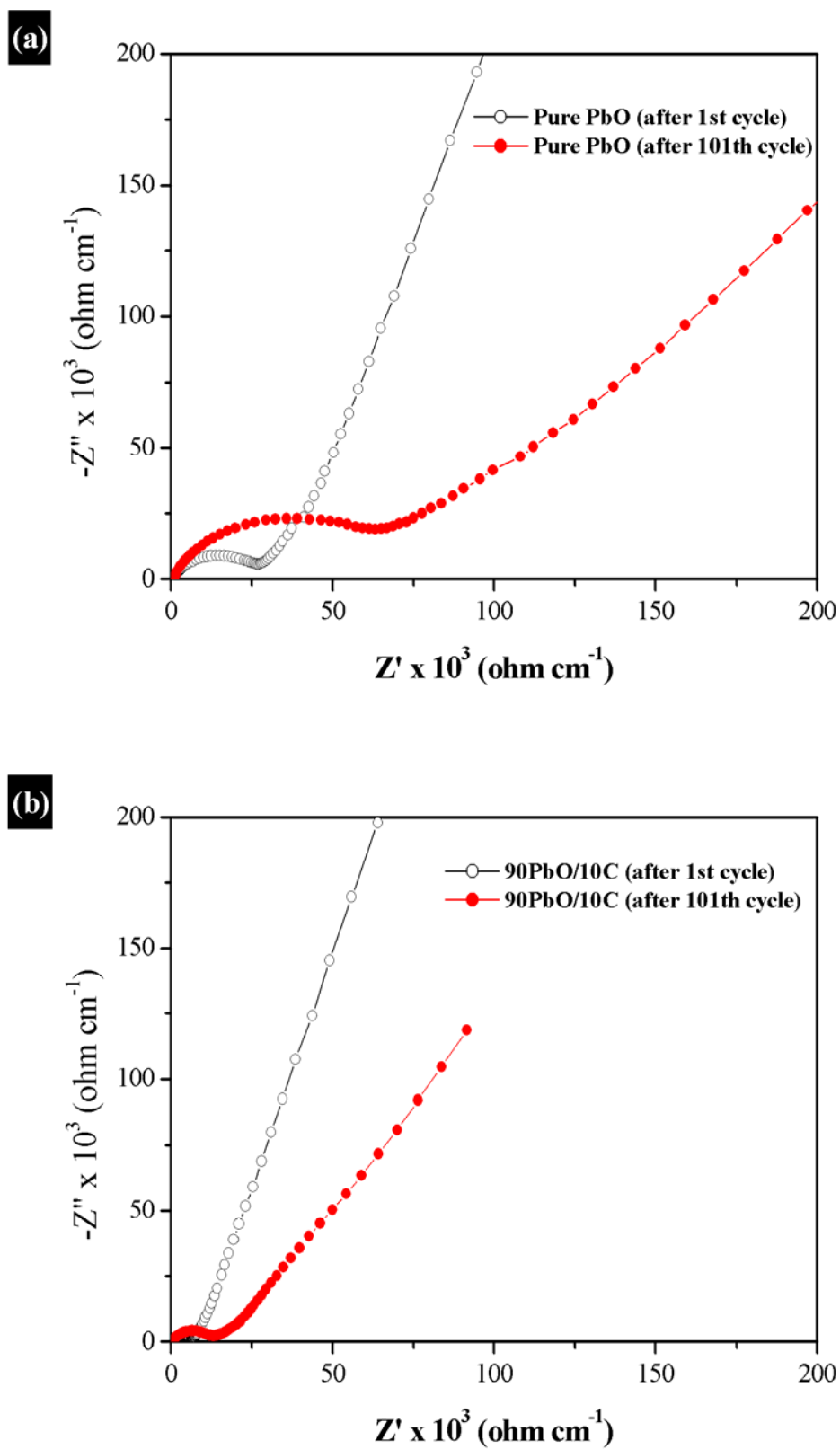


Fig. 5.14. Impedance plots for (a) pure PbO and (b) 90PbO/10C electrodes in the de-lithiated state.

5.5 Conclusions

A series of nanocrystalline PbO and PbO-carbon nanocomposites have been successfully synthesized via in-situ spray pyrolysis of $\text{Pb}(\text{NO}_3)_2$ /sugar solution at 800 °C and a flow rate of 3.14 mL min⁻¹. The spray-pyrolyzed powders are fine nanocrystalline PbO, homogeneously distributed within an amorphous carbon matrix with highly developed surface area. An increase of the furnace temperature from 600 to 800 °C leads to a three fold increase of the average crystal size from 31 to 102 nm. An increase in the concentration from 0.15 to 0.5 M dramatically suppresses the crystal size from 127 to 25 nm. The BET surface area of the sprayed PbO powders was increased up to 6.6 m² g⁻¹. Both the XRD patterns and TEM images revealed that the PbO-carbon nanocomposite crystal sizes were approximately 26-102 nm. The carbon content estimated by TGA shows that a huge amount of carbon mass (> 80 wt.%) was lost during the spray pyrolysis process. Raman spectroscopy also revealed increases in the amount of disordered carbon (from the pyrolyzed sugar solution) with increasing sugar content in the starting solution. The distribution of carbon in the sprayed samples was homogeneous, as revealed by the elemental EDX mapping. The alloying and de-alloying of lithium with lead over the 1.50 V to 0.01 V range yields various Li_xPb ($x < 4.5$) alloys. When applied as anode materials in Li-ion batteries, the PbO sprayed materials retain a reversible capacity above 60 mAh g⁻¹ beyond 50 cycles. The PbO-carbon nanocomposites showed an improved cycle life as the carbon content increased. We strongly believed that the presence of the carbon matrix, which is a good electric conductor, provides an effective cushion to absorb volume change during the alloying and de-alloying processes within the lead region.

CHAPTER 6

CARBON-COATED SILICON NANOCOMPOSITES AS HIGH-CAPACITY LI-ION BATTERY ANODES

6.1 Introduction

Lithium-ion batteries are now the most widely used secondary battery systems for portable electronic devices. Compared to conventional aqueous rechargeable batteries, such as nickel-cadmium and nickel metal hydride, lithium-ion batteries have higher energy density, higher operating voltages, lower self-discharge, and lower maintenance requirements [Tarascon and Armand, 2001]. These properties have made Li-ion batteries the highest performing secondary battery chemistry available. However, due to the rapid advances and highly competitive nature of the portable devices industry, a further increase in the mass capacities (Wh kg^{-1}) and energy densities (Wh L^{-1}) of the Li-ion rechargeable batteries is being vigorously pursued.

Graphite materials are currently used as anode materials for rechargeable lithium-ion batteries, in which lithium ions intercalate in and out reversibly. Graphite materials provide high electronic conductivity, and low electrochemical potential with respect to lithium metal. Yet these superb properties can hardly meet the demand for high energy

density from current electronic devices; research on alternative anodes is therefore focused on materials with higher lithium storage capacities. Among the candidates, metals that alloy with lithium are promising alternative anode materials due to their high specific capacities, e.g. Si (4200 mAh g^{-1}) [Weydanz et al., 1999] and Sn (994 mAh g^{-1}) [Idota et al., 1997], as compared to graphite, which gives a theoretical capacity of 372 mAh g^{-1} [Winter et al., 1998].

However, a general disadvantage is the large volume expansion/contraction [Lee et al., 2001] during the alloying/de-alloying of lithium, resulting in the formation of cracks, followed by pulverization of the active mass particles and permanent capacity loss. Studies of the Li-Si binary system [Sharma and Seefurth, 1976; Boukamp et al., 1981] have indicated that each silicon atom can accommodate up to 4.4 lithium atoms, leading to the formation of $\text{Li}_{22}\text{Si}_5$ alloy, which is accompanied by a volume expansion of 400 %. This huge volume change would give rise to the disintegration of the electrode and loss of electronic contact between the Si particles.

To overcome the large volume change and thus obtain better capacity retention and cycle life for Si anodes, various approaches have been used. Among them, the most promising approach is to create a nanocomposite structure in which nanosized Si particles are homogeneously dispersed in a ductile and active matrix [Kim et al., 1999; Roberts et al., 2002; Beaulieu et al., 2003; Wu et al., 2003; Asao et al., 2004]. A relatively low mass, good electronic conductivity, reasonable Li-insertion capability, and small volume expansion coupled with softness and compliance makes carbon the best active matrix [Kurita and Endo, 2002; Ng et al., 2006a].

Various methods have been employed for preparing Si-carbon (Si-C) composite anodes. Based on their preparation methods, they can be mainly classified into five categories: i.e. pyrolysis [Wilson et al., 1994] or chemical/thermal vapor deposition [Holzapfel et al., 2005a], ball milling [Wang et al., 1998] or mechanical milling [Liu et al., 2004], combination of pyrolysis and mechanical milling [Guo et al., 2005], chemical reaction of gels [Hasegawa et al., 2004], and other methods, such as dehydration of a carbon precursor [Yang et al., 2005a]. Although all these methods provide better cycling performance for the Si-C composite anodes compared to that of pure Si anodes, capacity fading has still been unavoidable. The most probable reason for this phenomenon is the lack of a homogeneous carbon-coating layer on the surface of the Si nanoparticles and, if possible, on each individual Si nanoparticle [Kasavajjula et al., 2007]. This will increase the chances of having electrical contact to the Si nanoparticles, even if they have been subjected to crystal degradation (upon prolonged cycling). For simple admixture of carbon with Si nanoparticles, this would be less probable, but if one always has some carbon on the surface of the Si nanoparticles, the electrical contact could be maintained, even if the Si crystal lattice breaks up.

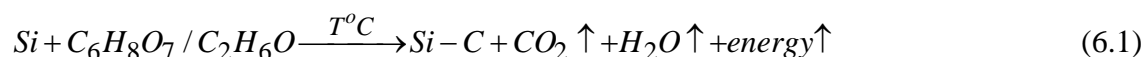
Herein, I report in detail on the effects of the spray pyrolysis processing temperature and the precursor solution (nano Si/citric acid in ethanol) concentration on the amorphous carbon content, the thickness of the carbon-coating layer, and the homogeneity of the carbon-coating. The influence of these parameters on the electrochemical performance of carbon-coated Si nanocomposites as high capacity anode materials for Li-ion batteries will also be studied and compared accordingly.

6.2 Effect of Spray Pyrolysis Processing Temperature

6.2.1 Synthesis Method

Citric acid ($C_6H_8O_7$) was dissolved in 200 mL of absolute ethanol under continuous stirring. Subsequently, nanocrystalline Si powder (< 100 nm) was mixed into the initial citric acid/ethanol solution in the weight ratio (Si : citric acid) of 1:10, via ultrasonication for 90 mins. Three types of nanocomposite materials were prepared in-situ via spraying of the Si/citric acid/ethanol suspensions at 300 °C, 400 °C, and 500 °C, in air, using a flow rate of 4 mL min⁻¹ in a vertical type spray pyrolysis reactor.

In this instance, citric acid was chosen as the carbon source, due to its low decomposition temperature (175 °C) and low oxygen content. Meanwhile, ethanol acts not only as an efficient solvent, but also as a reducing agent to protect the nanocrystalline Si particles from oxidation during the spray pyrolysis process. The spray-pyrolysis reaction of Si in citric acid/ethanol solution can be expressed as (Eq. 6.1):



The term “energy” in (Eq. 6.1) refers to the energy released during the decomposition of the citric acid/ethanol solution into carbon and water vapor. This energy is released to the atmosphere, as the decomposition process is an exothermic reaction.

6.2.2 Physical and Structural Characterizations

For quantifying the amount of amorphous carbon in the carbon-coated Si nanocomposite materials, thermogravimetric analysis (TGA) was carried out in air. The samples were heated from 50 °C to 700 °C at a rate of 5 °C min⁻¹. Figure 6.1 shows the TGA curves of the carbon-coated Si nanocomposite samples along with those of nanocrystalline Si powders and amorphous carbon spray-pyrolyzed in air at 400 °C.

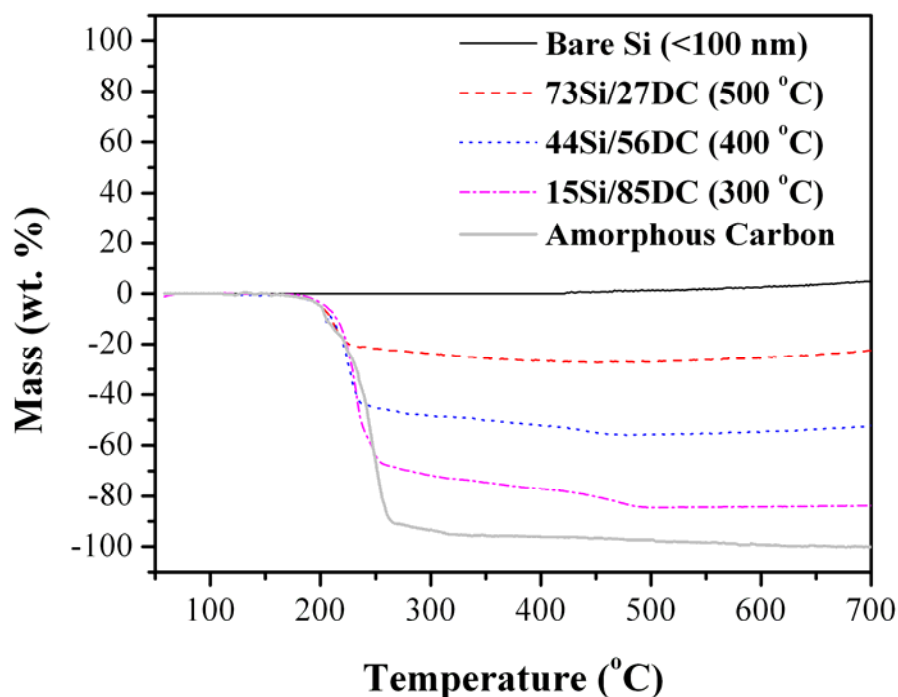


Fig. 6.1. Thermogravimetric analysis (TGA) curves of nanocrystalline Si precursor powder; carbon-coated Si nanocomposites spray-pyrolyzed in air at 500 °C, 400 °C, and 300 °C; and amorphous carbon spray-pyrolyzed from citric acid at 400 °C in air. The ratio Si/DC refers to the ratio of the amount of silicon by weight to the amount of disordered carbon in the spray-pyrolyzed nanocomposites, as estimated from the TGA curves.

As can be seen from Figure 6.1, nanocrystalline Si powder starts to oxidize slowly in air at temperatures above 500 °C, with rapid oxidation above 600 °C. Meanwhile, the carbon-coated Si nanocomposite materials show rapid mass loss between 150 and 480 °C. As the nanocrystalline Si powder remains stable in this temperature range, any weight change corresponds to the oxidation of amorphous carbon. Therefore, the change in weight before and after the oxidation of carbon directly translates into the amount of amorphous carbon in the carbon-coated Si nanocomposites. Using this method, it was estimated that the amount of pyrolyzed carbon in the composites was 84.6 wt.%, 56.0 wt.%, and 27.4 wt.% for the precursor solutions with weight ratios (Si : citric acid) of 1:10, spray-pyrolyzed in air at 300 °C, 400 °C, and 500 °C, respectively.

Table 6.1 summarizes the estimated carbon content in the spray-pyrolyzed carbon-coated Si nanocomposites. The carbon concentrations obtained after spray pyrolysis were below the targeted levels, except for the carbon-coated Si nanocomposite sample spray-pyrolyzed at 300 °C, which shows a higher value than the theoretical value. This might be due to the presence of impurities in the form of undecomposed citric acid in the sample. Therefore, temperatures above 300 °C are needed in order to fully decompose the citric acid during the spray pyrolysis process.

Figure 6.2 shows XRD patterns of (a) nanocrystalline Si precursor powders purchased from Nanostructured and Amorphous Materials Inc., (b)-(d) carbon-coated Si nanocomposites spray-pyrolyzed in air at different processing temperatures, and (e) spray-pyrolyzed amorphous carbon powder made from the citric acid/ethanol solution. The diffraction peak positions for all the Si-based samples (XRD patterns (a)-(d)) are

consistent with pure silicon phase (JCPDS 01-0787). No obvious peaks corresponding to bulk SiO₂ or SiC crystalline phase are observed in the diffraction patterns (b)-(d). This confirms that none of the Si-based samples spray-pyrolyzed in air were oxidized during the spray pyrolysis process. Moreover, no diffraction lines corresponding to crystalline carbon (graphite) were observed, indicating the amorphous nature of the carbon in the nanocomposites. Finally, XRD pattern (e) in Figure 6.2 shows a broad peak at ~23 °, indicating the formation of amorphous carbon phase in the spray-pyrolyzed citric acid sample.

Table 6.1: Theoretical and estimated carbon content in carbon-coated Si nanocomposites spray-pyrolyzed from a nano-Si/citric acid^a/ethanol starting solution at different processing temperatures.

Temperature (°C)	Theoretical weight % of carbon *	Estimated weight % of carbon (via TGA)	Mass loss % of carbon during spray pyrolysis **
300	78.95	84.60	- 7.16
400	78.95	55.98	29.09
500	78.95	27.44	65.24

^a C₆H₈O₇

* The calculation of “Theoretical weight % of carbon” is based on the weight ratio 1:10 for the nano-Si/citric acid solution and also on the assumption that all carbon content in the ethanol solvent is decomposed to carbon dioxide during spray pyrolysis.

** Mass loss % of carbon is calculated based on the following equation.

$$MassLoss(\%) = \frac{TheoreticalWeight(\%) - EstimatedWeight(\%)}{TheoreticalWeight(\%)} \times 100 \quad (6.2)$$

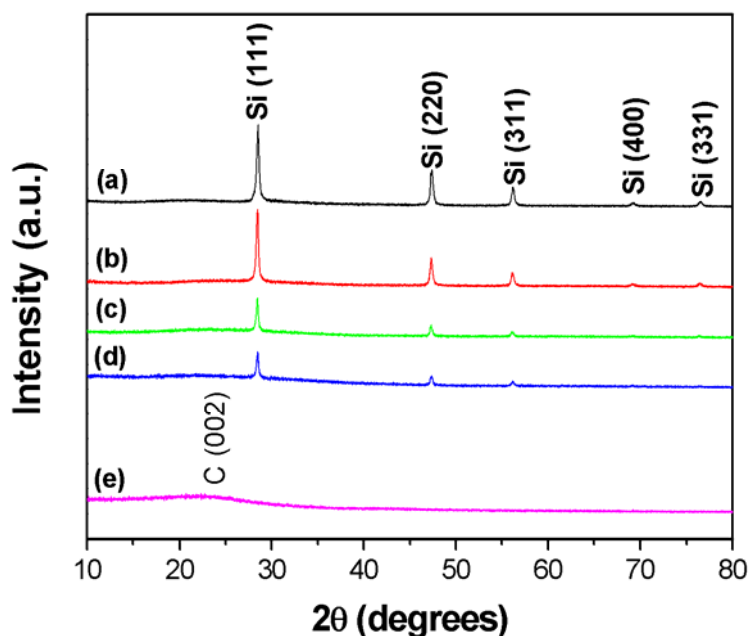


Fig. 6.2. X-ray diffraction patterns of (a) nanocrystalline Si precursor powder; carbon-coated Si nanocomposites spray-pyrolyzed in air at (b) 500 °C; (c) 400 °C; and (d) 300 °C; and (e) amorphous carbon spray-pyrolyzed from citric acid at 400 °C in air.

Scanning electron microscopy (SEM) images of the carbon-coated Si nanocomposites are shown in Figure 6.3. From SEM observations of the carbon-coated Si nanocomposites spray-pyrolyzed in air at 400 °C (Fig. 6.3(a)), it was revealed that the particles are mainly spherical agglomerates, which is typical for the spray process, with sizes in the range of 5-10 microns. In addition, it can also be observed (Fig. 6.3(b)-(d)) that the carbon-coated Si nanocomposites are well connected and homogeneously distributed. However, the presence of the carbon-coating layer increases the size of the individual particles. This is apparent in the case of carbon-coated Si nanocomposites spray-pyrolyzed in air at 300 °C (Fig. 6.3(d)), where the individual particles are heavily coated, resulting in large agglomerates. This might be due to the fact that the sample may contain partially undecomposed citric acid.

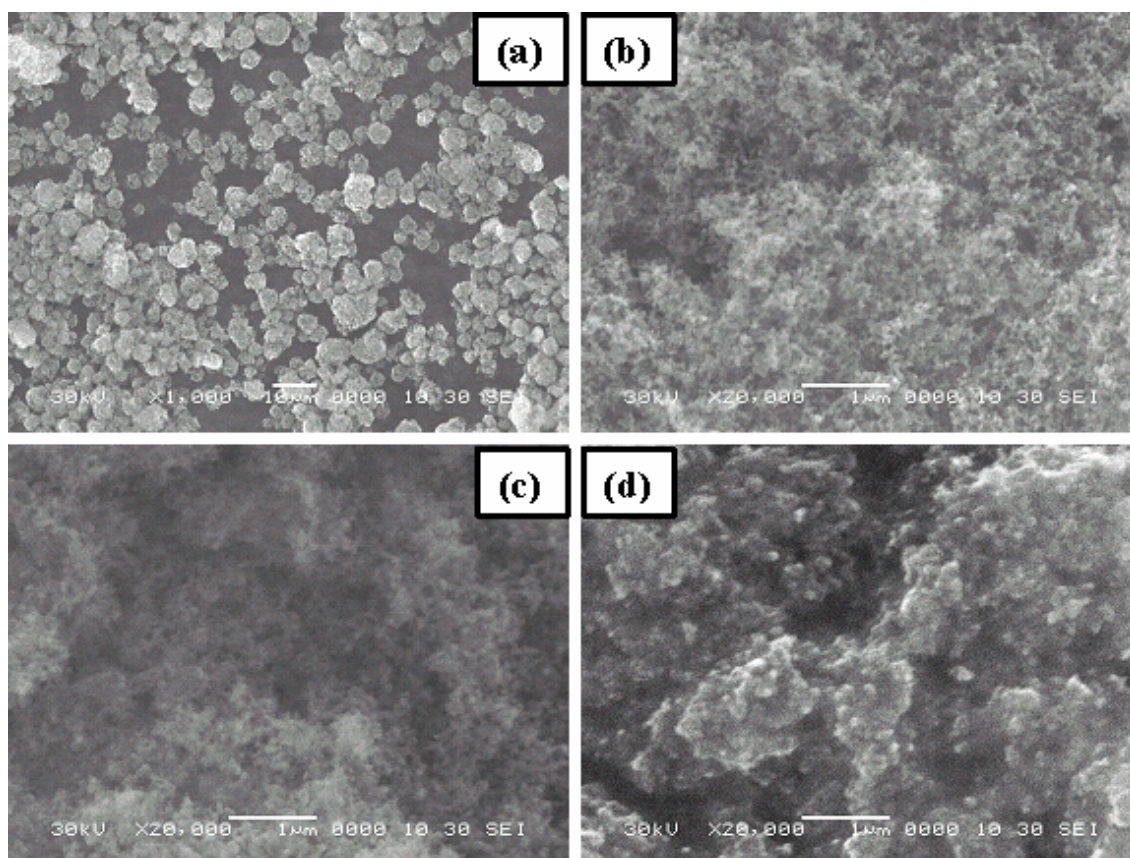


Fig. 6.3. SEM images of carbon-coated Si nanocomposites spray-pyrolyzed in air at (a) 400 °C (low-magnification image); (b) 500 °C; (c) 400 °C; and (d) 300 °C.

Figure 6.4 shows TEM images of the nanocrystalline Si particles (a) and carbon-coated Si nanocomposites (b)-(f). The size of the individual Si particles ranged from 10 nm to ~100 nm (Fig. 6.4(a)). The fine spotty rings of the associated selected area electron diffraction pattern (inset of Fig. 6.4(a)) correspond to nanocrystalline Si, although additional diffuse contrast within the diffraction rings may also indicate the presence of minor amounts of amorphous Si. The nanocrystalline Si particles were generally spheroidal in shape, although some of the larger ones were faceted. Figure 6.4(b) shows a typical image of the carbon-coated Si nanocomposites, where almost every individual Si nanoparticle is surrounded by a layer of carbon-coating.

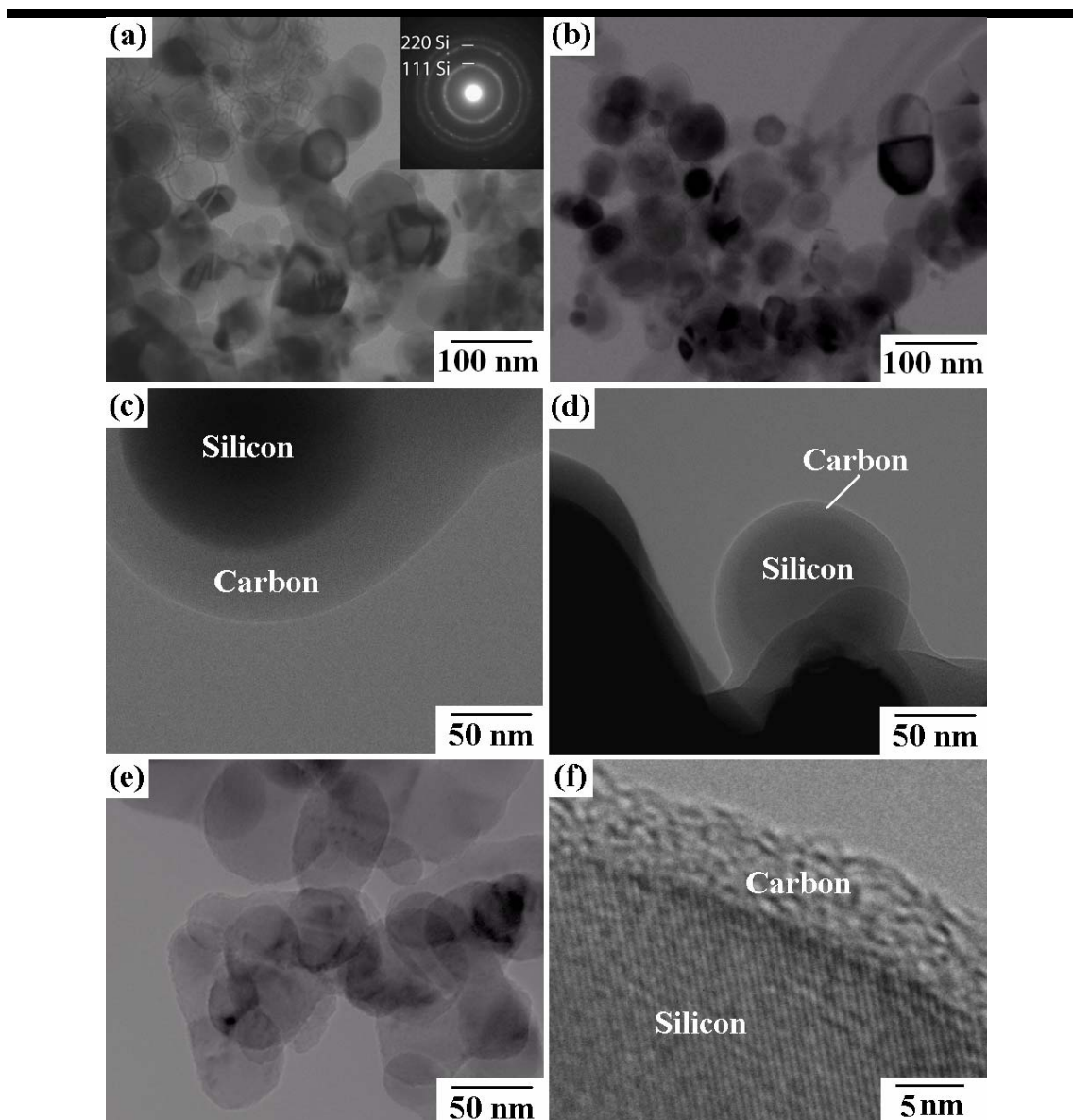


Fig. 6.4. TEM images of nanocrystalline Si and carbon-coated Si nanocomposites: (a) low-magnification image of nanocrystalline Si, with the indexed selected area diffraction pattern (inset) confirming the presence of Si particles; and (b) carbon-coated Si nanocomposite spray-pyrolyzed at 400 °C. (c), (d), and (e) are TEM images of carbon-coated Si nanocomposites spray-pyrolyzed at 300 °C, 400 °C, and 500 °C, respectively, revealing the thickness of the carbon-coating layer for each nanocomposite. (f) High-resolution image of carbon-coated Si spray-pyrolyzed at 400 °C, clearly showing the presence of an interface between the nanocrystalline Si particle and the amorphous carbon layer.

The thickness of the carbon-coating layer increases with decreasing processing temperature, i.e., the carbon-coating is thickest (~40 nm) when spray-pyrolyzed at 300 °C (Fig. 6.4(c)) and thinnest (~1 nm) when spray-pyrolyzed at 500 °C (Fig. 6.4(e)). The carbon-coating layer thickness (~10 nm) for samples spray-pyrolyzed at 400 °C (Fig. 6.4(d)) can be considered optimum, as an amorphous carbon layer homogeneously surrounds the spheroidal Si nanoparticles. The high-resolution TEM image in Figure 6.4(f) clearly demonstrates the coexistence of two phases, i.e., the crystalline Si phase and the amorphous carbon phase.

6.2.3 Electrochemical Performance

The electrochemical performance of the nanocrystalline Si and carbon-coated Si nanocomposite electrodes was systematically investigated. The anode was prepared by mixing nanocrystalline Si, carbon-coated Si nanocomposites, or spray-pyrolyzed amorphous carbon as active materials with 10 wt.% carbon black (Super P) and 10 wt.% polyvinylidene fluoride (PVDF) binder in N-methyl-2-pyrrolidinone (NMP) solvent to form a homogeneous slurry, which was then spread onto a copper foil, which serves as a current collector. The typical active mass loading of the electrodes was 2-3 mg cm⁻². The cells were galvanostatically discharged and charged in the range of 0.02-1.20 V at a constant current density of 100 mA g⁻¹. The ac impedance spectroscopy measurements were carried out by applying a sine wave of 5 mV amplitude over a frequency range of 100.00 kHz to 0.01 Hz. All impedance measurements were carried out in the fully delithiated state (state of charge).

Figure 6.5 shows the first electrochemical lithiation/de-lithiation of the nanocrystalline Si and carbon-coated Si nanocomposite electrodes. Different phenomena can be easily distinguished in these curves. At potentials from approximately 1.5 V to 0.5 V vs. Li/Li^+ , the passivation film, also known as the solid electrolyte interphase (SEI), is formed by the irreversible reduction of electrolyte on the surface of the active material, involving the formation of a lithium-ion conductive, but electrolyte-blocking, adhering layer [Holzapfel et al., 2005b].

As can be observed from Figure 6.5, the irreversible capacity contribution in this SEI formation region increased with increasing amorphous carbon content in the nanocomposite electrodes. A distinct plateau at potentials negative to 200 mV vs. Li/Li^+ can be observed, which represents the lithium alloying with the silicon active materials. Upon the following de-lithiation of the active materials, a plateau at around 300 mV vs. Li/Li^+ can be observed, which can be attributed to the lithium beginning to de-alloy from the silicon particles.

The first cycle discharge capacities were 3474 mAh g^{-1} , 3050 mAh g^{-1} , 2600 mAh g^{-1} , and 1090 mAh g^{-1} for the electrodes of nanocrystalline Si, and carbon-coated Si spray-pyrolyzed in air at 500°C , 400°C , and 300°C , respectively, with the corresponding first cycle charge capacities 2058 mAh g^{-1} , 1830 mAh g^{-1} , 1857 mAh g^{-1} , and 427 mAh g^{-1} . Therefore, the first cycle coulombic efficiencies were 59 %, 60 %, 71 %, and 39 % for the nanocrystalline Si electrode, and the carbon-coated Si electrodes spray-pyrolyzed in air at 500°C , 400°C , and 300°C , respectively.

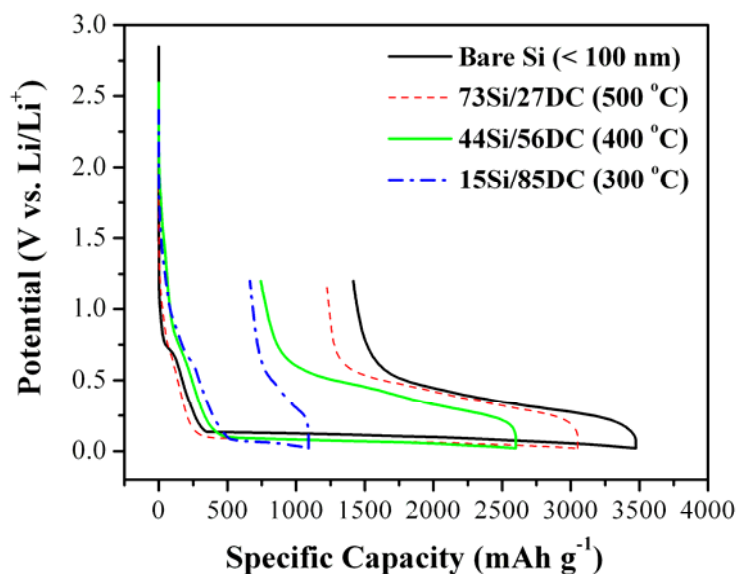


Fig. 6.5. The first discharge/charge plots of nanocrystalline Si and carbon-coated Si nanocomposite electrodes. Cycling took place between 0.02 V and 1.20 V versus Li/Li⁺ at a cycling rate of 100 mA g⁻¹.

Figure 6.6 summarizes the differential capacity data for the nanocrystalline Si and carbon-coated Si nanocomposite electrodes. The alloying/de-alloying of lithium with Si over the potential range of 1.20 V to 0.02 V vs. Li/Li⁺ yields various Li_xSi ($x < 4.4$) alloys. The first cycle differential capacity plots in Figure 6.6(a) exhibited essentially the same peak features for all the electrodes below 0.3 V vs. Li/Li⁺. However, the first cathodic peak was shifted from 0.12 V (Si) to below 0.09 V (carbon-coated Si). This is because the solid/electrolyte interphase (SEI) is different in the two cases (i.e., Si/electrolyte and carbon/electrolyte, respectively). Therefore, the surface kinetics will be different, resulting in the shifted peaks that are seen in the differential capacity curves [Liu et al., 2005a]. This has been confirmed by the peak shift in the SEI formation region, as shown in the inset of Figure 6.6(a). The above-mentioned results clearly demonstrate the presence of an amorphous carbon-coating layer.

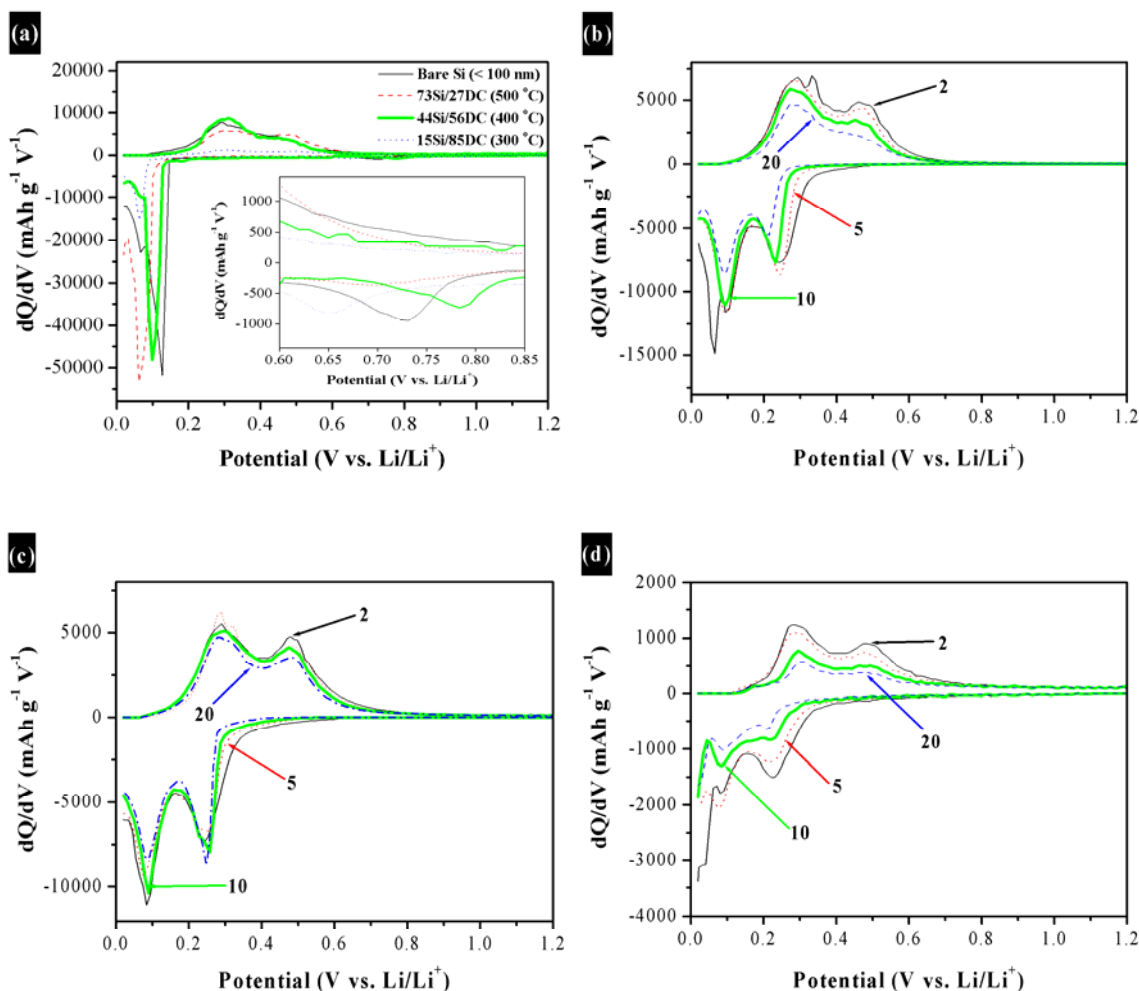


Fig. 6.6. (a) First cycle differential capacity plots of nanocrystalline Si and carbon-coated Si nanocomposite electrodes (inset: enlarged plot of (a)). (b), (c), and (d) are differential capacity plots for carbon-coated Si nanocomposites spray-pyrolyzed at 500 °C, 400 °C, and 300 °C, respectively, with the numbers indicating the cycle number. Cycling took place between 0.02 V and 1.20 V versus Li/Li^+ at a cycling rate of 100 mA g^{-1} .

The 2nd, 5th, 10th, and 20th cycle differential capacity plots for the carbon-coated Si nanocomposite electrodes are shown in Figure 6.6(b)-(d). It can be seen that the electrode composed of carbon-coated Si nanocomposite spray-pyrolyzed in air at 400 °C (Fig. 6.6(c)) maintained high activity and reversibility, even after 20 cycles, whereas the electrodes composed of carbon-coated Si nanocomposites spray-pyrolyzed in air at 500 °C (Fig. 6.6(b)) and 300 °C (Fig. 6.6(d)) show severe capacity fading and loss of kinetics with cycling.

Figure 6.7 shows the cycling behaviour of the nanocrystalline Si and carbon-coated Si nanocomposite electrodes. The calculated capacities were solely based on the active electromaterial, i.e., Si or carbon-coated Si nanocomposite particles in the electrodes. Using a non-restricted cycling procedure, the initial reversible capacities (2nd discharge capacity) were 2247 mAh g⁻¹, 2276 mAh g⁻¹, 2045 mAh g⁻¹, and 497 mAh g⁻¹ for the electrodes composed of nanocrystalline Si and of carbon-coated Si spray-pyrolyzed in air at 500 °C, 400 °C, and 300 °C, respectively. Subsequently, the corresponding discharge capacities beyond 100 cycles were maintained at 10 mAh g⁻¹, 288 mAh g⁻¹, 1120 mAh g⁻¹, and 116 mAh g⁻¹, as did the ratios of the specific capacities retained after 100 cycles to the first discharge capacities, which are 0.3 %, 9 %, 43 %, and 11 %, respectively. These results show that the optimum carbon-coating content is slightly above 50 % by weight, as demonstrated by the nanocomposite spray-pyrolyzed in air at 400 °C.

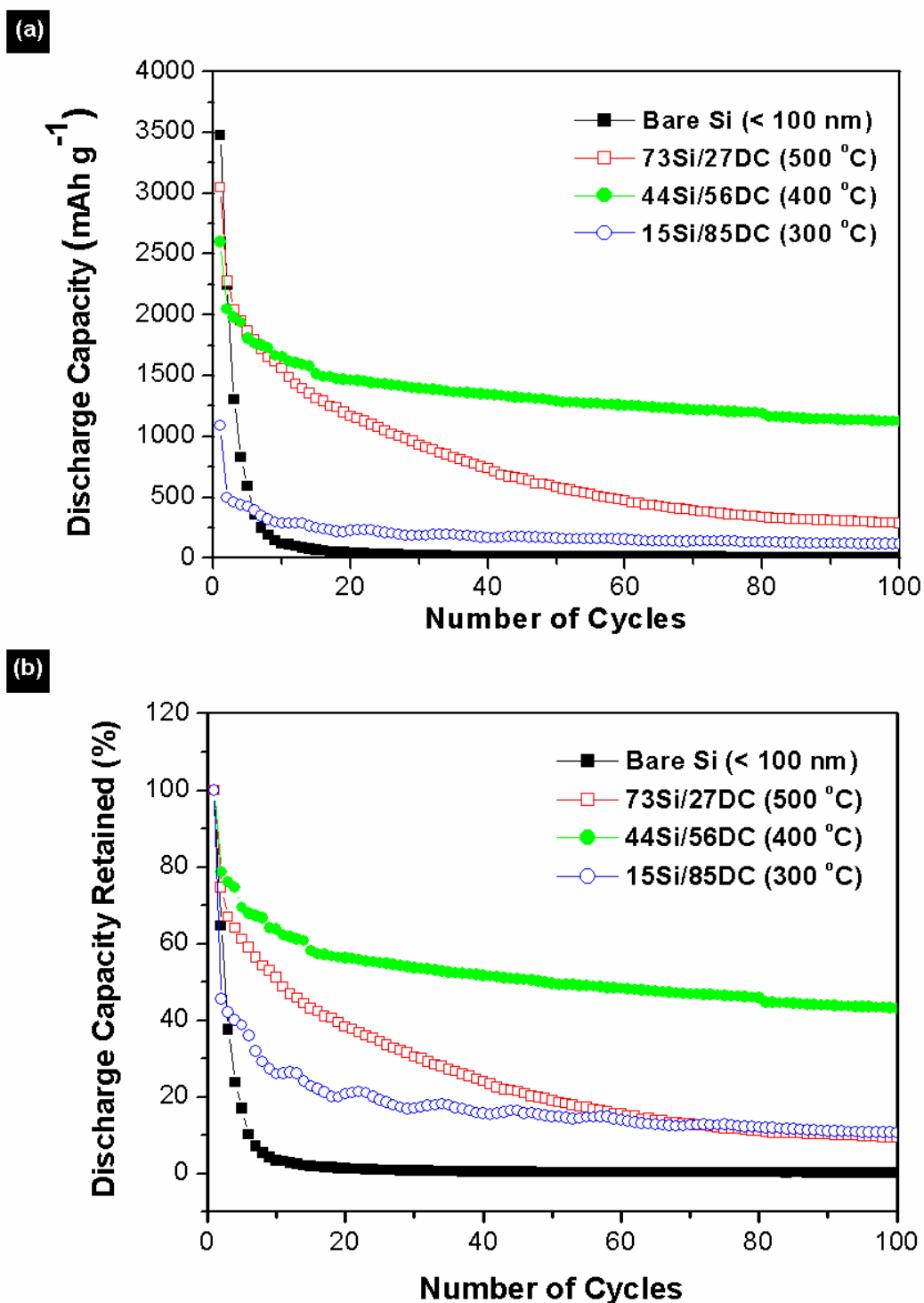


Fig. 6.7. (a) Cycle life of nanocrystalline Si and carbon-coated Si nanocomposite electrodes cycled between 0.02 V and 1.20 V versus Li/Li⁺ at a cycling rate of 100 mA g⁻¹. (b) The corresponding capacity retained with respect to the first discharge capacity in (a).

Figure 6.8 shows the cycling behaviour of the carbon-coated Si nanocomposite electrode with 44 wt% Si content and the corresponding cycling behaviour of the amorphous carbon prepared by spray pyrolysis of the citric acid/ethanol solution at 400 °C in air. The carbon-coated Si nanocomposite electrode shows a moderate capacity fading behaviour in the first 20 cycles, followed by a relatively flat and low capacity fading behaviour for the next 80 cycles. The carbon-coated Si nanocomposite electrode shows an irreversible capacity loss (Q_{irrev}) of less than 0.4 % per cycle. However, the capacity fading behaviour shown in the first 20 cycles can be attributed to the high irreversible capacity contributed by the large amorphous carbon content in the nanocomposite electrode.

This is clearly demonstrated in Figure 6.8(b), where the electrochemical lithiation/delithiation into/from amorphous carbon is illustrated. In the first cycle, the insertion capacity of the amorphous spray-pyrolyzed carbon is approximately 700 mAh g⁻¹. Since the carbon content in the carbon-coated Si electrode is 56 wt%, the insertion capacity can account to a large extent for the low coulombic efficiency of the carbon-coated Si electrode in the first cycle (see Fig. 6.8(a)). The low discharge capacity (~ 40 mAh g⁻¹) of the amorphous carbon after 100 cycles suggests that the degree of carbonization is very low. This may be due to the instantaneous nature of the spray pyrolysis process, which normally takes only a few minutes to produce the spray-pyrolyzed powder [Ng et al., 2006a].

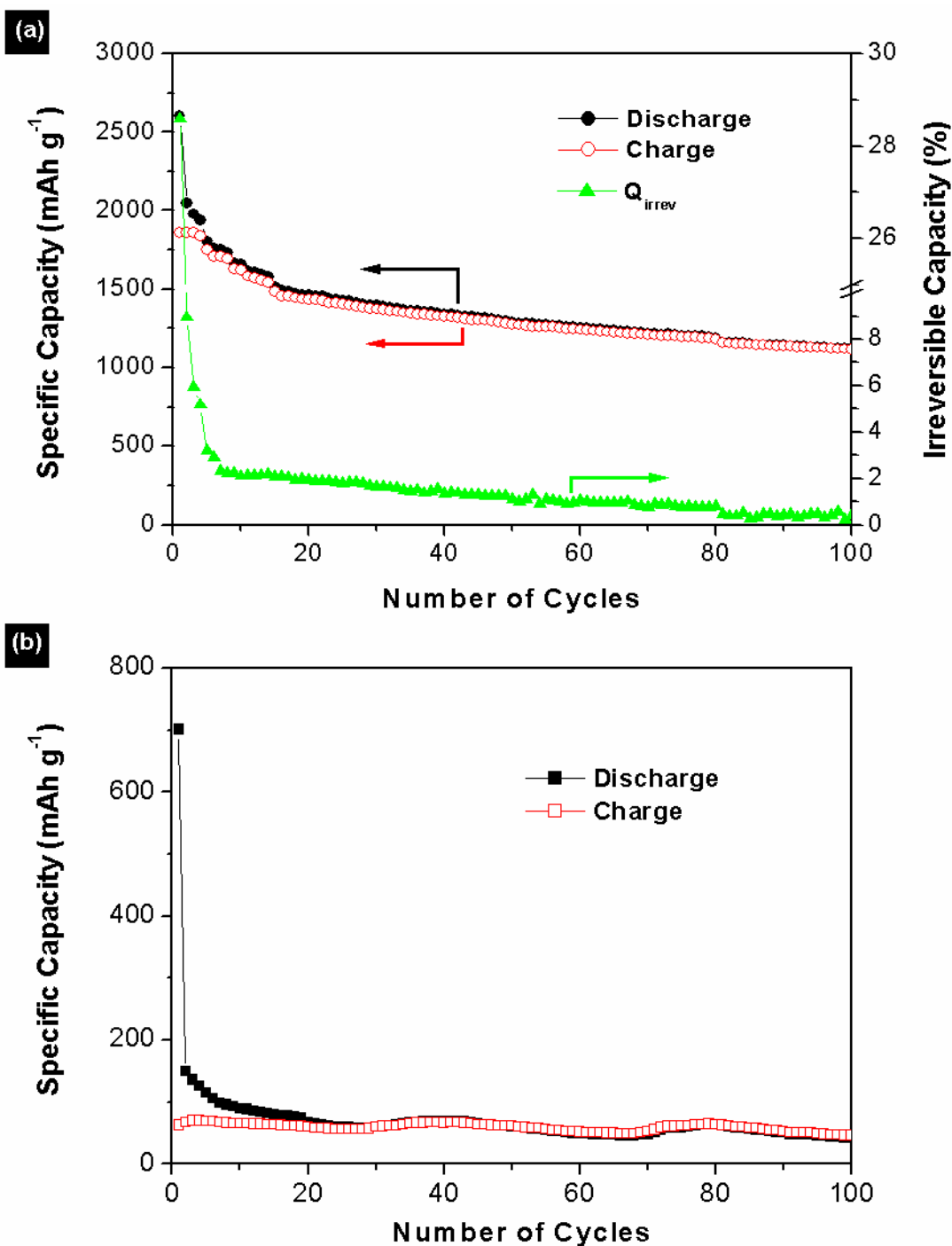


Fig. 6.8. Cycling behaviour for electrodes of (a) carbon-coated Si nanocomposite spray-pyrolyzed at 400 °C, with 44 wt.% Si content; and (b) amorphous carbon spray-pyrolyzed at 400 °C. Cycling took place between 0.02 V and 1.20 V versus Li/Li⁺ at a cycling rate of 100 mA g⁻¹.

Meanwhile, by subtracting the capacity contributed by the amorphous carbon ($\sim 40 \text{ mAh g}^{-1}$ after 100 cycles), the discharge capacity delivered by the Si active mass (44 wt.%) was estimated to be approximately 1098 mAh. Therefore, the specific capacity of Si in the nanocomposite electrode was calculated to be 2495 mAh g^{-1} after 100 cycles, which amounts to an impressive 60 % of the theoretical value (4200 mAh g^{-1}).

This shows the beneficial effect of the carbon-coating on the enhanced dimensional stability of the Si particles during the Li alloying/de-alloying process, which not only buffered the great volume changes during the cycling process, but also avoided possible agglomeration of the uniformly distributed silicon particles [Larcher et al., 1999; Dimov et al., 2003; Liu et al., 2005b].

In order to verify the effect of carbon-coating on the electronic conductivity of the nanocomposites, ac impedance measurements were conducted. The Nyquist plots obtained are compared in Figure 6.9 for the electrodes containing nanocrystalline Si (Fig. 6.9(a)) and carbon-coated Si nanocomposite spray-pyrolyzed at 400°C (Fig. 6.9(b)) after 1 and 100 cycles. The thickness of the electrodes was maintained at $50 \mu\text{m}$ and the coated area of the electrodes at 1 cm^2 . To maintain uniformity, electrochemical impedance spectroscopy (EIS) experiments were performed on working electrodes in the fully charged (de-lithiated) state.

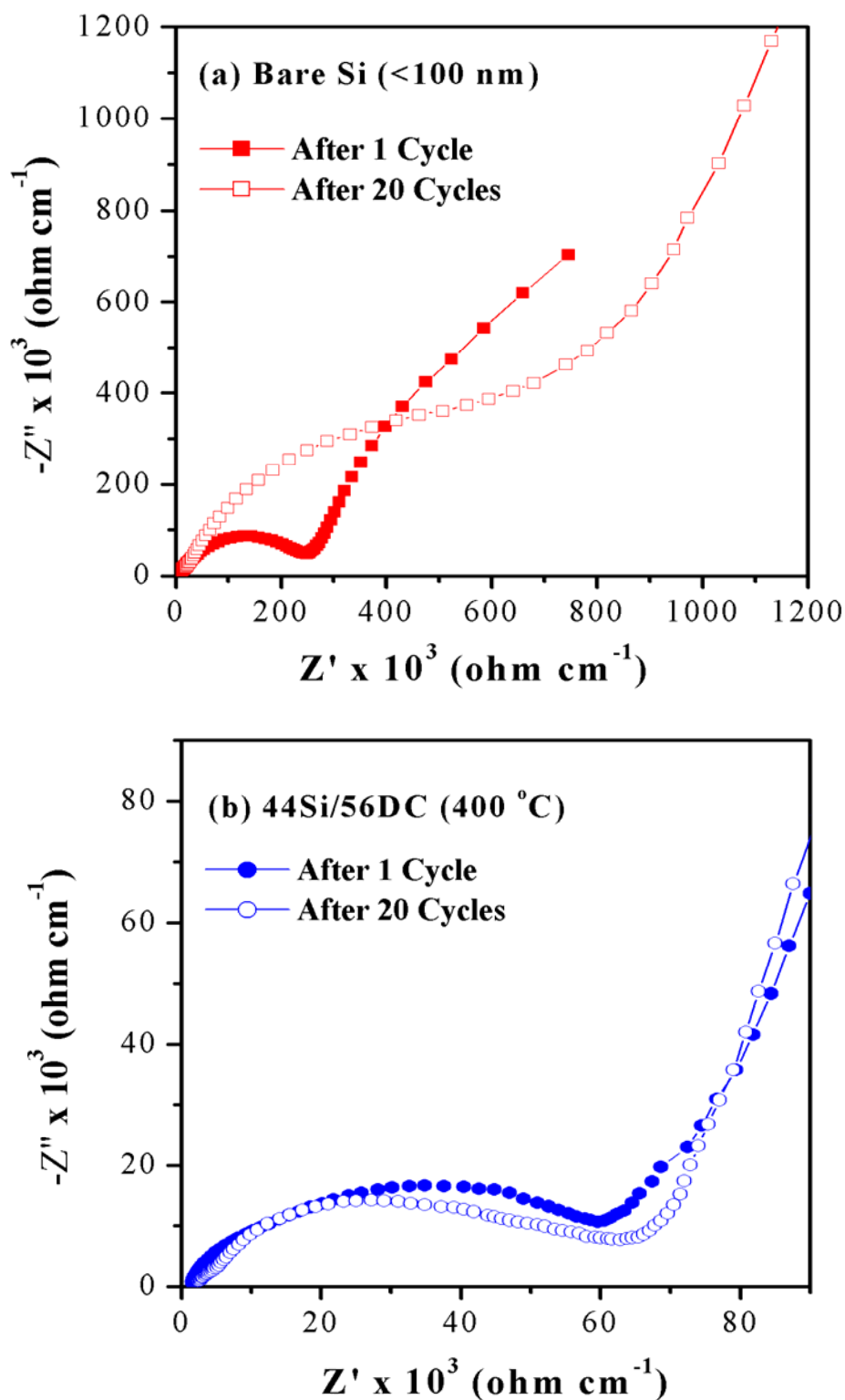


Fig. 6.9. Impedance plots for electrodes of (a) nanocrystalline Si; and (b) carbon-coated Si nanocomposite spray-pyrolyzed at 400 °C. All measurements were conducted in the de-lithiated state.

In general, one semicircle in the high frequency range was observed for all the samples. The diameter of the semicircle represents the interparticle contact resistance [Fan and Fedkiw, 1998]. Meanwhile, in the low frequency region, an angled straight line was obtained, which represents a diffusion-controlled process in the solid electrolyte interphase [Li et al., 1999b].

In addition, it is found that the diameter of the semicircles was enlarged after 100 cycles for all the samples. However, when Figure 6.9(a) is compared to Figure 6.9(b), considerable differences are observed. The diameter of the semicircle after 100 cycles increased by more than 200 % (from 250 to 750 $\text{k}\Omega \text{ cm}^{-1}$) in the case of nanocrystalline Si electrodes, compared to only an increase of approximately 17 % (from 60 to 70 $\text{k}\Omega \text{ cm}^{-1}$) for the electrodes of carbon-coated Si nanocomposite spray-pyrolyzed at 400 °C.

Therefore, it can be assumed that the interparticle contact resistance was suppressed by the carbon-coating, resulting in better cycling of the cells during the charge/discharge process [Fan and Fedkiw, 1998].

6.3 Effect of Precursor Solution (Nano-Si/Citric Acid/Ethanol) Concentration

6.3.1 Synthesis Method

Citric acid ($C_6H_8O_7$) was dissolved in 200 mL of absolute ethanol with continuous stirring. Subsequently, nanocrystalline Si powder (< 100 nm) was mixed into the initial citric acid/ethanol solution by ultrasonication for 90 mins. Four types of composite materials were prepared by mixing the initial solutions with nanocrystalline Si powder in weight ratios (nano-Si/citric acid) of 1/1, 1/3, 1/6 and 1/10, respectively. Finally, the composites were obtained in-situ via spraying of the Si/citric acid/ethanol suspensions in air at $400\text{ }^{\circ}\text{C}$ using a flow rate of 4 mL min^{-1} in a vertical type spray pyrolysis reactor.

6.3.2 Physical and Structural Characterizations

Figure 6.10 shows a typical TGA analysis of the Si/DC nanocomposite samples along with those of nanocrystalline Si powders. Using the same method as in Section 6.2.1, it was found that the amounts of disordered carbon in the composite were 16.78 wt.%, 31.68 wt.%, 49.37 wt.%, and 55.98 wt.% for the precursor solutions with weight ratios (nano-Si/citric acid) of 1/1, 1/3, 1/6, and 1/10, respectively. Table 6.2 summarizes the estimated amorphous carbon content in the spray-pyrolyzed Si/DC nanocomposites. The carbon concentrations obtained after spray pyrolysis were below the targeted levels. All samples undergo between 28-40 wt.% carbon losses during the spray process.

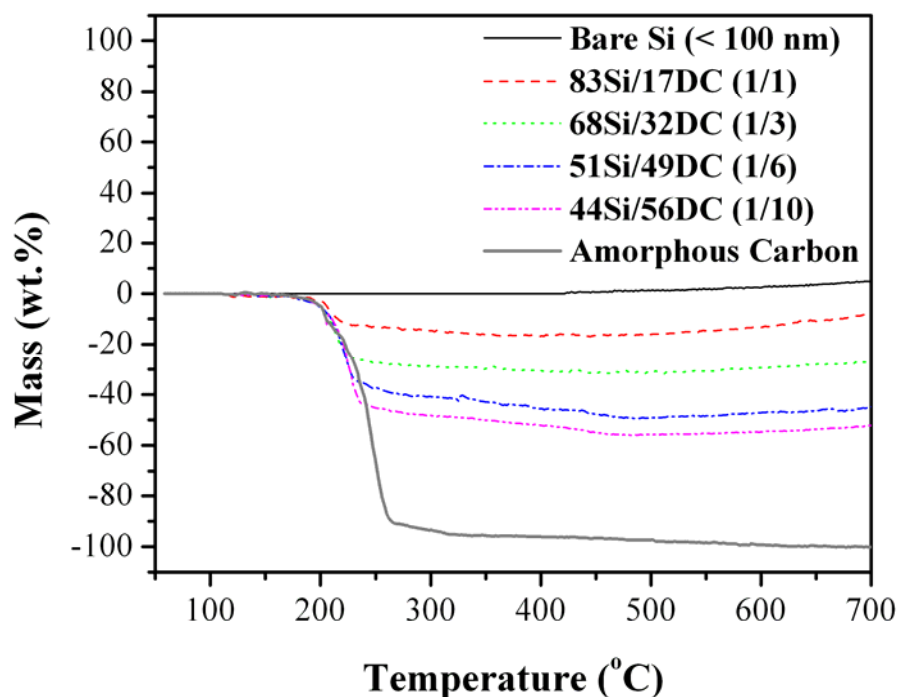


Fig. 6.10. Thermogravimetric analysis (TGA) curves of nanocrystalline Si precursor powder; carbon-coated Si nanocomposites spray-pyrolyzed in air at 400 °C with different initial precursor solution concentration; and amorphous carbon spray-pyrolyzed from citric acid at 400 °C in air, with initial precursor solution weight ratios (nano-Si/citric acid) of 1/10.

Figure 6.11 shows XRD patterns of the nanocrystalline Si precursor powder (a), Si/DC nanocomposites (b-e) prepared by spray pyrolysis at 400 °C in air at different precursor solution concentrations, and amorphous carbon spray-pyrolyzed from citric acid at 400 °C in air (f). All Si/DC nanocomposites in Figure 6.11 show only the Si peaks, indicating that there was no bulk SiO₂ crystalline phase formed during the spray pyrolysis process at 400 °C in air. Moreover, no diffraction lines from crystalline carbon (graphite) were observed, indicating the amorphous nature of the carbon in the nanocomposites.

Table 6.2: Theoretical and estimated carbon content in carbon-coated Si nanocomposites spray-pyrolyzed at 400 °C in air from nano-Si/citric acid/ethanol starting solutions with different concentrations of nano-Si/citric acid.

Nano-Si/Citric Acid ^a (w/w)	Theoretical weight % of carbon *	Estimated weight % of carbon (via TGA)	Mass loss % of carbon during spray pyrolysis **
1/1	27.27	16.78	38.47
1/3	52.94	31.68	40.16
1/6	69.23	49.37	28.69
1/10	78.95	55.98	29.09

^a C₆H₈O₇

* The calculation of “Theoretical weight % of carbon” is based on the assumption that all carbon content in ethanol is decomposed to carbon dioxide during spray pyrolysis.

** Mass loss % of carbon is calculated based on the (Eq. 6.2) in Section 6.2.2.

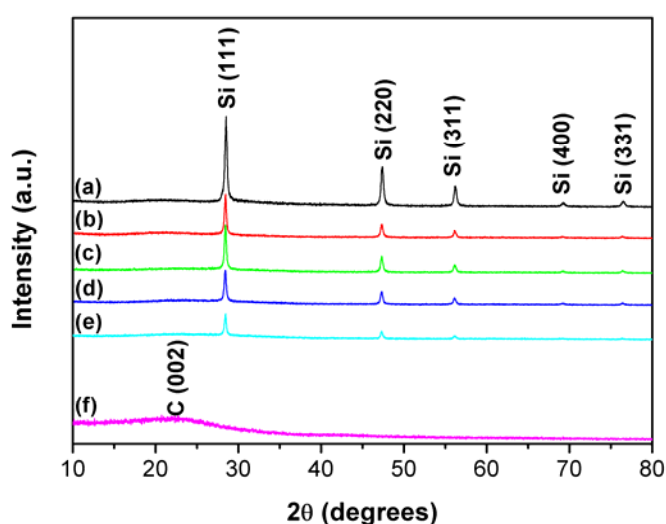


Fig. 6.11. X-ray diffraction patterns of (a) nanocrystalline Si precursor powder, (b) 83Si/17DC, (c) 68Si/32DC, (d) 51Si/49DC, (e) 44Si/56DC, and (f) amorphous carbon spray-pyrolyzed from citric acid at 400 °C in air.

6.3.3 Electrochemical Performance

Figure 6.12 shows the effect of the initial precursor solution concentration on the cycling behaviour of the Si/DC nanocomposite electrodes.

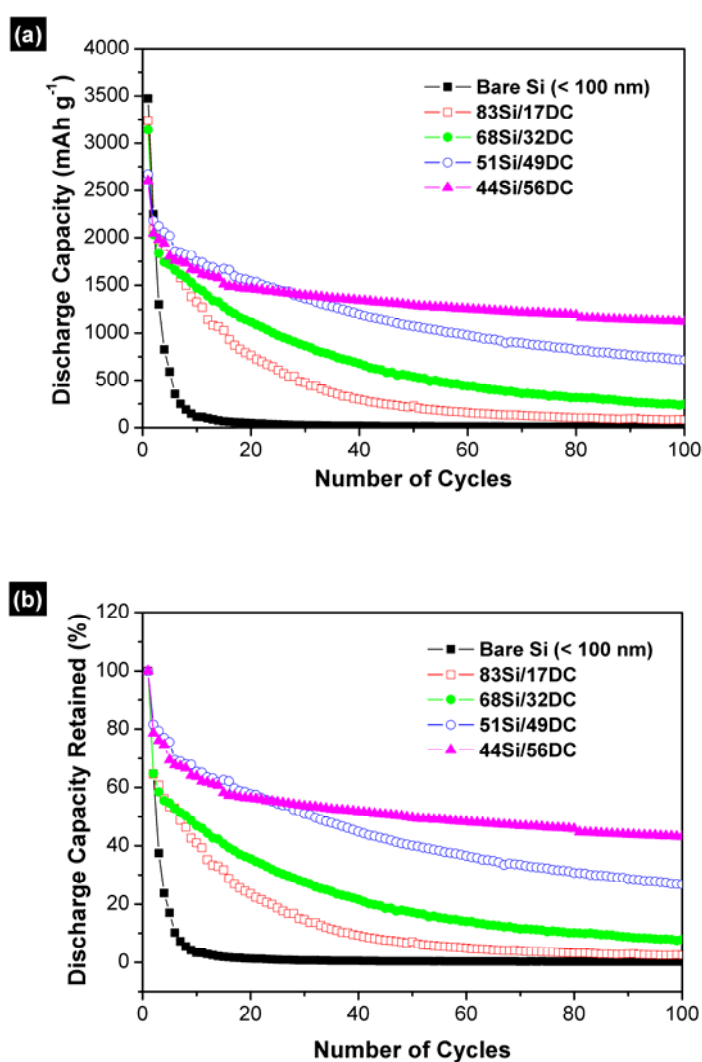


Fig. 6.12. (a) Cycling behaviour of the nanocrystalline Si and Si/DC nanocomposite electrodes cycled between 0.02 V and 1.20 V vs. Li/Li⁺ at a cycling rate of 100 mA g⁻¹. (b) The corresponding discharge capacity retained, compared to the first discharge capacity in (a).

Using a non-restricted cycling procedure, the initial reversible capacity (Fig. 6.12(a)) was as high as 2045 mAh g⁻¹ for the 44Si/56DC nanocomposite electrodes. Subsequently, the reversible capacity was maintained above 1120 mAh g⁻¹ beyond 100 cycles for the 44Si/56DC nanocomposite electrodes. Moreover, as demonstrated in Fig. 6.12(b), Si/DC nanocomposite electrodes with carbon content above 50 wt. % exhibited good cyclability beyond 100 cycles. For example, the specific capacity retained for the 44Si/56DC nanocomposite electrode after 100 cycles is 43.1 %, compared to 0.3 % for the nanocrystalline Si electrode. This shows that carbon coated Si nanocomposites are promising as anode materials for Li-ion batteries.

6.4 Conclusions

A series of carbon-coated Si nanocomposites have been successfully synthesized via in-situ spray pyrolysis of nano-Si/citric acid/ethanol solution in air with a flow rate of 4 mL min⁻¹ at three different processing temperatures; i.e., at 300 °C, 400 °C, and 500 °C, and also four different precursor solution (nano-Si/citric acid/ethanol) concentrations, i.e., at weight ratios (nano-Si/citric acid) of 1/1, 1/3, 1/6, and 1/10.

The spray-pyrolyzed powders are fine nanocrystalline Si homogeneously coated with an amorphous carbon layer. The thickness of the carbon-coating layer increased with decreasing processing temperature and increasing amount of citric acid in the (nano-Si/citric acid/ethanol) precursor solution.

The amorphous carbon content estimated by TGA shows that a small amount of impurities were present in the form of undecomposed citric acid for the carbon-coated Si nanocomposite spray-pyrolyzed in air at 300 °C. The disordered carbon content estimated by TGA shows that a moderate amount of carbon mass (28-40 wt.%) was lost during the spray pyrolysis process at 400 °C in air. Both the XRD and TEM results indicate that there was no bulk SiO₂ or SiC crystalline phase detected in the spray-pyrolyzed nanocomposites.

The alloying and de-alloying of lithium with Si over the 1.20 V to 0.02 V range yields various Li_xSi (x < 4.4) alloys. The discharge capacity of carbon-coated Si nanocomposite spray-pyrolyzed in air at 400 °C was 1120 mAh g⁻¹ after 100 cycles, corresponding to the Si active mass, which contributes a specific capacity of 2495 mAh g⁻¹. The carbon-coated Si nanocomposite electrodes show an improved cycle life compared to that of the pure Si electrode. The Si/DC nanocomposites also show an improved cycle life as the carbon content increases. It is strongly believe that the presence of the carbon-coating layer was responsible for the enhanced dimensional stability of the Si nanoparticles during the Li alloying/de-alloying processes, which then significantly improved the electrical conductivity of the composites.

In summary, spheroidal carbon-coated Si nanocomposite, prepared via a spray pyrolysis method in air, is a promising candidate for use as an anode material in the lithium-ion battery, as it has excellent specific capacity retention, high coulombic efficiency, and low cost due to the abundance of both Si and carbon sources.

CHAPTER 7

VANADIUM PENTOXIDE NANOSTRUCTURES FOR LITHIUM-ION BATTERY CATHODES

7.1 Introduction

As a result of the multiple valence state of vanadium, vanadium pentoxide (V_2O_5) has versatile redox-dependent properties and finds wide applications in catalysis [Karunakaran and Senthilvelan, 2005], electrochromism [Sanchez et al., 1983; Raju and Rao, 1991; Imawan et al., 2001], and electrochemistry [Goward et al., 1998; Lira-Cantu and Gomez-Romero, 1999; Shoji and Buttry, 2000]. The nanostructured form of this material has been employed in field-effect transistors (FETs) [Muster et al., 2000], sensors [Livage, 1991; Liu et al., 2005c], spintronic devices [Krusin-Elbaum et al., 2004], and nanolithography templates [Söörden et al., 2001; Ancona et al., 2003]. V_2O_5 is an attractive cathode material in lithium-ion batteries because of its unique features, such as high electrochemical activity, high energy density, and high stability towards lithium insertion [Koike et al., 1999]. The electro-reduction of V_2O_5 can occur in a large potential window between 4.0 to 1.5 V vs. Li/Li^+ , where approximately three moles of lithium per mole of V_2O_5 could be theoretically inserted, leading to a theoretical capacity of approximately 442 mAh g^{-1} [Tranchant et al., 1980].

The reversible electrochemical lithium intercalation into V_2O_5 at room temperature was first reported by Whittingham [1975]. Afterward, several phases were observed, depending on the amount of inserted lithium: α and ε phases exist for $x < 0.01$ and $0.35 < x < 0.7$ in $Li_xV_2O_5$, respectively, showing a V_2O_5 -type structure with increasing puckering of the layers [Cocciantelli et al., 1991]. The composition LiV_2O_5 corresponds to the δ phase formed by the gliding of one layer out of two [Galy, 1992]. For $x \leq 1$, the original V_2O_5 structure can be recovered upon lithium de-intercalation, and the phase transitions are fully reversible [Cava et al., 1986]. However, for further lithium intercalation ($x > 1$), a reconstruction mechanism leads to the irreversible transformation from the δ phase to the γ -phase [Cocciantelli et al., 1991]. This γ -phase can be reversibly cycled in the stoichiometric range $0 < x < 2$ without changing the γ -type structure [Labat and Cocciantelli, 1989; Cocciantelli et al., 1991]. Upon further intercalation of the third lithium, the γ -phase will be irreversibly transformed to the ω -phase with a rock-salt type structure.

Since the performance of V_2O_5 cathode heavily depends on its crystallinity and morphology, many studies have been done on modifying the form and structure of V_2O_5 to achieve higher specific capacities and better cyclability [Swider-Lyons et al., 2002]. These studies show that crystalline V_2O_5 has a high specific capacity, but exhibits a weak cyclability due to a crystal structure that is damaged during discharge/charge cycles, while amorphous and low crystallinity V_2O_5 allows faster lithium-ion diffusion and displays remarkable cyclability. Deformation associated with lithium intercalation may be easily relaxed in small crystallites with a high surface area, which also leads to higher ionic conductivity. Therefore, nanocrystalline V_2O_5 might be a good and promising cathode material for lithium-ion batteries [Patrissi and Martin, 2001].

Vanadium pentoxide nanostructures can be obtained by various physical and chemical techniques. Vanadium pentoxide powders have been prepared mostly by dry processes, such as vacuum evaporation [Fujita et al., 1985; Kobayashi et al., 1987] and sputtering [Wruck et al., 1989], although wet processes such as electrodeposition [Lakshmi et al., 1997] and the sol-gel method [Alonso and Livage, 1999] seem to be more advantageous in producing large scale films. There have been intensive worldwide research activities to obtain vanadium oxide compounds in the forms of nanotubes [Spahr et al., 1998; Satishkumar et al., 2000] and gels [Liu et al., 1997; Wong et al., 1998], which may enhance electronic and ionic properties. For example, Chen et al. [2004], prepared vanadium oxide nanotubes (VO_x-NTs) by making use of V₂O₅ sols as precursors on which hexadecylamine (HDA) acts as a structure-directing template via a modified sol-gel method followed by hydrothermal treatment. To enhance charge storage capability in batteries by making use of V₂O₅ nanofibers, Schlecht et al. [2004] investigated the electrical conduction properties of V₂O₅ nanofibers coated with silver nanoparticles.

However, synthesis of V₂O₅ one-dimensional nanostructures via a precipitation process followed by heating in vacuum or synthesis of V₂O₅ nanoparticles via flame spray pyrolysis (FSP) have never been explored to produce lithium-ion battery cathode materials. Therefore, in this study, well-crystallized V₂O₅ one-dimensional nanostructures with high surface area (above 40 m² g⁻¹) have been synthesized via a precipitation process followed by heat treatment in vacuum, and also by the flame spray pyrolysis process. The electrochemical properties of these V₂O₅ nanostructures will be examined and evaluated for use in lithium-ion battery cathodes. The effect of the cut-off potential on the electrochemical properties will also be investigated.

7.2 V₂O₅ Nanostructures Prepared via a Precipitation Process

7.2.1 Synthesis Method

A peristaltic pump delivered ammonium hydroxide (NH₄OH) droplet by droplet into a 0.5 M vanadium oxytrichloride (VOCl₃) solution. The solution was continuously stirred with a magnetic stirrer throughout the precipitation process. An excess of NH₄OH was used to avoid contamination with chloride. The precipitate was then filtered and washed several times with de-ionized water. Finally, the precipitate was heated for a varying duration at 300 °C in a vacuum oven to produce well-crystallized V₂O₅. Two types of V₂O₅ samples were synthesized via this new approach, differing only in the annealing time in the vacuum oven at 300 °C. One sample was annealed for 45 mins (sample A), while another was annealed under the same conditions for 1 hr (sample B).

7.2.2 Physical and Structural Characterizations

Both samples (A and B) were highly crystallized and the peak positions agree well with those of commercial V₂O₅ (JCPDS 41-1426), as shown in Figure 7.1. From the XRD patterns in Figure 7.1, it was estimated that sample A (b) has an average crystal size of 36 nm, while sample B (c) has an average crystal size of 83 nm. Meanwhile, as seen from Table 7.1, it was found that sample A had a higher BET specific surface area of 41 m² g⁻¹, compared to 17 m² g⁻¹ for sample B. Therefore, the average crystal size is reduced with a shorter annealing time, which leads to a higher specific surface area.

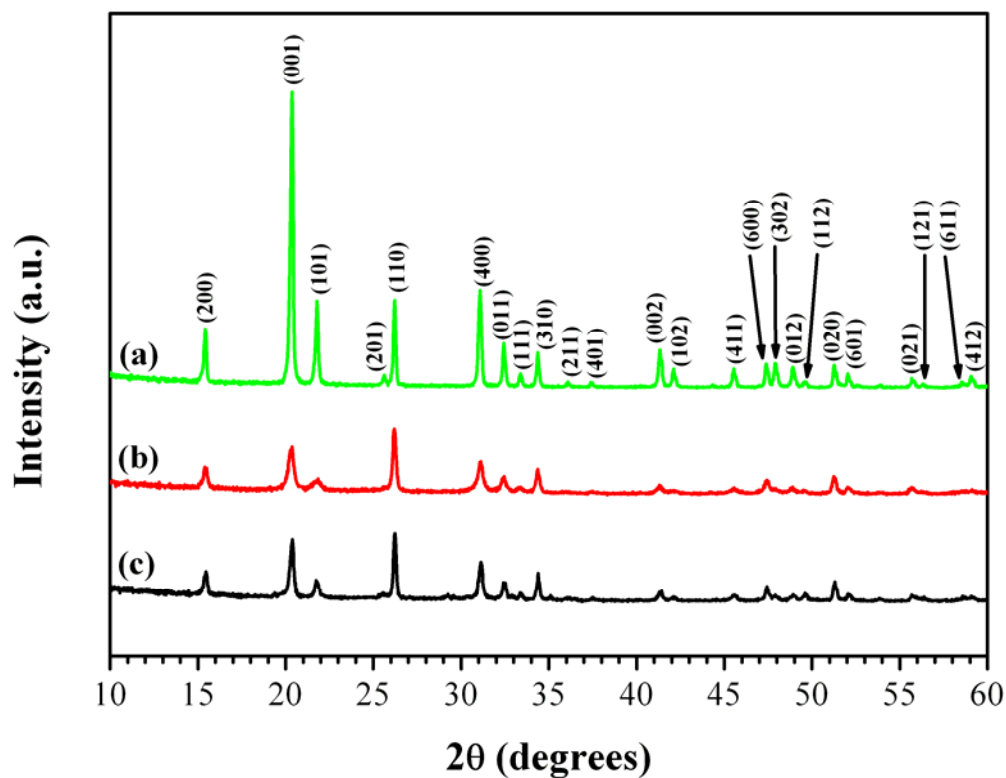


Fig. 7.1. XRD patterns for (a) commercial V_2O_5 , (b) V_2O_5 annealed for 45 mins at 300 °C (sample A), and (c) V_2O_5 annealed for 1 hr at 300 °C (sample B).

Table 7.1: Summary of experimental conditions and physical characteristics for the V_2O_5 nanostructures prepared via a precipitation method.

Sample ID	A	B
Annealing Temperature, T (°C)	300	300
Annealing Duration Under Vacuum, t (min)	45	60
Morphology (from SEM)	Nanoparticles Only	Nanoparticles + Nanofibers
Average Crystal Size, D_p (nm)	36	83
Specific Surface Area, S_{BET} ($m^2 g^{-1}$)	41	17

Figure 7.2 shows scanning electron microscope (SEM) images of the as-synthesized V_2O_5 one-dimensional nanostructures (sample A and sample B). Figure 7.2(a) and (b) contains SEM images of sample A, while Figure 7.2(c) and (d) shows SEM images of sample B. From the SEM images, it is very obvious that the oxides have become well crystallized and that there is a higher yield of nanofibers in sample B compared to the smaller, but also denser, nanoparticles in sample A. The estimated average particle size for sample A is approximately 150 nm, while the estimated diameter for the nanofibers in sample B is approximately 80 nm. The slightly bigger particle size of sample A might be due to agglomeration of the nanoparticles due to its high surface area.

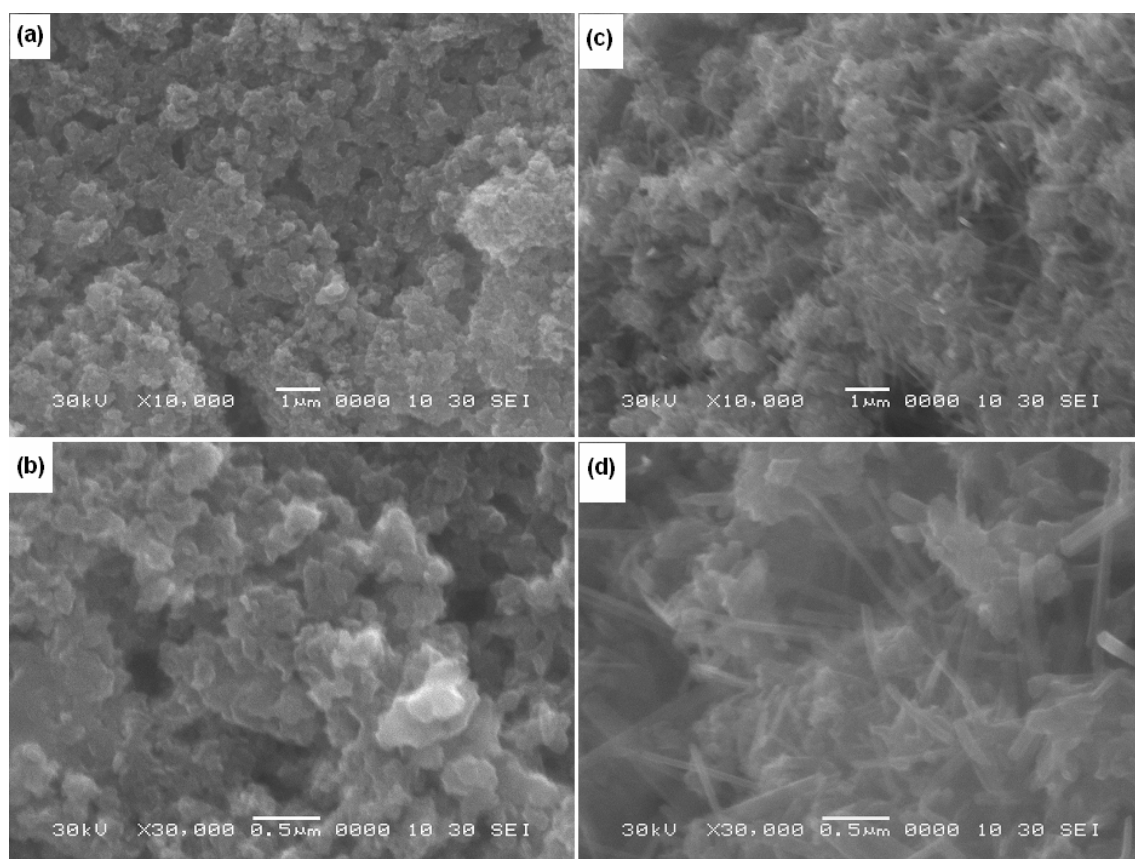


Fig. 7.2. SEM images of nanostructured V_2O_5 electrodes: (a) and (b) are for V_2O_5 annealed for 45 mins at 300 °C (sample A), while (c) and (d) are for V_2O_5 annealed for 1 hr at 300 °C (sample B).

7.2.3 Electrochemical Performance

The cathode was prepared by mixing V_2O_5 powders with 20 wt.% carbon black and 10 wt.% polyvinylidene fluoride (PVDF) binder in N-methyl-2-pyrrolidinone (NMP) solvent to form a homogeneous slurry, which was then spread onto aluminium foil. The coated electrodes were dried in a vacuum oven at 110 °C for 24 hrs and then pressed.

Cyclic voltammetry (CV) was used to analyze the active voltage range for the nanostructured V_2O_5 electrodes (Fig. 7.3). Well-defined, and almost identical reduction and oxidation peaks occur at 2.3 and 2.8 V, respectively, for both the sample A and sample B electrodes. However, sample B shows higher kinetics and reactivity towards Li^+ insertion and extraction compared to sample A. This may be due to the higher degree of crystallization and the well-grown nanostructure shown by the sample B electrode.

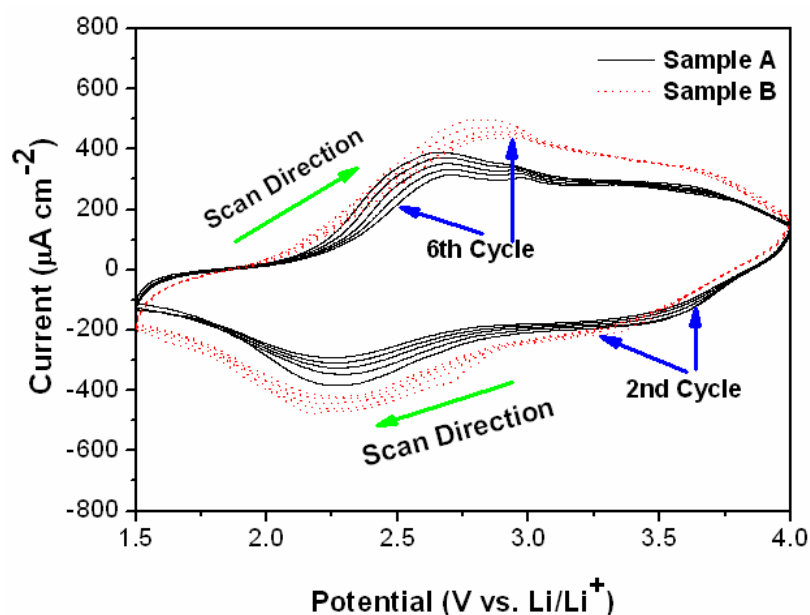


Fig. 7.3. Cyclic voltammograms of nanostructured V_2O_5 electrodes. The applied scan rate was 0.5 mV s^{-1} .

Electrochemical properties for both V_2O_5 samples were examined by galvanostatically discharging/charging in the range of 1.5-4.0 V at a constant current density of 50 mA g^{-1} . Figure 7.4 shows that both samples demonstrated an initial charge capacity above 300 mAh g^{-1} , followed by capacity fading after 20 cycles. However, the capacity fading in sample A is more significant, decreasing from 328 to 146 mAh g^{-1} after 20 cycles at a rate of 50 mA g^{-1} . This may be because some vanadium dissolution occurs when the oxide is discharged to 1.5 V [Sudant et al., 2004]. The vanadium dissolution in sample A may be enhanced because the higher specific surface area amplifies this phenomenon. This behaviour is also consistent with a report that amorphous materials dissolve more easily than crystallized ones [Arnoldussen, 1981].

Figure 7.5 shows the charge capacities for the different potential spans for sample B. From Figure 7.4, we already know that the charge capacity for both the samples decreases rapidly with increasing cycle number between 1.5 V and 4.0 V. Increasing the cut-off voltage to 2.0 V gave less capacity fading, and there was even better cycling stability when the cut-off voltage was increased to 2.5 V. Although the 136 mAh g^{-1} charge capacity obtained in the latter case is small, it is important to keep in mind that this capacity was obtained with a reduced voltage window (2.5 to 4.0 V).

Besides the possibility of vanadium dissolution when discharging to 1.5 V, the structural changes or damage inflicted upon the one-dimensional nanostructure of the oxides upon cycling in the larger potential span might be another reason for loss in the electroactivity of the material [Lao et al., 2006; Li et al., 2006]. Sample B shows good cyclability and high capacity (200 mAh g^{-1} after 20 cycles) in the voltage range of 2.0-4.0 V at a cycling rate of 50 mA g^{-1} .

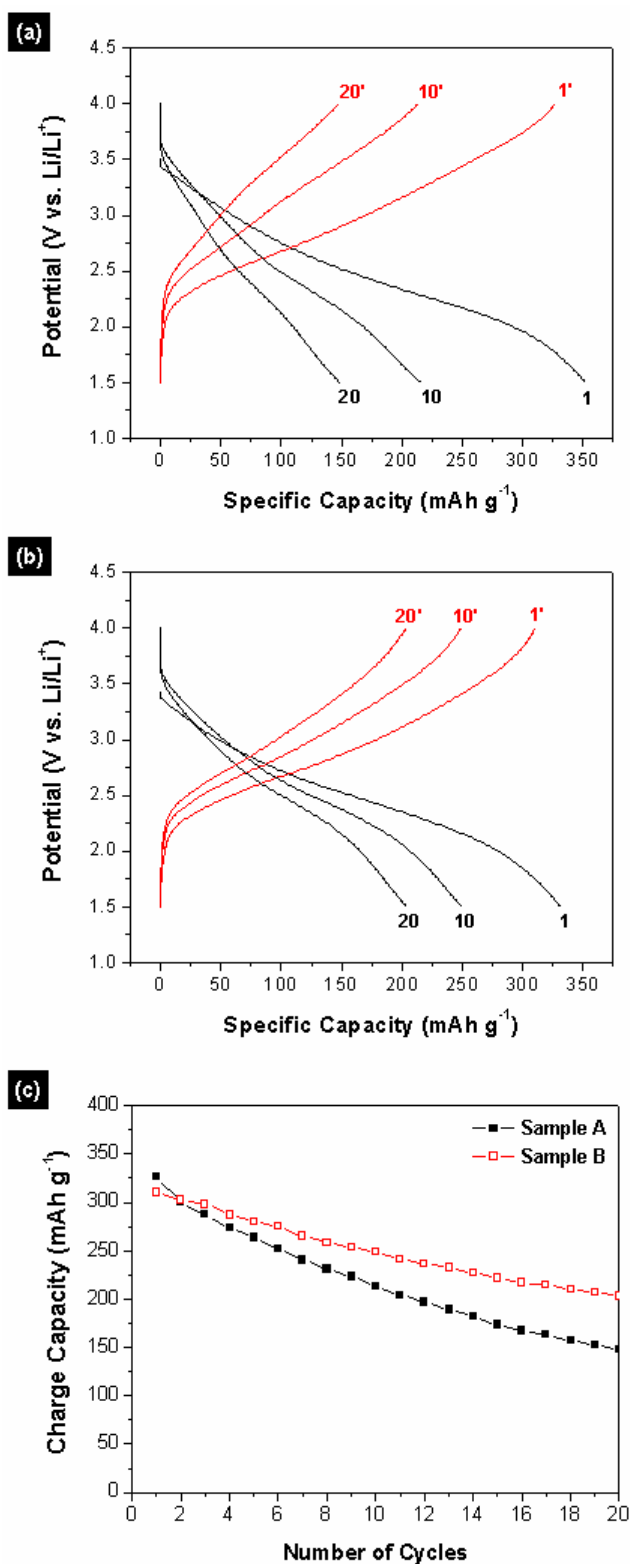


Fig. 7.4. The 1st, 10th, and 20th charge-discharge profiles of nanostructured V_2O_5 electrodes: (a) V_2O_5 annealed for 45 mins at 300 °C (sample A), and (b) V_2O_5 annealed for 1 hr at 300 °C (sample B). (c) Charge capacity vs. cycle number for nanostructured V_2O_5 electrodes cycled between 1.5 V and 4.0 V at a cycling rate of 50 $mA\ g^{-1}$.

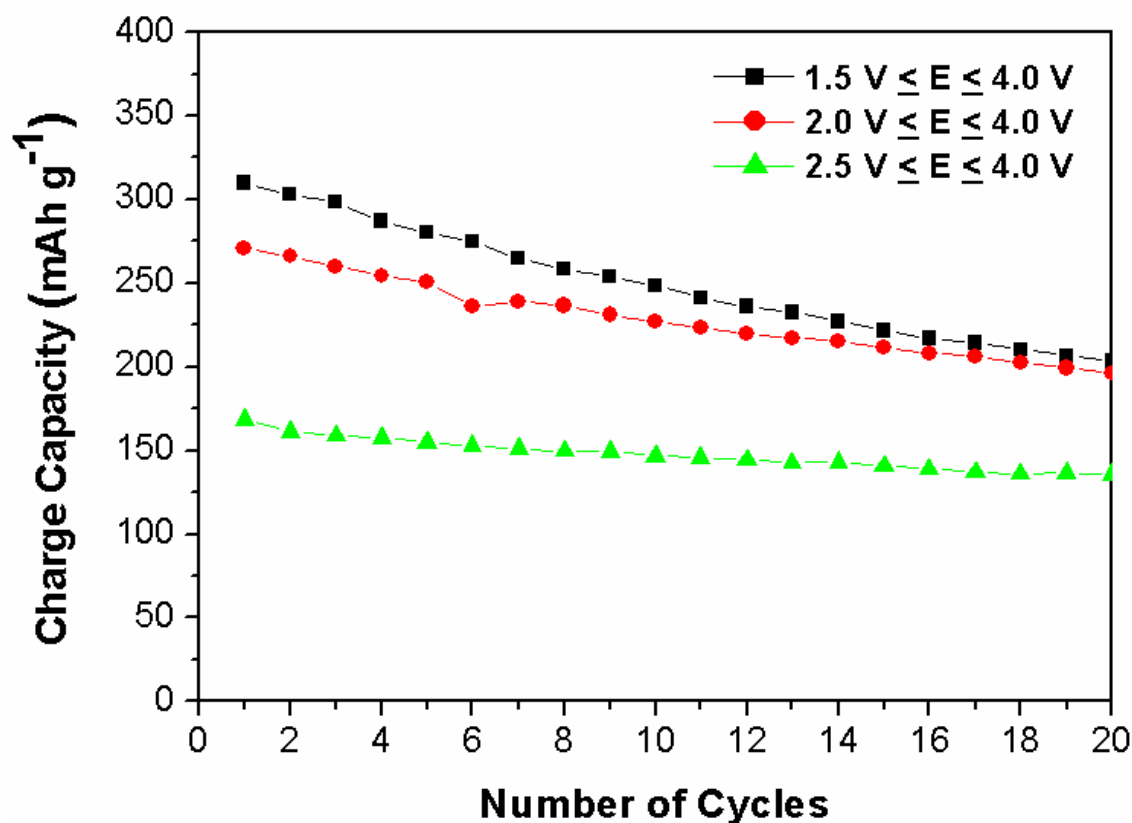


Fig. 7.5. Cycling behaviour for sample B V_2O_5 electrode at different cut-off voltages:

(a) 1.5 V, (b) 2.0 V, and (c) 2.5 V. The current density applied was 50 mA g^{-1} .

7.3 V_2O_5 Nanoparticles Prepared via a Flame Spray Pyrolysis Process

7.3.1 Synthesis Method

The experimental procedures for the flame spray pyrolysis (FSP) process are described earlier in Section 3.3.4. The precursor used for the flame synthesis was prepared by first dissolving 9.17 g of vanadium (V) oxytripropoxide into 18.5 mL of diethylene glycol (DEG). This solution was then stirred into 18.5 mL of toluene and 12.5 mL of tetrahydrofuran (THF). Subsequently, this precursor was injected at a rate of 5 mL min^{-1} through the reactor nozzle and dispersed with 5 L min^{-1} of oxygen into a fine spray

while maintaining a constant pressure drop of 1.5 bars across the nozzle tip. A premixed flame fueled by 1 L min⁻¹ of methane and 2 L min⁻¹ of oxygen was maintained to ignite and support the combustion of the spray. The powder was collected by placing a glass fiber filter above the flame and drawing the gas streams with a vacuum pump. The filter as well as the FSP unit was cooled by water to prevent overheating of the nozzle and precursor evaporation within the liquid feed lines.

7.3.2 Physical and Structural Characterizations

The peak positions for the flame spray pyrolyzed V₂O₅ nanoparticles agree well with those of commercial V₂O₅ (JCPDS 41-1426), as shown in Figure 7.6. From the XRD patterns in Figure 7.6, it was estimated that the flame spray pyrolyzed V₂O₅ nanoparticles (b) had an average crystal size of 40 nm. It was also determined that the flame spray pyrolyzed V₂O₅ nanoparticles had a BET specific surface area of 40 m² g⁻¹, which is comparable to the V₂O₅ nanoparticles produced by the precipitation method, as shown earlier in Section 7.3.1.

Figure 7.7 shows scanning electron microscope (SEM) images of the flame spray pyrolyzed V₂O₅ nanoparticles. From the low-magnification image (Fig. 7.7(a)), it is very obvious that the V₂O₅ nanoparticles are spherical in shape, with a fairly homogeneous particle size distribution. At higher magnification, field emission scanning electron microscope (FE-SEM) images confirmed the nanosize nature of the flame spray pyrolyzed V₂O₅ particles, with particles sizes ranging from 20-40 nm.

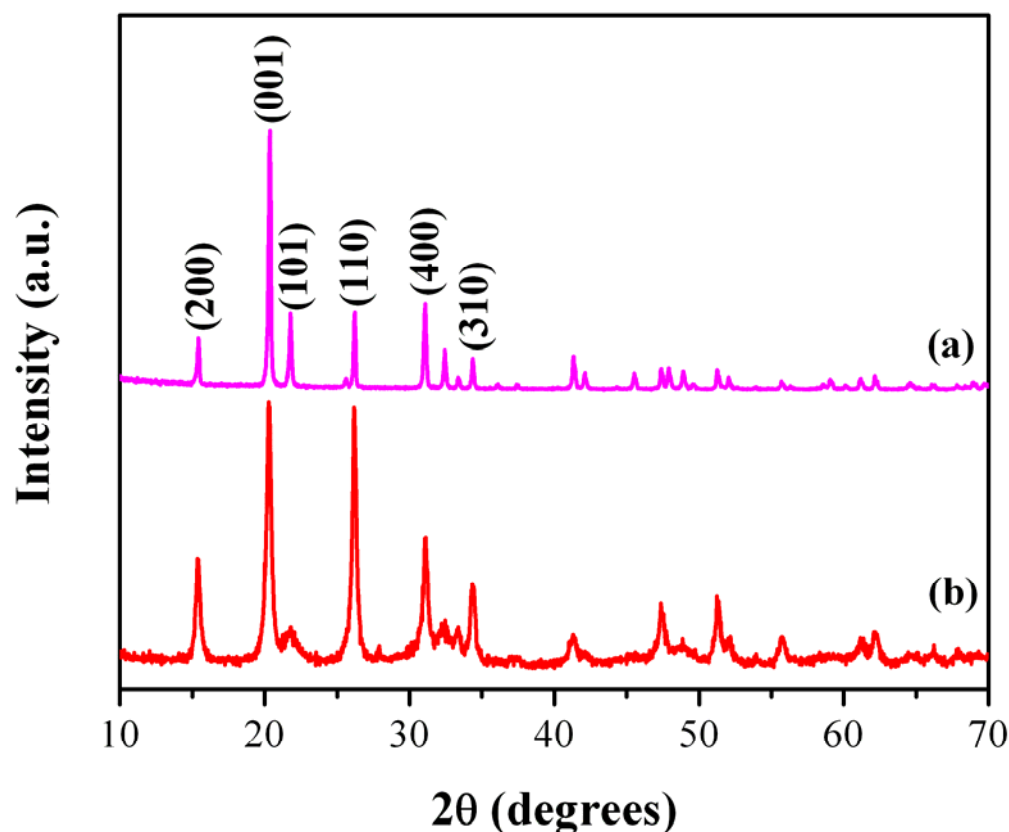


Fig. 7.6. XRD patterns for (a) commercial V₂O₅ (micron-sized), and (b) V₂O₅ (nano-sized) produced by a one-step flame spray pyrolysis process.

In addition, transmission electron microscope (TEM) images of the V₂O₅ nanoparticles synthesized via FSP are shown in Figure 7.8. As can be seen from Figure 7.8(a) and (b), the V₂O₅ nanoparticles are not exactly spherical in shape. Furthermore, from the high-resolution TEM image in Figure 7.8(c), the strongly crystalline structure of the flame spray pyrolyzed V₂O₅ nanoparticles is well-defined by the highlighted (200) lattice diffraction. The corresponding selected area electron diffraction (SAED) pattern for the flame spray pyrolyzed V₂O₅ nanoparticles in Figure 7.8(c) is shown in Figure 7.8(d), revealing the crystal lattice parameter of the V₂O₅ nanoparticles, which is in accordance with the orthorhombic phase of V₂O₅ (JCPDS 41-1426).

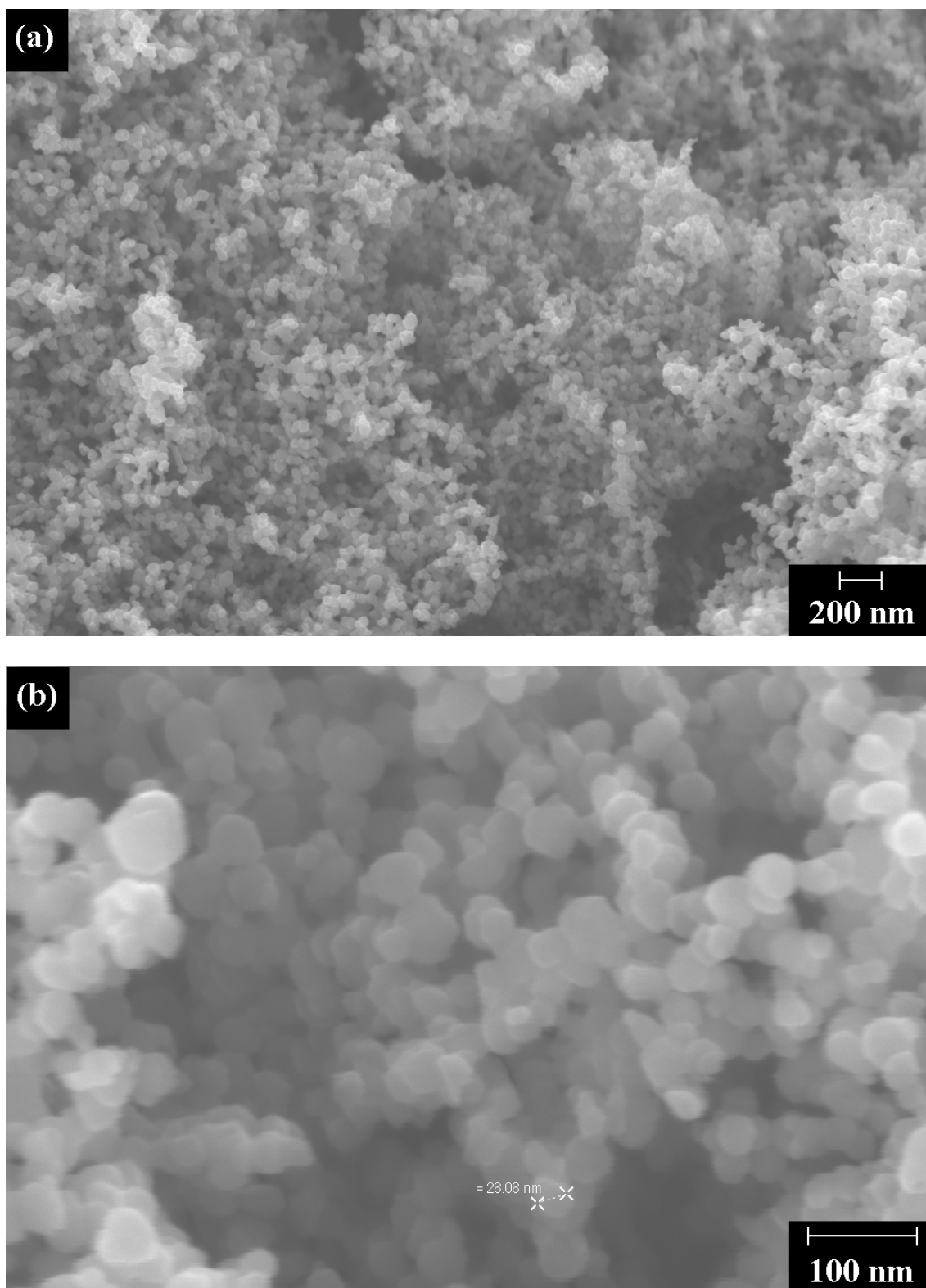


Fig. 7.7. SEM images of V_2O_5 nanoparticles synthesized via FSP: (a) low magnification image, revealing the homogeneity of the spherical-shaped particles, and (b) high-magnification, field emission SEM images, confirming the nanosized nature of the particles, with sizes ranging from 20-40 nm.

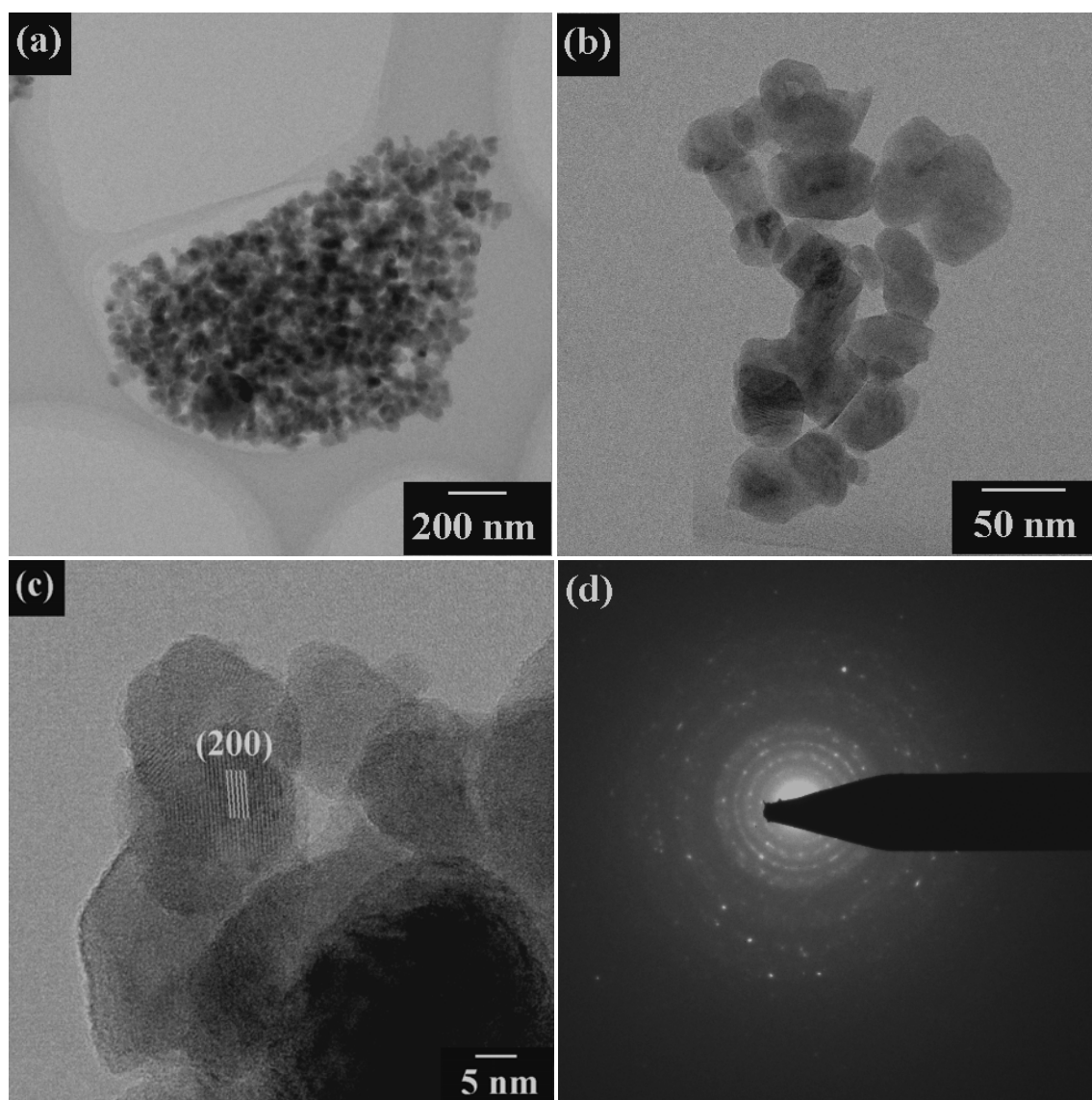


Fig. 7.8. TEM images of V_2O_5 nanoparticles synthesized via FSP: (a) and (b) are low resolution images, showing that the nanoparticles are not exactly spherical in shape; (c) is a high-resolution TEM image, with the (200) crystalline lattice parameter highlighted; and (d) is the corresponding selected area electron diffraction (SAED) pattern for the V_2O_5 nanoparticles in image (c).

7.3.3 Electrochemical Performance

A mixture of the nanosized V_2O_5 FSP-made powder, and two types of carbon black (Super P and Ensaco 350) in the weight ratio of 7:1:1, were dispersed within an organic solution of N-methylpyrrolidinone (NMP). This suspension was then added to a solution composed of 10 wt.% polyvinylidene fluoride (PVDF) dissolved in NMP, forming a viscous slurry. Subsequently, the slurry was doctor bladed at a thickness of 200 μm onto an aluminum foil and dried under vacuum at 110 $^{\circ}\text{C}$ overnight, in order to remove the NMP, thus forming the composite electrode that was used for the electrochemical testing. The active electromaterial, V_2O_5 , accounted for 70 wt.% of the composite electrodes.

Figures 7.9(a)-(c) show the cyclic voltammograms (CVs) of the electrode made from the flame spray pyrolyzed V_2O_5 nanoparticles. The CVs were taken at a scan rate of 0.1 mV s^{-1} with cycling at different discharge cut-off potentials. From Figure 7.9(a), it can be seen that during the cathodic scanning in the first cycle, four distinctive peaks are observed at 3.35, 3.15, 2.26, and 1.87 V vs. Li/Li^+ , which corresponds to a complicated multi-step lithium intercalation process [Cocciantelli et al., 1991]. As lithium ions were inserted into the layers of V_2O_5 , the phase transformation occurred consecutively from $\alpha\text{-}V_2O_5$ to $\epsilon\text{-Li}_{0.5}V_2O_5$ (3.35 V), $\delta\text{-Li}V_2O_5$ (3.15 V), $\gamma\text{-Li}_2V_2O_5$ (2.26 V), and $\omega\text{-Li}_3V_2O_5$ (1.87 V) [Cava et al., 1986; Labat and Cocciantelli, 1989; Broussely et al., 1991]. Among the various phases of $\text{Li}_xV_2O_5$, $\delta\text{-Li}V_2O_5$ can be restored to pristine V_2O_5 through lithium deintercalation, while $\gamma\text{-Li}_2V_2O_5$ and $\omega\text{-Li}_3V_2O_5$ (rock-salt type structure) are formed irreversibly.

In the following anodic scanning, two broad peaks were observed at around 2.67 and 3.26 V vs. Li/Li^+ , corresponding to the lithium extraction processes. The Li^+ intercalation and deintercalation process can be expressed by the following equation:

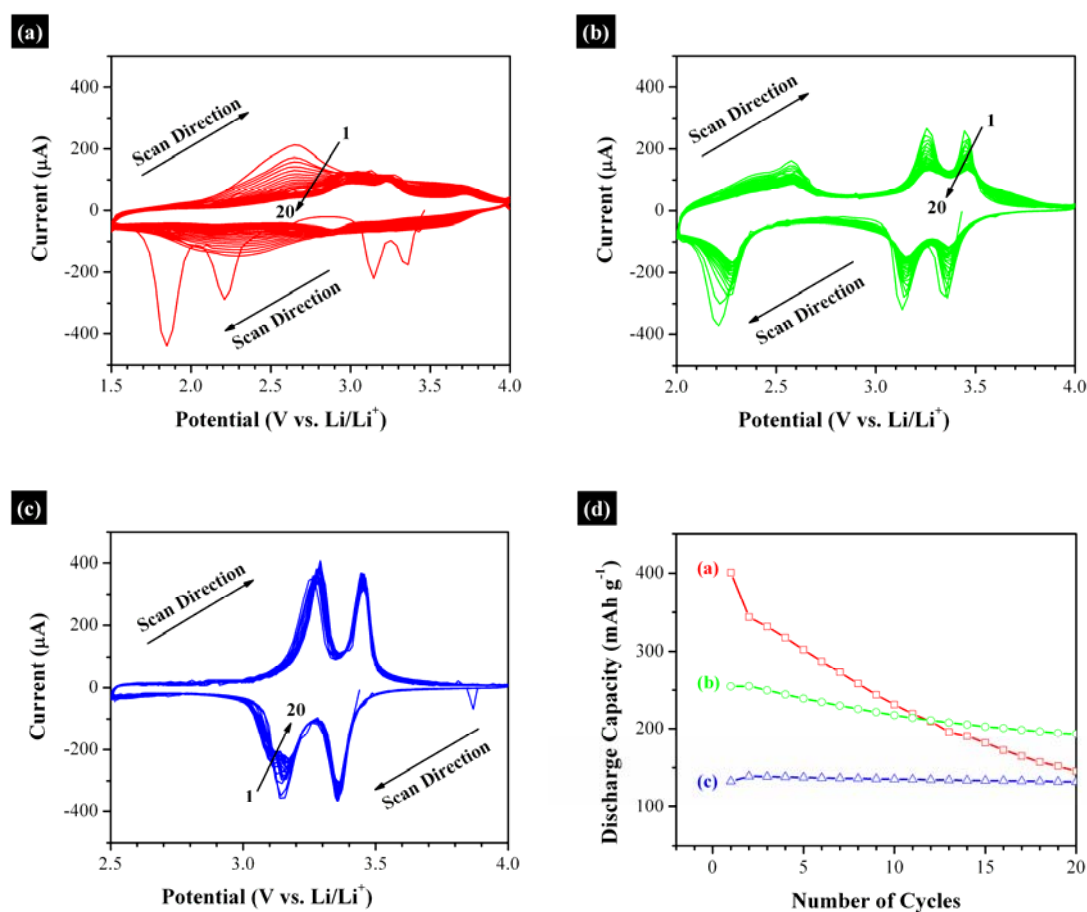
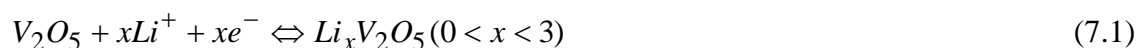


Fig. 7.9. Cyclic voltammograms (CVs) of the FSP-made nanostructured V_2O_5 electrodes for the first 20 cycles at different cut-off voltages: (a) 1.5 V, (b) 2.0 V, and (c) 2.5 V. The applied scan rate was 0.1 mV s^{-1} . (d) Plot of discharge capacity vs. cycle number for the corresponding CVs in plots (a), (b), and (c).

From Figure 7.9(b) and (c), it can be seen that the reversibility of the redox kinetics with cycling improves when the discharge cut-off potential is reduced to 2.5 V. This can be explained by the fact that the δ - LiV_2O_5 phase can be reversibly cycled without destroying the crystal structure of the V_2O_5 nanoparticles [Cocciantelli et al., 1991]. In addition, Figure 7.9(d) shows the corresponding discharge capacity of the CV curves in Figure 7.9(a) to (c) for the first 20 cycles. It was revealed that capacity fading increases with a larger charge-discharge potential window. Therefore, it is necessary for us to investigate further the effect of the discharge cut-off potentials. After prolonged cycling at 100 cycles, it was found that the V_2O_5 electrodes with a discharge cut-off potential at 2.5 V retain the highest discharge capacity of approximately 120 mAh g^{-1} , at a cycling rate of 100 mA g^{-1} (Figure 7.10).

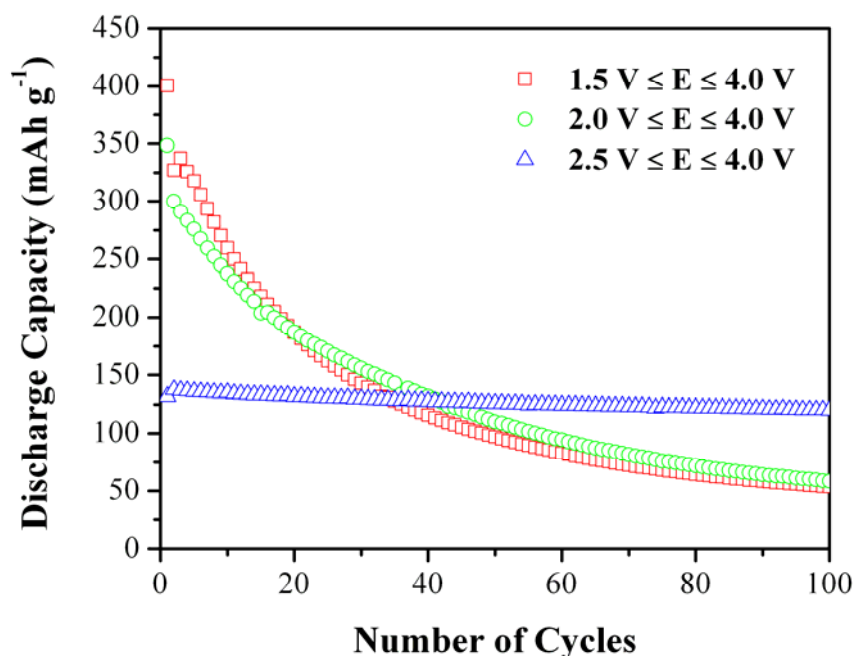


Fig. 7.10. Prolonged cycling behaviour for the FSP-made nanostructured V_2O_5 electrodes at different discharge cut-off voltages: 1.5 V, 2.0 V, and 2.5 V. The current density applied was 100 mA g^{-1} .

In order to fully understand the beneficial effect of the discharge cut-off potential at 2.5 V vs. Li/Li^+ , the cycling behaviour of the V_2O_5 nanoparticle electrodes was investigated. As can be seen from Figure 7.11(a), the initial discharge capacity and charge capacity of the V_2O_5 electrode were 132 mAh g^{-1} and 137 mAh g^{-1} , respectively, which corresponds to an irreversible capacity loss of minus 4.3 %. This means that there is less reduction reaction in the first cycle, which might be due to the lower open circuit potential (3.4 V) when compared to the upper potential limit (4.0 V) of the cycling. However, as the cycling was prolonged, the V_2O_5 electrode retained a discharge capacity of 120 mAh g^{-1} beyond 100 cycles, with an irreversible capacity loss of less than 1.2 % per cycle.

The power performance of Li-ion battery electrodes depends on the size of the particles making up the electrodes and on the electrode surface area [Patrissi and Martin, 2001]. To better understand these effects, it is important to investigate the rate capabilities of Li^+ insertion electrodes composed of monodispersed nanoscopic particles.

As can be seen from Figure 7.11(b), the V_2O_5 nanostructured electrodes have good rate capabilities, even up to the 15C rate (corresponding to 2000 mA g^{-1}), retaining a discharge capacity above 110 mAh g^{-1} . This may be because the distance Li^+ must diffuse in the nanoparticle is smaller and also due to the large surface area of the nanostructured electrode. Both effects delay concentration polarization to higher discharge currents, resulting in better rate capabilities and higher electrode capacity at high discharge rates [Patrissi and Martin, 2001].

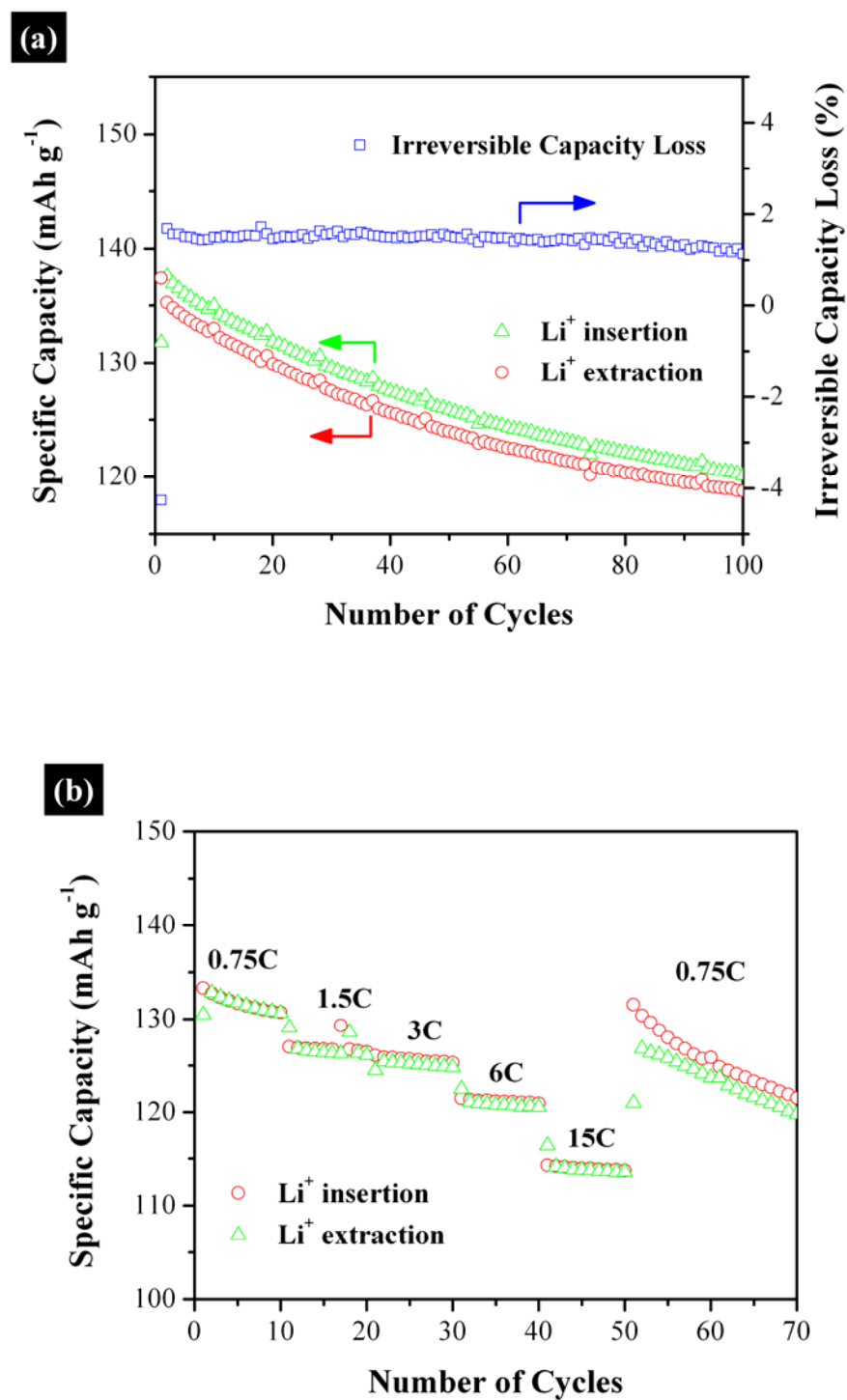


Fig. 7.11. (a) Electrochemical performance for the FSP-made nanostructured V_2O_5 electrode, cycled between 2.5 V and 4.0 V versus Li/Li^+ at a cycling rate of 100 mAh g^{-1} . (b) Cycling behaviour for the FSP-made nanostructured V_2O_5 electrode at different current densities, when cycled between 2.5 V and 4.0 V versus Li/Li^+ .

7.4 Conclusions

In this study, I have successfully prepared one-dimensional V_2O_5 nanostructures via a precipitation process followed by heating in vacuum at 300 °C, and also spherical V_2O_5 nanoparticles via the flame spray pyrolysis process in air. Both the XRD patterns and SEM images reveal that the V_2O_5 crystal sizes were approximately 36-83 nm for the precipitation-made oxides, while the FSP-made V_2O_5 powder gives an average crystal size of approximately 20-40 nm. The as-prepared V_2O_5 nanostructures from the precipitation process are well crystallized and give a higher yield of nanofibers with longer annealing time. However, the longer annealing time leads to a larger crystal size and consequently a lower BET specific surface area. Meanwhile, the FSP-made V_2O_5 powder gives a comparable BET specific surface area of 40 m² g⁻¹.

In addition, it was found that the V_2O_5 nanostructures are electrochemically active towards Li^+ insertion and extraction in the potential window of 1.5 V to 4.0 V. The V_2O_5 nanostructure shows an improved cycle life when the cut-off voltage for discharging is increased from 1.5 V to 2.5 V. It is strongly believe that the significant capacity loss when discharging to 1.5 V is related to the dissolution of vanadium and the structural changes upon cycling in the larger potential span. Good cyclability and capacity as high as 200 mAh g⁻¹ after 20 cycles are achieved in the voltage range of 2.0-4.0 V at a cycling rate of 50 mA g⁻¹ when the oxides are annealed in vacuum at 300 °C for 1 hour. Meanwhile, the flame spray pyrolyzed V_2O_5 nanoparticles show excellent cyclability when cycled between 2.5 V to 4.0 V vs. Li/Li^+ , retaining a discharge capacity of 120 mAh g⁻¹ beyond 100 cycles at a cycling rate of 100 mA g⁻¹, and also an incredibly high capacity at 110 mAh g⁻¹ at cycling rates up to 15C (or 2000 mA g⁻¹).

CHAPTER 8

LITHIUM TRIVANADATE NANOPARTICLES SYNTHESIZED BY FLAME SPRAY PYROLYSIS AS CATHODE MATERIAL FOR LITHIUM-ION BATTERIES

8.1 Introduction

Lithium-ion rechargeable batteries are currently used extensively in portable digital devices due to their relatively high cell voltage and energy density compared to other rechargeable batteries. LiCoO_2 is the current cathode material of choice, however, there is a demand for alternative cathode materials due to the cost, relative toxicity, and safety concerns associated with LiCoO_2 [Broussely et al., 1999; Whittingham, 2004]. LiV_3O_8 as a cathode material has the advantages of higher capacity, lower cost, and better safety features [Kannan and Manthiram, 2006]. An extensive amount of study has been conducted on related topics, which include the material's degree of crystallinity [Nassau and Murphy, 1981; Pasquali et al., 1986; Kawakita et al., 1999], aging mechanism [Jouanneau et al., 2005], numerous synthesis methods [Pistoia et al., 1990; Yang et al., 2005b; Kannan and Manthiram, 2006], and the polymer content in the composite electrode [Guy et al., 2004; Chew et al., 2007].

The power density of Li-ion batteries can be improved by increasing the interfacial area between the electrolyte and the active materials. Use of oxide nanoparticles as cathode materials in lithium-ion batteries presents numerous opportunities and challenges [Arico et al., 2005]. The opportunity exists to increase power density, and at the same time, there is a challenge in dealing with increased electrode/electrolyte side reactions. Both these phenomena are due to the high specific surface area of the nanoparticles compared to their micron-sized counterparts.

One process that can produce oxide nanoparticles on an industrial scale is flame spray pyrolysis (FSP). FSP is a flexible and scalable process [Mädler et al., 2002; Mueller et al., 2003], which is already used to produce fine powders for use as catalysts, coatings, dental fillers, etc. FSP was used by Ernst et al. [2007] to produce electrochemically active oxide nanoparticles with a spinel unit cell structure (LiMn_2O_4 , LiFe_5O_8 , and $\text{Li}_4\text{Ti}_5\text{O}_{12}$) [Ernst et al., 2007]. It has been demonstrated that FSP is a potentially cost-effective process for producing electrochemically active nano-sized spinel materials with controlled composition, crystallinity, and morphology. Furthermore, it can also be used to produce LiCoO_2 [Jang et al., 2004]. All these advantages make FSP an attractive process for producing nano-sized cathode materials.

In this work, LiV_3O_8 nanoparticles with crystallite sizes of about 24 nm were synthesized by FSP and electrochemically characterized. Aging mechanisms and engineering of the electrode are the main factors that contribute to capacity fading.

8.2 Synthesis Method

The experimental procedures for the flame spray pyrolysis (FSP) process are described earlier in Section 3.3.4. The precursor used for the flame synthesis was prepared by first dissolving 9.17 g of vanadium (V) oxytripropoxide into 18.7 mL of diethylene glycol (DEG). This solution was then stirred into 19.0 mL of toluene and 12.5 mL of 1.0 M lithium tert-butoxide (LTB) solution in tetrahydrofuran (THF). Subsequently, this precursor was injected at a rate of 3 mL min^{-1} through the reactor nozzle and dispersed with 5 L min^{-1} of oxygen into a fine spray. A pressure drop of 1.5 bars was maintained across the nozzle tip. A premixed flame fueled by 1 L min^{-1} of methane and 2 L min^{-1} of oxygen was maintained to ignite and support the combustion of the spray. A sheath gas of 5 L min^{-1} of oxygen surrounding the flame was used to ensure complete combustion. The powder was collected by placing a glass fiber filter above the flame and drawing the gas streams with a vacuum pump. The reactor was cooled with water to prevent overheating of the nozzle and precursor evaporation within the liquid feed lines.

8.3 Physical and Structural Characterizations

The X-ray diffraction (XRD) pattern of the as-synthesized LiV_3O_8 nanoparticles is shown in Figure 8.1. The XRD measurement was performed between 2θ angles of 10° and 70° at a scan rate of $0.03^\circ \text{ min}^{-1}$. The diffraction peak positions for the as-synthesized LiV_3O_8 nanoparticles matched well with the known layered-type LiV_3O_8 lattice constants given in the literature [Wadsley, 1957] (JCPDS 72-1193) as $a = 6.68 \text{ \AA}$, $b = 3.60 \text{ \AA}$, and $c = 12.03 \text{ \AA}$. Analysis of the XRD data indicated that the powder was

crystalline. When the Debye-Scherrer equation was applied to the (100) peak, it was calculated that the crystallite size of the as-synthesized LiV_3O_8 nanoparticles was 24 nm.

The overall morphology of the as-synthesized LiV_3O_8 nanoparticles was investigated by scanning electron microscopy (SEM). The average particle size observed in the SEM image (Fig. 8.2) is approximately 50 nm. Moreover, the particles are agglomerated in chain-like aggregates, which in principle could be broken with sufficient shear. Furthermore, the BET specific surface area was measured to be $30.5 \text{ m}^2 \text{ g}^{-1}$. This is significantly higher than those values ($< 6 \text{ m}^2 \text{ g}^{-1}$) reported in the literature [Yang et al., 2005b] for the sub-micron particles that could be produced with existing technologies.

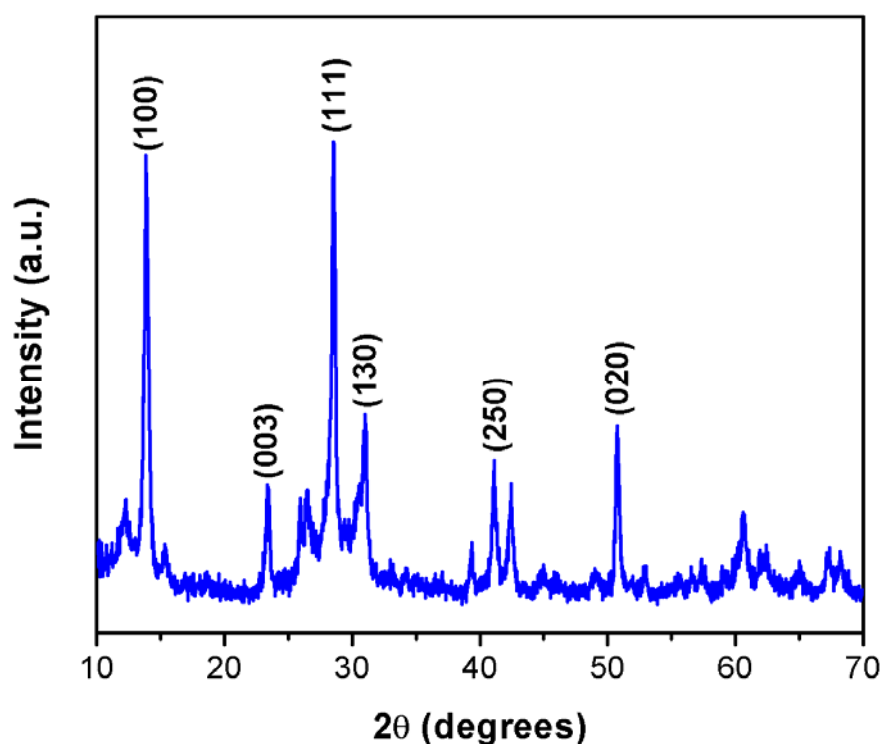


Fig. 8.1. XRD pattern of the LiV_3O_8 nanoparticles synthesized by FSP.

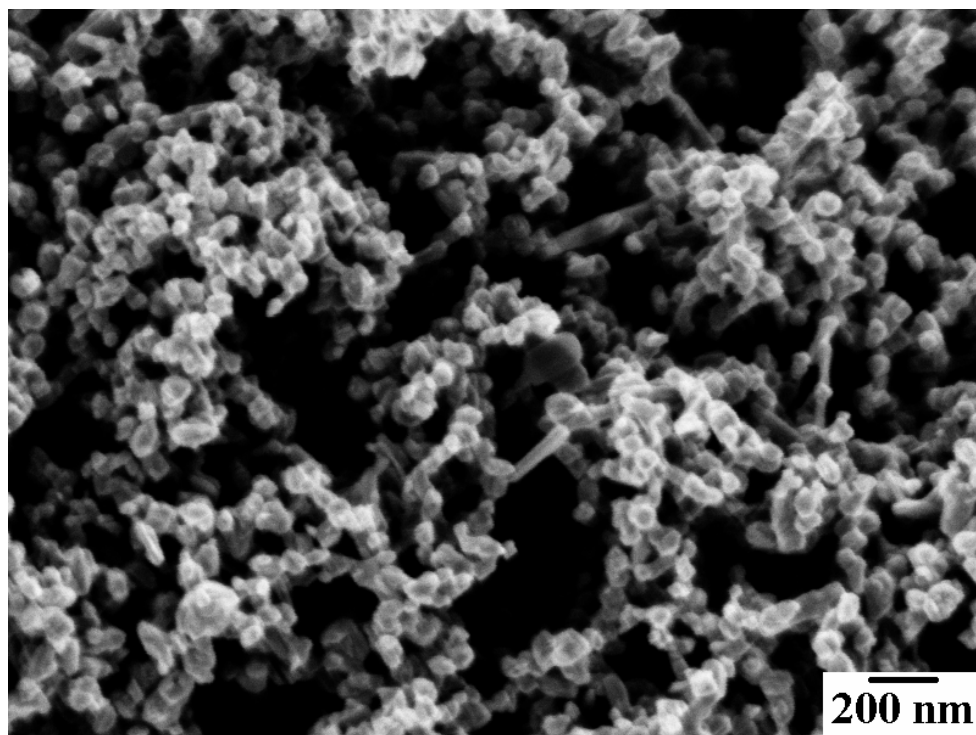


Fig. 8.2. SEM image of the LiV_3O_8 nanoparticles synthesized by FSP.

Transmission electron microscope (TEM) images of the LiV_3O_8 nanoparticles synthesized via FSP are shown in Figure 8.3. As can be seen from Figure 8.3(a), the LiV_3O_8 particles are nanosized in nature, but not exactly spherical in shape. The single particles are less than 100 nm in size, as can be seen in the TEM image (Fig. 8.3(a)), which is in good agreement with the estimation from the XRD pattern. Furthermore, from the high-resolution TEM image in Figure 8.3(b), the strongly crystalline structure of the flame spray pyrolyzed LiV_3O_8 nanoparticles is well-defined by the highlighted (100) lattice diffraction. Moreover, the corresponding selected area electron diffraction (SAED) pattern for the flame spray pyrolyzed LiV_3O_8 nanoparticles is shown in the inset of Figure 8.3(b), revealing the crystal lattice parameters of the LiV_3O_8 nanoparticles, which is in accordance with the monoclinic phase of LiV_3O_8 (JCPDS 72-1193).

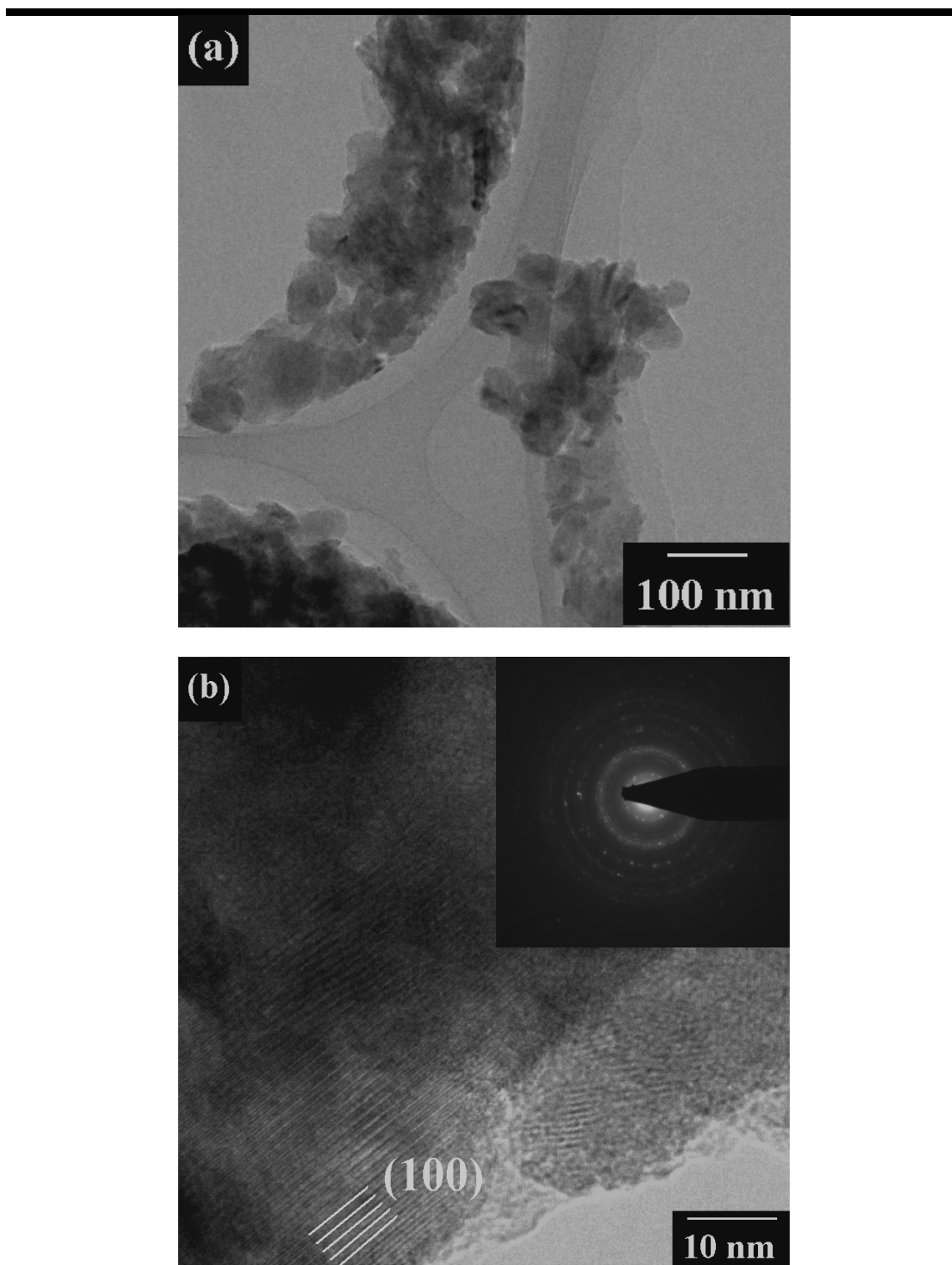


Fig. 8.3. TEM images of LiV_3O_8 nanoparticles synthesized via FSP: (a) low resolution image, showing the nanosized nature of the particles; and (b) high-resolution image, with the (100) crystalline lattice parameter highlighted (inset: the corresponding selected area electron diffraction (SAED) pattern for the LiV_3O_8 nanoparticles).

8.4 Electrochemical Performance

A mixture of the nanosized LiV_3O_8 FSP-made powder, and two types of carbon black (Super P and Ensaco 350) in the weight ratio of 7:1:1, were dispersed within an organic solution of N-methylpyrrolidinone (NMP). This suspension was then added to a solution composed of 10 wt.% polyvinylidene fluoride (PVDF) dissolved in NMP, forming a viscous slurry. Subsequently, the slurry was doctor bladed at a thickness of 200 μm onto an aluminum foil and dried under vacuum at 110 $^\circ\text{C}$ overnight, in order to remove the NMP, thus forming the composite electrode that was used for the electrochemical testing. The active electromaterial, LiV_3O_8 , accounted for 70 wt.% of the composite electrodes.

Cyclic voltammograms of the LiV_3O_8 powder are shown in Figure 8.4 for the first 20 charge-discharge cycles. The oxidative and reductive reactions are seen to diminish rapidly from the 1st to the 20th cycle due to capacity fading. Because the basic shape of these voltammograms remains roughly the same after 20 cycles, no significant change in the crystallography is expected between these cycles. This indicates that the decrease in specific capacity is likely due to the loss of electrochemically active mass contributing to the capacity. Possible losses could be due to the dissolution of LiV_3O_8 into the electrolyte [Jouanneau et al., 2005] or the reduction in contact between the active mass and electrolyte and/or electrically conductive network.

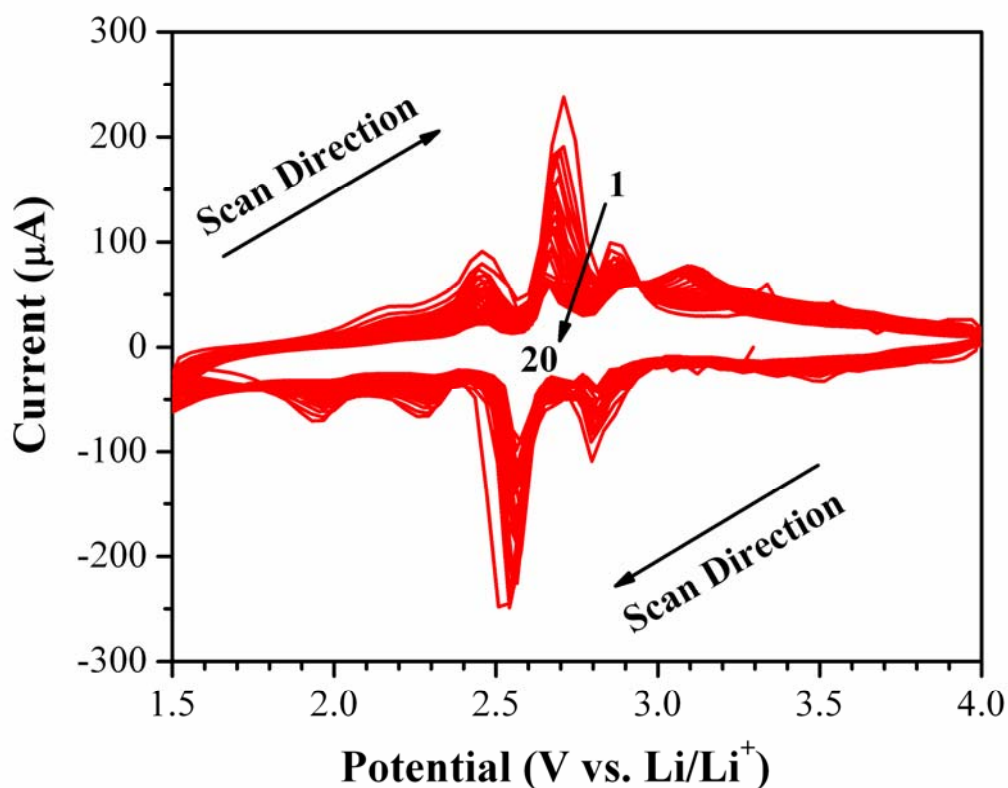


Fig. 8.4. Cyclic voltammograms (CVs) of flame spray pyrolyzed LiV_3O_8 nanoparticles, recorded at 0.1 mV s^{-1} from 1.5 to 4.0 V for the first 20 cycles.

Figure 8.5 shows the cycling behaviour of the as-synthesized LiV_3O_8 electrode. A non-restricted cycling procedure was used between 2 V and 4 V vs. Li/Li^+ at a cycling rate of 100 mA g^{-1} . The first discharge (Li^+ insertion) was done from the open circuit potential of about 3.3 V, amounting to a capacity of 271 mAh g^{-1} . This was then followed by charging (Li^+ extraction) to a potential of 4 V, amounting to a capacity of 315 mAh g^{-1} . The general trend thereafter is a gradual decrease in specific capacity.

Engineering of the electrode and active material dissolution would likely decrease the decline in specific capacity. It has been seen in other work that preparation of the electrode can play an important role in the cycling capacity of an active material [Guy et al., 2005]. Dissolution of lithium trivanadate has been seen to be a major aging mechanism for this substance [Jouanneau et al., 2005], and the high BET specific surface area of the material presented in this work ($> 30 \text{ m}^2 \text{ g}^{-1}$) would only increase the kinetics of the material's dissolution.

In this work, the irreversible capacity loss (Q_{irrev}) is defined as follows:

$$Q_{\text{irrev}}(\%) = \frac{C_D - C_C}{C_D} \times 100 \quad (8.1)$$

where C_D and C_C are the discharge and charge capacities, respectively.

What is noteworthy is that after the first 30 cycles, more lithium is extracted than inserted into the material, i.e., more lithium was coming out of the electrode than was put in during Li^+ insertion. One reason could be that the dissolution of LiV_3O_8 during Li^+ extraction (charging) causes additional Li^+ to be released. Another possibility could be that Li^+ ions are being trapped in the passivation layer during cycling. Nevertheless, further investigation is required to confirm one of these reasons with certainty.

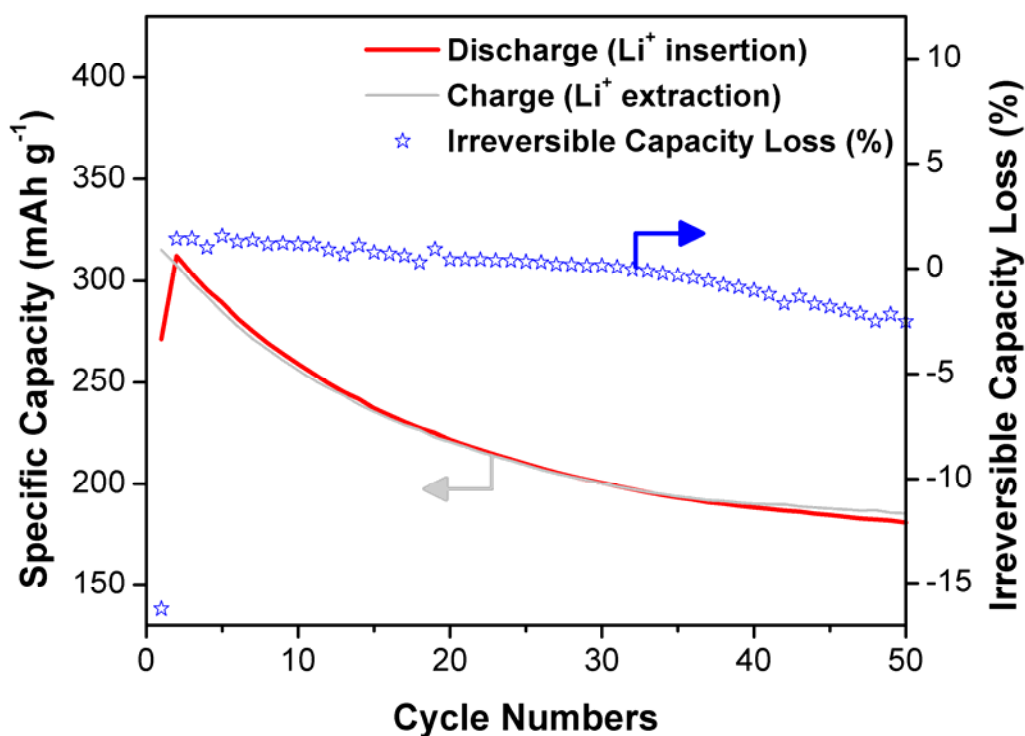


Fig. 8.5. Cycle life behaviour for a compound electrode with the FSP-made LiV_3O_8 nanoparticles as the active electromaterial. The current density applied was 100 mA g^{-1} , with cut-off potentials of 2 and 4 V.

Figure 8.6 summarizes the 2nd, 10th, and 50th electrochemical lithiation (discharge)/de-lithiation (charge) capacity data for the as-synthesized LiV_3O_8 electrode. The calculated capacities were solely based on the active material, LiV_3O_8 nanoparticles. It can be seen that the LiV_3O_8 electrode shows capacity fading behaviour upon prolonged cycling. However, the as-synthesized LiV_3O_8 electrode still maintained fairly high Li-ion insertion/de-insertion capacity even after 50 cycles, retaining a discharge capacity of 180 mAh g^{-1} . As the shape of the discharge-charge plots were similar even after 50 cycles, the likely reason for loss of capacity is the loss of active mass through dissolution into the electrolyte.

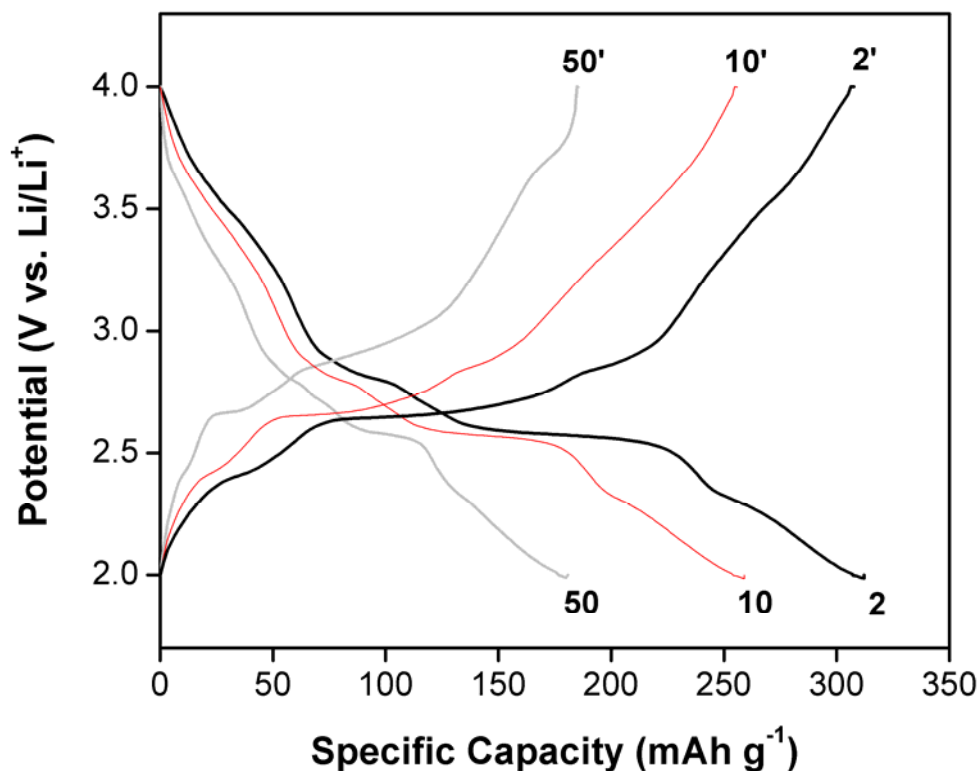


Fig. 8.6. The 2nd, 10th, and 50th cycle discharge/charge plots of LiV_3O_8 electrode, with the numbers indicating the cycle number. Cycling took place between 2 V and 4 V versus Li/Li^+ at a cycling rate of 100 mA g^{-1} .

The dependence of the specific capacity on the current density is shown in Figure 8.7, where the first discharge and charge were cycled between 2 and 4 V. The discharge capacity decreased as the current density increased, with the initial discharge capacity for the LiV_3O_8 nanostructured electrode 259 mAh g^{-1} (at 0.67C). Subsequently, the LiV_3O_8 nanostructured electrode demonstrated good rate capabilities, even up to the 16.7C rate (corresponding to 2500 mA g^{-1}), retaining a discharge capacity above 100 mAh g^{-1} . This may be because the distance Li^+ must diffuse in the nanoparticle is smaller (24 nm) and also due to the large surface area ($30.5 \text{ m}^2 \text{ g}^{-1}$) of the nanostructured electrode [Kannan and Manthiram, 2006].

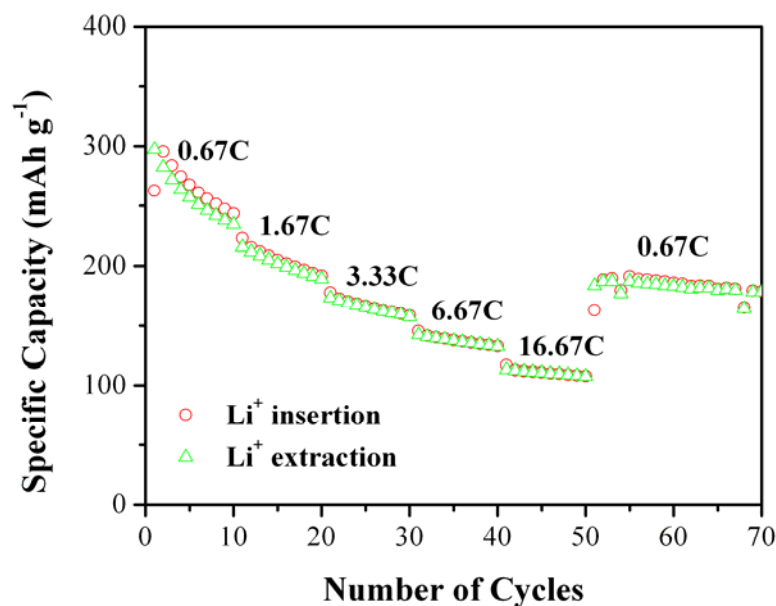


Fig. 8.7. Cycling behaviour for the FSP-made nanostructured LiV_3O_8 electrode at different current densities, when cycled between 2 V and 4 V versus Li/Li^+ . The 1C rate is assumed to be equivalent to 150 mA g^{-1} in this case.

Jouanneau et al. [2005] have shown a relationship between the grain morphology and texture and the electrochemical performance of $\text{Li}_{1.1}\text{V}_3\text{O}_8$, where they reported that the size and the aggregation of the grains play a major role in the initial capacity, while the crystal shape seems to be the main factor influencing the cyclability of the electrode. They also showed that the capacity fading was due to a two-phase phenomenon at 2.6 V, which could be related to an increasingly drastic change in the cell lattice constants, leading to local damage of the crystal structure. The dissolution of a small quantity of V^{III} in the electrolyte may occur during the last electrochemical phenomenon at 2.35 V. However, Jouanneau et al. [2005] also reported that the electrochemical process at 2.3 V in discharge and 2.4 V in charge (2.35 V average) only appeared in sample with smaller average particle sizes.

Therefore, as can be seen from Figure 8.7, the initial discharge capacities (Li^+ insertion) are higher than the charge capacities (Li^+ extraction) at lower current density (0.67C). However, at higher current density (up to 16.67C), the charge capacities are comparable to the discharge capacities. This means that cycling at higher current density might play a very important role in maximizing coulombic efficiency for electrodes with high surface area and small particle size. This might also minimize the vanadium dissolution and the impact of the phase transformation at 2.6 V. However, more studies in the future should address this problem.

8.5 Conclusions

LiV_3O_8 nanoparticles with sizes of approximately 24 nm have been synthesized by flame spray pyrolysis for the first time. This is an attractive process as it can be scaled to industrial production levels. Material and electrochemical characterizations were conducted for the as-synthesized powder. XRD analysis indicated that the powder is crystalline in nature, and the BET specific surface area was measured to be $30.5 \text{ m}^2 \text{ g}^{-1}$. The as-synthesized LiV_3O_8 electrode exhibited fairly high Li-ion insertion/de-insertion capacity even after 50 cycles, retaining a discharge capacity of 180 mAh g^{-1} . Capacity fading of the electrodes containing the FSP-made nanoparticles is attributed to the loss of active material through dissolution into the electrolyte and also to a phase transformation at 2.6 V. Nevertheless, this powder shows promise as a cathode material for use in high-powered applications in Li-ion batteries.

CHAPTER 9

LITHIUM MANGANESE OXIDE THIN FILM SYNTHESIZED BY PULSED LASER DEPOSITION AS MODEL CATHODE FOR LITHIUM-ION BATTERIES

9.1 Introduction

Technological improvements in rechargeable solid-state lithium ion batteries are being driven by an ever-increasing demand for portable electronic devices and the enormous interest in the hybrid electric vehicle market [Tarascon and Armand, 2001]. The search for materials that provide higher storage capacity, longer operating times, and faster recharging times, as well as safety, environmental compatibility, and low production costs for a large variety of applications, is a challenging task today [Winter et al., 1998]. However, in order to achieve the above-mentioned technical requirements, an in-depth understanding of the Li-ion transfer kinetics is necessary. Amongst the processes that take place in lithium-ion batteries are the diffusion of Li-ions through the active electromaterials and their subsequent migration through the electrolyte, the intercalation and deintercalation of the Li-ions, and also the influence of lattice defects on the charge/discharge cycles [Whittingham, 1976].

A good knowledge and understanding of these processes is essential for the optimization and also the enhancement of the battery's performance. The migration and diffusion of Li-ions are relatively slow and can be shortened by using small particle size active materials [Ammundsen and Paulsen, 2001]. This will increase the effective surface area of the electrodes, resulting in the interfacial reaction becoming the rate-controlling step of the overall electrochemical reactions, which also defines the performance of the battery [Kang et al., 2006].

LiMn_2O_4 is of great interest for use in rechargeable lithium-ion batteries because of its high voltage, low cost, and low toxicity [Thackeray et al., 1983; Shokoohi et al., 1991; Tarascon and Guyomard, 1993; Lanz et al., 2003]. Nevertheless, capacity fading at elevated temperatures and during overcharge has slowed the application of LiMn_2O_4 in commercial cells. Many studies have been dedicated to the understanding and resolution of the performance degradation. However, precise measurements of the kinetics of Li intercalation under conditions leading to degradation are difficult with porous electrodes, since degradation often leads to disconnection. Studies of rate processes within porous electrodes suffer from the additional complication of solid-phase and solution-phase resistances [Chen et al., 1997]. A thin film oxide electrode is a useful model system for the study of electrochemical properties without the above limitations. The influence of binders and conductive diluents is also avoided, and the effects of morphology may be quantifiable [Striebel et al., 1999]. Oxides such as LiMn_2O_4 form a spinel structure (with space group $Fd3m$), whose reaction sites can be very well defined [Striebel et al., 1999], and are therefore very suitable as model electrode materials for the investigation of the electrochemical properties of Li-ion batteries.

Different thin film growth techniques for making LiMn_2O_4 thin films have been employed in the literature, such as chemical vapour deposition [Liu et al., 1999b], electron beam evaporation [Shokoohi et al., 1992; Thackeray et al., 1997; Bates et al., 2000], electrostatic spray deposition [Chen et al., 1997; Uchida et al., 2001; Anzue et al., 2003; Shui et al., 2004], laser spark atomization [Singh et al., 2001], pulsed laser deposition [Striebel et al., 1996; Morcrette et al., 1998; Rougier et al., 1998a,b; Inaba et al., 1999; Julien et al., 2000; Singh et al., 2001 and 2002; Yamada et al., 2003; Dumont et al., 2006; Otsuji et al., 2006; Ouyang et al., 2006; Tang et al., 2006a,b and 2007], pyrolytic preparation [Miura and Kishi, 1995], RF magnetron sputtering [Hwang et al., 1994; Moon et al., 2003; Chen et al., 2004b; Lee et al., 2004; Chiu et al., 2005], sol–gel [Kostecki et al., 1999; Massarotti et al., 1999; Lee and Smith, 2005; Chiu et al., 2006; Rho et al., 2006], and most recently, the solution growth technique [Das et al., 2005; Wu et al., 2006 and 2007].

Among them, pulsed laser deposition (PLD) is a powerful and easy method for producing high quality and dense films without post-deposition annealing. PLD is also one of the most suitable methods for preparing thin films of complex oxides [Striebel et al., 1996], especially in the growth of materials containing evaporable components with complex stoichiometry. For this reason it is often used to fabricate the lithium transition metal oxides, especially for cathode materials, where lithium loss to volatilization could occur in conventional evaporation methods [Julien et al., 2000]. Previous studies of LiMn_2O_4 films, produced by PLD have shown them to be very stable during electrochemical cycling, even with over-discharge and over-charge to voltages up to 5 V vs. Li/Li^+ , as shown by cyclic voltammetry [Rougier et al., 1998].

In the present work, LiMn_2O_4 thin films were fabricated by PLD and were analyzed mainly by Mrs. Franziska Simmen (PhD Student, Material Group, Battery Group, Paul Scherrer Institute). These LiMn_2O_4 thin films were characterized physically by X-ray diffraction (XRD), Rutherford Backscattering Spectrometry (RBS), elastic recoil detection analysis (ERDA), Dektak profilometry, scanning electron microscopy (SEM), atomic force microscopy (AFM), and Raman spectroscopy, and also electrochemically by cyclic voltammetry (CV) and charge/discharge tests. The effect of the type of substrate used for deposition and that of the film thickness on the electrochemical performance of the LiMn_2O_4 thin films, especially on their interfacial properties, were also thoroughly investigated.

9.2 Synthesis Method

Figure 9.1(a) shows a schematic diagram of the experimental set-up for the PLD process. Thin films of LiMn_2O_4 were deposited by ablation of a rotating rod target of stoichiometric LiMn_2O_4 , which was fabricated by sintering a stoichiometric oxide of LiMn_2O_4 at 800 °C for 30 mins. The PLD experiments were carried out in a standard vacuum chamber (see Fig. 9.1(b)), which allows a background pressure of O_2 of approximately 0.2 mbar. The distance between the substrate and the target was kept at 4 cm. All deposition experiments were performed with a KrF excimer laser ($\lambda = 248$ nm), with a pulse width of 20 ns and a repetition rate of 10 Hz. The fluence (see Figure 9.1(c)) of the laser beam was kept constant in the range between 4.3 and 4.6 J cm^{-2} for all PLD experiments. The substrate temperature was kept at 773 K (or 500 °C) during the deposition process.

Among the experimental parameters that were varied for this research work were the type of substrate used (silicon or stainless steel with MgO) and the number of pulses from the laser beam (8400 to 27000 pulses) applied during the pulsed laser deposition of the LiMn_2O_4 thin films.

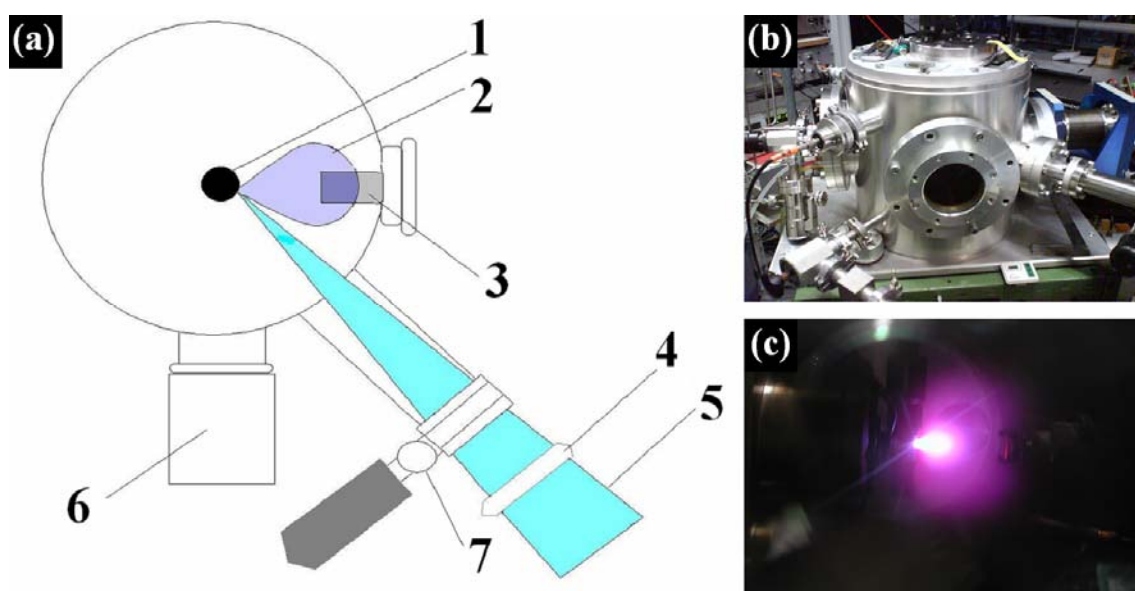


Fig. 9.1. (a) Schematic diagram of the experimental set-up for the pulsed laser deposition (PLD) of LiMn_2O_4 thin films: (1) cylindrical target rod, (2) plasma plume generated by the laser beam, (3) heated and rotating substrate, (4) focusing lens, (5) laser beam, (6) vacuum pump, and (7) inlet for oxygen; (b) a photograph depicting a real PLD chamber used in this research work at the Materials Group, Paul Scherrer Institute, Switzerland; and (c) a photograph showing a PLD experiment in action, where a plasma plume (purple cloud) that was generated from the laser beam heating the target is deposited onto the heated substrate [image obtained from Mrs. Franziska Simmen].

9.3 LiMn₂O₄ Thin Films Deposited on Silicon Substrate

Detailed deposition conditions for the fabrication of LiMn₂O₄ thin films on Si (100) substrates via PLD are summarized below in Table 9.1. The deposition conditions used here, such as a background oxygen pressure of 0.2 mbar, a substrate temperature of 773 K, and a target-substrate distance of 4 cm, were the optimum conditions recommended by Dumont et al. [2006], a former colleague of Mrs. Franziska Simmen, who prepared and analyzed these LiMn₂O₄ thin films in the Paul Scherrer Institute, Switzerland.

Table 9.1: Deposition conditions of LiMn₂O₄ thin films on Si (100) substrate.

Laser	KrF excimer laser
	Wavelength, λ : 248 nm
	Pulse width, τ : 20 ns
	Repetition rate: 10 Hz
	Laser Fluence, ϕ : 4.3-4.6 J cm ⁻²
No. of Pulses, N ^o	18000 Pulses
Target	LiMn ₂ O ₄ rod (stoichiometric)
Substrate	Si (100) wafer
Target-Substrate Distance, d _{t-s}	4 cm
Substrate Temperature, T _s	773 K (500 °C)
Oxygen Gas Background Pressure, Po ₂	0.2 mbar

9.3.1 Physical and Structural Characterizations

The crystallinity of LiMn_2O_4 thin film deposited on the Si (100) substrate was characterized by X-ray diffraction (XRD). The XRD pattern in Figure 9.2 shows that LiMn_2O_4 thin film deposited on silicon is polycrystalline, with a spinel structure, and is indexed using the $Fd3m$ symmetry. The peaks matched well with the standard cubic phase LiMn_2O_4 (JCPDS 35-0782). As can be seen from the XRD pattern, the (111) and (222) peaks are quite sharp, suggesting the presence of large crystalline grains in the film [Singh et al., 2001].

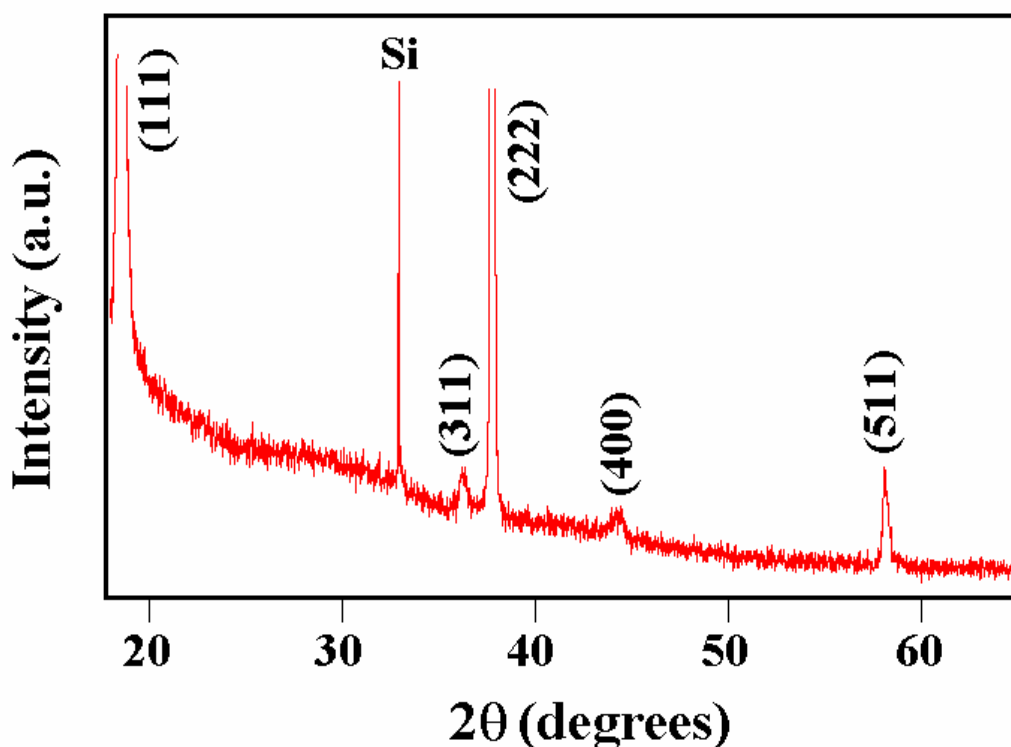


Fig. 9.2. X-ray diffraction (XRD) pattern of LiMn_2O_4 thin film on Si (100) substrate [analyzed by Mrs. Franziska Simmen]. Numbers on peaks denote the hkl index (JCPDS 35-0782).

In general, an XRD spectrum only provides qualitative information, such as the presence of spinel structure in the LiMn_2O_4 thin film. However, since amorphous species could not be detected by XRD, the ratio of crystalline to noncrystalline species in the thin film could not be obtained. Therefore, in this case, Rutherford Backscattering Spectrometry (RBS) and Elastic Recoil Detection Analysis (ERDA) analyzed the composition of the LiMn_2O_4 thin film deposited on silicon, for the determination of the O/Mn and Li/Mn ratios, respectively. ERDA was used to quantify the amount of lithium in the thin film because lithium is too light for analysis by RBS. Both the RBS and ERDA measurements were conducted by Dr. Max Döbeli and Dr. Marc Mallepell, from the Institute of Particle Physics at the Swiss Federal Institute of Technology (ETH), Zurich, Switzerland.

The Li/Mn and O/Mn ratios in the LiMn_2O_4 thin film deposited on silicon, calculated from the ERDA and RBS analysis, were $0.47 (\pm 0.02)$ and $1.95 (\pm 0.05)$, respectively. The LiMn_2O_4 thin film deposited on silicon is slightly lithium-deficient and oxygen-deficient, similar to the one analyzed by Dumont et al. [2006].

9.3.2 Electrochemical Performance

The LiMn_2O_4 thin film deposited on silicon was not able to be characterized electrochemically due to the poor electrical conductivity of the Si substrate. In order to electrochemically characterize the LiMn_2O_4 thin film fabricated under deposition conditions similar to those stated in Table 9.1, it is necessary to produce LiMn_2O_4 thin film on another type of substrate, preferably more conductive, such as stainless steel.

9.4 LiMn₂O₄ Thin Films Deposited on Stainless Steel Substrate

Detailed deposition conditions for the fabrication of LiMn₂O₄ thin films on stainless steel (SS) substrate via PLD are summarized below in Table 9.2. The deposition conditions used here, such as a background oxygen pressure of 0.2 mbar, a substrate temperature of 773 K, and a target-substrate distance of 4 cm, were the optimum conditions, similar to those applied earlier for the Si (100) substrate. All the LiMn₂O₄ thin films for this project were prepared and analyzed mainly by Mrs. Franziska Simmen (PhD Student, Material Group, Battery Group, Paul Scherrer Institute).

Table 9.2: Deposition conditions of LiMn₂O₄ thin films on stainless steel substrate.

Laser	KrF excimer laser
	Wavelength, λ : 248 nm
	Pulse width, τ : 20 ns
	Repetition rate: 10 Hz
	Laser Fluence, ϕ : 4.3-4.6 J cm ⁻²
No. of Pulses, N ^o	8400-27000 Pulses
Target	LiMn ₂ O ₄ rod (stoichiometric)
Substrate	Stainless steel grids
Target-Substrate Distance, d _{t-s}	4 cm
Substrate Temperature, T _s	773 K (500 °C)
Oxygen Gas Background Pressure, Po ₂	0.2 mbar
Post-Deposition Annealing	Cooling in air

9.4.1 Physical and Structural Characterizations

As can be seen from the stoichiometric data (ERDA/RBS) in Table 9.3, all LiMn_2O_4 thin films deposited on stainless steel substrate using different numbers of pulses and with cooling in air were highly lithium- and oxygen-deficient. Although the same deposition conditions were used as of those with the Si (100) substrate, the LiMn_2O_4 thin film compositions were totally different. However, as the number of pulses used was increased, both the lithium and oxygen contents were increased to values nearer to the optimum compositions. As the number of pulses used is increased, the chances of the light-weight lithium and oxygen atoms to be deposited onto the stainless steel surface would increase significantly [Striebel et al., 1996], resulting in higher lithium and oxygen content in the films.

Table 9.3: Stoichiometric (ERDA/RBS) and Raman data [measured and analyzed by Mrs. Franziska Simmen] for LiMn_2O_4 thin films deposited on stainless steel substrate with different numbers of pulses and cooling in air.

No. of Pulses, N°	Li/Mn Ratio	O/Mn Ratio	Raman Spectroscopy						
			Band Position (cm^{-1})						
$\lambda\text{-LiMn}_2\text{O}_4$ Powder *	0.50	2.00	382 (F_{2g})	426 (E_g)	483 (F_{2g})	580 (F_{2g})	625 (A_{1g})	N/A	N/A
8400 Pulses	0.29 ± 0.01	1.50 ± 0.08				570	613	655	723
18000 Pulses	0.40 ± 0.02	1.75 ± 0.09				571	609	640	724
27000 Pulses	0.39 ± 0.02	1.65 ± 0.08				597	635	658	

* The Raman spectroscopy band position values for the $\lambda\text{-LiMn}_2\text{O}_4$ powder are based on those reported by Julien and Massot [2003].

Moreover, from Table 9.3, the Raman spectroscopy data shows that there were peaks located above 625 cm^{-1} , which could be due to delithiated spinel such as $\text{Li}_{0.5}\text{Mn}_2\text{O}_4$, or in other words, the presence of lithium-deficient compounds in the films [Julien and Massot, 2003]. However, the Raman peaks located above 700 cm^{-1} that were observed in some of the LiMn_2O_4 thin films deposited on stainless steel substrate have not been previously reported. This could be interesting for further studies in future work related to LiMn_2O_4 thin film.

The XRD pattern in Figure 9.3 shows that LiMn_2O_4 thin films deposited on stainless steel substrate are polycrystalline, with a spinel structure, and can be indexed using the $Fd3m$ symmetry. The peaks matched well with the standard cubic phase LiMn_2O_4 (JCPDS 35-0782). However, for the LiMn_2O_4 thin films deposited at 8400 pulses (Fig. 9.3(a)), there are some unknown impurities present, which disappeared as the number of pulses used was increased to 27000 pulses (Fig. 9.3(b)). In addition, both films show fairly weak peaks, which corresponds to lower crystallinity.

The correlation between number of pulses used for deposition and the corresponding LiMn_2O_4 thin film thickness is shown in Figure 9.4. As the number of pulses increased from 8400 to 27000 pulses, the LiMn_2O_4 thin film thickness increased from 80 to 260 nm. However, the growth rate was non-linear. One of the possible reasons is the loss of lightweight lithium and oxygen atoms at lower pulse rates, resulting in lower film thickness at a lower pulse rate [Rougier et al., 1998a].

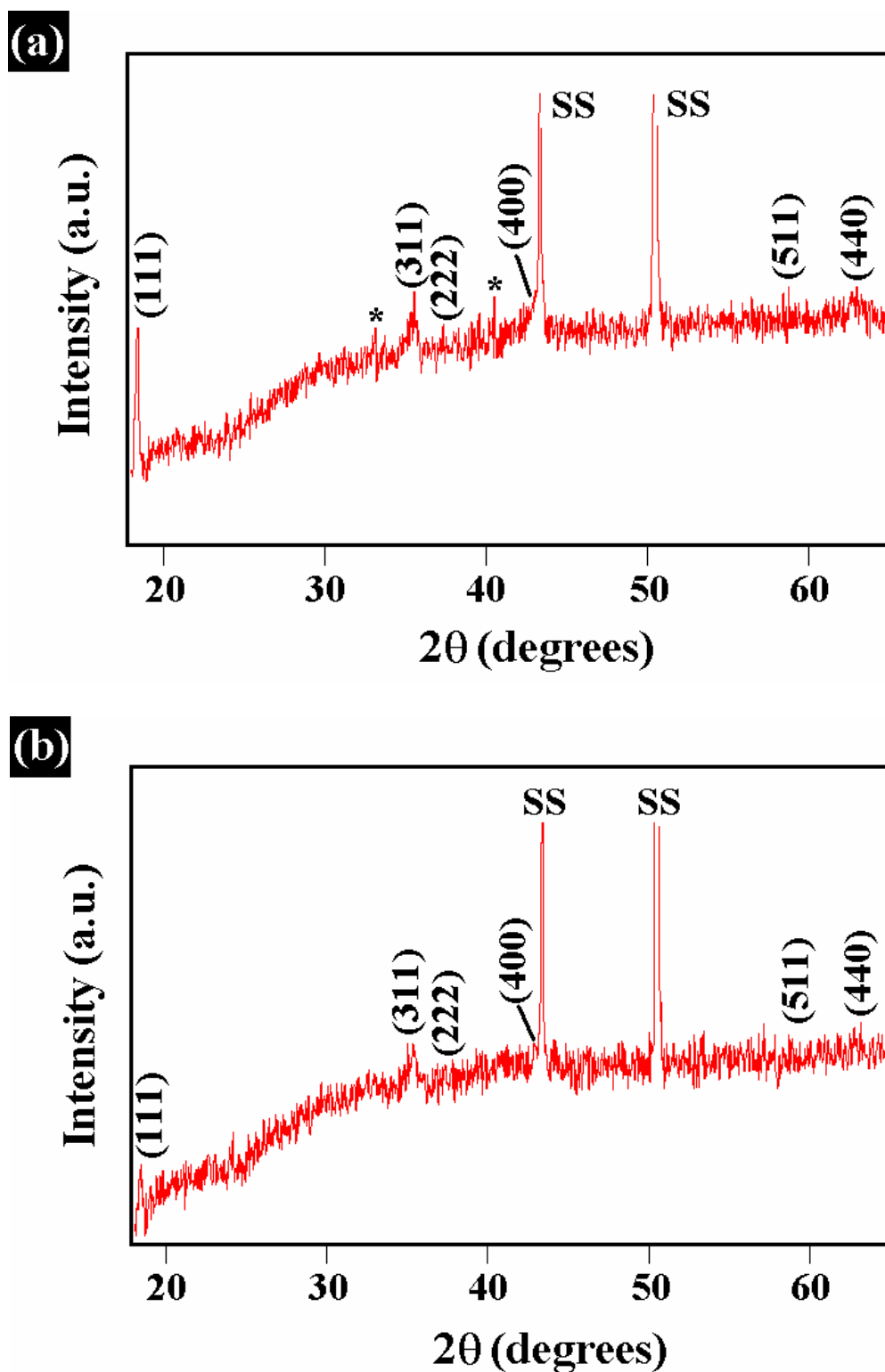


Fig. 9.3. XRD patterns of LiMn_2O_4 thin films deposited on stainless steel (SS) substrate:

(a) 8400 pulses, and (b) 27000 pulses [analyzed by Mrs. Franziska Simmen].

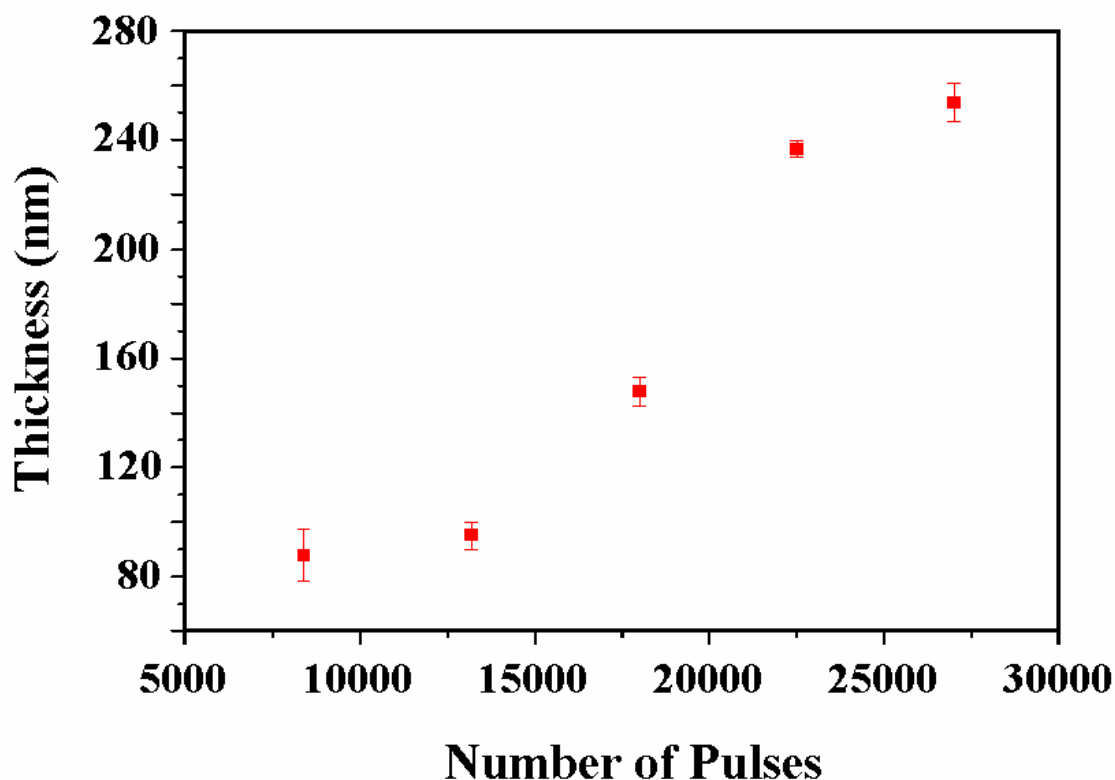


Fig. 9.4. Film thickness vs. number of pulses used in the deposition conditions when LiMn_2O_4 thin films were deposited onto stainless steel substrate heated to 500 °C and then cooled in an oxygen atmosphere [analyzed by Mrs. Franziska Simmen].

Figure 9.5 shows the surface topography measured by atomic force microscopy (AFM) of the as-deposited LiMn_2O_4 thin films on stainless steel substrate grown at 500 °C and cooled in an oxygen atmosphere with no further annealing. As the number of pulses increased from 8400 to 27000 pulses, the films' crystal sizes increased (to above 200 nm) and the surface of the films also became rougher and denser, with the root mean square (rms), roughness of the LiMn_2O_4 thin film deposited at 18000 pulses at approximately 39 nm.

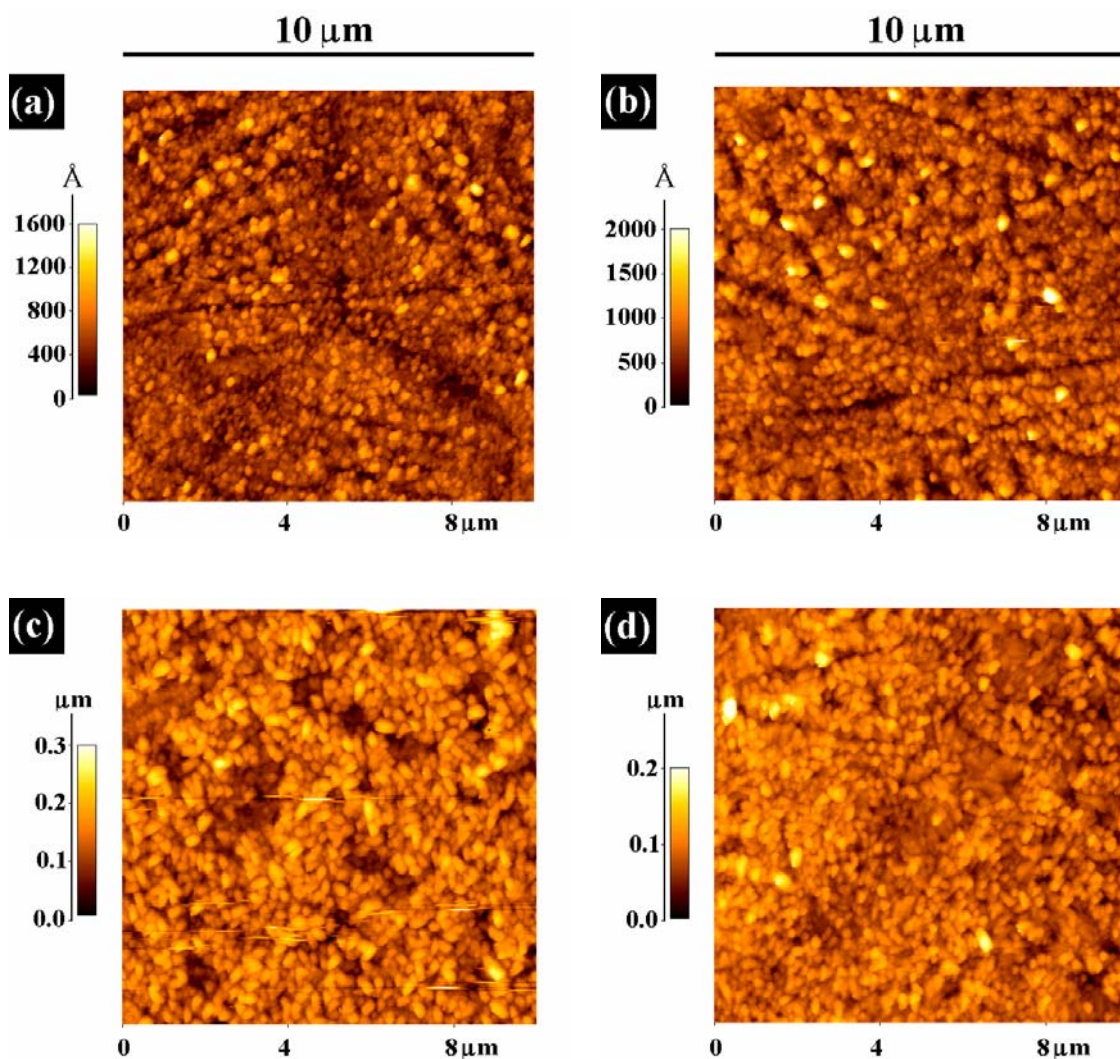


Fig. 9.5. Surface topography (flat images) as measured by atomic force microscopy (AFM) of the as-deposited LiMn₂O₄ thin films grown on stainless steel substrate at different numbers of pulses: (a) 8400 pulses, (b) 13200 pulses, (c) 18000 pulses, and (d) 27000 pulses. The films were cooled in air without post-deposition annealing.

9.4.2 Electrochemical Performance

For comparison purpose, LiMn_2O_4 electrodes were also prepared by the classical casting method. A mixture of micron-sized LiMn_2O_4 powder and carbon black (Super P), in the weight ratio of 7:2, was dispersed within an organic solution of N-methylpyrrolidinone (NMP). This suspension was then added to a solution composed of 10 wt.% polyvinylidene fluoride (PVDF) dissolved in NMP, forming a viscous slurry. Subsequently, the slurry was doctor bladed at a thickness of 200 μm onto aluminum foil and dried under vacuum at 110 $^\circ\text{C}$ overnight, in order to remove the NMP, thus forming the composite electrode that was used for the electrochemical testing. The active electromaterial, LiMn_2O_4 , accounted for 70 wt.% of the composite electrodes.

Cyclic voltammograms of the LiMn_2O_4 electrodes are shown in Figure 9.6 for the first 20 charge-discharge cycles. The oxidative and reductive reactions are seen to diminish rapidly from the 1st to the 20th cycle for the as-deposited LiMn_2O_4 thin film electrode (Fig. 9.6(b)). Because the basic shape of these voltammograms remains roughly the same after 20 cycles, no significant change in the crystallography is expected between these cycles. This indicates that the decrease in specific capacity is likely due to the loss of electrochemically active mass contributing to the capacity [Tarascon and Guyomard, 1993]. Comparing the maximum charge current for both LiMn_2O_4 electrodes, it can be estimated that the active mass of the as-deposited LiMn_2O_4 thin film electrode is approximately 0.17 mg compared to 5.33 mg for the classical LiMn_2O_4 electrode. Furthermore, the amount of polarization was significantly reduced when thin film electrode was used, compared to classical electrode, which may be due to lower resistance.

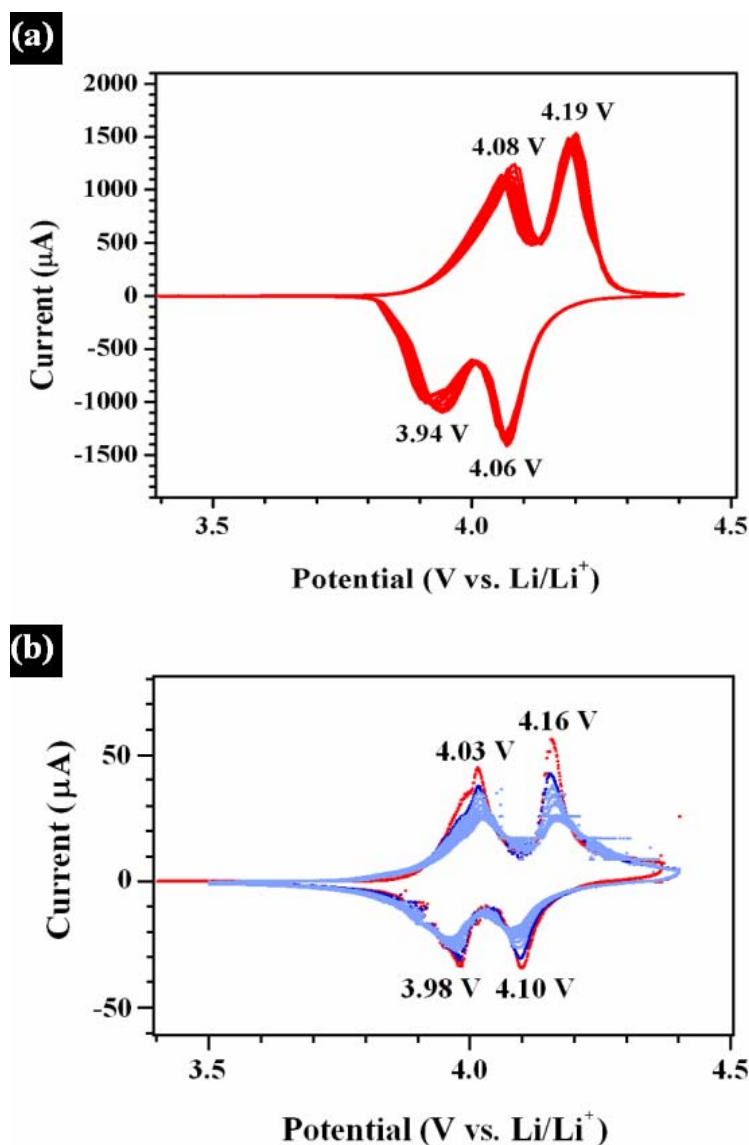


Fig. 9.6. Cyclic voltammograms (CVs) of different types of LiMn₂O₄ electrode recorded at 0.1 mV s⁻¹ from 3.5 to 4.4 V for the first 20 cycles: (a) classical method, where a (70 wt.% LiMn₂O₄ + 20 wt.% CB + 10 wt.% PVDF) slurry mixture was coated onto aluminium foil, and (b) as-deposited LiMn₂O₄ thin film grown on stainless steel substrate via PLD [analyzed by Mrs. Franziska Simmen]. The LiMn₂O₄ thin film was deposited at $N^{\circ} = 27000$ pulses, $T_s = 500$ °C, $d_{t-s} = 4$ cm, $\phi = 4.3$ J cm⁻², and cooled in air with no post-deposition annealing.

Figure 9.7 shows the cycling behaviour of the as-deposited LiMn_2O_4 thin film electrode on stainless steel substrate. A non-restricted cycling procedure was used between 3.5 V and 4.4 V vs. Li/Li^+ at a cycling rate of $50 \mu\text{A cm}^{-2}$. The film deposited at the lowest pulse rate (or the thinnest), i.e., 8400 pulses, had the best cycling performance, retaining $48 \mu\text{Ah cm}^{-2} \mu\text{m}^{-1}$ beyond 40 cycles. This translates into more than 85 % capacity retained compared to the first charge capacity. Film with lower thickness would have a shorter path for Li^+ diffusion and also lower electrolyte resistance [Tarascon and Guyomard, 1993].

Furthermore, after prolonged cycling beyond 100 cycles, the as-deposited LiMn_2O_4 thin film electrode on stainless steel substrate that was deposited at 8400 pulses still maintained fairly high Li-ion insertion/de-insertion capacity, retaining a charge and discharge capacity of 48 and $45 \mu\text{Ah cm}^{-2} \mu\text{m}^{-1}$, respectively (see Fig. 9.8). However, as the rate of Li^+ extraction is higher than that of Li^+ insertion, this indicates that the original thin film is lithium-rich or oxygen-deficient. Clearly, as demonstrated by other stoichiometric measurements, an oxygen-deficient case is more likely.

The dependence of the specific capacity on the cycling rate (or current density) is shown in Figure 9.9, where the first charge and discharge were cycled between 3.5 and 4.4 V. The specific capacity decreased as the current density increased, and the initial charge capacity for the as-deposited LiMn_2O_4 thin film electrode was $55 \mu\text{Ah cm}^{-2} \mu\text{m}^{-1}$ (at 2C). Subsequently, the as-deposited LiMn_2O_4 thin film electrode demonstrated good rate capabilities, even up to the 32C rate (corresponding to $160 \mu\text{A cm}^{-2}$), retaining a charge capacity above $40 \mu\text{Ah cm}^{-2} \mu\text{m}^{-1}$.

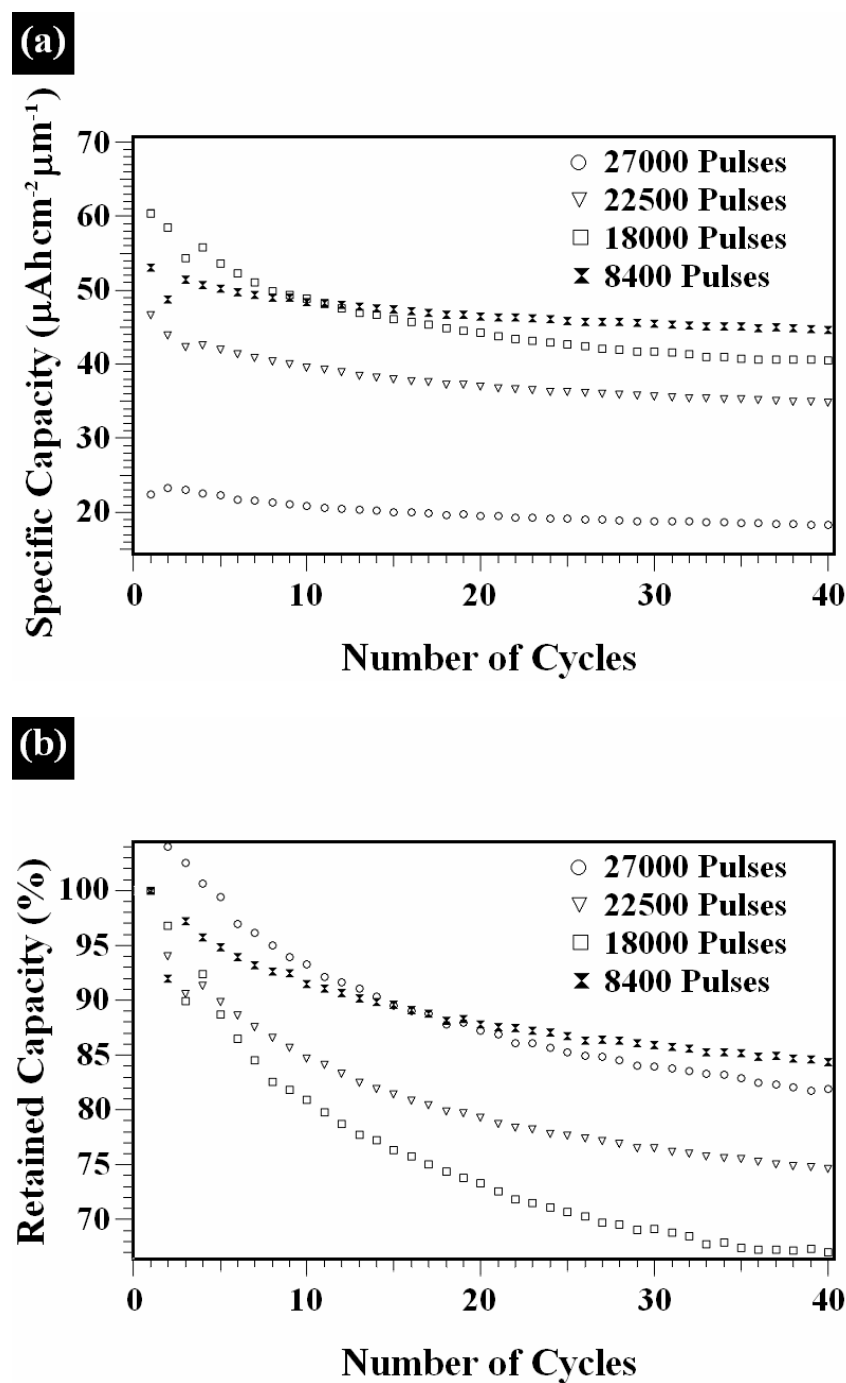


Fig. 9.7. (a) Cycle life of the as-deposited LiMn_2O_4 thin film electrodes on stainless steel substrate cycled between 3.5 V and 4.4 V versus Li/Li^+ at a cycling rate of $50 \mu\text{A cm}^{-2}$. (b) The corresponding capacity retained compared to the first discharge capacity in (a) [analyzed by Mrs. Franziska Simmen].

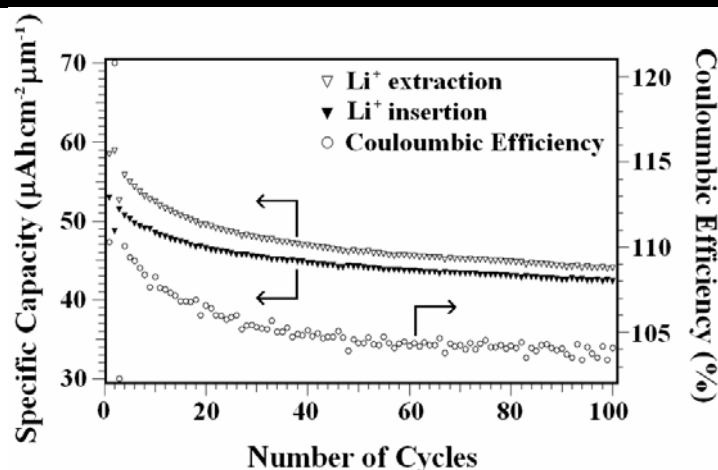


Fig. 9.8. Cycle life behaviour of the as-deposited LiMn_2O_4 thin film electrode on stainless steel substrate cycled between 3.5 V and 4.4 V versus Li/Li^+ at a cycling rate of $50 \mu\text{A cm}^{-2}$. The LiMn_2O_4 thin film was deposited at $N^0 = 8400$ pulses, $T_s = 500^\circ\text{C}$, $d_{t-s} = 4 \text{ cm}$, $\phi = 4.3 \text{ J cm}^{-2}$, and cooled in air with no post-deposition annealing [analyzed by Mrs. Franziska Simmen].

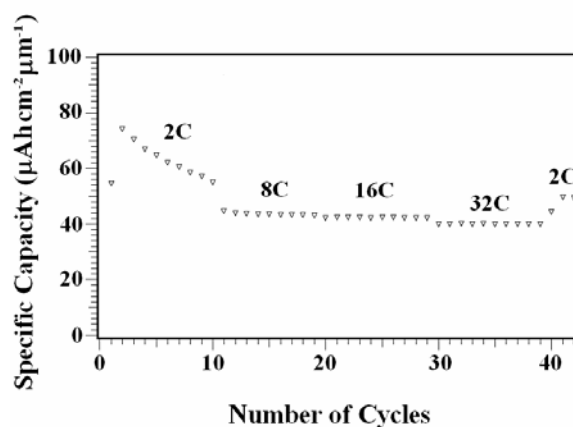


Fig. 9.9. Cycle life behaviour of the as-deposited LiMn_2O_4 thin film electrode on stainless steel substrate cycled between 3.5 V and 4.4 V versus Li/Li^+ at different cycling rates. The LiMn_2O_4 thin film was deposited at $N^0 = 13200$ pulses, $T_s = 500^\circ\text{C}$, $d_{t-s} = 4 \text{ cm}$, $\phi = 4.3 \text{ J cm}^{-2}$, and cooled in air with no post-deposition annealing [analyzed by Mrs. Franziska Simmen]. The 1C rate is assumed to be equivalent to $5 \mu\text{A cm}^{-2}$ in this case.

Figure 9.10 compares the changes in film morphology observed from SEM in the as-deposited state, before and after 100 charge-discharge cycles. The film mainly consists of crystalline agglomerates (> 200 nm), in agreement with what was observed from AFM (Fig. 9.5(c)). Significant changes were observed in the morphology of the LiMn_2O_4 thin film electrode after 100 charge-discharge cycles, revealing huge cracks and detachment of the electro-active LiMn_2O_4 thin film from the stainless steel substrate, with an obvious increment in film thickness (> 600 nm) as well. The presence of the cracks might be due to changes in crystal structure during the prolonged cycling or the dissolution of the manganese from the LiMn_2O_4 thin film electrode [Striebel et al., 1996], resulting in detachment from the substrate surface.

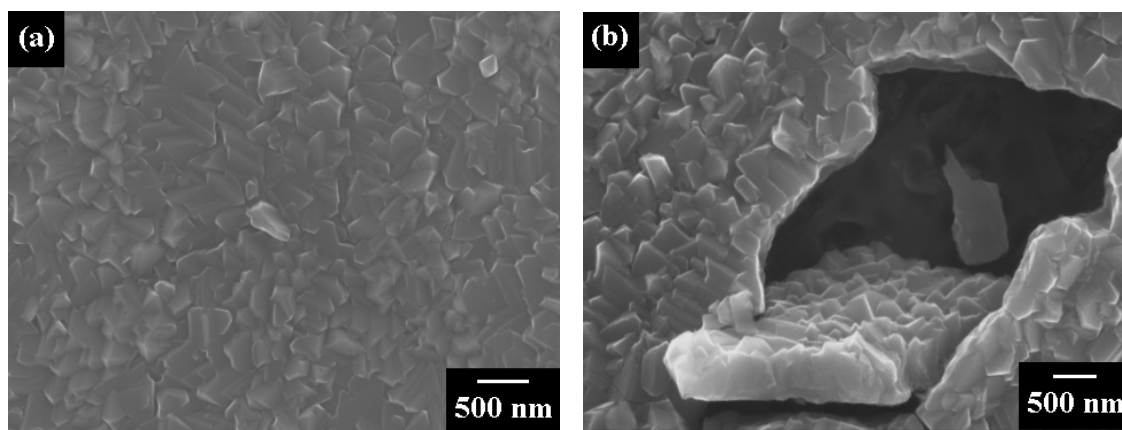


Fig. 9.10. SEM images of the as-deposited LiMn_2O_4 thin film electrode on stainless steel substrate: (a) before cycling, and (b) after 100 charge-discharge cycles. Cycling took place between 3.5 V and 4.4 V versus Li/Li^+ at a cycling rate of $50 \mu\text{A cm}^{-2}$. The LiMn_2O_4 thin film was deposited at $N^0 = 18000$ pulses, $T_s = 500^\circ\text{C}$, $d_{t-s} = 4$ cm, $\phi = 4.3$ J cm^{-2} , and cooled in air with no post-deposition annealing [measured by Dr. Anja Weber and obtained from Mrs. Franziska Simmen].

9.5 Conclusions

A series of LiMn_2O_4 thin films on either Si (100) or stainless steel substrate were successfully prepared via pulsed laser deposition (PLD). It was found that the compositions of the as-deposited LiMn_2O_4 thin films were not the same when deposited on stainless steel as compared to Si (100) substrate, even when the same deposition parameters were used in both cases. The as-deposited LiMn_2O_4 thin films on stainless steel substrate are highly lithium- and oxygen-deficient, as confirmed by ERDA/RBS and Raman analysis. Lithium and oxygen contents increased when the pulse rate was increased, leading to thicker films. However, LiMn_2O_4 thin film with the lowest deposition pulse rate (or the thinnest film) exhibited the best electrochemical performance, retaining a charge capacity of $48 \mu\text{Ah cm}^{-2} \mu\text{m}^{-1}$ beyond 100 cycles. The rate capability of the as-deposited LiMn_2O_4 thin film was also impressive, retaining a charge capacity above $40 \mu\text{Ah cm}^{-2} \mu\text{m}^{-1}$ even at 32C (equivalent to $160 \mu\text{A cm}^{-2}$).

CHAPTER 10

GENERAL CONCLUSIONS AND OUTLOOK

10.1 General Conclusions

The aim of this doctoral work was to broaden our knowledge on the electrochemical properties of nanostructured materials for use as electrodes in lithium-ion rechargeable batteries, by means of physical, structural, and electrochemical characterization techniques. In the following sections, a summary of the outcomes will be given.

10.1.1 Nanostructured Anode Materials for Li-ion Storage

In this study, three major anode materials have been reviewed and analyzed in detail: SWCNT-based free-standing electrode, lead oxide (PbO) and lead oxide-carbon (PbO-C) nanocomposite electrodes, and also carbon-coated Si (Si-C) nanocomposite electrode. Two main techniques have been employed for the fabrication of the above-mentioned anode materials, i.e., the filtration method for the fabrication of free-standing SWCNT-based electrodes and the spray pyrolysis technique for the synthesis of nanocrystalline PbO, PbO-C nanocomposites, and carbon-coated Si nanocomposite materials.

Free-standing SWCNT paper electrodes have several advantages over the conventional slurry-pasted Cu-based electrodes, since they are lightweight, flexible, have good conductivity, and can be fabricated easily without using any metal substrate (Cu foil) or binder (PVDF). With the addition of both the carbon black and nanosized Si particles, the electrical conductivity and specific capacity of the free-standing SWCNT paper electrode were greatly enhanced, retaining a capacity of 400 mAh g⁻¹ beyond 100 cycles. However, the large irreversible capacity during the first cycle coupled with the high cost of SWCNTs at present might hamper the practical usage of the SWCNT paper electrodes for industrial or large-scale applications. Nevertheless, the use of this new design will provide a lightweight, self-supporting and free-standing electrode, with the possibility that it can be used in lithium-ion batteries for powering medical and miniature devices.

Nanocrystalline PbO and PbO-carbon nanocomposites have been successfully synthesized via in-situ spray pyrolysis of Pb(NO₃)₂/sugar solution at 800 °C. The spray-pyrolyzed powders consist of fine nanocrystalline PbO, which is homogeneously distributed within an amorphous carbon matrix and has a highly developed surface area (up to 6.6 m² g⁻¹). An increase in the average crystal size with increased furnace temperature or with decreased precursor solution concentration was observed and confirmed via XRD, SEM, and TEM analysis. A huge amount of carbon mass (> 80 wt.%) was lost during the spray pyrolysis process, when sugar (or sucrose) was used as the high-temperature carbon source. When applied as anode materials in Li-ion batteries, the PbO sprayed materials retain a reversible capacity above 60 mAh g⁻¹ beyond 50 cycles. The PbO-carbon nanocomposites showed an improved cycle life as the disordered carbon content increased. The presence of the carbon matrix, which is a

good electric conductor, provides an effective cushion to absorb volume change during the alloying and de-alloying processes within the lead region. However, the low reversible capacity achieved would not make the PbO-based system an attractive anode material for replacing the current graphite-based anode materials. Nevertheless, the experience obtained from the spray pyrolysis technique and also the prediction of carbon mass loss from this study will be greatly beneficial for other studies using the spray pyrolysis technique.

A similar spray pyrolysis technique used for the synthesis of PbO-C nanocomposites was applied for the preparation of carbon-coated Si nanocomposites. The only differences were the replacement of sugar with citric acid as the low-temperature carbon source and also the direct usage of nano-Si particles to form a suspension in ethanol, rather than a liquid precursor for the spray pyrolysis process. An amorphous carbon layer was successfully and homogeneously coated onto the nano-Si surface, with the average thickness between 1 and 10 nm. Thermogravimetric analysis (TGA) showed that a small amount of impurity was present in the form of undecomposed citric acid for the carbon-coated Si nanocomposite spray-pyrolyzed in air at 300 °C. A moderate amount of carbon mass (28-40 wt.%) was lost during the spray pyrolysis process at 400 °C in air, which was much better compared to sugar as the carbon source. No bulk SiO₂ or SiC crystalline phase was detected in the spray-pyrolyzed nanocomposites, as confirmed by XRD and TEM analysis. Carbon-coated Si nanocomposite showed a high discharge capacity of 1120 mAh g⁻¹ after 100 cycles, corresponding to the Si active mass contributing a specific capacity of 2495 mAh g⁻¹. The presence of the carbon-coating layer is responsible for the enhanced dimensional stability of the Si nanoparticles during the Li alloying/de-alloying processes, which then significantly

improves the electrical conductivity of the composites. In general, spheroidal carbon-coated Si nanocomposite is a promising candidate for use as a high-capacity anode material in the lithium-ion battery, as it has excellent specific capacity retention, high coulombic efficiency, and low cost, due to the abundance of both Si and carbon sources. However, the large first cycle irreversible capacity ($> 20\%$) would have to be reduced significantly in order for it to have any practical usage as a high-capacity anode material when combined with other cathode materials in a full cell.

10.1.2 Nanostructured Cathode Materials as Li-ion Providers

In this study, three major cathode materials have been reviewed and analyzed in detail, i.e., nanostructured vanadium oxide (V_2O_5) electrode, nanocrystalline lithium trivanadate (LiV_3O_8) electrode, and also lithium manganese oxide ($LiMn_2O_4$) thin film electrode. Three main techniques have been employed for the fabrication of the above-mentioned cathode materials: the co-precipitation method for the fabrication of nanostructured V_2O_5 electrode, the flame spray pyrolysis (FSP) technique for the synthesis of nanocrystalline V_2O_5 and LiV_3O_8 electrode, and the pulsed laser deposition (PLD) technique for the fabrication of $LiMn_2O_4$ thin film electrode.

V_2O_5 nanostructures were successfully prepared via a co-precipitation process followed by heating in vacuum at $300\text{ }^{\circ}\text{C}$ and also via the flame spray pyrolysis process in air. Both the precipitation-made and the FSP-made V_2O_5 powders were nanosized in nature (20-90 nm) and give a comparable BET specific surface area of $40\text{ m}^2\text{ g}^{-1}$. One-dimensional V_2O_5 nanofibers were also obtained with longer annealing time during the precipitation process. The V_2O_5 nanostructures are electrochemically active towards Li^+

insertion and extraction in the potential window of 1.5 V to 4.0 V. The V_2O_5 nanostructure shows an improved cycle life when the cut-off voltage for discharging is increased from 1.5 V to 2.5 V. The significant capacity loss when discharging to 1.5 V might be related to the dissolution of vanadium and the structural changes upon cycling in the larger potential span. However, when cycled between 2.5 V to 4.0 V vs. Li/Li^+ , the V_2O_5 nanostructured electrode retained a discharge capacity of 120 mAh g^{-1} beyond 100 cycles at a cycling rate of 100 mA g^{-1} and also an incredibly high capacity of 110 mAh g^{-1} at cycling rates up to 15C (or 2000 mA g^{-1}).

LiV_3O_8 nanoparticles with sizes of approximately 24 nm have been synthesized by flame spray pyrolysis for the first time. This is an attractive process as it can be scaled up to industrial production levels. The LiV_3O_8 powder is crystalline in nature with a specific surface area of $30.5 \text{ m}^2 \text{ g}^{-1}$. The flame-sprayed LiV_3O_8 nanocrystalline electrode exhibited fairly high specific capacity, retaining a discharge capacity of 180 mAh g^{-1} beyond 50 cycles. Capacity fading of the electrodes containing the FSP-made nanoparticles is attributed to the loss of active material through dissolution into the electrolyte and is also due to the phase transformation at 2.6 V.

However, both the V_2O_5 and LiV_3O_8 nanoparticles have to be prepared in a Li-rich phase, such as $\text{Li}_x\text{V}_2\text{O}_5$ or $\text{Li}_{1+x}\text{V}_3\text{O}_8$, in order to first be charged in a full cell. This is because cathode materials are Li-ion providers in a full cell, which means that they need to release the Li-ions in the first step of electrochemical cycling. This is necessary for the vanadium-based oxide materials to be incorporated as cathode materials in lithium-ion batteries. Nevertheless, both vanadium-based oxide powders show promise as cathode materials for use in high-powered applications in Li-ion batteries.

LiMn₂O₄ thin films deposited on either Si (100) or stainless steel substrate were successfully prepared via the pulsed laser deposition (PLD) method. The compositions of the as-deposited LiMn₂O₄ thin films were quite different when different substrates were used, even though the same deposition parameters were applied. The as-deposited LiMn₂O₄ thin films on stainless steel substrate were highly lithium- and oxygen-deficient, as confirmed by ERDA/RBS and Raman analysis. However, the precision of both the ERDA/RBS methods is still not error-proof, with a relative error of 5 %, which is still good compared to other methods, such as Nuclear Reaction Analysis (NRA). The lithium and oxygen contents increased when the pulse rate was increased, leading to thicker films. The LiMn₂O₄ thin film with the lowest deposition pulse rate (or thinnest film) exhibited the best electrochemical performance, retaining a charge capacity of 48 $\mu\text{Ah cm}^{-2} \mu\text{m}^{-1}$ beyond 100 cycles, and even a charge capacity above 40 $\mu\text{Ah cm}^{-2} \mu\text{m}^{-1}$ at 32C (equivalent to 160 $\mu\text{A cm}^{-2}$).

In order to fully understand the electrochemical kinetics and Li-ion insertion mechanisms, preferentially oriented and stoichiometric LiMn₂O₄ thin films need to be deposited on conductive substrates (such as stainless steel). Without the correct stoichiometric thin film, any conclusions drawn (as in most of the literature) are almost certain to be inaccurate to some extent. It is also not true to simply accept the practice of assuming that the thin films will have the same compositions as films deposited on different substrates, even if the same deposition parameters are applied. In addition, a standard unit of measurement for the specific capacity is needed for easier cross-reference and comparison for researchers working in the thin film area. The author would recommend the usage of $\mu\text{Ah cm}^{-2} \mu\text{m}^{-1}$ as the standard unit for specific capacity, as all the dimensions of the thin film are taken into account.

10.2 Outlook

In this doctoral work, the experimental work had been mainly focused on the synthesis of nanostructured materials and on applying them as electrode materials for use in lithium-ion batteries. However, based on the results obtained from the earlier chapters in this thesis work, some areas of particular interest should be further studied in future research directions. Some of the opportunities to understand the electrochemical behaviour of nanostructured electrodes will be suggested here for future reference.

For the SWCNT paper electrode, a reduction in cost could be implemented by partially substituting or fully replacing the SWCNT content with double-walled carbon nanotubes (DWCNTs) or multi-walled carbon nanotubes (MWCNTs). In order to reduce the large first cycle irreversible capacity, the specific surface area of the bucky paper has to be reduced significantly to less than $100 \text{ m}^2 \text{ g}^{-1}$, if possible, in order to reduce the huge surface decomposition reaction of the electrolyte. One of the main properties of a free-standing material is the ability to support itself, which means having excellent mechanical properties. Therefore, it is essential to gauge the mechanical properties of the bucky paper during the dry state and after immersion into the electrolyte system. Another possible route to improve the specific capacity of the bucky paper would be to incorporate other active electromaterials such as tin-based oxides into the walls or the inner tube surface of the carbon nanotube in order to obtain a homogenous and uniform dispersion of active mass in the nanotubes for higher efficiency and better electrochemical properties. Finally, it is also important to calculate the actual capacity of the free-standing material for the total mass of the system and compare it to a classical electrode, including the Cu foil mass.

For the carbon-coated Si nanocomposites, the attention needs to be focused on fully understanding the reasons behind the greatly improved electrochemical performance of the composite compared to pure nanocrystalline Si particles. This could be done by investigating the role of the amorphous carbon layer, or even the possible presence of an intermediate layer matrix between the nanocrystalline Si particle and amorphous carbon layer, with assistance from *in-situ* measurement techniques, such as Raman spectroscopy, X-ray photoelectron spectroscopy (XPS), dilatometry analysis, high-resolution electron energy loss spectroscopy (HR-EELS), differential electrochemical mass spectroscopy (DEMS), and electrochemical impedance spectroscopy (EIS). Furthermore, the influence of other spray parameters, such as the type of solvent used, the Si particle size, and also the different types of low-temperature carbon sources used, should be investigated and reviewed in detail in order to fully optimize the amount of carbon content in the Si nanocomposite materials.

For the vanadium-based oxide cathode materials, the most important aspect for future studies would be to determine the optimum amount of lithium-ion insertion needed for a stable specific capacity. This means that we need to find the optimum cut-off potentials in order to maximize the specific capacity for prolonged cycling, with a capacity of at least 200 mAh g⁻¹ required for any possible replacement of the current LiCoO₂ cathode materials. It is equally important to understand the reasons behind the stable capacity retention at that particular potential window, via *in-situ* analysis such as XRD, dilatometry, vanadium dissolution by ICP, and other structural characterization methods. When the optimum Li-ion content is obtained, this optimal lithium-rich vanadium oxide should be synthesized synthetically and applied directly as a cathode

material. This would make it more industrially oriented and suitable for application in lithium-ion battery cathodes.

As for the LiMn_2O_4 thin film area, subsequent research work should focus on preparing a stoichiometric film on other conductive substrates, such as glassy carbon or highly doped Si substrate. If the stainless steel were still applied as the substrate, it would be highly beneficial if thin films with a preferentially oriented lattice phase were obtained, such as in the (111) direction, in order to study the influence of surface direction on the formation of the solid-electrolyte interphase (SEI) during the electrochemical cycling. A quick and reliable method should be derived to estimate the stoichiometric amount of lithium in the thin films, in order to reduce the difficulties of using the RBS/ERDA method, which is time consuming and rather complicated. Finally, applying the lithium spinel thin film as a cathode material would need a targeted absolute capacity value for easy comparison and reference to other relevant research work in the thin films area.

The need to understand the surface kinetics and the corresponding structural and compositional changes during the electrochemical cycling are greater than ever, due to the almost saturated electrochemical performance of the current electrode materials for use in lithium-ion batteries, especially for high-power applications such as electric vehicles. *In-situ* characterization tools are one of the possible ways to move forward in order to drive further breakthroughs in lithium-ion battery performance. Nevertheless, the author believes the scientific challenges are being slowly overcome and that research is moving in the right direction, as has been shown in this thesis work.

REFERENCES

- Abraham, K. M., Goldmann, J. L., and Dempsey, M. D. (1981), *J. Electrochem. Soc.*, **128**, 2493-2501.
- Alonso, B., and Livage, J. (1999), *J. Solid State Chem.*, **148**, 16-19.
- Alvarez, L., Righi, A., Guillard, T., Rols, S., Anglaret, E., Laplaze, D., and Sauvajol, J. L. (2000), *Chem. Phys. Lett.*, **316**, 186-190.
- Ammundsen, B., and Paulsen, J. (2001), *Adv. Mater.*, **13**, 943-956.
- Ancona, M. G., Kooi, S. E., Kruppa, W., Snow, A. W., Foos, E. E., Whitman, L. J., Park, D., and Shirey, L. (2003), *Nano Lett.*, **3**, 135-138.
- Ando, Y., and Iijima, S. (1993), *Jpn. J. Appl. Phys.*, **32**, L107-L109.
- Andrievski, R. A., and Glezer, A. M. (2001), *Scripta Materialia*, **44**, 1621-1624.
- Antaya, M., Dahn, J. R., Preston, J. S., Rossen, E., and Reimers, J. N. (1993), *J. Electrochem. Soc.*, **140**, 575-578.
- Anzue, N., Itoh, T., Mohamedi, M., Umeda, M., and Uchida, I. (2003), *Solid State Ionics*, **156**, 301-307.
- Aricò, A. S., Bruce, P., Scrosati, B., Tarascon, J. M., and van Schalkwijk, W. (2005), *Nat. Mater.*, **4**, 366-377.
- Armand, M. (1978), *French Patent*, 7832977.
- Arnoldussen, T. C. (1981), *J. Electrochem. Soc.*, **128**, 117-123.
- Asao, M., Kawakami, S., and Ogura, T. (2004), *U.S. Patent Application*, 0248011.
- Aurbach, D., Markovsky, B., Weissman, I., Levi, E., and Ein-Eli, Y. (1999), *Electrochim. Acta*, **45**, 67-86.

-
- Bach, S., Henry, M., Baffier, N., and Livage, J. (1990), *J. Solid State Chem.*, **88**, 325-333.
- Bates, J. B., Dudney, N. J., Neudecker, B., Ueda, A., and Evans, C. D. (2000), *Solid State Ionics*, **135**, 33-45.
- Baughman, R. H., Cui, C., Zakhidov, A. A., Iqbal, Z., Barisci, J. N., Spinks, G. M., Wallace, G. G., Mazzoldi, A., Rossi, D. D., Rinzler, A. G., Jaschinski, O., Roth, S., and Kertesz, M. (1999), *Science*, **284**, 1340-1344.
- Baughman, R. H., Zakhidov, A. A., and de Heer, W. A. (2002), *Science*, **297**, 787-792.
- Beaulieu, L. Y., Hewitt, K. C., Turner, R. L., Bonakdarpour, A., Abdo, A. A., Christensen, L., Eberman, K. W., Krause, L. J., and Dahn, J. R. (2003), *J. Electrochem. Soc.*, **150**, A149-A156.
- Besenhard, J. O., Hess, M., and Komenda, P. (1990), *Solid State Ionics*, **40/41**, 525-529.
- Besenhard, J. O., Winter, M., Yang, J., and Biberacher, W. (1995), *J. Power Sources*, **54**, 228-231.
- Besenhard, J. O., Yang, J., and Winter, M. (1997), *J. Power Sources*, **68**, 87-90.
- Bewlay, S. L., Konstantinov, K., Wang, G. X., Dou, S. X., and Liu, H. K. (2004), *Materials Letters*, **58**, 1788-1791.
- Bonino, F., Ottaviani, M., and Scrosati, B. (1987), *J. Power Sources*, **20**, 333-338.
- Bonino, F., Ottaviani, M., Scrosati, B., and Pistoia, G. (1988), *J. Electrochem. Soc.*, **135**, 12-15.
- Boukamp, B. A., Lesh, G. C., and Huggins, R. A. (1981), *J. Electrochem. Soc.*, **128**, 725-728.
- Bragg, W. H., and Bragg, W. L. (1913), *Proceedings of the Royal Society of London Series A – Containing Papers of a Mathematical and Physical Character*, **88**, 428-438.

-
- Brett, C. M. A., and Brett, A. M. O. (1993), *Electrochemistry: Principles, Methods, and Applications*, Oxford University Press, Oxford.
- Broussely, M., Perton, F., and Labat, J. (1993), *J. Power Sources*, **43-44**, 209-216.
- Broussely, M., Biensan, P., and Simon, B. (1999), *Electrochim. Acta*, **45**, 3-22.
- Broussely, M., and Archdale, G. (2004), *J. Power Sources*, **136**, 386-394.
- Broussely, M. (2005), *PSI Symposium Day*, Villigen, Switzerland.
- Buqa, H., Würsig, A., Goers, D., Hardwick, L. J., Holzapfel, M., Novák, P., Krumeich, F., and Spahr, M. E. (2005), *J. Power Sources*, **146**, 134-141.
- Campana, F. R. (2005), *PhD Thesis*, Paul Scherrer Institute, Switzerland.
- Cava, R. J., Santoro, A., Murphy, D. W., Zahurak, S. M., Fleming, R. M., Marsh, P., and Roth, R. S. (1986), *J. Solid State Chem.*, **65**, 63-71.
- Ceder, G., Chiang, Y. M., Sadoway, D. R., Aydinol, M. K., Jang, Y. I., and Huang, B. (1998), *Nature*, **392**, 694-696.
- Chaklanabish, N. C., and Maiti, H. S. (1986), *Solid State Ionics*, **21**, 207-212.
- Che, G., Lakshmi, B. B., Fisher, E. R., and Martin, C. R. (1998), *Nature*, **393**, 346-349.
- Chen, C. H., Kelder, E. M., and Schoonman, J. (1997), *J. Power Sources*, **68**, 377-380.
- Chen, W., Peng, J., Mai, L., Zhu, Q., and Xu, Q. (2004a), *Mater. Lett.*, **58**, 2275-2278.
- Chen, G. S., Chen, G., Hsiao, H. H., Louh, R. F., and Humphreys, C. J. (2004b), *Electrochem. Solid State Lett.*, **7**, A235-A238.
- Chew, S. Y. (2006), *Higher Degree Research Postgraduate Progress Report*, University of Wollongong, Australia.
- Chew, S. Y., Feng, C., Ng, S. H., Wang, J., Guo, Z., and Liu, H. (2007), *J. Electrochem. Soc.*, **154**, A633-A637.
- Chiu, K. F., Lin, H. C., Lin, K. M., and Tsai, C. H. (2005), *J. Electrochem. Soc.*, **152**, A2058-A2062.

-
- Chiu, K. F., Lin, H. C., Lin, K. M., and Chen, C. C. (2006), *J. Electrochem. Soc.*, **153**, A1992-A1997.
- Chung, S. Y., Bloking, J. T., and Chiang, Y. M. (2002), *Nat. Mater.*, **1**, 123-128.
- Claye, A. S., Fischer, J. E., Huffman, C. B., Rinzler, A. G., and Smalley, R. E. (2000a), *J. Electrochem. Soc.*, **147**, 2845-2852.
- Claye, A., Fischer, J. E., and Métrot, A. (2000b), *Chem. Phys. Lett.*, **330**, 61-67.
- Cocciantelli, J. M., Doumerc, J. P., Pouchard, M., Broussely, M., and Labat, J. (1991), *J. Power Sources*, **34**, 103-111.
- Coluccia, M. (2000), *PhD Thesis*, Paul Scherrer Institute, Switzerland.
- Courtney, I. A., McKinnon, W. R., and Dahn, J. R. (1999), *J. Electrochem. Soc.*, **146**, 59-68.
- Cruz, M., Hernan, L., Morales, J., and Sanchez, L. (2002), *J. Power Sources*, **108**, 35-40.
- Cushing, B. L., Kolesnichenko, V. L., and O'Connor, C. J. (2004), *Chem. Rev.*, **104**, 3893-3946.
- Das, S. R., Majumder, S. B., and Katiyar, R. S. (2005), *J. Power Sources*, **139**, 261-268.
- de Heer, W. A. (2004), *MRS Bull.*, **29**, 281-285.
- Denis, S., Baudrin, E., Touboul, M., and Tarascon, J. M. (1997), *J. Electrochem. Soc.*, **144**, 4099-4109.
- Dimov, N., Kugino, S., and Yoshio, M. (2003), *Electrochim. Acta*, **48**, 1579-1587.
- Disma, F., Lenain, C., Beaudoin, B., Aymard, L., and Tarascon, J. M. (1997), *Solid State Ionics*, **98**, 145-155.
- Dresselhaus, M. S., and Thomas, I. L. (2001), *Nature*, **414**, 332-337.
- Drexler, K. E. (1986), *Engines of creation: the coming era of nanotechnology*, New York.

-
- Dumont, Th., Lippert, T., Döbeli, M., Grimmer, H., Ufheil, J., Novák, P., Würsig, A., Vogt, U., and Wokaun, A. (2006), *Appl. Surf. Sci.*, **252**, 4902-4906.
- Edelstein, A. S., Murday, J. S., and Rath, B. B. (1997), *Prog. Mater. Sci.*, **42**, 5-21.
- Endo, M., Kim, C., Nishimura, C. K., Fujino, T., and Miyashita, K. (2000), *Carbon*, **38**, 183-197.
- Ernst, F. O., Kammler, H. K., Roessler, A., Pratsinis, S. E., Stark, W. J., Ufheil, J., and Novák, P. (2007), *Mater. Chem. Phys.*, **101**, 372-378.
- Fan, J., and Fedkiw, P. S. (1998), *J. Power Sources*, **72**, 165-173.
- Fey, G. T. K., Hsieh, M. C., Jaw, H. K., and Lee, T. J. (1993), *J. Power Sources*, **43-44**, 673-680.
- Fong, R., Vonsacken, U., and Dahn, J. R. (1990), *J. Electrochem. Soc.*, **137**, 2009-2013.
- Frackowiak, E., Gautier, S., Gaucher, H., Bonnamy, S., and Béguin, F. (1999), *Carbon*, **37**, 61-69.
- Frackowiak, E., and Béguin, F. (2002), *Carbon*, **40**, 1775-1787.
- Fujita, Y., Miyazaki, K., and Tatsuyama, C. (1985), *Jpn. J. Appl. Phys.*, **24**, 1082-1086.
- Galy, J. (1992), *J. Solid State Chem.*, **100**, 229-245.
- Gao, B., Kleinhammes, A., Tang, X. P., Bower, C., Fleming, L., Wu, Y., and Zhou, O. (1999), *Chem. Phys. Lett.*, **307**, 153-157.
- Garcia, B., Farcy, J., Pereira-Ramos, J. P., Perichon, J., and Baffier, N. (1995), *J. Power Sources*, **54**, 373-377.
- Giacovazzo, C. (2002), *Fundamentals of crystallography*, Oxford University Press, Oxford.
- Goodenough, J. B., Nanjundaswamy, K. S., and Masquelier, C. (1997), *International Patent Application*, WO 97/40541.
- Goward, G. R., Leroux, F., and Nazar, L. F. (1998), *Electrochim. Acta*, **43**, 1307-1313.

-
- Grugeon, S., Laruelle, S., Herrera-Urbina, R., Dupont, L., Poizot, P., and Tarascon, J. M. (2001), *J. Electrochem. Soc.*, **148**, A285-A292.
- Gummow, R. J., Liles, D. C., and Thackeray, M. M. (1993), *Mater. Res. Bull.*, **28**, 1249-1257.
- Guo, Z. P., Ahn, J. H., Liu, H. K., and Dou, S. X. (2004), *J. Nanosci. Nanotechnol.*, **4**, 162-166.
- Guo, Z. P., Wang, J. Z., Liu, H. K., and Dou, S. X. (2005a), *J. Power Sources*, **146**, 448-451.
- Guo, Z. P., Milin, E., Wang, J. Z., Chen, J., and Liu, H. K. (2005b), *J. Electrochem. Soc.*, **152**, A2211-A2216.
- Guy, D., Lestriez, B., Guyomard, D. (2004), *Adv. Mater.*, **16**, 553-557.
- Guy, D., Lestriez, B., Bouchet, R., Gaudefroy, V., and Guyomard, D. (2005), *Electrochem. Solid State Lett.*, **8**, A17-A21.
- Ha, B., Park, J., Kim, S. Y., and Lee, C. J. (2006), *J. Phys. Chem. B*, **110**, 23742-23749.
- Hammou, A., and Hammouche, A. (1988), *Electrochim. Acta*, **33**, 1719-1720.
- Hardwick, L. J. (2007), *PhD Thesis*, Paul Scherrer Institute, Switzerland.
- Hasegawa, T., Mukai, S. R., Shirato, Y., and Tamon, H. (2004), *Carbon*, **42**, 2573-2579.
- Helmus, M. (2006), *Nature Nanotechnol.*, **1**, 157-158.
- Hikmet, R. A. M. (2001), *J. Power Sources*, **92**, 212-220.
- Holzapfel, M., Buqa, H., Scheifele, W., Novak, P., and Petrat, F. M. (2005a), *Chem. Commun.*, **12**, 1566-1568.
- Holzapfel, M., Buqa, H., Krumeich, F., Novak, P., Petrat, F. M., and Veit, C. (2005b), *Electrochem. Solid-State Lett.*, **8**, A516-A520.
- Hopper, A., and North, J. M. (1983), *Solid State Ionics*, **9-10**, 1161-1166.

- Hoshino, K., Murakami, T., Atsuka, A., Ozaki, Y., Watanabe, S., and Takahashi, Y. (1994), *Nat. Technol. Rep.*, **40**, 31-35.
- Huggins, R. A. (1989), *J. Power Sources*, **26**, 109-120.
- Huggins, R. A. (1998), *Solid State Ionics*, **113-115**, 57-67.
- Huggins, R. A. (1999), *J. Power Sources*, **81-82**, 13-19.
- Hwang, K. H., Lee, S. H., and Joo, S. K. (1994), *J. Electrochem. Soc.*, **141**, 3296-3299.
- Hwang, S. M., Lee, H. Y., Jang, S. W., Lee, S. M., Lee, S. J., Baik, H. K., and Lee, J. Y. (2001), *Electrochem. Solid-State Lett.*, **4**, A97-A100.
- Idota, Y., Mishima, M., Miyaki, Y., Kubota, T., and Miyasaki, T. (1994), *Canadian Patent Application*, 2134052.
- Idota, Y., and Mishima, M. (1995), *Canadian Patent Application*, 2143388.
- Idota, Y., Kubota, T., Matsufuji, A., Maekawa, Y., and Miyazaki, T. (1997), *Science*, **276**, 1395-1397.
- IEA World Energy Outlook (1998).
- Iijima, S. (1991), *Nature*, **354**, 56-58.
- Imawan, C., Steffes, H., Solzbacher, F., and Obermeier, F. (2001), *Sens. Actuators B*, **77**, 346-351.
- Inaba, M., Doi, T., Iriyama, Y., Abe, T., and Ogumi, Z. (1999), *J. Power Sources*, **81-82**, 554-557.
- Institute of Information Technology Ltd. (2002), *Annual Report*, Japan.
- Jang, H. D., Seong, C. M., Suh, Y. J., Kim, H. C., and Lee, C. K. (2004), *Aerosol Sci. Technol.*, **38**, 1027-1032.
- Jiang, C., Hosono, E., and Zhou, H. (2006), *Nano Today*, **1**, 28-33.
- Johnston, W. D., Heikes, R. R., and Sestrich, D. (1958), *J. Phys. Chem. Solids*, **7**, 1-13.

-
- Jorio, A., Pimenta, M. A., Souza Filho, A. G., Saito, R., Dresselhaus, G., and Dresselhaus, M. S. (2003), *New J. Phys.*, **5**, 139.1-139.17.
- Jouanneau, S., Le Gal La Salle, A., Verbaere, A., and Guyomard, D. (2005), *J. Electrochem. Soc.*, **152**, A1660-A1667.
- Julien, C., Haro-Poniatowski, E., Camacho-Lopez, M. A., Escobar-Alarcon, L., and Jimenez-Jarquin, J. (2000), *Mater. Sci. Eng. B*, **72**, 36-46.
- Julien, C. M., and Massot, M. (2003), *J. Phys.: Condens. Matter*, **15**, 3151-3162.
- Kang, Y. M., Kim, K. T., Lee, K. Y., Lee, S. J., Jung, J. H., and Lee, J. Y. (2003), *J. Electrochem. Soc.*, **150**, A1538-A1543.
- Kannan, A. M., and Manthiram, A. (2006), *J. Power Sources*, **159**, 1405-1408.
- Karunakaran, C., and Senthilvelan, S. (2005), *J. Colloid Interface Sci.*, **289**, 466-471.
- Kasamatsu, S., Shimamura, H., and Nitta, Y. (2003), *U.S. Patent*, 6548208.
- Kasavajjula, U., Wang, C., and Appleby, A. J. (2007), *J. Power Sources*, **163**, 1003-1039.
- Kataura, H., Kumazawa, Y., Maniwa, Y., Umezu, I., Suzuki, S., Ohtsuka, Y., and Achiba, Y. (1999), *Synth. Met.*, **103**, 2555-2558.
- Kawakita, J., Kato, T., Katayama, Y., Miura, T., and Kishi, T. (1999), *J. Power Sources*, **82**, 448-453.
- Kawamura, T., Makidera, M., Okada, S., Koga, K., Miura, N., and Yamaki, J. I. (2005), *J. Power Sources*, **146**, 27-32.
- Kepler, K. D., Vaughey, J. T., and Thackeray, M. M. (1999), *Electrochem. Solid-State Lett.*, **2**, 307-309.
- Kim, H., Choi, J., Sohn, H., and Kang, T. (1999), *J. Electrochem. Soc.*, **146**, 4401-4405.
- Kobayashi, S., Takemura, T., and Kaneko, F. (1987), *Jpn. J. Appl. Phys.*, **26**, L1274-L1276.

-
- Koike, S., Fujieda, T., Sakai, T., and Higuchi, S. (1999), *J. Power Sources*, **81-82**, 581-584.
- Komiyama, H., Yamaguchi, Y., and Noda, S. (2004), *Chem. Eng. Sci.*, **59**, 5085-5090.
- Konstantinov, K., Wang, J., Bewlay, S., Wang, G. X., Liu, H. K., Dou, S. X., and Ahn, J. H. (2003), *J. Metastable and Nanocrystalline Materials*, **15-16**, 325-330.
- Konstantinov, K., Bewlay, S., Wang, G. X., Lindsay, M., Wang, J. Z., and Liu, H. K. (2004a), *Electrochim. Acta*, **50**, 419-424.
- Konstantinov, K., Zhao, Z. W., Yuan, L., Liu, H. K., and Dou, S. X. (2004b), *Proceedings Advanced Materials for Energy Conversion II, TMS Annual Meeting Charlotte, USA*, 331-338.
- Kostecki, R., Kong, F., Matsuo, Y., and McLarnon, F. (1999), *Electrochim. Acta*, **45**, 225-233.
- Kroto, H. W., Heath, J. R., O'Brien, S. C., Curl, R. F., and Smalley, R. E. (1985), *Nature*, **318**, 162-163.
- Krusin-Elbaum, L., Newns, D. M., Zeng, H., Derycke, V., Sun, J. Z., and Sandstrom, R. (2004), *Nature*, **431**, 672-676.
- Kurita, N., and Endo, M. (2002), *Carbon*, **40**, 253-260.
- Labat, J., and Cocciantelli, J. M. (1989), *French Patent Application*, 8916337.
- Lakshmi, B. B., Patrissi, C. J., and Martin, C. R. (1997), *Chem. Mater.*, **9**, 2544-2550.
- Lampe-Önnerud, C., Thomas, J. O., Hardgrave, M., and Yde-Andersen, S. (1995), *J. Electrochem. Soc.*, **142**, 3648-3651.
- Lanz, M., Kormann, C., and Novák, P. (2003), *J. Solid State Electrochem.*, **7**, 658-664.
- Lao, Z. J., Konstantinov, K., Tournayre, Y., Ng, S. H., Wang, G. X., and Liu, H. K. (2006), *J. Power Sources*, **162**, 1451-1454.

-
- Larcher, D., Mudalige, C., George, A. E., Poter, V., Gharghour, M., and Dahn, J. R. (1999), *Solid State Ionics*, **122**, 71-83.
- Larcher, D., Sudant, G., Leriche, J. B., Chabre, Y., and Tarascon, J. M. (2002), *J. Electrochem. Soc.*, **149**, A234-A241.
- Lecerf, A., Broussely, M., and Gabano, J. P. (1989), *U.S. Patent*, 4980080.
- Lee, S. J., Lee, J. K., Chung, S. H., Lee, H. Y., Lee, S. M., and Baik, H. K. (2001), *J. Power Sources*, **97-98**, 191-193.
- Lee, K. T., Jung, Y. S., and Oh, S. M. (2003), *J. Am. Chem. Soc.*, **125**, 5652-5653.
- Lee, K. L., Jung, J. Y., Lee, S. W., Moon, H. S., and Park, J. W. (2004), *J. Power Sources*, **130**, 241-246.
- Lee, W. G., and Smith, R. L. (2005), *J. Electrochem. Soc.*, **152**, A1054-A1059.
- Leroux, F., Metenier, K., Gautier, S., Frackowiak, E., Bonnamy, S., and Beguin, F. (1999), *J. Power Sources*, **81**, 317-322.
- Li, H., Huang, X., Chen, L., Wu, Z., and Liang, Y. (1999a), *Electrochem. Solid State Lett.*, **2**, 547-549.
- Li, H., Huang, X., and Chen, L. (1999b), *Solid State Ionics*, **123**, 189-197.
- Li, H., Huang, X., and Chen, L. (1999c), *J. Power Sources*, **81-82**, 340-345.
- Li, N., Martin, C. R., and Scrosati, B. (2000a), *Electrochem. Solid State Lett.*, **3**, 316-318.
- Li, N., Patrissi, C. J., Che, G., and Martin, C. R. (2000b), *J. Electrochem. Soc.*, **147**, 2044-2049.
- Li, H., Shi, L., Lu, W., Huang, X., and Chen, L. (2001), *J. Electrochem. Soc.*, **148**, A915-A922.
- Li, L., Meyer, W. H., Wegner, G., and Mehrens, M. W. (2005), *Adv. Mater.*, **17**, 984-988.

-
- Li, H. X., Jiao, L. F., Yuan, H. T., Zhang, M., Guo, J., Wang, L. Q., Zhao, M., and Wang, Y. M. (2006), *Electrochem. Commun.*, **8**, 1693-1698.
- Linden, D., and Reddy, T. B. (2002), *Handbook of Batteries*, **3rd Edition**, McGraw-Hill, New York.
- Lindsay, M. J., Wang, G. X., and Liu, H. K. (2003), *J. Power Sources*, **119**, 84-87.
- Lindsay, M. J. (2004), *PhD Thesis*, University of Wollongong, Australia.
- Lindstrom, H., Sodergren, S., Solbrand, A., Renamo, H., Hjelm, J., Hagfeldt, A., and Lindquist, S. E. (1997), *J. Phys. Chem. B*, **101**, 7717-7722.
- Lira-Cantú, M., and Gómez-Romero, P. (1999), *J. Electrochem. Soc.*, **146**, 2029-2033.
- Liu, P., Moudrakovski, I. L., Liu, J., and Sayari, A. (1997), *Chem. Mater.*, **9**, 2513-2520.
- Liu, C., Fan, Y. Y., Liu, M., Cong, H. T., Cheng, H. M., and Dresselhaus, M. S. (1999a), *Science*, **286**, 1127-1129.
- Liu, P., Zhang, J. G., Turner, J. A., Tracy, C. E., and Benson, D. K. (1999b), *J. Electrochem. Soc.*, **146**, 2001-2005.
- Liu, Y., Hanai, K., Horikawa, K., Imanishi, N., Hirano, A., and Takeda, Y. (2004), *Mater. Chem. Phys.*, **89**, 80-84.
- Liu, W. R., Wang, J. H., Wu, H. C., Shieh, D. T., Yang, M. H., and Wu, N. L. (2005a), *J. Electrochem. Soc.*, **152**, A1719-A1725.
- Liu, Y., Matsumura, T., Imanishi, N., Hirano, A., Ichikawa, T., and Takeda, Y. (2005b), *Electrochem. Solid-State Lett.*, **8**, A599-A602.
- Liu, J., Wang, X., Peng, Q., and Li, Y. (2005c), *Adv. Mater.*, **17**, 764-767.
- Liu, H. K., Wang, G. X., Guo, Z., Wang, J., and Konstantinov, K. (2006), *J. Nanosci. Nanotechnol.*, **6**, 1-15.
- Livage, J. (1991), *Chem. Mater.*, **3**, 578-593.

-
- Lu, W., and Chung, D. D. L. (2001), *Carbon*, **39**, 493-496.
- Macklin, W. J., Neat, R. J., and Sandhu, S. S. (1992), *Electrochim. Acta*, **37**, 1715-1720.
- Mädler, L., Kammler, H. K., Mueller, R., and Pratsinis, S. E. (2002), *J. Aerosol Sci.*, **33**, 369-389.
- Maingot, S., Baffier, N., Pereira-Ramos, J. P., and Willman, P. (1993), *Solid State Ionics*, **67**, 29-34.
- Manev, V., Momchilov, A., Nassalevska, A., Pistoia, G., and Pasquali, M. (1995), *J. Power Sources*, **54**, 501-507.
- Manthiram, A., and Kim, J. (1998), *Chem. Mater.*, **10**, 2895-2909.
- Martos, M., Morales, J., Sanchez, L., Ayouchi, R., Leinen, D., Martin, F., and Ramos Barrado, J. R. (2001), *Electrochim. Acta*, **46**, 2939-2948.
- Martos, M., Morales, J., and Sanchez, L. (2003), *Electrochim. Acta*, **48**, 615-621.
- Massarotti, V., Capsoni, D., Bini, M., Chiodelli, G., Azzoni, C. B., Mozzati, M. C., and Paleari, A. (1999), *J. Solid State Chem.*, **147**, 509-515.
- Meunier, V., Kephart, J., Roland, C., and Berhole, J. (2002), *Phys. Rev. Lett.*, **88**, 7.
- Miura, T., and Kishi, T. (1995), *Mater. Res. Soc. Symp. Proc.*, **393**, 69-77.
- Miyaki, Y. (2005), *U.S. Patent Application*, 0181276.
- Mizushima, K., Jones, P. C., Wiseman, P. J., and Goodenough, J. B. (1980), *Mater. Res. Bull.*, **15**, 783-789.
- Moon, H. S., Lee, W., Reucroft, P. J., and Park, J. W. (2003), *J. Power Sources*, **119-121**, 710-712.
- Morcrette, M., Barboux, P., Perrière, J., and Brousse, T. (1998), *Solid State Ionics*, **112**, 249-254.
- Moriga, T., Watanabe, K., Tsuji, D., Massaki, S., Nakabayashi, I. (2000), *J. Solid State Chem.*, **153**, 386-390.

- Morita, T., and Takami, N. (2006), *J. Electrochem. Soc.*, **153**, A425-A430.
- Morris, R. S., Dixon, B. G., Gennett, T., Raffaele, R., and Heben, M. J. (2004), *J. Power Sources*, **138**, 277-280.
- Mueller, R., Mädler, L., and Pratsinis, S. E. (2003), *Chem. Eng. Sci.*, **58**, 1969-1976.
- Mukerjee, S., Thurston, T. R., Jisrawi, N. M., Yang, X. Q., McBreen, J., Daroux, M. L., and Xing, X. K. (1998), *J. Electrochem. Soc.*, **145**, 466-472.
- Murphy, D. W., Christian, P. A., DiSalvo, F. J., and Carides, J. N. (1979), *J. Electrochem. Soc.*, **126**, 497-499.
- Murphy, D. W., Christian, P. A., DiSalvo, F. J., Carides, J. N., and Waszcsak, J. V. (1981), *J. Electrochem. Soc.*, **128**, 2053-2060.
- Muster, J., Kim, G. T., Krstić, V., Park, J. G., Park, Y. W., Roth, S., and Burghard, M. (2000), *Adv. Mater.*, **12**, 420-424.
- Nagaura, T., and Tozawa, K. (1990), *Prog. Battery Solar Cells*, **9**, 209-217.
- Naoi, K., Ogihara, N., Igarashi, Y., Kamakura, A., Kusachi, Y., and Utsugi, K. (2005), *J. Electrochem. Soc.*, **152**, A1047-A1053.
- Nassau, K., and Murphy, D. W. (1981), *J. Non-Cryst. Solids*, **44**, 297-304.
- Needham, S. A. (2007), *PhD Thesis*, University of Wollongong, Australia.
- Ng, S. H., Wang, J., Guo, Z. P., Chen, J., Wang, G. X., and Liu H. K. (2005), *Electrochim. Acta*, **51**, 23-28.
- Ng, S. H., Wang, J., Konstantinov, K., Wexler, D., Chen, J., and Liu, H. K. (2006a), *J. Electrochem. Soc.*, **153**, A787-A793.
- Ng, S. H., Wang, J., Wexler, D., Konstantinov, K., Guo, Z. P., and Liu, H. K. (2006b), *Angew. Chem. Int. Ed.*, **45**, 6896-6899.
- Novak, P. (2007), *Interface Electrochemistry: The Scientific Key to Long-Lasting Lithium-Ion Batteries*, Paul Scherrer Institute, Switzerland.

- Ohzuku, T., Kitagawa, M., and Hirai, T. (1990), *J. Electrochem. Soc.*, **137**, 769-775.
- Ohzuku, T., and Ueda, A. (1994), *J. Electrochem. Soc.*, **141**, 2972-2977.
- Ohzuku, T., Ueda, A., and Yamamoto, N. (1995), *J. Electrochem. Soc.*, **142**, 1431-1435.
- Otsuji, H., Kawahara, K., Ikegami, T., and Ebihara, K. (2006), *Thin Solid Films*, **506-507**, 120-122.
- Ouyang, C., Deng, H., Ye, Z., Lei, M., and Chen, L. (2006), *Thin Solid Films*, **503**, 268-271.
- Owen, J. R. (1997), *Chem. Soc. Rev.*, **26**, 259-267.
- Padhi, A. K., Nanjundaswamy, K. S., and Goodenough, J. B. (1997), *J. Electrochem. Soc.*, **144**, 1188-1194.
- Pan, Q., Guo, K., Wang, L., and Fang, S. (2002), *J. Mater. Chem.*, **12**, 1833-1838.
- Panero, S., Pasquali, M., and Pistoia, G. (1983), *J. Electrochem. Soc.*, **130**, 1225-1230.
- Park, M. S., Lee, Y. J., Rajendran, S., Song, M. S., Kim, H. S., and Lee, J. Y. (2005), *Electrochim. Acta*, **50**, 5561-5567.
- Pasquali, M., Pistoia, G., Manev, V., and Moshtev, R. V. (1986), *J. Electrochem. Soc.*, **133**, 2454-2458.
- Pasquali, M., and Pistoia, G. (1991), *Electrochim. Acta*, **36**, 1549-1553.
- Patrissi, C. J., and Martin, C. R. (2001), *J. Electrochem. Soc.*, **148**, A1247-A1253.
- Peled, E. (1979), *J. Electrochem. Soc.*, **126**, 2047-2051.
- Pereira, N., Balasubramanian, M., Dupont, L., McBreen, J., Klein, L. C., and Amatucci, G. G. (2003), *J. Electrochem. Soc.*, **150**, A1118-A1128.
- Pereira-Ramos, J. P. (1995), *J. Power Sources*, **54**, 120-126.
- Pervov, V. S., Kedrinskii, I. A., and Makhonina, E. V. (1997), *Inorg. Mater.*, **33**, 869-877.
- Piotto, A. P. (2004), *PhD Thesis*, Paul Scherrer Institute, Switzerland.

-
- Pistoia, G., Panero, S., Tocci, M., Moshtev, R. V., and Manev, V. (1984), *Solid State Ionics*, **13**, 311-318.
- Pistoia, G., Pasquali, M., Tocci, M., Moshtev, R. V., and Manev, V. (1985a), *J. Electrochem. Soc.*, **132**, 281-284.
- Pistoia, G., Pasquali, M., Tocci, M., Manev, V., and Moshtev, R. V. (1985b), *J. Power Sources*, **15**, 13-25.
- Pistoia, G., Rodante, F., and Tocci, M. (1986), *Solid State Ionics*, **20**, 25-30.
- Pistoia, G., Di Vona, M. L., and Tagliatesta, P. (1987), *Solid State Ionics*, **24**, 103-109.
- Pistoia, G., Pasquali, M., Wang, G., and Li, L. (1990), *J. Electrochem. Soc.*, **137**, 2365-2370.
- Pistoia, G., Wang, G., and Zane, D. (1995), *Solid State Ionics*, **76**, 285-291.
- Pletcher, D. (1991), *A First Course in Electrode Processes*, The Electrochemistry Consultancy, Alresford, Hants.
- Poizot, P., Laurelle, S., Grugeon, S., Dupont, L., and Tarascon, J. M. (2000), *Nature*, **407**, 496-499.
- Prengaman, R. D. (1997), *J. Power Sources*, **67**, 267-278.
- Prosini, P. P., Carewska, M., Scaccia, S., Wisniewski, P., Passerini, S., and Pasquali, M. (2002), *J. Electrochem. Soc.*, **149**, A886-A890.
- Raju, A. R., and Rao, C. N. R. (1991), *J. Chem. Soc. Chem. Commun.*, **18**, 1260-1261.
- Rao, A. M., Eklund, P. C., Bandow, S., Thess, A., and Smalley, R. E. (1997), *Nature*, **388**, 257-259.
- Reimers, J. N., and Dahn, J. R. (1992), *J. Electrochem. Soc.*, **139**, 2091-2097.
- Reimers, J. N., Fuller, E. W., Rossen, E., and Dahn, J. R. (1993), *J. Electrochem. Soc.*, **140**, 3396-3401.
- Rho, Y. H., Dokko, K., and Kanamura, K. (2006), *J. Power Sources*, **157**, 471-476.

-
- Ritchie, A. G. (2004), *J. Power Sources*, **136**, 285-289.
- Roberts, G. A., Cairns, E. J., and Reimer, J. A. (2002), *J. Power Sources*, **110**, 424-429.
- Rougier, A., Graveau, P., and Delmas, C. (1996), *J. Electrochem. Soc.*, **143**, 1168-1175.
- Rougier, A., Striebel, K. A., Wen, S. J., and Cairns, E. J. (1998a), *J. Electrochem. Soc.*, **145**, 2975-2980.
- Rougier, A., Striebel, K. A., Wen, S. J., Richardson, T. J., Reade, R. P., and Cairns, E. J. (1998b), *Appl. Surf. Sci.*, **134**, 107-115.
- Sanchez, C., Morineau, R., and Livage, J. (1983), *Phys. Status Solidi A*, **76**, 661-666.
- Satishkumar, B. C., Govindaraj, A., Nath, M., and Rao, C. N. R. (2000), *J. Mater. Chem.*, **10**, 2115-2119.
- Schlecht, U., Guse, B., Raible, I., Vossmeier, T., and Burghard, M. (2004), *Chem. Commun.*, **19**, 2184-2185.
- Scrosati, B., Selvaggi, A., Croce, F., and Gang, W. (1988), *J. Power Sources*, **24**, 287-294.
- Scrosati, B. (1995), *Nature*, **372**, 557-558.
- Sharma, R. A., and Seefurth, R. N. (1976), *J. Electrochem. Soc.*, **123**, 1763-1768.
- Shimoda, H., Gao, B., Tang, X. P., Kleinhammes, A., Fleming, L., Wu, Y., and Zhou, O. (2002), *Phys. Rev. Lett.*, **88**, 015502.
- Shodai, T., Okada, S., Tobishima, S., and Yamabi, J. (1996), *Solid State Ionics*, **786**, 86-88.
- Shokoohi, F. K., Tarascon, J. M., and Wilkens, B. J. (1991), *Appl. Phys. Lett.*, **59**, 1260-1262.
- Shokoohi, F. K., Tarascon, J. M., Wilkens, B. J., Guyomard, D., and Chang, C. C. (1992), *J. Electrochem. Soc.*, **139**, 1845-1849.
- Shouji, E., and Buttry, D. A. (2000), *Electrochim. Acta*, **45**, 3757-3764.

-
- Shui, J. L., Jiang, G. S., Xie, S., and Chen, C. H. (2004), *Electrochim. Acta*, **49**, 2209-2213.
- Sides, C. R., Croce, F., Young, V. Y., Martin, C. R., and Scrosati, B. (2005), *Electrochem. Solid-State Lett.*, **8**, A484-A487.
- Singh, D., Houriet, R., Giovannini, R., Hofmann, H., Craciun, V., and Singh, R. K. (2001), *J. Power Sources*, **97-98**, 826-831.
- Singh, D., Kim, W. S., Craciun, V., Hofmann, H., and Singh, R. K. (2002), *Appl. Surf. Sci.*, **197-198**, 516-521.
- Söörda, R., Burghard, M., and Kern, K. (2001), *Appl. Phys. Lett.*, **79**, 2073-2075.
- Spahr, M. E., Bitterli, P., Nesper, R., Müller, M., Krumeich, F., and Nissen, H. U. (1998), *Angew. Chem. Int. Ed.*, **37**, 1263-1265.
- Spahr, M. E., Buqa, H., Würsig, A., Goers, D., Hardwick, L., Novák, P., Krumeich, F., Dentzer, J., and Vix-Guterl, C. (2006), *J. Power Sources*, **153**, 300-311.
- Stark, W. J., and Pratsinis, S. E. (2002), *Powder Technol.*, **126**, 103-108.
- Steele, B. C. H., Lagos, G. E., Spurdens, P. C., Forsyth, C., and Ford, A. D. (1983), *Solid State Ionics*, **9-10**, 391-398.
- Strano, M. S., Zheng, M., Jagota, A., Onoa, G. B., Heller, D. A., Barone, P. W., and Usrey, M. L. (2004), *Nano Lett.*, **4**, 543-550.
- Striebel, K. A., Deng, C. Z., Wen, S. J., and Cairns, E. J. (1996), *J. Electrochem. Soc.*, **143**, 1821-1827.
- Striebel, K. A., Rougier, A., Horne, C. R., Reade, R. P., and Cairns, E. J. (1999), *J. Electrochem. Soc.*, **146**, 4339-4347.
- Strobel, P., LeCras, F., and Anne, M. (1996), *J. Solid State Chem.*, **124**, 83-94.
- Sudant, G., Baudrin, E., Dunn, B., and Tarascon, J. M. (2004), *J. Electrochem. Soc.*, **151**, A666-A671.

-
- Sudant, G., Baudrin, E., Larcher, D., and Tarascon, J. M. (2005), *J. Mater. Chem.*, **15**, 1263-1269.
- Sumanasekera, G. U., Adu, C. K. W., Fang, S., and Eklund, P. C. (2000), *Phys. Rev. Lett.*, **85**, 1096-1099.
- Swider-Lyons, K. E., Love, C. T., and Rolison, D. R. (2002), *Solid State Ionics*, **152-153**, 99-104.
- Tang, S. B., Lai, M. O., Lu, L., and Tripathy, S. (2006a), *J. Solid State Chem.*, **179**, 3831-3838.
- Tang, S. B., Lai, M. O., and Lu, L. (2006b), *Electrochim. Acta*, **52**, 1161-1168.
- Tang, S. B., Lai, M. O., and Lu, L. (2007), *J. Power Sources*, **164**, 372-378.
- Taniguchi, N. (1974), *Proc. Int. Conf. Prod. Eng. Tokyo*, **Part II**, Japan Society of Precision Engineering.
- Tarascon, J. M., and Guyomard, D. (1991), *J. Electrochem. Soc.*, **138**, 2864-2868.
- Tarascon, J. M., and Guyomard, D. (1993), *Electrochim. Acta*, **38**, 1221-1231.
- Tarascon, J. M., and Armand, M. (2001), *Nature*, **404**, 359-367.
- Thackeray, M. M., David, W. I. F., Bruce, P. G., and Goodenough, J. B. (1983), *Mater. Res. Bull.*, **18**, 461-472.
- Thackeray, M. M., Mansuetto, M. F., and Bates, J. B. (1997), *J. Power Sources*, **68**, 153-158.
- Thess, A., Lee, R., Nikolaev, P., Dai, H., Petit, P., Robert, J., Xu, C., Lee, Y. H., Kim, S. G., Rinzler, A. G., Colbert, D. T., Scuseria, G. E., Tomanek, D., Fischer, J. E., and Smalley, R. E. (1996), *Science*, **273**, 483-487.
- Tirado, J. L. (2003), *Mater. Sci. Eng. R*, **40**, 103-136.
- Torralba, M. (1976/1977), *J. Power Sources*, **1**, 301-310.

-
- Tranchant, A., Messina, R., and Perrichon, J. (1980), *J. Electroanal. Chem.*, **113**, 225-232.
- Tsumura, T., Shimizu, A., and Inagaki, M. (1993), *J. Mater. Chem.*, **3**, 995-996.
- Uchida, I., Mohamedi, M., Dokko, K., Nishizawa, M., Itoh, T., and Umeda, M. (2001), *J. Power Sources*, **97-98**, 518-524.
- Uchiyama, M., Slane, S., Plichta, E., and Salomon, M. (1987), *J. Power Sources*, **10**, 279-286.
- Vohrer, U., Kolaric, I., Haque, M. H., Roth, S., and Detlaff-Weglikowska, U. (2004), *Carbon*, **42**, 1159-1164.
- Wadsley, A. D. (1957), *Acta Cryst.*, **10**, 261-267.
- Wagemaker, M., Kentgens, A. P. M., and Mulder, F. M. (2002), *Nature*, **418**, 397-399.
- Walk, C. R., and Gore, J. S. (1975), *J. Electrochem. Soc.*, **122**, C68.
- Wang, J., Raistrick, I. D., and Huggins, R. A. (1986), *J. Electrochem. Soc.*, **133**, 457-460.
- Wang, B., Qiu, W., and Liu, Q. (1992), *Solid State Ionics*, **52**, 363-365.
- Wang, C. S., Wu, G. T., Zhang, X. B., Qi, Z. F., and Li, W. Z. (1998), *J. Electrochem. Soc.*, **145**, 2751-2758.
- Wang, G. X., Chen, Y., Konstantinov, K., Yao, J., Ahn, J., Liu, H. K., and Dou, S. X. (2002), *J. Alloy Comp.*, **340**, L5-L10.
- Wang, T., Ma, Z., Xu, F., and Jiang, Z. (2003), *Electrochem. Commun.*, **5**, 599-602.
- Wang, G. X., Ahn, J. H., Yao, J., Bewlay, S., and Liu, H. K. (2004), *Electrochem. Commun.*, **6**, 689-692.
- Wang, G. X., Yang, L., Bewlay, S. L., Chen, Y., Liu, H. K., and Ahn, J. H. (2005), *J. Power Sources*, **146**, 521-524.
- Wautelet, M. (2001), *Eur. J. Phys.*, **22**, 601-611.

-
- West, K., Zachau-Christiansen, B., and Jacobsen, T. (1983), *Electrochim. Acta*, **28**, 1829-1833.
- West, K., Zachau-Christiansen, B., Jacobsen, T., and Atlung, S. (1985), *J. Power Sources*, **14**, 235-245.
- West, K., Zachau-Christiansen, B., Østergård, M. J. L., and Jacobsen, T. (1987), *J. Power Sources*, **20**, 165-172.
- Weydanz, W. J., Wohlfahrt-Mehrens, M., and Huggins, R. A. (1999), *J. Power Sources*, **82**, 237-242.
- Whittingham, M. S. (1976), *J. Electrochem. Soc.*, **123**, 315-320.
- Whittingham, M. S. (1976), *Science*, **192**, 1126-1127.
- Whittingham, M. S. (2004), *Chem. Rev.*, **104**, 4271-4301.
- Whittingham, M. S., Song, Y., Lutta, S., Zavalij, P. Y., and Chernova, N. A. (2005), *J. Mater. Chem.*, **15**, 3362-3379.
- Wiechert, D. U., Grabowski, S. P., and Simon, M. (2005), *Thin Solid Films*, **484**, 73-82.
- Wilkinson, S. (2000), *Chem. Eng. News*, **78**, 11-13.
- Willmott, P. R. (2004), *Prog. Surf. Sci.*, **76**, 163-217.
- Wilson, A. M., Reimers, J. N., Fuller, E. W., and Dahn, J. R. (1994), *Solid State Ionics*, **74**, 249-254.
- Wilson, A. M., and Dahn, J. R. (1995), *J. Electrochem. Soc.*, **142**, 326-332.
- Winter, M., Besenhard, J. O., Spahr, M. E., and Novak, P. (1998), *Adv. Mater.*, **10**, 725-763.
- Winter, M., and Besenhard, J. O. (1999), *Electrochim. Acta*, **45**, 31-50.
- Winter, M., and Brodd, R. J. (2004), *Chem. Rev.*, **104**, 4245-4269.
- Wong, H. P., Dave, B. C., Leroux, F., Harreld, J., Dunn, B., and Nazar, L. F. (1998), *J. Mater. Chem.*, **8**, 1019-1027.

-
- Wruck, D., Ramamurthi, S., and Rubin, M. (1989), *Thin Solid Films*, **182**, 79-86.
- Wu, Y. P., Rahm, E., and Holze, R. (2003a), *J. Power Sources*, **114**, 228-236.
- Wu, X., Wang, Z., Chen, L., and Huang, X. (2003b), *Electrochem. Commun.*, **5**, 935-939.
- Wu, X. M., He, Z. Q., Chen, S., Ma, M. Y., Xiao, Z. B., and Liu, J. B. (2006), *Mater. Lett.*, **60**, 2497-2500.
- Wu, X. M., Chen, S., He, Z. Q., Ma, M. Y., Xiao, Z. B., and Liu, J. B. (2007), *Mater. Chem. Phys.*, **101**, 217-220.
- Xu, K. (2004), *Chem. Rev.*, **104**, 4303-4417.
- Yamada, I., Abe, T., Iriyama, Y., and Ogumi, Z. (2003), *Electrochem. Commun.*, **5**, 505-505.
- Yang, J., Winter, M., and Besenhard, J. O. (1996), *Solid State Ionics*, **90**, 281-287.
- Yang, Z., Wu, H. Q., and Simard, B. (2002), *Electrochem. Commun.*, **4**, 574-578.
- Yang, X., Wen, Z., Zhu, X., and Huang, S. (2005a), *Electrochem. Solid-State Lett.*, **8**, A481-A483.
- Yang, G., Wang, G., and Hou, W. (2005b), *J. Phys. Chem. B*, **109**, 11186-11196.
- Yazami, R., Lebrun, N., Bonneau, M., and Molteni, M. (1995), *J. Power Sources*, **54**, 389-392.
- Yoon, S. H., Park, C. W., Yang, H. J., Korai, Y., Mochida, I., Baker, R. T. K., and Rodriguez, N. M. (2003), *Carbon*, **42**, 21-32.
- Yoshikawa, M., Katagiri, G., Ishida, H., and Ishitani, A. (1988), *Solid State Commun.*, **66**, 1177-1180.
- Yoshino, A. (1985), *Japanese Patent*, 1989293.
- Yoshio, M., Noguchi, H., Tominaga, K., and Tanaka, H. (1992), *Progress in Batteries and Battery Materials*, **11**, 158-164.

- Yoshio, M., Wang, H., Fukuda, K., Umeno, T., Dimov, N., and Ogumi, Z. (2002), *J. Electrochem. Soc.*, **149**, A1598-A1603.
- Yuan, Z., Huang, F., Feng, C., Sun, J., and Zhou, Y. (2003), *Mater. Sci. Phys.*, **79**, 1-4.
- Yuan, L., Konstantinov, K., Wang, G. X., Liu, H. K., and Dou, S. X. (2005), *J. Power Sources*, **146**, 180-184.
- Zhang, F., Zavalij, P. Y., and Whittingham, M. S. (1997), *Mater. Res. Bull.*, **32**, 701-707.
- Zhang, F., and Whittingham, M. S. (2000), *Electrochem. Commun.*, **2**, 69-71.
- Zhang, S. (2003), *Materials Today*, **6**, 20-27.

APPENDIX A

LIST OF PUBLICATIONS

- 1) **S.H. Ng**, J. Wang, K. Konstantinov, D. Wexler, S.Y. Chew, Z.P. Guo and H.K. Liu, “Spray-pyrolyzed silicon/disordered carbon nanocomposites for lithium-ion battery anodes”, *Journal of Power Sources*, **In Press, Corrected Proof, Available Online 29 June 2007**. IF 3.521
- 2) **S.H. Ng**, S.Y. Chew, J. Wang, D. Wexler, Y. Tournayre, K. Konstantinov and H.K. Liu, “Synthesis and electrochemical properties of V_2O_5 nanostructures prepared via a precipitation process for lithium-ion battery cathodes”, *Journal of Power Sources*, **In Press, Corrected Proof, Available Online 29 June 2007**. IF 3.521
- 3) **S.H. Ng**, J. Wang, D. Wexler, S.Y. Chew and H.K. Liu, “Amorphous carbon-coated silicon nanocomposites: A low temperature synthesis via spray pyrolysis, and their application as high capacity anodes for Li-ion batteries”, *The Journal of Physical Chemistry C* **111** (2007) 11131-11138. IF N/A
- 4) **S.H. Ng**, D.I. dos Santos, S.Y. Chew, D. Wexler, J. Wang, S.X. Dou and H.K. Liu, “Polyol-mediated synthesis of ultrafine tin oxide nanoparticles for reversible Li-ion storage”, *Electrochemistry Communications* **9** (2007) 915-919. IF 3.484

-
- 5) **See-How Ng**, Jiazhao Wang, David Wexler, Konstantin Konstantinov, Zai-Ping Guo and Hua-Kun Liu, "Highly reversible lithium storage in spheroidal carbon-coated silicon nanocomposites as anodes for lithium-ion batteries", *Angewandte Chemie International Edition* **45** (2006) 6896-6899. *Angewandte Chemie* **118** (2006) 7050-7053. IF 10.232
- 6) **S.H. Ng**, J. Wang, K. Konstantinov, D. Wexler, J. Chen and H.K. Liu, "Spray pyrolyzed PbO-carbon nanocomposites as anode for lithium-ion batteries", *Journal of the Electrochemical Society* **153** (2006) A787-A793. IF 2.387
- 7) **S.H. Ng**, J. Wang, Z.P. Guo, J. Chen, G.X. Wang and H.K. Liu, "Single wall carbon nanotube paper as anode for lithium-ion battery", *Electrochimica Acta* **51** (2005) 23-28. IF 2.955
- 8) **S.H. Ng**, J. Wang, K. Konstantinov, D. Wexler, and H.K. Liu, "Effect of carbon source as additive in spray-pyrolyzed PbO as anode for Li-ion batteries", <http://www.aip.org.au/wagga2006/> (available online 17 July 2006).
- 9) **S.H. Ng**, J. Wang, D. Wexler, and H.K. Liu, "Single-walled carbon nanotube/carbon black composite paper for Li-ion battery anodes", <http://www.aip.org.au/wagga2006/> (available online 17 July 2006).
- 10) T.J. Patey, **S.H. Ng**, R. Büchel, N. Tran, F. Krumeich, J. Wang, H.K. Liu and P. Novák, "Electrochemistry of LiV_3O_8 nanoparticles made by flame spray pyrolysis", *Electrochemical and Solid-State Letters* (submitted 24 September 2007). IF 2.009

-
- 11) J. Wang, **S.H. Ng**, S.Y. Chew, D. Wexler, G.X. Wang and H.K. Liu, "Characterization of nanosize molybdenum trisulfide for lithium batteries and MoS_3 structure confirmation via electrochemistry", *Electrochemical and Solid-State Letters* **10** (2007) A204-A207. IF 2.009
- 12) Z.P. Guo, **S.H. Ng**, J.Z. Wang, Z.G. Huang, H.K. Liu, C.O. Too and G.G. Wallace, "Electrochemical hydrogen storage in single-walled carbon nanotube paper", *Journal of Nanoscience and Nanotechnology* **6** (2006) 713-718. IF 2.194
- 13) K. Konstantinov, **S.H. Ng**, J.Z. Wang, G.X. Wang, D. Wexler and H.K. Liu, "Nanostructured PbO materials obtained in-situ by spray solution technique for Li-ion batteries", *Journal of Power Sources* **159** (2006) 241-244. IF 3.521
- 14) J. Wang, **S.H. Ng**, G.X. Wang, J. Chen, L. Zhao, Y. Chen and H.K. Liu, "Synthesis and characterization of nanosize cobalt sulfide for rechargeable lithium batteries", *Journal of Power Sources* **159** (2006) 287-290. IF 3.521
- 15) S.Y. Chew, C. Feng, **S.H. Ng**, J. Wang, Z. Guo and H. Liu, "Low-temperature synthesis of polypyrrole-coated LiV_3O_8 composite with enhanced electrochemical properties", *Journal of the Electrochemical Society* **154** (2007) A633-A637. IF 2.387

-
- 16) Jiazhao Wang, Guoxiu Wang, Li Yang, **See How Ng** and Huakun Liu, “An investigation on electrochemical behavior of nanosize zinc sulfide electrode in lithium-ion cells”, *Journal of Solid State Electrochemistry* **10** (2006) 250-254. IF 1.542
- 17) Z.J. Lao, K. Konstantinov, Y. Tournayre, **S.H. Ng**, G.X. Wang and H.K. Liu, “Synthesis of vanadium pentoxide powders with enhanced surface-area for electrochemical capacitors”, *Journal of Power Sources* **162** (2006) 1451-1454. IF 3.521
- 18) J. Wang, S.Y. Chew, D. Wexler, G.X. Wang, **S.H. Ng** and H.K. Liu, “Nanostructured nickel sulfide synthesized via a polyol route as a cathode material for the rechargeable lithium battery”, *Electrochemistry Communications* **9** (2007) 1877-1880. IF 3.484
- 19) J. Wang, J. Chen, K. Konstantinov, L. Zhao, **S.H. Ng**, G.X. Wang, Z.P. Guo and H.K. Liu, “Sulphur-polypyrrole composite positive electrode materials for rechargeable lithium batteries”, *Electrochimica Acta* **51** (2006) 4634-4638. IF 2.955
- 20) S.Y. Chew, Z.P. Guo, J.Z. Wang, J. Chen, P. Munroe, **S.H. Ng**, L. Zhao and H.K. Liu, “Novel nano-silicon/polypyrrole composites for lithium storage”, *Electrochemistry Communications* **9** (2007) 941-946. IF 3.484